TECHNISCHE UNIVERSITÄT MÜNCHEN

TUM School of Medicine and Health

Development and Biological Evaluation of Novel Positron Emission Tomography (PET) Radiotracers for the In Vivo Imaging of α-Synuclein Aggregates

Bright Chukwunwike Uzuegbunam

Vollständiger Abdruck der von der TUM School of Medicine and Health

der Technischen Universität München zur Erlangung eines

Doctor of Philosophy (Ph.D.)

genehmigten Dissertation.

Vorsitz: Prof. Dr. Angelika Harbauer

Betreuer: Prof. Dr. Wolfgang A. Weber

Prüfende der Dissertation:

1. Priv.-Doz. Dr. Behrooz H. Yousefi
2. Prof. Dr. Susanne Kossatz

Die Dissertation wurde am 17.08.2023 bei der Fakultät für Medizin der Technischen Universität München eingereicht und durch die TUM School of Medicine and Health
am 05.10.2023 angenommen.

1. Acknowledgment

The success of this project relies on the synergy between individuals working towards a shared objective: generating robust results that validate or refute a theory. This collaborative approach requires not only the sharing of expertise but also access to specialized facilities that facilitate the research process. Given its interdisciplinary nature, this dissertation brings together insights from organic chemistry, radiopharmacy, neuroscience, pharmacology, and mathematics, demonstrating the power of collaborative research.

I would like to extend my gratitude to the following individuals who significantly contributed to the success of this project. Given the novelty of 4,4´-disarylbisthiazoles (DABTAs), much of the methodology was developed in-house, and their expertise and dedication were invaluable. Prof. Dr. Wolfgang Weber for his support in ensuring the smooth progress of the project and for his valuable insights. I am also thankful that he took over the role of my primary supervisor following the departure of PD Dr. Behrooz Yousefi to Philipps University, Marburg. Additionally, I would like to thank PD Dr. Behrooz Yousefi, my co-supervisor, for recognizing my potential. His support—from securing the DAAD scholarship to his continued supervision, even in absentia—along with his valuable guidance and insights, contributed to my development as an independent researcher. I am also grateful to Prof. Dr. Susanne Kossatz for her valuable support and assistance throughout the project.

Special thanks to Dr. Thomas Arzberger, who not only selected and provided us with valuable post-mortem brain sections exhibiting proteinopathies but also contributed important insights to the results and offered clarifications on the subject. I extend my sincere gratitude to Mr. Michael Herz and Mr. Reinhold Klitsch for ensuring the consistent availability of fluorine-18 and carbon-11 for the radiosyntheses. I am also grateful to Dr. Stephanie Robu for her support. I would like to thank Ms. Sandra Sühnel, Mr. Markus Mittelhäuser, Dr. Nadine Setzer, Ms. Sybille Reder, Mr. Hannes Robelski, and the animal technicians at TranslaTUM for their assistance with animal experimentation. Furthermore, I appreciate the help of Ms. Marina Schenk and Mr. Matthias Heinzl in providing solvents necessary for the chemical and radiochemical syntheses. My gratitude also goes to Mr. Jakob Allman, Ms. Simone Keber, and Mr. Maximilian Perzl for their efforts to minimize radioactivity contamination throughout the project. Finally, I am thankful to everyone at the Nuclear Medicine Department for their support, whether direct or indirect.

I would also like to acknowledge Prof. Dr. Per Svenningsson and Dr. Wojciech Paslawski for their warm reception at the Svenningsson Lab, where I was able to conduct valuable experiments and acquire new skills. I am also grateful to PD Dr. Jeroen Goos and Ms. Åsa Södergren for generously sharing their expertise in autoradiography. Finally, I would like to thank Prof. Dr. Hans Ågren and Dr. Junhao Li for the fruitful collaboration on *in silico* DABTA design.

In memoriam, Eng. Chike Uzuegbunam, until 2020

2. Declaration

I declare on oath that this thesis is my own work. Contributions from any other person(s) were acknowledged in the thesis. Published data were referenced appropriately. This work has not been submitted in any form for a degree or diploma at any other university or institution of higher learning. Information from the published or unpublished works of others was cited appropriately in the text, accompanied by a list of references.

3. Abstract

Purpose

The deposition of α-synuclein fibrils (α-syn) is a common feature of a group of neurodegenerative diseases collectively known as the α-synucleinopathies. These include Parkinson's disease (PD), dementia with Lewy bodies (DLB), and multiple system atrophy (MSA). Due to the increasing incidence and prevalence of these diseases in the aging population, there is enormous interest in non-invasive PET (positron emission tomography) imaging of α-syn deposition in the brain for early diagnosis and treatment monitoring. Moreover, the detection of α-syn is complicated by the presence of other protein aggregates such as β-amyloid plaques (Aβ) and tau fibrils. Presently, no α-syn specific radiotracers are available for the specific detection of α-syn in humans. Here are reported the development and preclinical characterization of new α-syn specific radiotracers based on a DABTA scaffold.

Method

A focused library of fifty-three precursors and standard compounds was synthesized via a modified two-step Hantzsch thiazole synthesis, with an additional third step for the phenol/pyrimidinol DABTAs. The precursors were subsequently radiolabeled via ruthenium-mediated S_NAr deoxyradiofluorination, halogen-fluorine exchange S_NAr, S_N2-mediated two-step radiofluorination reactions, or S_N2-mediated two-step [^{11}C]methylation. The standard compounds were used for the characterization of the radiotracers as high-performance liquid chromatography (HPLC) references, blocking experiments, and in vitro competition binding assays. Further characterization of the radiotracers was accomplished via log $D_{7.4}$ (octanol-water distribution coefficient at pH 7.4) determination, in vitro plasma stability, plasma binding experiments, and in vitro autoradiography with mouse and postmortem human brain tissues (PHBT). Additionally, ex vivo biodistribution, ex vivo metabolite studies and in vivo small animal PET/MR (magnetic resonance) dynamic brain scans were also carried out on healthy mice.

Result

The two-step synthesis of the DABTAs gave an overall yield between 15.6–70.9%. Radiochemical yields (RCY) were mostly moderate to high. For the tracers (**[^{18}F]d$_2$** and **[^{18}F]d$_4$**) obtained via ruthenium-mediated S_NAr deoxyradiofluorination RCY was ≥13.8%. The tracers (**[^{18}F]d$_6$** and **[^{18}F]d$_8$)** were obtained at an RCY of ≥20.0% via halogen-fluorine exchange S_NAr reaction. For the tracers (**[^{18}F]d$_{10}$**, **[^{18}F]d$_{17}$**, **[^{18}F]d$_{19}$**, and **[^{18}F]d$_{21}$**) also obtained via halogen-fluorine exchange S_NAr reaction but without optimization, RCY was between 5.0% and 14%. In the case of the tracers (**[^{18}F]f$_4$** to **[^{18}F]f$_{14}$**) obtained via direct S_N2 radiofluorination RCY was ≥24.9% for the majority. Two-step radiofluorination afforded **[^{18}F]f$_4$**, **[^{18}F]f$_5$**, **[^{18}F]f$_6$**, **[^{18}F]f$_7$**,

[^{18}F]f$_9$, and **[^{18}F]f$_{10}$** in RCY (10.4–72.4%). Two-step [^{11}C]methylation yielded **[^{18}F]f$_{15}$** and **[^{18}F]f$_{16}$** in 19.0% and 26.7% RCY. A more consistent molar activity (A_m) was observed for the two-step radiolabeling 53.2–131.6 GBq/μmol, than for the one-step radiolabeling 16.9–145.9 GBq/μmol. All the tracers were stable in human plasma for 120 min. Their log $D_{7.4}$ was between 2.0–3.1 and free plasma fraction (*fp*) 0.05–1.18%. The ligands displayed high binding affinity to α-syn (0.10–2.27 nM) in the in vitro competition binding assays, with some (**d$_8$**, **f$_6$**, **f$_9$**, and **f$_{10}$**) even in the subnanomolar range and over 55-fold selectivity over Aβ and tau. In vitro autoradiography showed that all the tested DABTAs stained α-syn in the MSA PHBT, while only the [^{18}F]fluoroethylated/PEGylated tracers (**[^{18}F]f$_4$** to **[^{18}F]f$_{14}$**) and **[^{18}F]d$_4$** stained with varying intensities α-syn in DLB PHBT. None of the tracers stained tau fibrils in the tau PHBT. Staining-selectivity over Aβ varied with higher selectivity observed mostly in the DABTAs with the [1,3]dioxolo[4,5-b]pyridine ring, such as **[^{18}F]f$_4$**, **[^{18}F]f$_9$**, and **[^{18}F]f$_{13}$** except for **[^{18}F]d$_4$**. Out of the twelve tracers evaluated in biodistribution experiments, six showed an initial brain uptake of > 4 %ID/g (percentage of injected activity per gram of brain tissue) at 5 min post-injection (p.i.), out of which five displayed a fast brain clearance with less than one-third of the initial activity remaining in the healthy mouse brains at 60 min p.i. PET dynamic scans with **[^{18}F]d$_6$** and **[^{18}F]d$_8$** confirmed the ex vivo biodistribution experiments. Finally, **[^{18}F]d$_6$**, **[^{18}F]d$_8$**, **[^{18}F]f$_4$**, **[^{18}F]f$_5$**, **[^{18}F]f$_6$**, and **[^{18}F]f$_7$** displayed a low amount of brain radiometabolites (> 96% parent compounds at 20 min p.i.).

Conclusion

[^{18}F]f$_4$, **[^{18}F]f$_5$**, **[^{18}F]f$_6$** and **[^{18}F]f$_7$** show high binding affinity and specificity for recombinant α-syn and α-syn deposited in human brain tissue. In addition, they displayed favorable in vivo pharmacokinetics and high in vivo stability in mice. This makes them promising candidates for α-syn PET imaging. **[^{18}F]f$_{13}$**, although not evaluated in vivo, seems also promising because it stained α-syn in both DLB and MSA PHBT. These tracers can be easily chemically synthesized as well as radiolabeled. Further preclinical and clinical characterizations of these new radiotracers are warranted.

Keywords

α-synuclein aggregates, 4,4'-disarylbisthiazole, [^{18}F]radiofluorination, [^{11}C]methylation, PET radiotracers, binding affinity, autoradiography, brain uptake, brain clearance, pharmacokinetics.

Zusammenfassung

Ziel

Die Ablagerung von α-Synuclein-Fibrillen (α-syn) ist ein gemeinsames Merkmal der neurodegenerativen Erkrankungen, die als α-Synucleinopathien bezeichnet werden. Dazu gehören u. a. die Parkinson-Krankheit (PD), die Demenz mit Lewy-Körperchen (DLB) und die multiple Systematrophie (MSA). Aufgrund der rasch zunehmenden Inzidenz und Prävalenz dieser Krankheiten in alternden Bevölkerungen besteht ein enormes Interesse an einer nicht-invasiven PET (Positronen Emissions Tomographie) -Bildgebung von α-Syn zur Frühdiagnose und Therapiekontrolle. Der spezifische Nachweis von α-syn wird jedoch häufig durch die Anwesenheit anderer Proteinaggregate wie β-Amyloid-Plaques (Aβ) und Tau-Fibrillen erschwert. Derzeit sind keine α-syn-spezifischen Radiotracer für den in vivo spezifischen Nachweis von α-syn verfügbar. Hier wird über die Entwicklung und präklinische Charakterisierung neuer α-syn-spezifischer Radioliganden berichtet, die als Positronen-Emissions-Tomographie (PET)-Tracer auf einem DABTA (4,4'-Disarylbisthiazole)-Gerüst basieren.

Methodik

Dreiundfünfzig Vorläufer und Standardverbindungen wurden durch eine zweistufige modifizierte Hantzsch Thiazolsynthese synthetisiert, mit einem zusätzlichen dritten Schritt für die Phenol/Pyrimidinol DABTAs. Die Vorläufer wurden durch Ruthenium-vermittelte S_NAr-Desoxyradiofluorierung (RVSD), Halogen-Fluor-Austausch S_NAr (HFAS), S_N2-vermittelte einstufige (SVE) Radiofluorationsreaktionen und S_N2-vermittelte zweistufige Radiofluorierung (SVZR) und [^{11}C]Methylierung (SVZM) radio-markiert. Diese Standardverbindungen wurden als HPLC-Referenzen (high performance liquid chromatography), für Blockierungsexperimente und Bindungsassays gegen rekombinante α-syn, Aβ und tau verwendet. Daten zur molaren Aktivität (A_m), log $D_{7.4}$ (Octanol-Wasser Verteilungskoeffizient bei pH 7.4), Plasmastabilität und freie Plasmafraktion (*fp*) der Tracer wurden ebenfalls erhoben. In-vitro Autoradiographie-Experimente wurden an erkrantem postmortem-humanem Gehirngewebe (PHBT) und erkranktem Mäusehirngewebe durchgeführt. An gesunden Mäusen wurden ex-vivo Biodistributionstudien, ex-vivo Metabolitenstudien und dynamische PET/MR-Bildgebung durchgeführt.

Ergebnisse

Die chemischen Ausbeuten der DABTAs lagen bei 15.6–70.9%. Die radiochemischen Ausbeuten (RCY) für die Radiotracer ([^{18}**F]d$_2$** und **[^{18}F]d$_4$**) mittels RVSD waren ≥13.8%. Für die über HFAS synthetisierten Tracer (**[^{18}F]d$_6$** und **[^{18}F]d$_8$**) betrug der RCY ≥ 20.0%. Für die Tracer (**[^{18}F]d$_{10}$**, **[^{18}F]d$_{17}$**, **[^{18}F]d$_{19}$** und **[^{18}F]d$_{21}$**), die ebenfalls über HVS synthetisiert wurden aber ohne Optimisierung, lag der RCY zwischen 5.0% und 14.0%. Für die Tracer (**[^{18}F]f$_4$** bis **[^{18}F]f$_{14}$**), die über SVE synthetisiert wurden, betrug RCY ≥ 24.9% für die Mehrheit. SVZR erbrachte für **[^{18}F]f$_4$**, **[^{18}F]f$_5$**, **[^{18}F]f$_6$**, **[^{18}F]f$_7$**, **[^{18}F]f$_9$** und **[^{18}F]f$_{10}$** eine RCY

von 10.4–72.4 %. SVZM ergab bei **[^{18}F]f$_{15}$** und **[^{18}F]f$_{16}$** 19.0% bzw. 26.7% RCY. Molare Aktivitäten befanden sich bei 53.2–131.6 GBq/µmol und bei 16.9–145.9 GBq/µmol für die einstuftigen bzw. zweistuftigen Markierungen. Alle Tracer waren im humanen Plasma über 120 Minuten stabil. Ihr log $D_{7.4}$ lag zwischen 2.0–3.1 und die *fp* zwischen 0.05–1.18%. Die Liganden zeigten eine hohe Bindungsaffinität zu α-syn (0.1–2.27 nM), wobei einige (**d$_8$**, **f$_6$**, **f$_9$** und **f$_{10}$**) im subnanomolaren Bereich lagen und eine 55-fache Selektivität gegenüber Aβ und tau zeigten. In-vitro Autoradiographie zeigte, dass alle getesteten DABTAs α-syn in MSA PHBT anfärbten. Aber nur die [^{18}F]fluoroethylierten/PEGylierten Tracer **([^{18}F]f$_4$** bis **[^{18}F]f$_{14}$**) und **[^{18}F]d$_4$** in DLB PHBT färbten mit unterschiedlicher Intensität α-syn an. Keiner von den getesten Tracern färbte Tau in Tau-PHBT. Die Anfärbung von Aβ war unterschiedlich stark, wobei geringere Intensitäten vor allem bei den Tracern mit dem [1,3]Dioxolo[4,5-b]pyridin-Ring (**[^{18}F]f$_4$**, **[^{18}F]f$_9$** und **[^{18}F]f$_{13}$**) beobachtet wurden. Von den zwölf in ex-vivo Biodistributionstudien bewerteten Tracern zeigten sechs eine Gehirnaufnahme von >4 %ID/g bei 5 min p.i (post injection). Von diesen zeigten fünf eine schnelle Gehirnclearance, die bei 60 min mindestens dreimal niedriger war als die initiale Speicherung. Die dynamische PET-Bildgebung mit **[^{18}F]d$_6$** und **[^{18}F]d$_8$** korrelierten mit ihren ex-vivo Biodistributionsexperimenten. Bei den untersuchten Tracern **[^{18}F]d$_6$**, **[^{18}F]d$_8$**, **[^{18}F]f$_4$**, **[^{18}F]f$_5$**, **[^{18}F]f$_6$** und **[^{18}F]f$_7$** wurde nach 20 min p.i. eine geringe Menge an Radiometaboliten im Gehirn (< 4%) festgestellt.

Schlussfolgerungen

Alle Tracer konnten gut radio-markiert werden und in gute radiochemische Ausbeute (RCY ≥ 25%) isoliert werden. Basierend auf der Bindungsaffinität sowohl zu rekombinanten α-syn als auch auf der Selektivität gegenüber Tau und Aβ, der Bindung an α-syn in MSA und DLB PHBT, der Hirnpharmakokinetik und der *In-vivo*-Stabilität sind **[^{18}F]f$_4$**, **[^{18}F]f$_5$**, **[^{18}F]f$_6$** und **[^{18}F]f$_7$** die bisher vielversprechendsten Tracer. Obwohl **[^{18}F]f$_{13}$** nicht *in-vivo* untersucht wurde, scheint es ebenfalls vielversprechend zu sein, da es sowohl von DLB- als auch von MSA-PHBT α-syn färbte. Eine weitere präklinisch und klinische Testung dieser Verbindung ist gerechtfertigt.

Stichworte

α-Synuclein-Aggregate, 4,4'-Disarylbisthiazol, [^{18}F]Radiofluorierung, [^{11}C]Methylierung, PET-Radiotracer, Bindungsaffinität, Autoradiographie, Gehirnaufnahme, Gehirnclearance, Pharmakokinetik.

4. INTRODUCTION

4.1 The α-synucleinopathies as a group of NDD

The incidence of neurodegenerative diseases (NDD) markedly increases with age. Due to significant progress in the treatment of infectious diseases, cancer, and cardiovascular diseases, there is now a rapidly growing population of elderly individuals who are susceptible to NDD [1].

NDD are a heterogeneous group of conditions characterized by progressive neurodegeneration in the CNS and PNS with a resulting loss of function [2,3]. This can lead to disorders associated with cognition, mobility, coordination, sensation, and strength. Heterogeneous as they are, many of them share some key features, the most important being the aggregation of misfolded proteins [4]. NDD are classified histopathologically by the location and nature of the protein deposits in the nervous system. The pathologies are not completely isolated categories, but rather form a continuum, as shown in **Figure 1** [5]. For instance, the presence of α-syn pathology is not limited to PD but extends to other dementing disorders like PDD, DLB, and AD as a secondary feature. Tauopathy is also usually seen in several pathologies primarily known as the α-synucleinopathies and might contribute to the clinical heterogeneity of the diseases.

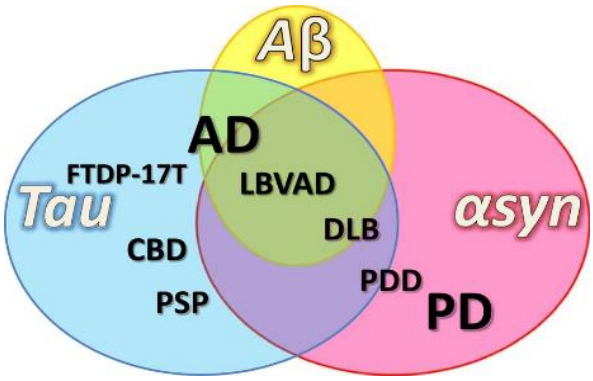

Figure 1. The overlap of proteinopathies [5]. This overlap complicates their differential diagnosis. Color pink: α-synucleinopathy, Color yellow: β-amyloidopathy, Color blue: tauopathy. The explanations of the abbreviations are in the glossary (Appendix II).

The α-synucleinopathies are a disparate group of NDD characterized by the deposition of insoluble α-synuclein protein (α-syn) in neurons and glia in the brain [6–8]. It is believed that these aggregates are present in all stages of the disease [9], hence they are an ideal biomarker for the early diagnosis of this disease as well as the tracking of disease progression [10].

With this in mind, we aimed to develop radiotracers that would enable non-invasive in vivo detection and quantification of small changes in α-syn at preclinical and clinical stages. This would in turn facilitate an

earlier initiation of treatment, which could halt or slow down further neuronal deterioration. A positive outcome would be particularly beneficial to patients who have a higher predisposition to these diseases based on family history. For the time being, there is no suitable radiotracer that can detect α-syn in vivo, the reasons for which will be further discussed later.

4.2 The α-synucleinopathies

The α-synucleinopathies are characterized by the accumulation of α-syn in Lewy bodies (LB) and Lewy neurites (LN) in neuronal cells in PD and DLB. However, in MSA, they are found in the oligodendrocytes as glial cytoplasmic inclusions (GCI) [7,11].

4.2.1 Parkinson's disease (PD)

PD is one of the most common age-related NDD [6,11]. The most common movement-related NDD [8] and the most common α-synucleinopathy [6]. It is a complex, progressive NDD characterized by tremor, rigidity, and bradykinesia, with postural instability appearing in some patients as the disease progresses. Its prevalence increases with age: PD affects 1% of the population past the age of 60, with only 5–10% showing a genetic predisposition to the disease.

The basal ganglia are mainly compromised in PD [12]. Neuropathologically, the disease features a neurochemical deficit, which is the loss of the dopaminergic neurons (DN) in the substantia nigra pars compacta (SNpc), with the loss being more marked in the ventral lateral SN **Figure 2**. This leads to a reduction of dopaminergic activity in the basal motor regions, in the putamen particularly since there is a slow but progressive loss of innervation from the SNpc. This underlies the cardinal motor symptoms of PD, which include bradykinesia (lethargic initiation and execution of movement), muscle rigidity, and tremor at rest [13]. These motor signs become apparent after the loss of approximately 60–80% of the DN [12]. Nerve cell loss, in addition to that of the SN can also be seen in the NBM, the LC, and the DMV [14].

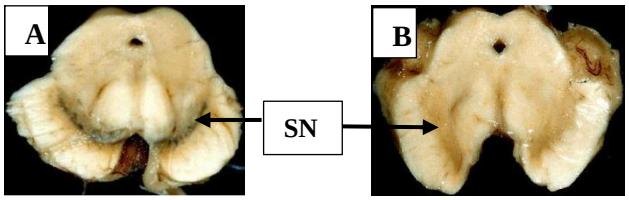

F

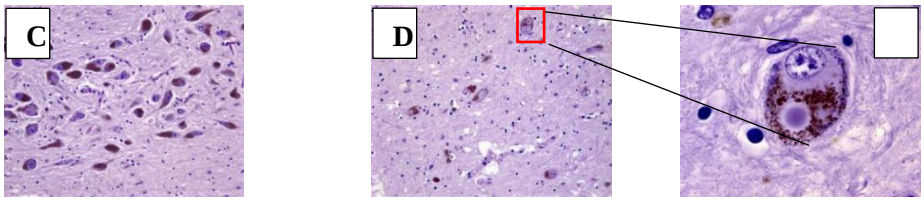

Figure 2.The loss of SN neurons in PD. Photographed images of the transverse sections of human midbrain showing the dark pigmentation of the SN between the decussation of the SCP and CP in a neurological control (A) and its reduction in PD or DLB (B) [15,16]. The magnification of the SN regions shows a dense network of the SN neurons (C), which are almost lost in PD (D). LB (in higher magnification) can be found in the remaining neurons in PD composed of α-syn, other proteins and melanin granules (reddish-brown) (E) also present in the cytosol of all the SN neurons (C-E). Adapted from Agamanolis 2006.

Another important neuropathological finding in PD is the presence of eosinophilic intracytoplasmic inclusions known as LB and LN in the SNpc. In addition to the SNPc, in several cases, LB can also be found in the DMV, the raphe nuclei, the olfactory bulb, the NBM, the LC, the MEWN, the cerebral cortex, and some autonomic ganglia [8,11,14]. The accumulation of LB and LN in other brain regions as well as the degeneration of other nerve types might partly play a role in the non-motor symptoms that also characterize PD, such as seborrhea, autonomic instability, loss of olfaction, RMD, excessive salivation, constipation and dementia [8,17]. Other pathological findings include the presence of extracellular melanin released from degenerating neurons as well as reactive gliosis [8].

4.2.2 Dementia with Lewy bodies (DLB)

Although overall DLB is a rare cause of dementia **Figure 3**, it is the most common dementia among the α-synucleinopathies **Figure 3** [18–20]. The differential diagnosis of DLB from Parkinson's disease dementia (PDD) can be challenging, since DLB and PDD share both clinical and pathological similarities [18–22].

Generally, one-fourth of patients with LBD display cortical Aβ deposition **Figure 4**, with the highest load observed in DLB patients, followed by PDD patients [18]. In some cases, some DLB subjects have enough Aβ to fulfill the CERAD criteria for AD [23], but only a few meet the tangle-based Braak stages V and VI for AD [19]. Those few are more likely to show a disease presentation like AD, whereas those with fewer tangles show clinical phenotypes typical of DLB. Furthermore, in DLB, not only AD-related NFTs and Aβ but also FTLD-related pathologies can be observed and have implications for the prognosis of the disease, with alterations to the clinical presentation of the disease [19,20,24].

Postmortem examination of the brains of DLB patients shows the presence of LB (composed of neurofilament proteins, ubiquitin aggregates, and α-syn) in the SN. Although LB are found in the neocortex of some patients with idiopathic PD, they are found in all patients with DLB [20–22]. This is accompanied

by extensive cerebral atrophy, a structural change that it shares with AD. Even though there is less damage to the medial temporal lobe in DLB, there is a characteristic loss of nigral DN reminiscent of PD. Nevertheless, damage to the neocortex and limbic system stands out as a major pathological finding in DLB. PDD, on the other hand, exhibits more dopaminergic neuronal loss than DLB, with fewer striatal AD and limbic-related pathologies, which correlate often with the clinical phenotypes of the disorders [20].

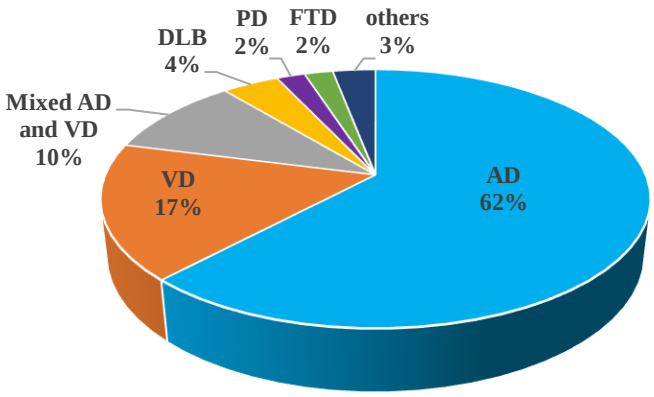

Figure 3. Distribution of the different forms of dementia diagnosed in patients in the United Kingdom [25]. Dementia typically affects older adults; however, an estimated 42,000 people under the age of 65 have dementia.

Unlike in PD, in DLB, coupled with the reduction of several neurotransmitters, ACh is especially diminished, to such a degree as or even worse than observed in AD. It is believed that the neurotransmitter deficit and the presence of LN correlate better with the clinical presentation of the disease. This is because the amount of LB in the neocortex does not accurately correlate with dementia severity or duration, except in cases with the concomitant presence of LB and Aβ in the midfrontal cortex [19,22].

The signs and symptoms seen in DLB might be partly because of the diminished information flow to the limbic cortex neocortex (especially to the frontal lobe) from the striatum due to alteration in the levels of neurotransmitters/neuromodulators such as ACh and dopamine, which facilitate interneuronal information transfer [26,27]. As well as the alteration in blood flow in different parts of the brain [28].

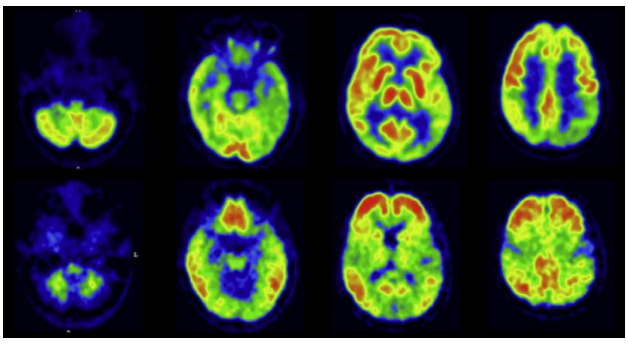

Figure 4. Visual analysis of axial [^{18}F]FDG (top) and [^{11}C]PiB PET (bottom) images of a patient with DLB. FDG PET images shows parietooccipital hypometabolism. [^{11}C]PiB images highlight diffuse amyloid uptake [29].

4.2.3 Multiple system atrophy

MSA is a sporadic, adult-onset, inexorably and rapidly progressive (faster than PD), severe, fatal, multisystem NDD. It is clinically characterized by varying severity and combinations of parkinsonian presentations, autonomic, cerebellar, and urogenital dysfunction as well as corticospinal disorders. Neuropathologically, the disorder is defined by characteristic lesions, demyelination, loss of olivopontocerebellar (OPC) neurons and striatonigral structures of the brain and spinal cord coupled with an abundance of distinct GCIs **Figure 5** or Papp Lantos bodies consisting majorly of fibrillated α-synuclein, with other protein such as tau, ubiquitin, DJ-1, LRRK2, p25α, GFAP, MBP [30]. The presence of the GCIs in the oligodendrocytes is needed to make a definite diagnosis of MSA posthumously. As the disease progresses the GCIs deposits increase especially in the premotor and primary motor cortices. Neurodegeneration is not limited only to the OPC and striatonigral structures but also affects other parts of the CNS, PNS, and ANS which underpins the multisystem feature of the pathology [30–34].

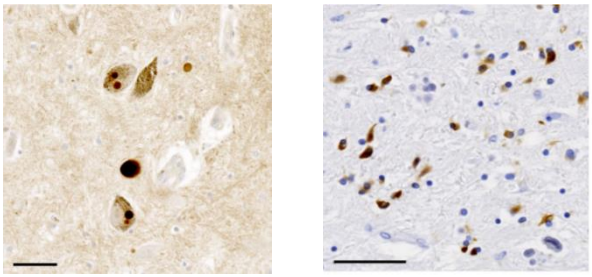

LB pathology (i) **GCI pathology (ii)**

Figure 5. Neuropathological lesions in synucleinopathies. Lewy bodies are present in patients with PD, PDD and DLB (i). Glial cytoplasmic inclusions (GCIs) are present in patients with MSA (ii). Scale bar, 50 μm [37]. The abundance of the GCIs makes them less elusive targets than the LBs (see **6.4.2.3**.)

There are two main morphological variants of MSA, OPC atrophy and striatonigral degeneration (SND) are categorized into two major phenotypes depending on the predominant phenotype: MSA-parkinsonian type (MSA-P) **Figure 6a** that is, MSA with predominant parkinsonian symptoms, as extrapyramidal preponderate and MSA-cerebellar type (MSA-C), that is, MSA with predominant cerebellar features, as cerebellar ataxia prevails [30–32].

MSA is accompanied by around a 20% reduction of neurons in the motor and supplementary motor cortex (with the loss of the pyramidal cells of Betz and cerebral astrocytosis) which is preceded and driven by early degeneration of the basal ganglia. Cognitive decline is shown in more recent studies to be due to the presence

of GCI, NCI, LB-like, and frontostriatal deafferentation in MSA patients, with amyloid pathology being very uncommon **Figure 6b**. However, impairment in carrying out executive functions and cognition is significantly more severe in MSA patients with neocortical neuronal loss [31,32,35].

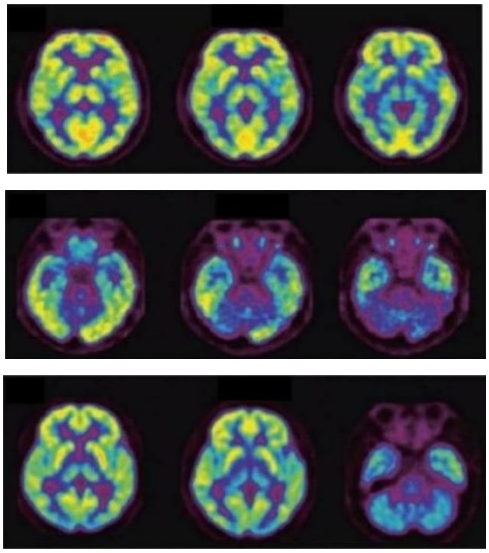

Figure 6a. Visual analysis of [^{18}F]FDG PET images of patients with MSA-P (top), MSA-C (middle) and PD (bottom). The image from a patient with MSA-P shows diminished glucose metabolism in the posterolateral portion of the putamen. PET images of the patient with MSA-C revealed decreased glucose metabolism in the pons and cerebellum. There was no hypometabolism of glucose in the patient with PD in the putamen, pons or cerebellum [36].

Multidomain autonomic failure in MSA (an initial symptom in 41–47% of MSA patients) is due to the degeneration of the preganglionic autonomic neurons of the spinal cord and the brainstem. MSA interestingly shares some prodromal symptoms with PD, such as genitourinary/sexual dysfunction, cardiovascular autonomic failure, orthostatic hypotension, respiratory disorders, and RBD [35].

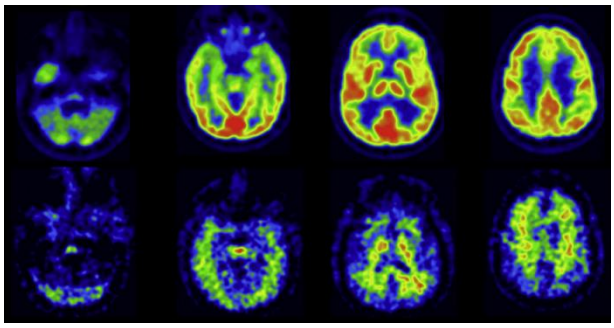

Figure 6b. Visual analysis of axial [^{18}F]FDG (top) and [^{11}C]PiB (bottom) PET images of a patient with MSA-C. The [^{18}F]FDG PET images illustrate a reduction in cerebellar glucose metabolism. The PiB images indicate lack of β-amyloid plaques [29].

4.3 Risk factors of PD, DLB and MSA

4.3.1 Age and Gender

Age is an important factor in the development of the α-synucleinopathies, with the incidence increasing with age [37]. Based on data from studies conducted in non-human primates (NHP), Collier et al. proposed that age engenders a pre-parkinsonian state and that PD is an accelerated form of normal aging normally accompanied by the death of DN, which is aggravated by a combination of genetic and environmental factors [38].

For both genders, increasing age increases the incidence of PD (both with and without dementia), but with a sharper increase in males at the ages of 60–69 and 70–79 [39,40]. The age of onset of PD in females (53.4) lags behind that of males (51.3) by 2.1 years [41]. Nonetheless, women show a faster progression after onset and a higher mortality rate [42,43].

According to a study reported by Dorsey et al. there is an expected increase in the number of people over 50 suffering from PD [44]. Worldwide, it is estimated that presently, up to 10 million people are living with PD [45,46]. Furthermore, autopsy studies revealed that DLB makes up 10–20% of dementia in the US. This was comparable to autopsy studies in Europe and Japan [19,22]. In another incidence study, it was reported that DLB accounts for 3.2–7.1% of dementia cases [47]. Also, it was observed that the incidence of DLB increases progressively with age, conversely, the incidence of PD decreases after the age of 85 [49]. Like PD, the incidence of DLB based on most studies, is significantly higher in men than in women [48].

Generally, the incidence of MSA increases with age. Twelve cases per 100 000 individual-years for persons over 70 years [35]. In western countries, there is a predominance of MSA-P making up 66–82% of MSA patients. Conversely, in Asian countries, such as Japan, the subtype MSA-C is seen more, with an occurrence of up to 67% among MSA patients with mixed phenotypes being more prevalent as a consequence of environmental or genetic factors [30–32,35]. Compared to MSA-P, the average age of disease onset in MSA-C is earlier, however, disease progression to disability is more common for the former.

Although it is reported to affect men more than women (with a ratio of 1:2, and some studies reporting ratios from 1:3 to 1:9), this difference is believed to result from the earlier and easier diagnosis of impotence in males, typically at a mean age of 52.5–55 years. In both genders, motor symptoms begin to appear around 56 ± 9 years of age. A prodromal/preclinical stage is observed in MSA, reminiscent of PD, affecting 20–75% of MSA patients and potentially preceding motor symptoms by months or years.

4.3.2 Genetic factors

The origin of most late-onset NDD is considered more sporadic than genetic. Notwithstanding, it has also been discovered that certain genetic aberrations could predispose to some NDD which may not have a Mendelian pattern of inheritance [49–52].

This includes the mutations unique to PD, such as the parkin gene, which causes EOPD, with onset as early as ≤ 30 years old [53–57], the LRRK2 gene associated with familial mid-to-late-onset PD as well as sporadic PD, with a slower disease progression effect [57,60–62] and inconsistent neuropathology [58–60]. Peculiar to DLB is the mutation of the APOE ε4 allele, which is also a genetic risk factor for late-onset sporadic AD [47,61,62] and the loss of function mutation of the COQ_2 gene for MSA [34,49,63]. Common to PD, DLB, and MSA are the mutations of the SNCA and the GBA-1 genes.

4.3.2.1 The α-synuclein gene (SNCA, PARK1/4) mutation

The SNCA mutation is relevant to all the α-synucleinopathies as already mentioned. The heterogeneity of disease presentation, age of onset, and underlying pathological mechanism might be due to the position of the genetic variant and its effect on protein function [62].

The mutation of the SNCA gene causes autosomal dominant PD. Although a rare mutation, it results in the early onset of PD (≤ 50 years) with fast progression. Several missense mutations of the SNCA associated have been recognized, such as the highly penetrant p.A53T mutation, the p.A30P, and p.E46K mutations [56,64–66]. These three-point mutations lead to the formation of stable pathological β-sheets of α-synuclein, followed by the formation of toxic oligomers, protofibrils, and fibrils [59]. There have also been reported duplications and triplications of the entire SNCA gene [56], which results in the accumulation of α-synuclein. This in turn blocks protein trafficking from the ER to the Golgi apparatus leading to ER stress, which interferes with the normal functioning of the cell [67].

Heterozygous duplication, homozygous duplication, and heterozygous triplication as a result of locus multiplication of the SNCA gene have been reported for DLB as well as for PD and PDD. Fortunately, not all duplications are fully penetrant, nevertheless, triplications cause the overexpression of SNCA, mRNA, and the gene product, resulting in an earlier disease onset as well as a more severe disease phenotype [68,69]. It has also been reported that SNCA methylation is notably decreased in DLB compared to healthy controls and might help in the diagnosis of DLB [47,48]. In an SNP association study, it was demonstrated that genetic variants (SNPs) within the SNCA locus are linked with a higher risk for MSA in the Caucasian population [49]. The identified risk variants, however, were not associated with MSA risk in East Asian populations. This underscores population heterogeneity at the SNCA locus [70,71].

4.3.2.2 The glucocerebrosidase-1 (GBA-1) mutation

Mutations in the GBA gene are one of the most frequent genetic risk factors for the development of PD, and have also been found to be a risk factor for DLB [72]. The activity of the GBA enzyme decreases with aging in sporadic PD and DLB [73]. Heterozygous variants of this mutation put a carrier at risk of developing PD and a higher risk DLB with an earlier age at disease onset, higher severity, faster disease progression, and earlier death [28,47,74]. The risk of either of the α-synucleinopathies or the presentation of either depends on the type of the disease-associated variant [62]. The incidence of cognitive decline in PD is nearly 2.4-fold higher in PD patients with the GBA variant, [75] hence worse is expected in DLB with a higher risk. There is nevertheless mounting but conflicting evidence about the association of MSA to the GBA gene, especially with MSA-C [34,71].

Despite the low incidence of inherited α-synucleinopathies, genetic studies have nevertheless revealed pathways that play a role in the development and progression of these disorders. These pathways seem to have in common features that affect the function and survival of the DN owing to oxidative damage, abnormal protein accumulation and phosphorylation, and mitochondrial dysfunction [55].

4.3.3 Toxicant exposure

There have been many classic epidemiological studies that point to the role of toxicants in the development of PD. Nevertheless, the role of toxicants in the pathogenesis of DLB and MSA has not been studied conclusively, although some of the environmental factors that could predispose individuals to PD are suspected to be involved in the development of the other α-synucleinopathies in combination with genetic factors. The mechanism underlying disease development could be viewed as an overlap of both genetic and environmental factors.

Implicated in the development of PD are agents which increase uncontrolled oxidation in the neurons, such as MPTP, rotenone, dithiocarbamates, organochlorine pesticides and heavy metals. Some interfere with the respiratory chain, which leads to the backup of electrons in the mitochondrial matrix, while others, by virtue of their intrinsic oxidizing properties, initiate redox reactions themselves, such as heavy metals and paraquat. Others directly or indirectly facilitate the toxicity of other toxicants like aluminum, which, although a non-transition metal, increases the toxicity of iron. This causes cellular stress, reduced ATP synthesis, and the generation of free radicals by the mitochondria, which causes the peroxidation of lipids, accompanied by membrane disruption, and depletion of antioxidants, resulting in a positive feedback loop that causes bioenergetic failure and cell death. There is also an inhibition of peptidases, which in turn causes the accumulation of α-synuclein monomers, which are prone to aggregation in these conditions.

The vulnerability of nigral DN to these toxicants can be traced to several factors. The DN are in a state of oxidative stress even in normal physiological conditions. The enzymes involved in the synthesis and metabolism of dopamine enable the formation of hydrogen peroxide [76,77]. The selective vulnerability of DN to MPP^+ is because the dopamine transporter (DAT), which facilitates the re-uptake of dopamine, also has a high affinity for MPP^+ [80,81]. The vulnerability of nigral neurons to the cytotoxic effects of iron is believed to be due to the presence of neuromelanin (NM) in this brain region [78,80]. NM normally sequesters iron and other transition metals and plays a protective role in preventing them from inducing oxidative stress [76,77]. However, the death of neurons containing NM exposes it to the extracellular medium, where it promotes reactive processes that further worsen the pathogenic process. MPTP and rotenone may also increase free iron: the former increases the expression of the metal ion transporter (DCT1), while the latter facilitates the release of Fe^{2+} from transferrin [78].

4.4 The synuclein proteins

The aggregated form of α-synuclein **Figure 7a** is the main component of LB and LN in PD and DLB, as well as GCIs in MSA.

In 1988, Maroteaux et al. reported the first synuclein nucleotide and amino acid sequences from the electric organ of *Torpedo Californica* [11,79]. The later discovery of the non-amyloid-β component precursor (NACP), so named because of its presence in some amyloid plaques in postmortem AD brains, from the human brain by Ueda et al. in 1993 [80], guided the later discovery of human α-synuclein (140 amino acids in length) and β-synuclein (134 amino acids in length) by Jake et al. in the following year [81,82].

Both α-synuclein and β-synuclein share identical domain organization with a similar amino acid sequence. The domains are characterized based on their amino acid constituents: the amphipathic positively charged amino-terminal lipid-binding domain, followed by an amyloid-binding central region (NAC), which is responsible for the formation of fibrils as well as the aggregation, and a negatively charged carboxy-terminal disordered region, which enables interaction with small molecules, proteins, metals, and the other domains. The last two parts are identical in both proteins, but the amino terminal differs by the number of amino acids in the inter-repeat region. γ-Synuclein (highly abundant in human breast cancer tissue) was discovered 4 years later by Ji et al. It contains 13 fewer amino acids than α-synuclein and shares the same domain organization as the other two synuclein proteins [11,82–84]. Interestingly, unlike the tau protein, there is no proof of the existence of any isoform of the synuclein proteins [11,85].

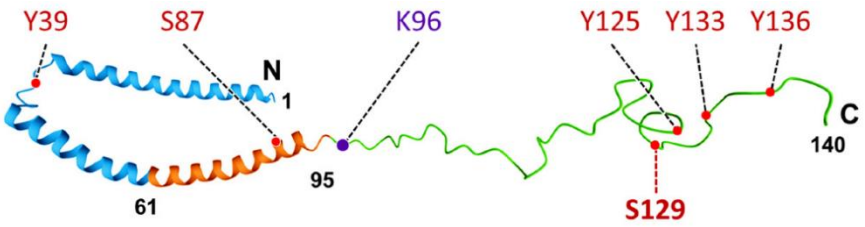

Figure 7a. Schematic representation of the α-synuclein protein structure. Blue: N-terminal amphipathic region, amino acids (AA) 1-60; orange: NAC AA 61-95; green: C-terminal acidic region; purple: site of ubiquitination; red: sites of phosphorylation [86].

The mRNA of all the synuclein proteins is highly expressed in the nervous system, and the heart too for γ-synuclein, with lower transcript levels in other tissues. Unlike α- and β-synuclein proteins, which are predominantly present in the nerve terminals with slight presence in the neuronal dendrites and somas in the brain (striatum, neocortex, hippocampus, thalamus, and cerebellum), γ-synuclein is present all over the neurons, especially in the PNS (motor neurons, primary sensory neurons, and sympathetic neurons), and has also been found in the brain, olfactory epithelium, breast, and ovarian tumors. It appears that α- and β-synuclein proteins comprise 0.1–0.2% of the total brain proteins [11,82,83].

4.4.1 Functions of the synuclein proteins

The physiological roles of the synuclein proteins are not fully understood, however, some experimental studies have shown some of the putative roles of these proteins. Both α- and β-synuclein protein are believed to play a role in the maintenance of cell membrane integrity as well as the regulation of vesicular transport [11,82,83]. α-Synuclein prevents SNARE complex-mediated lipid membrane fusion at the presynaptic membranes by multimerizing at synapses, which seemingly inhibits the release of synaptic vesicles and causes their clustering instead. It was shown that mice overexpressing α-synuclein displayed decreased release of dopamine [82,83,87].

In vivo, α-synuclein rescues the loss of the CSPα, which, like α-synuclein is a synaptic vesicle protein and is also independently associated with neurodegeneration. Probably by binding to acidic phospholipids in the membranes. For instance, A30P α-synuclein has low lipid-binding ability and, conceivably, due to this, cannot mitigate neurodegeneration caused by CSPα deficiency [82,87–89].

Mitochondrial fragmentation upon binding with α-synuclein (and to a lesser extent β- and γ-synuclein) may underlie one of the mechanisms through which SNCA gene multiplication can induce neuronal death. The primary location of α-synuclein proteins in normal neurons in the nerve terminals prevents their interaction with the mitochondria, which are mostly located in the nerve soma and dendrites. However, it is possible that the overexpression of α-synuclein causes their migration to the soma, where they interact with the

mitochondria. Fragmentation is accompanied by decreased respiration and the death of neurons. Synuclein-induced mitochondrial fragmentation is mitigated by the co-expression of parkin, PINK1, or DJ-1. However, PD-associated mutation of these proteins eliminate their rescue function [11,90,91]. The role γ-synuclein plays is largely unknown, although there is increased invasiveness and metastasis of breast tumors when the protein is exogenously expressed [83].

4.4.2 The synucleins in NDD

Of all the mammalian synucleins, α-synuclein is the most well-documented to contribute to the pathogenesis of α-synucleinopathies. The oligomerization and aggregation of this protein are generally believed to drive neurotoxicity, as well as being an etiologic factor in NDD. Hence, it is not surprising that lesions (LB/LN) in brains that accompany PD/DLB are majorly constituted of aggregated α-synuclein (α-syn) [85,89,94,95]. Although β- and γ-synuclein may rescue α-synuclein-induced toxicity, they themselves may also contribute to degeneration, not only due to a reduction in their protective functions but also by themselves with the formation of axonal spheroids [89,95]. β-synuclein accumulation has been discovered in the brain regions responsible for memory formation, like the hippocampus. Its mutation has also been associated with certain types of LBD, leading to more severe memory defects [92].

The deposition of α-synuclein is not only peculiar to the α-synucleinopathies, but also to other groups of NDD. For instance, LB pathology is also found in AD in at least 60% of the cases, with α-synuclein deposits in the amygdala, as opposed to PD or DLB, which have a wider spread LB pathology. The presence of LB pathology in other NDD is indicative of the roles of the synucleins as reporters, which are sensitive to specific defects in cells and may take part in the response to injury [87].

The ubiquity of α-synuclein in neurodegeneration is proposed to be a function of its NAC (amino acids 71–82) component **Figure 7a**. The NAC region is suggested to be essential for the in vitro formation of β-sheet-rich aggregates and resistance to proteolytic breakdown in α-synuclein filaments. This region is [93] partially missing in β-synuclein and incompletely conserved in γ-synuclein resulting in increased hydrophilicity, which may explain their diminished presence in LB pathology. Furthermore, the absence of γ-synuclein in the CNS but just in the PNS could also explain its reduced role in the pathogenesis of the α-synucleinopathies. In addition to the NAC region, it is also proposed that neurotoxicity can also be initiated by excess binding of α-synuclein to membranes. β- and γ-synuclein are also believed to cause cytotoxicity via this mechanism independent of the NAC region and the aggregation it promotes, as their N-terminal regions are similar [84,94].

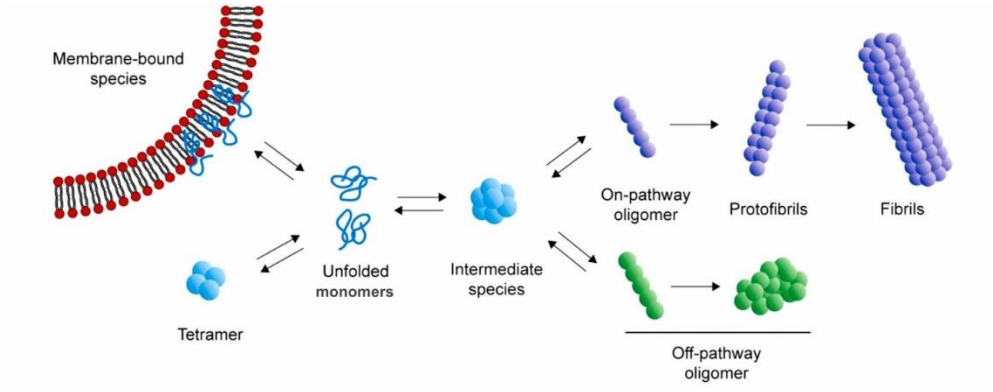

Figure 7b. The process of α-synuclein aggregation [95]. In physiological conditions, α-synuclein subsists as unfolded monomers in equilibrium with the membrane-bound species, which promote SNARE-complex assembly and the formation of tetramers that are resistant to normal aggregation. When there is a disruption of the balance between α-syn clearance and aggregation, the monomers aggregate to form oligomers (both off-pathway and on-pathway oligomers). The on-pathway oligomers go on to form protofibrils and fibrils eventually. The off-pathway cannot form amyloid fibrils.

Factors that trigger the aggregation of α-synuclein are still yet to be elucidated. However, as mentioned above mutations and gene multiplication play roles, as do efficiency of protein clearance, membrane saturation, interactions with toxic substances and other amyloidogenic proteins, PTM, which influence their interactions with metals [96] amongst others **Figure 7a**. As already hinted at earlier, the pathological effects of these factors reinforce the preexisting dyshomeostasis of α-synuclein [84,97,98].

It is proposed that the propagation of α-synuclein aggregates and their transmission follow a prion-like mechanism. This mechanism involves the ability of misfolded α-synuclein to convert normal α-synuclein to a pathological form (homotypic seeding) in a process that involves the NAC region. This pathological form is then transmitted from cell to cell. Aggregation of α-synuclein can also be initiated via its interaction with other pathologic proteins such as tau, Aβ, or huntingtin (heterotypic seeding).

The prion-like mechanism of the spread of α-syn is supported by the gut-brain hypothesis of the pathogenesis of PD put forward by Braak in 2003 [9,99,100]. The model follows that neurotrophic pathogens, toxins or inflammatory agents might induce pathological aggregation of α-synuclein, which subsequently gets transmitted to the brain via retrograde axonal transport aided by the vagus nerve to the DMV and finally to the SN. This theory has been evidenced in other studies [84,99,101–111].

The Braak model is not without its limitations. There are patients with some genetic forms of PD who do not develop pervasive LB pathology. Moreover, there are elderly patients who lack a clinical presentation of the disease, although they have widespread LB pathology. Also, the absence of brain pathology upon the post-mortem examinations of patients with only peripheral LB pathology negates the Braak model. These findings suggest that disease progression may not be driven by the spread of LB pathology. Furthermore,

the Braak model proposed that the pattern and propagation of α-syn pathology are facilitated by neuroanatomic connectivity, which is not always the case. This indicates that apart from the trans-synaptic transmission, there might be other mechanistic bases for the spread of α-syn pathology. It is possible that the microenvironment of the PD brain is enough to initiate LB pathology without cell-to-cell transfer of misfolded α-synuclein [84].

Notwithstanding these contradictions, human studies still indicate that the α-syn pathology can be spread intercellularly as well as intracellularly, however, the precise nature of the seeds that drive this process is yet to be known [112]. Different types of strains of α-syn are known (fibrils, ribbons, preformed fibrils, and oligomers) **Figure 7b** which can induce a specific type of α-syn pathology [113,114]. For instance, it is speculated that α-syn strains responsible for the MSA pathology facilitate the protracted persistence of α-syn (LN) in the axonal segments. These LN could promote axonal pruning and uptake by the oligodendrocytes leading to the formation of GCIs. In contrast, the α-syn strains that cause PD and DLB could facilitate the formation of axonal LN with the capability of faster retrograde movement towards the neuronal cell body. Thus, the oligodendrocytes do not have enough time to react to the passing aggregates. This could also underlie the lack of GCIs in DLB and PD [115].

4.4.3 α-Synuclein aggregates as a biomarker

Regardless of the inconsistencies in the propagation and spread of α-syn pathology, overwhelming evidence points toward the role of α-synuclein aggregation in the pathogenesis of α-syn pathology, especially in the context of PD.

To date, the diagnosis of the α-synucleinopathies is based on the clinical presentation of symptoms, with confirmation of the exact pathology at autopsy. Furthermore, there are cases where the classical clinical presentations are not observed, which makes it difficult to differentially diagnose the α-synucleinopathies not only from each other but also from other NDD and non-NDD that also cause movement disorders, especially in the early stages of the disease. For instance, 15% of individuals diagnosed with PD do not meet the strict clinical requirement for PD, and 35% show a different diagnosis at autopsy after a postmortem examination of the brain. Hence, α-synuclein which has been linked to the disease, may help to avoid such difficulties by monitoring disease progression in addition to tracking the efficacy of drugs [116,117].

This resulted in the examination of the CSF for the determination of alterations in the levels of α-synuclein in patients with α-synucleinopathies. Although many studies did report a lower average total α-synuclein in the CSF of PD patients compared to age-matched controls or other NDDs, there are other studies that failed to observe any significant depression in comparison with controls, even compared to other movement

disorders such as PSP, CBD, MSA, and VP. Nevertheless, it seemed that combined measurement of the ratios of α-synuclein oligomers/total α-synuclein and β-GBA activity, or $A\beta_{42}$/total-tau enhanced the precision of the diagnosis of PD. Notwithstanding, there is a report that the α-synuclein/β-synuclein ratio may be useful for the diagnosis of PDD [92].

Moreover, the investigation of the CSF could be confounded by hemolyzed erythrocytes, which release α-synuclein, thereby falsely elevating α-synuclein levels [92]. Furthermore, CSF collection is an invasive procedure that is associated with a significant risk of complications. Overall, α-synuclein measurements in the CSF are therefore limited for the diagnosis and differential diagnosis of α-synucleinopathies [117].

4.5 Diagnosis of the α-Synucleinopathies via Neuroimaging

4.5.1 General overview

An alternative to the invasive CSF evaluation of α-syn [84] is the usage of non-invasive in vivo imaging modalities such as PET and SPECT. They function via radiotracers that bind directly to α-syn and enable non-invasive monitoring of disease progression and tracking the efficacy of therapy. In contrast to CSF analyses, they could also provide information about the neuroanatomic spread of the pathology since the regional deposition of α-syn in different α-synucleinopathies differs from one another [118].

The early differential diagnosis of degenerative parkinsonism based only on the clinical presentations can be challenging, and PD can be misdiagnosed as another neurodegenerative movement disorder (PSP, MSA, CBD) or non-neurodegenerative (DIP, ET, VP) parkinsonian disorders and vice versa [119–121].

4.5.2 Comparison of PET, SPECT, and MRI for the molecular imaging of α-syn

Compared to MRI and MRS, which have sensitivity in the orders of magnitude 10^{-4} M and 10^{-3}–10^{-5} M, PET and SPECT have considerably higher sensitivity (10^{-9}–10^{-12} M) [122–125]. In the case of the α-synucleinopathies, the target (α-syn) concentration is low; hence, a more sensitive modality is needed for its detection, which PET and SPECT represent.

SPECT imaging offers some advantages over PET imaging. For instance, it allows for dual isotope imaging, since the different gamma energies of the used isotopes can be separated by the SPECT cameras. Thus, simultaneous images of the distribution of two radiopharmaceuticals in the brain can be acquired. In contrast, all positron-emitting radiotracers afford 511 KeV gamma photons; dual isotope imaging is not easily possible with PET tracers. In terms of cost, SPECT scanners are generally less expensive than PET scanners.

However, in SPECT scans, far fewer photons are usually available for imaging since the low-energy photons emitted are absorbed and scattered in the patient, resulting in only a small fraction of photons getting to the detectors from the patient. A metal collimator is hence needed for the removal of the scattered photons; otherwise, the images will be considerably degraded. This means that there are lower photon counts, and higher noise observed in SPECT compared to PET. PET has higher sensitivity owing to coincidence detection, which is an important advantage of PET over SPECT, which precludes the use of a physical collimator in favor of electronic collimation. This results in higher image quality compared to SPECT, with better spatial and contrast resolution.

Furthermore, the low sensitivity of SPECT (2–3 orders of magnitude less than PET imaging) means a longer scan duration in order to acquire enough counts (low temporal resolution) for a SPECT image, which results in an increase in artifacts due to the movement of the patient. Owing to the limitations of SPECT imaging, all the radiotracers described in this thesis bear a positron-emitting radioisotope.

4.5.3 Non-α-syn targeted PET and SPECT radiotracers and their shortcomings

There are radiotracers which, although they do not bind to α-syn, enable the imaging of abnormalities in the brain of patients with the α-synucleinopathies. Unfortunately, most of them lack specificity and are unable to differentiate one α-synucleinopathy from the other, although they could be useful in the differential diagnosis of parkinsonism.

In clinical trials, the cocaine analogs **[^{123}I]β-CIT**- and **[^{123}I]FP-CIT**-SPECT (**Figure 8**) enable to differentially diagnose tremors due to idiopathic PD and PPS from essential tremor, medication-induced parkinsonism, dystonic tremor, and psychogenic disorders. However, they do not differentiate PD from other atypical parkinsonism such as PSP and MSA [126]. The cocaine analogs can also be used to evaluate the function of the DAT in DLB patients as well as for differential diagnosis from AD, with which it shares the symptom of cognitive decline. For instance, compared to AD, there is reduced **FP-CIT** binding in the putamen and almost diminished binding in the caudate in DLB [127].

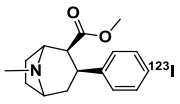

[^{123}I]β-CIT

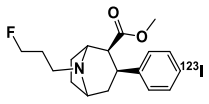

[^{123}I]FP-CIT

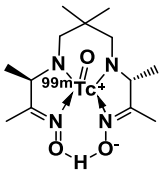

([^{99m}Tc]HMPAO

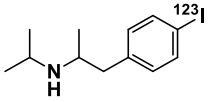

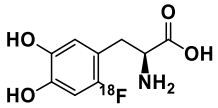

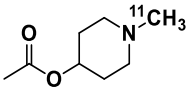

[^{123}I]Iofetamine

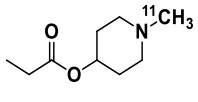

[^{11}C]MP4P

[^{18}F]Fluorodopa

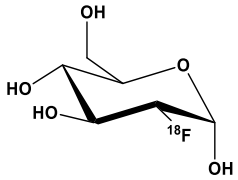

2-Deoxy-2-[^{18}F]fluoroglucose ([^{18}F]FDG)

[^{11}C]MP4A

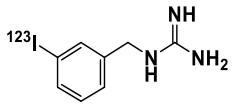

[^{123}I]MIBG

Figure 8. Non-α-syn specific PET and SPECT radiotracers used for diagnosis of the α-synucleinopathies. These tracers enable imaging of the abnormalities in the brains of PD patients, but not the deposited α-syn.

SPECT radiopharmaceuticals such as **[^{99m}Tc]ECD**, **[^{99m}Tc]HMPAO** and **[^{123}I]Iofetamine** (**Figure 8**) showed that, compared to AD, there is distinct occipital hypoperfusion in DLB, with the primary visual cortex and visual association cortices affected. The tracers are, however, unable to differentiate between DLB and PDD. On one other hand, PET studies in DLB patients with FDG confirmed hypoperfusion in the occipital cortex in addition to the visual association cortices, with reduced damage to the posterior cingulate, which in AD is usually severely affected [128]. On the other hand, **F-dopa** (**Figure 8**), the isotopologue of **L-dopa** did not show any differences between PDD and DLB [127].

Assessing the integrity of the cholinergic system in DLB using the PET ligands **MP4A** and **MP4P** (**Figure 8**), Klein et al. [26]were able to demonstrate that in DLB and PDD there is severe cholinergic deafferentation of the neocortex, especially in the occipital cortex, but not in PD without dementia, in which there might be mild cortical cholinergic transmission.

[^{123}I]β-CIT (**Figure 8**) -SPECT also showed that there is reduced uptake of the tracer in the pontine and midbrain regions in MSA-P patients [130]. In **FDG** PET studies, reduced glucose metabolism was found in the putamen, caudate nucleus, frontal cortex, and cerebellum, especially in patients with OPCA [31,129–131]. There was also decreased **F-dopa** in the putamen, caudate nucleus, GPe, red nucleus, and ventral striatum. Even though such striatal alterations are also present in PD patients with the same disease duration, alterations in the red nucleus and the GPe show up later. Furthermore, in comparison to PD, no compensatory increase in **F-dopa** in other brain areas is observed in MSA [132].

For the differentiation of MSA (early after the onset of autonomic dysfunction) from PD scintigraphy with **[^{123}I]MIBG** (**Figure 8**), which shows up to 95% and 90% sensitivity. Its ability to accumulate in presynaptic terminals in the heart [133,134] allows it to evaluate heart myocardial function in patients with PD and MSA. There were significant differences between the accumulation of the tracer in PD and MSA-C but not

MSA-P in the heart myocardium [137]. Being a relatively non-specific approach, **MIBG** scintigraphy is limited by the presence of other comorbidities that decrease the cardiac uptake of **MIBG** [20].

PET imaging of altered cerebral metabolism using **[^{18}F]FDG** is not only useful in the differential diagnosis of PD and other atypical parkinsonian syndromes (APS) like MSA, CBD, and PSP but also renders the imaging of nigrostriatal integrity with the cocaine-analogues **[^{123}I]β-CIT** and **[^{123}I]FP-CIT** redundant. Notwithstanding, the accuracy of the clinical diagnosis used as the reference standard is limited and requires further studies supported by postmortem confirmation in order to validate the diagnostic imaging patterns [135,136].

It is evident that aforementioned radiotracers, similar to MRI modality, can detect changes only after structural alterations have occurred in the brain. According to Braak staging , α-synuclein accumulation occurs before any brain tissue changes are visible [9]. Moreover, up to 50% of the DN in the SN are lost before motor deficits manifest [137]. This indicates that earlier detection of the disease would allow for the timely initiation of treatment for α-synucleinopathies. Radiotracers capable of in vivo detection of α-syn will therefore play a crucial role in this early diagnosis.

4.5.4 α-Syn-targeted PET and SPECT radiotracers

Over the years, a diverse group of ligands has been developed by various researchers for the labeling of α-syn. Various strategies, such as high-throughput screening and rational drug design, have been employed in the development of these radiotracers. Although none has made it into clinical practice, they have introduced good lead structures, the optimization of which will lead to the development of a tracer that fulfills all the criteria listed by Korat et al. [10].

More success has been achieved on other fronts. There are already PET radiotracers that have gained regulatory approval such as **Neuraceq** and **Amyvid** for Aβ PET imaging and Flortaucipir for tau PET imaging [85,138]. Not long ago, advances in Aβ, tau, and α-syn radiotracer development were summarized [85]. Highlighted, were the reasons which guided the choice of the chemical scaffold and functional groups, alongside the efficacy of the radiotracers.

Below will be given a brief discussion of already published α-syn ligands. Focus will be on ligands with interesting properties or those that have served as a basis for the development of improved α-syn ligands.

4.5.4.1 The fluorescent dyes

The development of α-syn tracers began with the discovery that fluorescent dyes such as **ThS** and **ThT** (**Figure 9**) could also bind to α-syn [85,139]. These ligands however lack selectivity; hence they were optimized to obtain dyes with improved binding affinity and selectivity. The new dyes like their predecessors showed increased fluorescence intensity upon interaction with α-syn, but low fluorescent signals in the presence of α-synuclein monomers. Their affinity to α-syn was, however, in the lower micromolar range [140–142].

The first of these were the N-arylaminonapthalene sulfonate-based ligands **2,6-ANS** and **2,6-TNS** (**Figure 9**) developed by Celej et al. [141]. Followed by the monomethine cyanine dyes **T-284** and **SH-516**. The latter was used further to study the interaction of dyes with amyloids. It was discovered that the monomethine dyes bind in a long groove that runs parallel to the length of the axis of α-syn [140,143,144]. Improved methine dyes (tri- and pentamethine cyanines) were consequently developed. The trimethine cyanine dye **SH-299** (**Figure 9**) showed affinity to both oligomeric α-synuclein and α-syn, while the pentamethine cyanine dye **SL-631** displayed affinity only to the oligomeric species. It was therefore concluded that the wide aromatic system of the pentamethine dye is incapable of accessing and binding in the channels formed by β-sheets but could bind better on the relatively less dense oligomeric forms. **SH-299**, in contrast, is less bulky and, due to its more crescent shape, can easily access the groove of the β-pleated structure [142].

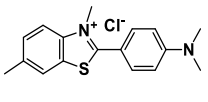

Th-T

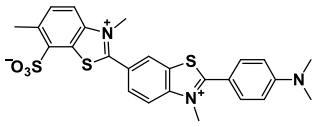

Th-S

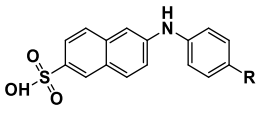

2,6-ANS: R = H;
2,6-TNS: R = CH_3

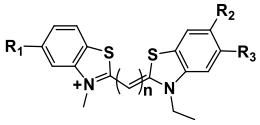

T-284: R_1 = H, R_2 = $N(CH_3CH_2)_2$, R_3 = H, n =1. **SH-516**: R_1 = $(CH)_2Ph$, R_2 = H, R_3 = CH_3, n = $CH_2CHC(CH_3)CHCH_2$

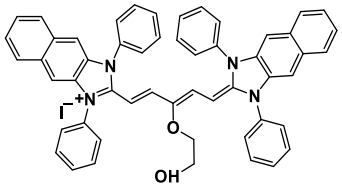

SL-631

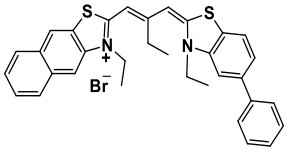

SH-299

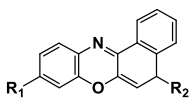

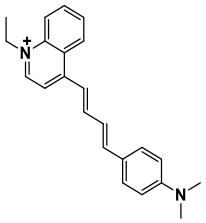

NR: $R_1 = N(CH_3CH_2)_2$, $R_2 = =O$; **LDS-798**
NB: $R_1 = C=N(CH_3CH_2)_2$, $R_2 = NH_2$

Figure 9. The chemical structures of the fluorescent ligands and cyanine dyes. The main drawback of these compounds is their relatively low affinity for α-syn, which is in the micromolar range and lack of selectivity.

Three interesting fluorescent dyes **LDS-798** (**Figure 9**) and the phenoxazine derivatives, **Nile red (NR) and blue (NB)** (**Figure 9**) among others were also developed by Neal et al. in 2013, which labeled LB in PHBT of PD and DLB. Selectivity over tau and amyloid pathology was also observed [145]. Promising as the ligands were, no further investigations with the ligands have not been reported.

4.5.4.2 The tricyclic α-syn ligands

4.5.4.2.1 The phenothiazines derivatives

This class of α-syn tracers known as the SILs **Figure 10** is one of the first class of tracers developed for the in vivo imaging of α-syn in 2012 [146]. Although they did not show particularly high affinity to α-syn or selectivity over tau and Aβ, they represented a step in the right direction since their affinity to α-syn was in the nanomolar range compared to the fluorescent dyes. Compared to more recent α-syn tracers [10], their binding properties are not adequate for in vivo imaging. Nevertheless, **SIL23** was labeled with iodine-125 and tested against LB and LN in PD PHBT as well as tau and $A\beta_{1\text{-}42}$ fibrils. With an affinity of 148 nM to α-syn, selectivity over Aβ fibrils was < 5-fold and barely 2-fold over tau fibrils. It remains, however, a tool for the determination of the binding profile of new α-syn tracers [118].

Other interesting ligands in this class are **SIL5** and **SIL26**, which, although not performing significantly better than **SIL23**, were nevertheless the best in the group **Figure 10**. Both showed good brain uptake in biodistribution experiments in male Sprague-Dawley rats at 5 min p.i. The relatively less lipophilic **[^{11}C]SIL5** displayed both higher brain uptake at 5 min p.i., as well as faster brain clearance at 60 min p.i. For this reason, it was chosen for further investigation in healthy cynomolgus macaque using PET imaging. Homogenous brain distribution and good washout kinetics were also observed. Further structural modifications of the tracer are needed to obtain a more specific radiotracer for the in vivo imaging of α-syn.

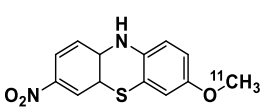

[^{11}C]SIL5

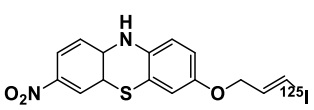

[^{125}I]SIL23

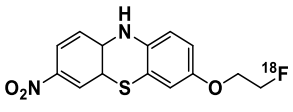

[^{18}F]SIL26

Figure 10. The chemical structures of the presented tracers of the phenothiazine class. Although they were revolutionary for their time, they pale in comparison to more recent tracers in terms of their affinity for α-syn.

4.5.4.3 The Benzoxazole derivatives

4.5.4.3.2 BF-227

The first tracer in this group was **BF-227** (**Figure 11**) can be radiolabeled both with carbon-11 [147] and fluorine-18 [148,149]. **BF-227** was initially developed as a PET ligand for Aβ imaging [150]. It was coincidentally discovered during its biological evaluation that it also binds to α-syn with an affinity (K_d 9.6 nM)**.** Its higher affinity (K_d 1.3 nM) for Aβ [148] already counted it out as a prospective tracer for the imaging of α-syn due to the concomitant co-localization of both amyloid aggregates in most NDD [151].

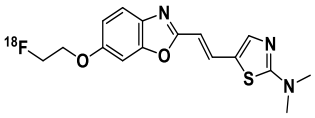

[^{18}F]BF-227

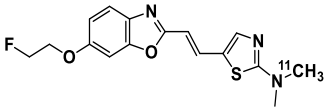

[^{11}C]BF-227

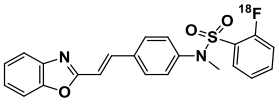

[^{18}F]2FBox

Figure 11. The chemical structures of tracers of the benzoxazole class. In as much as [^{18}F]2FBox fared better than [^{18}F]BF-227 in terms of selectivity over Aβ, it was still unable to detect α-syn both in PD and MSA cases.

Notwithstanding, the ligand was further evaluated as an α-syn tracer. This was met by inconsistent results regarding its ability to detect α-syn in PD, DLB, and MSA PHBT: it could detect α-syn in PD but not DLB brain tissues [147], α-syn in only MSA cases [147], or that it did not bind to neither α-syn in PD, DLB, or MSA cases [149]. In the case of **BF-227**, one of the pitfalls in the development of α-syn tracers is boldly highlighted. False positive results are possible due to interference by another coexisting protein aggregate. Aβ is the usual suspect due to its high density and ubiquity in NDD [151,152].

Attempts to improve affinity to α-syn and selectivity over Aβ were met with little success. These included fluoroPEGylation, or the complete substitution of the fluoroethyl group with iodine or fluorine, or the substitution of the tertiary amine with a hydrogen atom. Selectivity was improved with the substitution of the fluoroethyl group with the halogens, however, affinity to α-syn remained > 70 nM [153].

4.5.4.3.3 The FBox tracers

These are benzofuran derivatives based on the BF-277 scaffold with an additional sulfonamide group [154]. They were designed based on a rational drug design approach. The most interesting tracer in this group was **[^{18}F]2FBox** (**Figure 11**). It displayed a K_i of 3.3 ± 2.8 nM and 145 ± 114.5 nM to α-syn and Aβ fibrils, respectively. **[^{18}F]2FBox** was able to detect the synthetic α-syn hitherto injected in rat brains in autoradiography experiments. However, it failed to show specific binding to the same synthetic α-syn in in vivo PET imaging conducted with the same rats. This was unexpected because the brain uptake of

[^{18}F]2FBox was high enough (0.47 %ID/g at 12 min p.i., SUV 1.6) to enable in vivo imaging, with suitable brain washout (0.094 %ID/g at 50 min p.i.).

This was believed to be a result of both the low spatial resolution of PET imaging compared to in vitro autoradiography and the high non-displaceable binding property of the tracer, which could hamper selective imaging. **[^{18}F]2FBox** also failed to detect α-syn in the medulla oblongata of PD and MSA cases in autoradiography experiments. This is a common feature of some α-syn tracers and highlights the possible influence of in vivo PTM on the affinity of ligands already proven to bind to synthetic α-syn.

4.5.4.4 The Indolinone and Indolinonediene derivatives

This class of α-syn tracers was well-described in the review [85]. The most promising tracer of this class **46a** (Z, E configuration) **Figure 12** compared to its E, E isomer (E, E-46b). **46a** showed a combination of high affinity to α-syn in both in vitro ThT-based competitive (K_i 2.1 nM) and saturation binding assays (K_d 8.9 nM). Selectivity over Aβ and tau was high as well in both assays. In the competition binding assays, selectivity over Aβ and tau was 58-fold and 236-fold, respectively, and in the saturation, binding assays, 30-fold, and 6-fold, respectively.

Z,E-46a **E,E-46b**

Figure 12 . The chemical structures of the Z, E and Z, Z configurations of the indolinonediene derivative. 46a (K_i α-syn 2.1, Aβ 142.4, tau 80.1) and **46b** (K_i α-syn 76.1, Aβ 125.3, tau 455.7). High lipophilicity was a major obstacle for the presented tracers.

Despite these positive results, the tracer was not further investigated due to its considerably high lipophilicity (Clog P 5.6), evidenced by its slow brain washout in PET imaging studies in NHP [151]. There were also concerns about the in vivo reduction of the nitro-group and the eventual loss of potency. Nonetheless, a less lipophilic **ligand-20** (structure unknown) with fluorescent properties from this class was used to stain PD and PD/DLB PHBT. The results showed that the ligand was able to label both Aβ and α-syn [153]. The structural optimization of **46a** is needed to reduce its lipophilicity since it seems promising.

4.5.4.5 The thiazole and thiophene derivatives

Some ligands which bear the thiazole moiety have already been described above. Such as the fluorescent dyes **ThS**, **T-284**, **SH-299**, and **SH-516** (**Figure 9**), which contain the thiazole moiety fused in a benzothiazole ring. **BF-277** (**Figure 11**) also bears this moiety, as well as our DABTA tracers, which are based on a bisthiazole scaffold, with each thiazole ring bearing an aryl or a heteroaryl moiety.

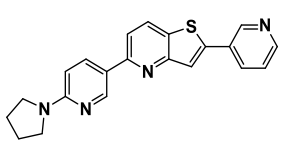

L-32

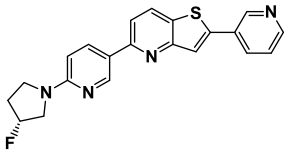

L-44

Figure 13. The chemical structures of the representatives of the diphenylthiazole and thienopyridine series. These compounds appear promising; however, there is limited information available about them.

Two compounds **L-32** and **L-44** (**Figure 13**) which belong to a series of thiazolopyridine and thienopyridine derivatives developed by Molette et al.[155], showed high affinity (K_d 7.9 nM and 9 nM) α-syn in PD homogenates in a backscattering interferometry-based affinity experiment. **L-32** also specifically and intensely stained PD brain sections, whereas **L-44** showed weak staining. On the other hand, **L-44** showed no staining of AD brain sections. Further reports are awaited regarding the potency of these ligands as α-syn ligands.

4.5.4.6 The benzothiazole derivatives

One of the most interesting ligands of this class is **C05-01** (**Figure 14**). It was developed as a result of structural modification of the tau tracer **[^{11}C]PBB-3** (**Figure 14**), which was initially developed as a PET tracer for the detection of tau aggregates [156]. In preclinical studies, it was discovered that it also binds to LB, LN, and GCIs. However, according to fluorescent imaging, affinity to α-syn was only possible at high concentrations of the ligand. This was confirmed in autoradiography experiments, in which the tracer at a concentration of 10 nM (A_m 133 GBq/µmol) was unable to bind to LB in DLB PHBT at a concentration of 10 nM, but it could stain the dense GCIs in MSA PHBT [157].

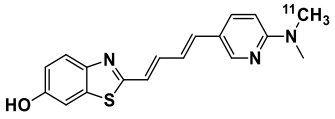

[^{11}C]PBB-3

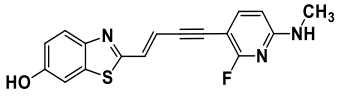

C05-01

Figure 14.The chemical structures of the representatives of the benzothiazole class. The double bonds in the molecules could pose a problem due to increased reactivity and sensitivity to UV light.

C05-01 was chosen from a series of PBB-derived ligands and was further investigated due to its more intense fluorescence upon interaction with α-syn in LB compared to the other 44 ligands in the series. The study was based on a qualitative assessment via the use of fluorescent microscopy and the eventual semiquantitative evaluation of the fluorescence signals which correspond to α-syn using the high-throughput molecular analysis tool tissue microarray (TMA).

It was found in in vitro binding assays with recombinant α-syn and brain homogenates, that **C05-01** has a higher affinity (K_d and K_i 25–30 nM for α-syn, K_i 3.5 nM for brain homogenates) to α-syn compared to PBB3 (k_d 58 nM). **[^{3}H]C05-01** was further evaluated via autoradiography using TMA and frozen PD, MSA, Pick's disease, VD, and AD PHBT. The results showed specific binding to α-syn, tau, and Aβ aggregates, as well as non-specific and off-target bindings. No in vivo experiments have been reported yet for this tracer, nonetheless, the authors believe that further structural optimization is still needed to improve the physicochemical properties of the ligand. Notwithstanding, the use of TMAs stood out as a useful tool for an easier evaluation of radiolabeled or fluorescent ligands to protein aggregates [158].

4.5.4.7 The benzoimidazole derivatives

4.5.4.7.4 Azaindole derivatives

This class of α-syn ligands is distinguished by the triple bond in the molecules [159]. They could be described as a disubstituted acetylene, where the acetylene is bonded on either side to an azaindole moiety and a phenyl moiety. All the ligands showed not only a high affinity to recombinant α-syn (K_d 0.73–3.35 nM), but also to Aβ (2–22-fold lower) and tau. Affinity to tau was in most cases higher than affinity to α-syn except in two cases where it was a mere 2.4–3.4-fold lower **Figure 15**. No explanation was offered by author regarding this low selectivity over the Aβ and tau. However, it could be concluded that the triple bond with its high electron density facilitates binding to the possibly electron-deficient protein aggregates. Further research on the utility of this class of α-syn ligands remains to be reported.

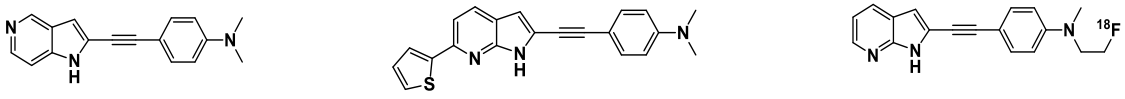

22d **25a** **[^{18}F]28**

Figure 15. The chemical structures of the representatives of the azaindole class. 22d (Ki α-syn 1.0, Aβ 3.6, tau 2.4); **25a** (Ki α-syn 0.5, Aβ 4.9, tau 1.7); **[^{18}F]28** (Ki α-syn 2.4, Aβ 1.2, tau 1.0). The role of the triple bonds in the binding characteristics of these compounds merits further examination.

4.5.4.8 The diphenylpyrazole derivatives

The most notable tracer of this class so far is **MODAG-001 [160]** (**Figure 16***)*, which is a structural improvement of the α-syn oligomer modulator **anle138b**, developed as a tau aggregation inhibitor [161]. It showed high affinity for α-syn (K_d 0.6 ± 0.1 nM) and ~20-fold selectivity over Aβ and tau. It was labeled with carbon-11 and used for in vivo PET imaging in mice. Due to its in vivo instability, it was deuterated. Deuteration was able to reduce the rate of the biotransformation of the tracer, but there were still up to a total of 13% of brain radiometabolites 15 min after p.i. in healthy mice. The deuterated analog (**d_3)-[^{11}C]MODAG-001** was also used for further in vivo experiments. The deuterated tracer showed high BBB penetration, rapidly peaking at an SUV of 1.7 immediately after administration. It was also able to label α-syn injected in rat striata, which was also visualized via PET imaging. However, tritiated **(d_3)-[^{3}H]MODAG-001** in autoradiography experiments was unable to detect α-syn in DLB PHBT but detected Aβ in AD PHBT; it showed no specific binding to tau in AD and PSP PHBT [160].

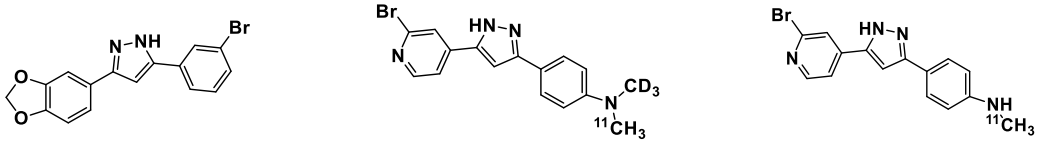

anle138b **[^{11}C]MODAG-001** **[^{11}C]MODAG-005**

Figure 16. The chemical structures of anle138b, (d_3)-[^{11}C]MODAG-001 and [^{11}C]MODAG-005. These compounds/tracers are characterized by the presence of a bromine atom that may play a role in their affinity to α-syn.

Recently, in vivo PET study was carried out by Raval et al. with the tracer in pigs, in whose brains were stereotactically injected either PFF, DLB brain homogenates (Braak stage II), or AD brain homogenates (Braak stage IV, devoid of α-syn) [162]. The results showed that the DLB injected region did not differ compared to the reference regions and that the tracer was bound to both the PFF and Aβ fibrils. However, the TAC and BPND values showed that the tracer may be sensitive to the concentration of α-syn in the brain. A new tracer (**MODAG-005**) was recently introduced by the group and seems promising [163].

4.5.4.9 Chalcone derivatives

4.5.4.9.5 The IDP tracers

These tracers are reminiscent of the azaindole derivatives **Figure 17**, where selectivity was minimal [164]. They are also one of the few α-syn tracers labeled with iodine-125 for SPECT imaging. The tracers showed a length-dependent affinity for α-syn. It was also observed in binding experiments that the shorter the α,β-unsaturated ketone bridge, the lower the affinity for α-syn. Unfortunately, the most notable tracer **[^{125}I]IDP-4** (**Figure 17**) (K_i 5.4; > 2.5-fold selectivity over Aβ) with the longest α,β-unsaturated ketone bridge suffered from the disadvantage of having the highest ClogP 5.5, which could be partly attributed to both the bridge and the radiohalide iodine-125. Iodine-125 not only increased the lipophilicity of the tracer but also

increased its MW parameters, which resulted in reduced brain uptake. It was therefore unsurprising that the initial brain uptake at 2 min p.i. in healthy was < 0.5 %ID/g, with almost no change at 60 min p.i. Notwithstanding, two of the tracers in this group **[^{125}I]IDP-4** included were able to visualize α-syn in PD brain sections via fluorescent and IHC staining.

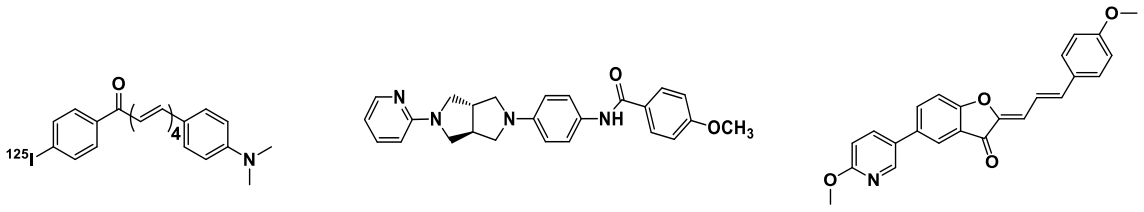

[^{125}I]IDP-4 **L-132** **Tg-52**

Figure 17. The chemical structures of the IDP, N-phenylbenzamide and Benzofuranone representatives. None of these tracers met the criteria for an effective α-syn tracer suitable for in vivo imaging.

4.5.4.10 The N-phenylbenzamide derivatives

Six ligands of this series showed a high percentage displacement of a tritiated ligand of this series in an autoradiography experiment on A30P mice brain sections at a concentration of 1 µM [165]. Although some of them showed low selectivity over Aβ in AD PHBT, compound **L-132** (**Figure 17**) seemed promising, with up to 82% displacement in the A30P mice brain sections and only 20% in the AD PHBT.

The ligands were all tritiated and administered to A30P transgenic mice, in which all displayed good BBB penetration 30 min p.i. and specific binding in the pons, midbrain, and subthalamic region, with no significant off-target binding observed in ex vivo autoradiograms. In vitro autoradiography experiments with AD PHBT brain sections, however, revealed that the tracers also bind to Aβ. The selectivity of the tracers still needs optimization, and more evidence of the brain pharmacokinetics of the tracers is still awaited.

4.5.4.11 The Benzofuranone derivatives

These are a class of ligands with structural similarities with the indolinonediene derivatives, such as **46a** (**Figure 12**). In this class, **Tg-52** (**Figure 17**) was identified as the best compound [166]. It showed an affinity of K_i 2.3 nM and IC_{50} 1.18 nM for two sites on the α-syn fibril. Taking advantage of its fluorescent properties, it was investigated at a concentration of 10 µM via in vitro fluorescent staining of PD, AD, and MSA PHBT. The results showed a high ligand-target engagement with the LB in PD PHBT sections, as well as Aβ plaques in AD PHBT. It failed to label LN; likewise, there was weak interaction with the GCIs in the MSA sections. This suggests that each α-syn species might have its own unique binding sites for small molecules. In vivo studies with this ligand are yet to be carried out.

4.5.5 Factors that hinder the development of suitable α-syn tracers

The development of brain tracers is usually fraught with difficulties, starting with the lipophilicity of the tracer, which ensures permeability across the BBB. This plays twice as much a role in the development of α-syn tracers. The location of LB, like that of the tau aggregates, is predominantly intraneuronal, while the GCI are intraglial. They can also be found extracellularly, due to neuronal death or secretion. This implies that the prospective tracer must be sufficiently lipophilic to partition across both the BBB and the neuronal membrane, or it has to be taken up via active transport [151,152]. Optimal lipophilicity ensures high brain uptake (early standard uptake value (SUV) > 1.0) in 5–10 min post-injection (p.i.), fast clearance of non-specifically bound tracers from the brain, fast plasma clearance (at least 30 min p.i., to reduce background signals from the blood), and less extensive hepatic metabolism, which could result in the production of brain-penetrant metabolites. These properties enable uncomplicated kinetic modeling and facilitate suitable quantification and reproducibility [135,148,164]. MW is another factor that affects the brain bioavailability of the tracers. BBB penetration is inversely proportional to the square root of the MW of a ligand, hence why bulky positron-emitting radionuclides such as I-124 were avoided [167,168].

Additionally, the development of α-syn radiotracers is replete with its own unique problems. In comparison to the other amyloid aggregate proteins, such as Aβ and tau, the absolute concentration of α-syn in the LBD and MSA brains is believed to be lower. In fact, it is more than 10-fold lower than the concentration of Aβ in an AD brain [151,152]. This means that the prospective tracer must bind to α-syn in the nanomolar range and, if possible, in the subnanomolar range. Moreover, the possible co-existence of these protein aggregates in the brain in pathology further complicates detection. β-amyloid pathology is found in 80% of LBD and MSA cases, and in nearly 50% of the α-synucleinopathies in the third stage of Braak staging and upwards (with tau pathology present as well). β-amyloid pathology is also typical for LBD, and it is present in approximately 85% of dementia cases, as well as tau pathology in 30% of the cases, in Braak stages V and VI [151]. A low level of tau pathology (stages 0–2 of Braak staging) is also found in some PD patients (posthumously at autopsy), although restricted to the hippocampus [169]. Furthermore, the structural similarity of the three amyloid protein aggregates owing to the presence of similar β-pleated sheets brings about an additional complexity. This means that the putative tracer must be selective over these protein aggregates in cases with an overlap of pathologies, in the range of 10–50-fold [118].

Again, like tau aggregates, α-syn is prone to PTM, such as phosphorylation at the serine and tyrosine residues. Nitration at the tyrosine residues is also common [170]. It is possible that these PTMs could result in a variety of substructures that may affect the binding of a radiotracer [151]. Additionally, similar to NFTs [151], α-syn derived from PD, DLB, and MSA PHBT display different structural differences. Patient-derived fibrils from PD and MSA cases resemble the ribbon fibrillar polymorph with a flat and twisted

appearance, while those from DLB were cylindrical with no twists and bore resemblance to the fibrillar polymorph [171]. It was reported that there is structural heterogeneity between brain-derived PD and MSA α-syn [172,173]. There is, therefore, a possibility that not all tracers could bind to all types of fibrillar polymorphs. Combined with PTM, the existence of different types of α-syn polymorphs could underlie the failure of some tracers that showed an excellent affinity for recombinant α-syn to show the same affinity for patient-derived α-syn [10,154,173].

In vivo evaluation of α-syn is also problematic due to the lack of a suitable disease model for the α-synucleinopathies. There is still speculation about whether the quantity of α-syn in the genetically modified rodent models is sufficient for in vivo imaging. Even at that, the long duration needed for the development of the synucleinopathy as well as the high cost restrict the use of these animal models. To navigate these problems, viral vector models, rodents seeded with PFF, and a combination of both seem to be suitable alternatives [114,174,175]. The injection of α-syn fibrils in the striatum of rats and carrying out in vivo imaging a week after inoculation was another alternative shown by Verdurand et al. [154]. Not long ago, a group in Copenhagen showed the possibility of in vivo imaging in pigs, after the injection of PFF and brain homogenates from DLB patients into the animals [162]. The comparatively large pigs´ brains make it possible to perform neurosurgical procedures. Moreover, the pigs can withstand several PET scans in addition to frequent blood sampling, compared to smaller rodents.

Notwithstanding this recent progress in the field, the evaluation of prospective tracers should be based on patient-derived α-syn since there is growing evidence that in vitro and in vivo assays based on recombinant α-synuclein fibrils [173] do not translate well to clinical application of the tracers. Nevertheless, obtaining these patient-derived materials is not easy, and this considerably slows down the development and screening of new tracers.

4.6 Scopes and objectives of the project

Despite the above-mentioned limitations, several research groups are making considerable efforts to develop α-syn tracers that will make it into to clinical practice [10,85]. Our contribution to these efforts is based on a DABTA scaffold. Over the past four years, several attempts have been made, some of which have been successful, to ensure our tracer meets all the criteria of a good α-syn radiotracer.

Our approach was a ligand-based approach, based on the alteration of the 4,4'-diaryl-2,2'-bithiazole (DABTA) scaffold **Figure 18** [176] with the goal of improving the affinity of the ligand to α-syn and selectivity over Aβ and tau fibrils as well as improving the pharmacokinetics of the ligands as well. In collaboration with the Hans Ågren group (Uppsala University), different DABTA derivatives were designed

for improved affinity to α-syn and selectivity over Aβ and tau. This was accomplished using multiple *in silico* modeling techniques. By means of molecular docking, MM/GBSA, free energy calculations, and metadynamics stimulation, the interactions between the DABTAs and the fibrils (α-syn, Aβ, and tau) were studied [138]. Based on these studies the benefits of some functional groups and chemical moieties were identified and efforts were made to include them in all the DABTAs synthesized thereafter. Consequently, the promising ligands were chemically synthesized for experimental in vitro binding experiments.

Over the duration of the project, the effects of different functional groups and chemical moieties were tested, culminating in the selection of certain functional groups over others. The objectives of the project are essentially established on this premise and include:

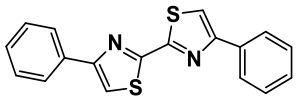

Figure 18. The disarylbisthiazole scaffold. The DABTA scaffold comprises planar, hydrophobic aromatic rings that facilitate both interaction with binding sites and partitioning across the blood-brain barrier.

i. Devise a protocol to easily synthesize the DABTAs and obtain the final products with high chemical yield and purity.
ii. Establish a radiolabeling protocol that allows for quick labeling of the precursors in high RCY, RCP, and A_m.
iii. Evaluate the tracers via *in vitro* binding affinity assays (using both recombinant protein fibrils and autoradiography on PHBT), biodistribution experiments and ex vivo metabolite experiments.

The tools and methods used to achieve the above-set objectives are outlined below in detail.

5. MATERIALS AND METHODS

5.1 General methods

All commercial reagents and solvents were used without further purification. The building blocks were purchased from commercial suppliers, Chemspace (Latvia) and Sigma Aldrich (Germany). Semipreparative reversed-phase HPLC was performed using a Zorbax Bonus RP column, 9.4 x 250 mm, 5.0 µm connected to a Shimadzu system (Japan), which comprised two LC-20AP quaternary low-pressure gradient pumps, an SPD-M30A photodiode array detector, and a CBM-20A system controller. Reaction completion (for all the synthesis carried out), quality control for chemical and radiosynthesis were carried out with a high-performance analytical HPLC system (Shimadzu, Japan) with a photo diode array detector (Shimadzu) and a GABI Star γ detector using a Chromolith RP18e (4.6 × 100 mm). The eluents used were water (0.1% v/v formic acid, solvent A) and MeCN (0.1% v/v formic acid, solvent B) at a flow rate of 3 mL/min. MW was carried out with LCMS-2020 ESI (Shimadzu) connected to the above analytical HPLC system. The ^{1}H (500 MHz) and ^{13}C (126 MHz) spectra were recorded on a cryo Bruker 500 MHz spectrometer (Bruker, Massachusetts, U.S.). Sonication was performed with an Ultrasonic cleaner USC-TH sonicator (VWR, Germany). During experiments involving radioactivity, activity was quantified with a Capintec CRC® 15R dose calibrator (American Laboratory Trading, San Diego, U.S.). For the in vivo and ex vivo experiments, the activity in the tissue/organ samples was measured using a PerkinElmer Wizard 2480 automatic gamma counter (PerkinElmer, Connecticut, U.S.). Evaporation of solvents was done with Büchi Rotavapor® R-100 (Germany) and lyophilized with a Christ Alpha 1-2 LDplus freeze dryer (Rieger, Austria). The NMR and mass-spectrometric characterization of the compounds are listed in the appendix **10.5**.

5.2 Chemical synthesis

5.2.1 General procedure for the synthesis of the 4-aryl/heteroarylthiazole-2-carbothioamide intermediate, b

To a 1.5 mL DMF solution of DTO 180.3 mg (1.5 mmol. equiv.) in a 10 mL vial while stirring was added dropwise the corresponding phenacyl/heteroacylbromide or a 3,4-methylenedioxy(phenacylbromide) (1 mmol) in 500 µL of DMF and left to react overnight at rt **Scheme 1.** Deviations from the general procedure are specified in **5.2.2**.

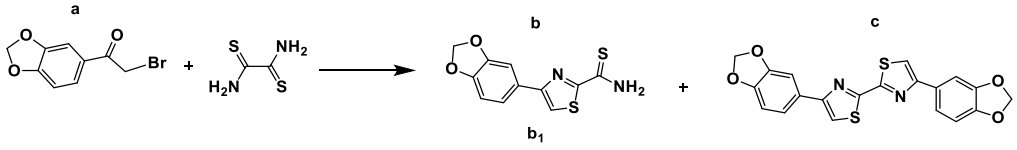

Scheme 1a

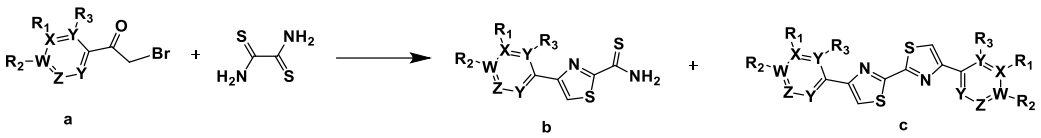

Scheme 1b

b	W	X	Y	Z	R_1	R_2	R_3
b_3	C	C	CH	CH	OH	OCH_3	H
b_4	C	C	CH	CH	F	OCH_3	H
b_7	C	CH	CH	N	H	Br	H
b_8	C	CH	CH	N	H	F	H
b_9	C	N	CH	N	-	Cl	H
b_{10}	C	N	CH	N	-	F	H
b_{11}	C	CH	N	N	H	OH	-
b_{12}	C	C	CH	CH	F	OH	H
b_{13}	C	CH	CH	CH	H	OH	H
b_{14}	C	C	CH	CH	NO_2	Cl	H
b_{15}	N	C	CH	CH	Cl	-	H
b_{16}	C	C	CH	CH	H	OH	OH

Scheme 1. Synthesis of the 4-aryl/heteroarylthiazole-2-carbothioamide intermediates, b. Scheme 1a shows the synthesis of 4-(benzo[d][1,3]dioxol-5-yl)thiazole-2-carbothioamide and **Scheme 1b** the synthesis of the other 4-aryl/heteroarylthiazide-2-carbothiamide intermediates. Since 4-(benzo[d][1,3]dioxol-5-yl)thiazole-2-carbothioamide is quite stable and easy to purify, the synthesis of all compounds containing the 1,3-benzodioxole moiety begins with this intermediate.

5.2.2 Detailed procedure for the chemical synthesis of the 4-aryl/heteroarylthiazole-2-carbothioamide intermediates, b

5.2.2.1 4-(benzo[d][1,3]dioxol-5-yl)thiazole-2-carbothioamide, b_1

b_1 was synthesized according to the general procedure using 180.3 mg DTO and 243.1 mg of 1-(benzo[d][1,3]dioxol-5-yl)-2-bromoethan-1-one. Semiprep HPLC purification (SHP) with 30% aqueous MeOH solution, 0.1% THF, 0.1% TFA (solvent A) and MeCN, 0.1 % TFA (solvent B), at a flow rate of 5 mL/min and a gradient A/B: 80:20 to 18:82 in 17 min. **b_1** was obtained in a 64.7 ± 3.86% (n = 5) yield with ≥99% HPLC purity.

5.2.2.2 4-(3-hydroxy-4-methoxyphenyl)thiazole-2-carbothioamide, b_3

b_3 was synthesized according to the general procedure using 180.3 mg DTO and 245.1 mg of 2-bromo-1-(3-hydroxy-4-methoxyphenyl)ethan-1-one. SHP with 30% aqueous MeOH solution, 0.1% THF, 0.1% TFA (solvent A) and MeCN, 0.1 % TFA (solvent B), at a flow rate of 5 mL/min and a gradient A/B: 95:5 to 23:77 in 17 min. **b_3** was obtained in a 75.6 ± 4.37% (n = 2) yield, with ≥99% HPLC purity.

5.2.2.3 4-(3-fluoro-4-methoxyphenyl)thiazole-2-carbothioamide, b_4

b_4 was synthesized according to the general procedure using 180.3 mg DTO and 247.1 mg of 2-bromo-1-(3-fluoro-4-methoxyphenyl)ethan-1-one. SHP with an aqueous mixture of THF and MeOH solution (20%:10%), 0.1% TFA (solvent A) and MeCN, 0.1 % TFA (solvent B), at a flow rate of 5 mL/min and a gradient A/B: 70:30 to 32:68 in 17 min. **b_4** was obtained in a 60.0 ± 1.04% (n = 2) with ≥99% HPLC purity.

5.2.2.4 4-(6-bromopyridin-3-yl)thiazole-2-carbothioamide, b_7

b_7 was synthesized according to the general procedure using 180.3 mg DTO and 279.0 mg of 2-bromo-1-(6-bromopyridin-3-yl)ethan-1-one. SHP with an aqueous mixture of THF and MeCN solution (0.3%:40%), 0.1% TFA (solvent A) and MeCN, 0.1 % TFA (solvent B), at a flow rate of 5 mL/min and a gradient A/B: 90:10 to 20:80 in 18 min. **b_7** was obtained in a 38.0 ± 7.18% (n = 3) yield with ≥99% HPLC purity.

5.2.2.5 4-(6-fluoropyridin-3-yl)thiazole-2-carbothioamide, b_8

b_8 was synthesized according to the general procedure using 180.3 mg DTO and 219.0 mg of 2-bromo-1-(6-fluoropyridin-3-yl)ethan-1-one. SHP with an aqueous mixture of THF and MeOH solution (0.2% and 40% respectively), 0.1% TFA (solvent A) and acetonitrile, 0.1 % TFA (solvent B), at a flow rate of 5 mL/min and a gradient A/B: 90:10 to 25:75 in 18 min. **b_8** was obtained in a 88.2% (n =1) yield with ≥99% HPLC purity.

5.2.2.6 4-(2-chloropyrimidin-4-yl)thiazole-2-carbothioamide, b_9

To a 1.0 mL DMF solution of DTO (92.0 mg, 0.7644 mmol) in a 10 mL vial, while stirring, was added dropwise 2-bromo-1-(2-chloropyrimidin-5-yl)ethan-1-one (80 mg, 0.3397 mmol) in 0.5 mL of DMF. The mixture was left to run for 2 days at 50°C. 5 mL of DMF was added to dissolve the precipitated **b_9**, then the mixture was transferred to a 10 mL falcon tube and centrifuged at 6000 r.p.m for 10 min. The supernatant was decanted, and 1 mL of 95% aqueous MeCN was added to it. The mixture was then kept at -20°C for 2 days. Precipitated **b_9** was sonicated 3 times in 5 mL MeCN with 1% DMSO each time, followed by centrifugation as already described, until a 98% HPLC-pure **b_9** precipitate was obtained. The MeCN supernatants were combined and purified with the semiprep HPLC. SHP was carried out with an aqueous mixture of THF and MeOH solution (7.5% and 28% respectively), 0.1% TFA (solvent A) and MeCN, 0.1 % TFA (solvent B), at a flow rate of 5 mL/min and a gradient A/B: 90:10 to 30:79 in 17 min. A combination of the **b_9** purified via trituration and the semiprep gave a 30.0% (n =1) yield with ≥98% HPLC purity.

5.2.2.7 4-(2-fluoropyrimidin-4-yl)thiazole-2-carbothioamide, b_{10}

To a 1.0 mL DMF solution of DTO (62.9 mg, 0.5243 mmol) in a 10 mL vial, while stirring, was added dropwise 2-bromo-1-(2-fluoropyrimidin-5-yl)ethan-1-one (82.3 mg, 0.3495 mmol) in 0.5 mL of DMF. The mixture was left to run overnight at rt. SHP was carried out with 30% aqueous MeCN solution, 0.1% TFA (solvent A) and MeCN, 0.1 % TFA (solvent B), at a flow rate of 5 mL/min and a gradient A/B: 92:08 to 22:78 in 17 min. **b_{10}** was obtained in a 32 % (n = 1) yield with ≥98% HPLC purity.

5.2.2.8 4-(5-hydroxypyrimidin-2-yl)thiazole-2-carbothioamide, b_{11}

b_{11} was synthesized according to the general procedure using 180.3 mg DTO and 217 mg of 2-bromo-1-(5-hydroxypyrimidin-2-yl)ethan-1-one. SHP with 30% aqueous MeOH solution, 0.1% THF, 0.1% TFA (solvent A) and MeCN, 0.1 % TFA (solvent B), at a flow rate of 5 mL/min and a gradient A/B: 90:10 to 30:70 in 17 min. **b_{11}** was obtained in a 73.3 ± 2.42% (n = 2) yield with ≥99% HPLC purity.

5.2.2.9 4-(3-fluoro-4-hydroxyphenyl)thiazole-2-carbothioamide, b_{12}

To a 1.0 mL DMF solution of DTO (116.0 mg, 0.9655 mmol) in a 10 mL vial, while stirring was added dropwise 2-bromo-1-(3-fluoro-4-hydroxyphenol)ethan-1-one (150 mg, 0.6436 mmol) in 1.0 mL of DMF. The mixture was left to run over night at rt. SHP with 30% aqueous MeOH solution with 0.1% THF and 0.1% TFA (solvent A) and MeCN, 0.1 % TFA (solvent B), at a flow rate of 5 mL/min and a gradient A/B: 90:10 to 22:78 in 16 min. **b_{12}** was obtained in a 76.1 ± 2.51% (n = 3) yield with ≥99% HPLC purity.

5.2.2.10 4-(4-hydroxyphenyl)thiazole-2-carbothioamide, b_{13}

To a 0.5 mL DMF solution of DTO (83.8 mg, 0.6975 mmol) in a 10 mL vial while stirring was added dropwise 2-bromo-1-(4-hydroxyphenyl)ethan-1-one (100 mg, 0.4650 mmol) in 0.5 mL of DMF. The mixture was left to run over night at rt. SHP was carried out with 30% aqueous MeOH solution with 0.1% TFA and 0.1% THF (solvent A), and MeCN, 0.1 % TFA (solvent B), at a flow rate of 5 mL/min and a gradient A/B: 70:30 to 20:80 in 18 min. **b_{13}** was obtained in a 72.2 % (n = 1) yield with ≥99% HPLC purity.

5.2.2.11 4-(4-chloro-3-nitrophenyl)thiazole-2-carbothioamide, b_{14}

To a 0.5 mL DMF solution of DTO (64.7 mg, 0.5386 mmol) in a 10 mL vial while stirring was added dropwise 2-bromo-1-(3-chloro-4-nitrophenyl)ethan-1-one (100 mg, 0.3591 mmol) in 0.5 mL of DMF. The mixture was left to run overnight at rt. SHP was carried out with 20% aqueous MeCN solution, 0.1% TFA and 0.4% THF (solvent A) and MeCN, 0.1 % TFA (solvent B), at a flow rate of 5 mL/min and a gradient A/B: 70:30 to 20:80 in 17 min. **b_{14}** was obtained in a 60.0 % (n = 1) yield with ≥99% HPLC purity.

5.2.2.12 4-(2-chloropyridin-4-yl)thiazole-2-carbothioamide, b_{15}

To a 1.0 mL DMF solution of DTO (180.0 mg, 1.5 mmol) in a 10 mL vial while stirring was added dropwise 2-bromo-1-(2-chloropyridin-4-yl)ethan-1-one (285.0 mg, 1.0 mmol) in 0.5 mL of DMF. The mixture was left to run over night at rt. SHP was carried out with 30% aqueous MeOH solution with 0.1% TFA and 0.2% THF (solvent A), and MeCN, 0.1 % TFA (solvent B), at a flow rate of 5 mL/min and a gradient A/B: 66:34 to 20:80 in 16 min. The compound was obtained in a 78.4% (n = 1) yield with ≥99% HPLC purity.

5.2.2.13 4-(2,4-dihydroxyphenyl)thiazole-2-carbothioamide, b_{16}

To a 1.0 mL DMF solution of DTO (120 mg, 1.5 mmol) in a 10 mL vial while stirring was added dropwise 4-(2,4-dihydroxyphenyl)thiazole-2-carbothioamide (100 mg, 0.4328 mmol) in 0.5 mL of DMF. The mixture was left to run overnight at rt. SHP was carried out with 30% aqueous MeOH solution, 0.1% TFA and 0.2% THF (solvent A), and MeCN, 0.1 % TFA (solvent B) at a flow rate of 5 mL/min and a gradient A/B: 95:05 to 16:84 in 17 min. The compound was obtained in a 70.6 % (n = 1) yield with ≥99% HPLC purity.

5.2.3 General procedure for the synthesis of the asymmetric DABTAs, d

To a 1.0 mL DMF solution of another phenacyl/heteroacylbromide or a 3,4-methylenedioxy (heteroacylbromide) (1.3 mmol equiv.) **Scheme *2***, in a 10 mL vial while stirring, was added the corresponding 4-aryl/heteroarylthiazole-2-carbothioamides intermediates (**b**) in 500 µL of DMF (quantity is specified for each compound) and stirred overnight. A solid precipitate (the product, **d**) is formed as a result (deviations will be stated). Centrifugation carried during trituration was done at 10°C. All the compounds were dried in vacuo to remove the organic solvents, followed by lyophilization to remove residual water. The reaction schemes are shown below in **Scheme 2a-b**.

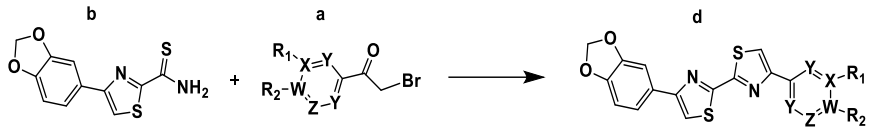

d	W	X	Y	Z	R_1	R_2
d_1	C	C	CH	CH	OH	OCH_3
d_2	C	C	CH	CH	F	OCH_3
d_5	C	CH	CH	N	H	Br
d_6	C	CH	CH	N	H	F
d_{12}	C	CH	N	CH	H	OH
d_{14}	C	CH	CH	CH	H	OH
d_{18}	N	C	CH	CH	Cl	-

Scheme 2a

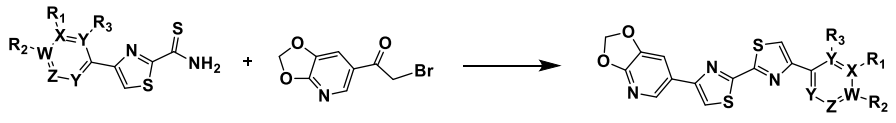

Scheme 2b

d	W	X	Y	Z	R_1	R_2	R_3
d_3	C	C	CH	CH	OH	OCH_3	H
d_4	C	C	CH	CH	F	OCH_3	H
d_7	C	CH	CH	N	H	Br	H
d_8	C	CH	CH	N	H	F	H
d_9	C	N	CH	N	-	Cl	H
d_{10}	C	N	CH	N	-	F	H
d_{11}	C	CH	N	CH	H	OH	-
d_{13}	C	C	CH	CH	F	OH	H
d_{15}	C	CH	CH	CH	H	OH	H
d_{16}	C	C	CH	CH	NO_2	Cl	H
d_{20}	N	C	CH	CH	Cl	-	H
d_{22}	C	CH	CH	CH	H	OH	OH

Scheme 2. Synthesis of the asymmetric DABTAs, d. **Scheme 2a** shows the synthesis of the symmetric DABTAs via the 4-(benzo[d][1,3]dioxol-5-yl)thiazole-2-carbothioamide intermediate, while **Scheme 2b** shows via the other 4-aryl/heteroarylthiazide-2-carbothiamide intermediates.

5.2.4 Detailed procedure for the chemical synthesis of the asymmetric DABTAs, d

5.2.4.1 5-(4'-(benzo[d][1,3]dioxol-5-yl)-[2,2'-bithiazol]-4-yl)-2-methoxyphenol, d_1

193.1 mg of 2-bromo-1-(3-hydroxy-4-methoxyphenyl)ethan-1-one dissolved in 500 µL DMF was added to 160.0 mg (0.6060 mmol) of **b_1** dissolved in 500 µL of DMF in a 10 mL glass vial. The mixture was stirred overnight at 50°C. The resulting mixture was transferred into a 10 mL falcon tube, 5 mL of methanol was added, and the mixture was centrifuged at 6000 r.p.m for 10 min. The resulting sediment was then dissolved in DMSO. Both the supernatant and the dissolved sediment in the DMSO solution were then purified using semipreparative HPLC. SHP was carried out with a 20% aqueous solution of THF, 0.1% TFA (solvent A), and MeCN with 0.1 % TFA (solvent A) at a flow rate of 5 mL/min and a gradient A/B: 40:60 to 14:86 in 18 min. **d_1** was obtained as a pale yellow amorphous solid after solvent removal with ≥99% purity.

5.2.4.2 4-(benzo[d][1,3]dioxol-5-yl)-4'-(3-fluoro-4-methoxyphenyl)-2,2'-bithiazole, d_2

15.6 mg bromo-1-(3-fluoro-4-methoxyphenyl)ethan-1-one dissolved in 500 µL DMF was added to 20.0 mg (0.04849 mmol) of **b_1** dissolved in 500 µL of DMF solution in a 10 mL vial. The mixture was stirred overnight at 45°C. The resulting mixture was transferred into a 10 mL falcon tube and centrifuged at 6000 r.p.m for 10 min. The resulting sediment was sonicated twice in 5 mL of acetone for 10 min. Each time, followed by centrifugation for 10 min (6000 r.p.m) till 99% HPLC purity of **d_2**. **d_2** was obtained as a pale violet amorphous solid after solvent removal.

5.2.4.3 5-(4'-([1,3]dioxolo[4,5-b]pyridin-6-yl)-[2,2'-bithiazol]-4-yl)-2-methoxyphenol, d_3

188.7 mg of 1-([1,3]dioxolo[4,5-b]pyridin-6-yl)-2-bromoethan-1-one dissolved in 500 µL DMF acidified with 25 µL of glacial acetic acid was added to 158.4 mg (0.5948 mmol) of **b_3** dissolved in 500 µL of DMF acidified with 25 µL of glacial acetic acid in a 10 mL glass vial. The mixture was stirred overnight at 50°C. The resulting mixture was transferred into a 10 mL falcon tube, and the mixture was centrifuged at 6000 r.p.m for 10 min. The resulting sediment was sonicated twice in 5 mL of MeOH for 10 min. Each time followed by centrifugation for 10 min, yielding **d_3** with 99% HPLC purity. The resulting supernatants were combined and purified using semiprep HPLC. SHP was carried out with 30% aqueous MeOH solution with 0.4% THF and 0.1% TFA (solvent A), and MeCN with 0.1 % TFA (solvent B) at a flow rate of 5 mL/min and a gradient A/B: 80:20 to 14:86 in 19 min. Overall, **d_3** was obtained with ≥99% HPLC purity as a brownish-white amorphous solid after solvent removal.

5.2.4.4 6-(4'-(3-fluoro-4-methoxyphenyl)-[2,2'-bithiazol]-4-yl)-[1,3]dioxolo[4,5-b]pyridine, d_4

23.6 mg of 1-([1,3]dioxolo[4,5-b]pyridin-6-yl)-2-bromoethan-1-one dissolved in 500 µL DMF acidified with 25 µL of glacial acetic acid was added to 20.0 mg (0.5948 mmol) of **b_4** dissolved in 500 µL of DMF acidified with 25 µL of glacial acetic acid in a 10 mL glass vial. The mixture was stirred overnight at 45°C. The resulting mixture was then transferred to a 10 mL falcon tube. The rest followed as described in **5.2.4.2**. **d_4** was obtained with ≥99% HPLC purity as a pale yellow amorphous solid after solvent removal.

5.2.4.5 4-(benzo[d][1,3]dioxol-5-yl)-4'-(6-bromopyridin-3-yl)-2,2'-bithiazole, d_5

92.1 mg of bromo-1-(6-bromopyridin-3-yl)ethan-1-one dissolved in 500 µL DMF was added to 140.0 mg (0.5297 mmol) of **b_1** dissolved in 500 µL of DMF solution in a 10 mL vial. The mixture was stirred overnight at 35°C. The resulting mixture was transferred into a 10 mL falcon tube and centrifuged at 6000 r.p.m for 10 min. The resulting sediment was sonicated twice in 5 mL of MeOH for 10 min. Each time, followed by centrifugation for 10 min (6000 r.p.m) until 99% HPLC purity of **d_5**. **d_5** was obtained as an off-white amorphous solid after solvent removal.

5.2.4.6 4-(benzo[d][1,3]dioxol-5-yl)-4'-(6-fluoropyridin-3-yl)-2,2'-bithiazole, d_6

37.5 mg of bromo-1-(6-fluoropyridin-3-yl)ethan-1-one dissolved in 500 µL DMF was added to 35.0 mg (0.1324 mmol) of **b_1** dissolved in 500 µL of DMF solution in a 10 mL vial. The mixture was stirred overnight at 35°C. The resulting mixture was transferred into a 10 mL falcon tube and centrifuged at 6000 r.p.m for 10 min. The resulting sediment was sonicated twice in 5 mL of MeOH for 10 min. Each time followed by

centrifugation for 10 min (6000 r.p.m) till 99% HPLC purity of **d_6**. **d_6** was obtained as an off-white amorphous solid after solvent removal.

5.2.4.7 6-(4'-(6-bromopyridin-3-yl)-[2,2'-bithiazol]-4-yl)-[1,3]dioxolo[4,5-b]pyridine, d_7

126.8 mg of 1-([1,3]dioxolo[4,5-b]pyridin-6-yl)-2-bromoethan-1-one dissolved in 500 µL DMF acidified with 25 µL of glacial acetic acid was added to 120.0 mg (0.3997 mmol) of **b_7** dissolved in 500 µL of DMF acidified with 25 µL of glacial acetic acid in a 10 mL glass vial. The mixture was stirred overnight at 45°C. The resulting mixture was then transferred to a 10 mL falcon tube. The rest followed as described in **5.2.4.2**. **d_7** was obtained with ≥99% HPLC purity as a brownish-white amorphous solid after solvent removal.

5.2.4.8 6-(4'-(6-fluoropyridin-3-yl)-[2,2'-bithiazol]-4-yl)-[1,3]dioxolo[4,5-b]pyridine, d_8

46.4 mg of 1-([1,3]dioxolo[4,5-b]pyridin-6-yl)-2-bromoethan-1-one dissolved in 500 µL DMF acidified with 10 µL of glacial acetic acid was added to 35.0 mg (0.1463 mmol) of **b_7** dissolved in 500 µL of DMF acidified with 15 µL of glacial acetic acid in a 10 mL glass vial. The mixture was stirred overnight at rt. The resulting mixture was transferred into a 10 mL falcon tube and centrifuged at 6000 r.p.m for 10 min. The resulting sediment was sonicated twice in 10 mL of a 1:1 mixture of acetone and methanol for 5 min. Each time followed by centrifugation for 10 min (6000 r.p.m) till 99% HPLC purity of **d_8**. **d_8** was obtained as an off-white amorphous solid after solvent removal.

5.2.4.9 4-(4'-(2-chloropyrimidin-5-yl)-[2,2'-bithiazol]-4-yl)-[1,3]dioxolo[4,5-b]pyridine, d_9

96.7 mg of 1-([1,3]dioxolo[4,5-b]pyridin-6-yl)-2-bromoethan-1-one dissolved in 500 µL DMF acidified with 25 µL of glacial acetic acid and added to 78.0 mg (0.3047 mmol) of **b_9** dissolved in 500 µL of DMF acidified with 25 µL of glacial acetic acid in a 10 mL glass vial. The mixture was stirred overnight at 50°C. The resulting mixture was transferred into a 10 mL falcon tube and centrifuged at 6000 r.p.m for 10 min. The resulting sediment was sonicated twice in 10 mL of acetone for 10 min. Each time followed by centrifugation for 10 min (6000 r.p.m) till 99% HPLC purity of **d_9**. **d_9** was obtained as an off-white amorphous solid after solvent removal.

5.2.4.10 4-(4'-(2-fluoropyrimidin-5-yl)-[2,2'-bithiazol]-4-yl)-[1,3]dioxolo[4,5-b]pyridine, d_{10}

38.0 mg of 1-([1,3]dioxolo[4,5-b]pyridin-6-yl)-2-bromoethan-1-one dissolved in 200 µL DMF acidified with 10 µL of glacial acetic acid was added to 28.8 mg (0.1199 mmol) of **b_{10}** dissolved 400 µL of DMF acidified with 20 µL of glacial acetic acid in a 10 mL glass vial. The rest followed as described in **5.2.4.2**. **d_{10}** was obtained with ≥99% HPLC purity as a yellowish-white amorphous solid after solvent removal.

5.2.4.11 2-(4'-([1,3]dioxolo[4,5-b]pyridin-6-yl)-[2,2'-bithiazol]-4-yl)pyrimidin-5-ol, d_{11}

170.0 mg of 1-([1,3]dioxolo[4,5-b]pyridin-6-yl)-2-bromoethan-1-one in 500 µL DMF acidified with 25 µL of glacial acetic acid was added to 128.0 mg (0.5372 mmol) of **b_{11}** dissolved in 500 µL of DMF acidified with 25 µL in a 10 mL glass vial. The mixture was stirred overnight at 45°C. The resulting mixture was transferred into a 10 mL falcon tube and centrifuged at 6000 r.p.m for 10 min. The resulting sediment was sonicated twice in 10 mL of MeOH for 5 min. Each time followed by centrifugation for 10 min (6000 r.p.m) till 99% HPLC purity of **d_{11}**. **d_{11}** was obtained as brown amorphous solid after solvent removal.

5.2.4.12 2-(4'-(benzo[d][1,3]dioxol-5-yl)-[2,2'-bithiazol]-4-yl)pyrimidin-5-ol, d_{12}

160.0 mg of 2-bromo-1-(5-hydroxypyrimidin-2-yl)ethan-1-one dissolved in 500 µL DMF was added to 150.0 mg (0.5675 mmol) of **b_1** dissolved in 500 µL of DMF in a 10 mL glass vial. The mixture was stirred overnight at 40°C. The rest followed as described in **5.2.4.2**. ≥99% HPLC-pure **d_{12}** was obtained as a yellowish amorphous solid.

5.2.4.13 4-(4'-([1,3]dioxolo[4,5-b]pyridin-6-yl)-[2,2'-bithiazol]-4-yl)-2-fluorophenol, d_{13}

125.0 mg of 1-([1,3]dioxolo[4,5-b]pyridin-6-yl)-2-bromoethan-1-one dissolved in 500 µL DMF acidified with 25 µL of glacial acetic acid was added to 100.0 mg (0.3932 mmol) of **b_{12}** dissolved in 500 µL of DMF acidified with 100 µL glacial acetic acid in a 10 mL glass vial. The mixture was stirred overnight at rt. The rest followed as described in **5.2.4.11**. ≥99% HPLC-pure **d_{13}** was obtained as an off-white solid.

5.2.4.14 4-(4'-(benzo[d][1,3]dioxol-5-yl)-[2,2'-bithiazol]-4-yl)phenol, d_{14}

87.5 mg of 2-bromo-1-(4-hydroxyphenyl)ethan-1-one dissolved in 500 µL DMF acidified with 50 µL was added to 75.4 mg (0.2853 mmol) of **b_1** dissolved in 500 µL of DMF in a 10 mL glass vial. The mixture was stirred overnight at 40°C. The resulting mixture was transferred into a 10 mL falcon tube and Milli-Q® water was added until a 10 mL mixture resulting in the precipitation of **d_{14}**. The mixture was left at -20°C for 20 min, then centrifuged at 15°C for 10 min at 6000 r.p.m. The rest followed as described in **5.2.4.11**. ≥99% HPLC pure **d_{14}** was obtained as a white solid.

5.2.4.15 4-(4'-([1,3]dioxolo[4,5-b]pyridin-6-yl)-[2,2'-bithiazol]-4-yl)phenol, d_{15}

47.1 mg of 1-([1,3]dioxolo[4,5-b]pyridin-6-yl)-2-bromoethan-1-one dissolved in 500 µL DMF acidified with 100 µL of glacial acetic acid was added to 30.4 mg (0.1286 mmol) of **b_{13}** dissolved in 300 µL of DMF acidified with 100 µL glacial acetic acid in a 10 mL glass vial. An additional 50 µL glacial acetic acid was added to the mixture. The mixture was stirred overnight at rt. The resulting mixture was transferred into a

10 mL falcon tube and centrifuged at 6000 r.p.m for 10 min. The rest followed as described in **5.2.4.11**. ≥99% HPLC-pure **d_{15}** was obtained as an off-white amorphous solid.

5.2.4.16 6-(4'-(4-chloro-3-nitrophenyl)-[2,2'-bithiazol]-4-yl)-[1,3]dioxolo[4,5-b]pyridine, d_{16}

66.7 mg of 1-([1,3]dioxolo[4,5-b]pyridin-6-yl)-2-bromoethan-1-one dissolved in 500 µL DMF acidified with 100 µL of glacial acetic acid was added to 60 mg (0.2103 mmol) of **b_{14}** dissolved in 300 µL of DMF acidified with 100 µL glacial acetic acid in a 10 mL glass vial. The mixture was stirred overnight at rt. The resulting mixture was transferred into a 10 mL falcon tube and centrifuged at 6000 r.p.m for 10 min. The rest followed as described in **5.2.4.11**. ≥99% HPLC pure **d_{16}** was obtained as a yellow amorphous solid.

5.2.4.17 4-(benzo[d][1,3]dioxol-5-yl)-4'-(2-chloropyridin-4-yl)-2,2'-bithiazole, d_{18}

42.8 mg of 1-(benzo[d][1,3]dioxol-5-yl)-2-bromoethan-1-one in 300 µL DMF was added to 30 mg (0.1173 mmol) of **b_{15}** dissolved in 500 µL of DMF 10 mL glass vial. The mixture was stirred overnight at rt. The resulting mixture was transferred into a 10 mL falcon tube and centrifuged at 6000 r.p.m for 10 min. The rest followed as described in **5.2.4.11**. ≥99% HPLC pure **d_{18}** was obtained as an off-white solid.

5.2.4.18 6-(4'-(2-chloropyridin-4-yl)-[2,2'-bithiazol]-4-yl)-[1,3]dioxolo[4,5-b]pyridine, d_{20}

66.7 mg of 1-([1,3]dioxolo[4,5-b]pyridin-6-yl)-2-bromoethan-1-one dissolved in 500 µL DMF acidified with 25 µL of glacial acetic acid was added to 40 mg (0.1564 mmol) of **b_{15}** dissolved in 500 µL of DMF acidified with 25 µL glacial acetic acid in a 10 mL glass vial. The reaction was left to run overnight at 45°C. The resulting mixture was transferred into a 10 mL falcon tube and centrifuged at 6000 r.p.m for 10 min. The rest followed as described in **5.2.4.11**. ≥99% HPLC pure **d_{20}** was obtained as an orange amorphous solid.

5.2.4.19 4-(4'-([1,3]dioxolo[4,5-b]pyridin-6-yl)-[2,2'-bithiazol]-4-yl)benzene-1,3-diol, d_{22}

d_{22} was synthesized according to the general procedure. 54.2 mg of 1-([1,3]dioxolo[4,5-b]pyridin-6-yl)-2-bromoethan-1-one dissolved in 500 µL DMF acidified with 100 µL of glacial acetic acid was added to 40 mg (0.1585 mmol) of **b_{16}** dissolved in 500 µL of DMF acidified with 100 µL glacial acetic acid in a 10 mL glass vial. The reaction was left to run overnight at 45°C. The resulting mixture was transferred into a 10 mL falcon tube and centrifuged at 6000 r.p.m for 10 min. The rest followed as described in **5.2.4.11**. ≥99% HPLC-pure **d_{22}** was obtained as an orange-yellow amorphous solid.

5.2.5 Third step of DABTA synthesis

This involved the optimization of the phenol and pyrimidinol derivatives of the DABTAs towards one-step radiofluorination. For **d_1** and **d_3**, the guaiacol rings were complexed with ruthenium to facilitate the conversion of the bad LG, the -OH group, into a good LG **Scheme 3**. In the case of the ligands **$h_{4\text{-}14}$**, the ligands were optimized to circumvent two-step radiofluorination, which is both challenging and time-consuming **Scheme 4**. Additionally, in this step, the standard compounds (**$f_{4\text{-}10}$**), that is, the cold versions of the tracers, were synthesized either via O-methylation, O-fluoroalkylation, or fluoroPEGylation of the phenol and pyrimidinol DABTAs **Scheme 5**.

5.2.5.1 Synthesis of the ruthenium complexes of f_1, and f_3

Under an atmosphere of argon, to a 4 mL vial equipped with a magnetic stirring bar, was added 120 mg of **d_1** (0.2923 mmol), (η^5-cyclopentadienyl)(η^6-naphthalene)ruthenium(+)trifluoromethanesulfonate (129.6 mg, 0.2923 mmol, 1.00 equiv), MeCN (0.1 mL), and dichloroethane (0.9 mL). The orange suspension was heated to 60°C. After 2 hours, the suspension became a clear red solution **Scheme 3**. After 24 hours, the solution was analyzed by LC-MS, and ~80% conversion was observed. The reaction mixture was concentrated in vacuo to dryness. The brown residue was purified by semprep-HPLC on an YMC-Actus Triart C18 column ((30×150 mm, 5 μm + 30×50 mm, 5 μm), flow rate = 42.5 mL/min, 35°C) with a linear gradient from 50:50 (0.1% TFA in H_2O:MeOH, v:v) to 03:97 (0.1% TFA in H_2O:MeOH, v:v) over 10 min. The collected fractions containing the product were combined and diluted with 50 mL brine and 20 mL distilled water. The resulting suspension was concentrated by rotary evaporation (100 mbar, 35°C) until no more MeCN was evaporated. The suspension was extracted with dichloromethane (3 × 50 mL), and the combined organic layers were dried over sodium sulfate, filtered, and concentrated in vacuo to dryness to afford ruthenium phenol complex, **f_1**, as a brown powder (70 mg, 0.1016 mmol, 58 % yield). It was confirmed by ESI-MS, [M+1] = 577.2. The synthesis of the **f_3** ruthenium complex followed the same procedure with 120 mg (0.2916 mmol) of **d_3** and was produced as a brown powder (70 mg, 0.1014 mmol, 58% yield). It was confirmed by ESI-MS, [M+1] = 578.2.

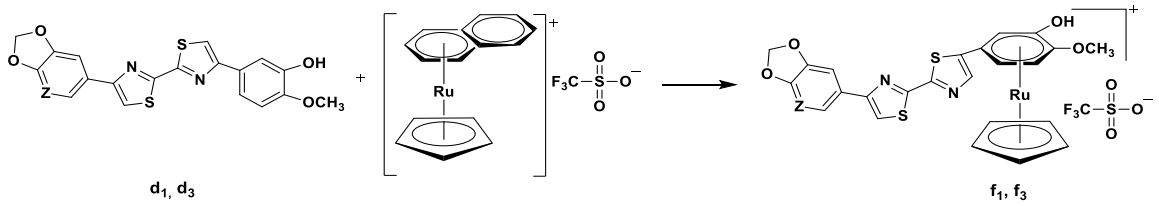

Scheme 3. Synthesis of the Ruthenium Complexes from d_1 (Z = CH) and d_3 (Z = N). After the semipreparative purification of **f_1** and **f_3** using solvents acidified with trifluoroacetic acid, the trifluoromethanesulfonate anion is exchanged for the trifluoroacetate anion.

5.2.5.2 Synthesis of precursors from the phenol and pyrimidinol DABTAs

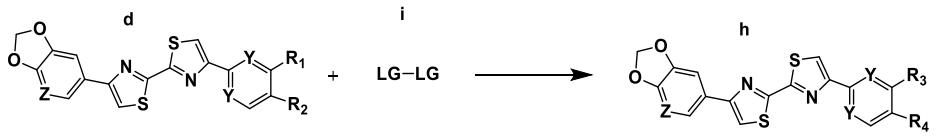

h	Z	Y	R_1	R_2	R_3	R_4	LG
$\mathbf{h_4}$	N	N	H	OH	H	$O(CH_2)_2Br$	Br
$\mathbf{h_5}$	CH	N	H	OH	H	$O(CH_2)_2Br$	Br
$\mathbf{h_{5*}}$	CH	N	H	OH	H	$O(CH_2)_2Tos$	Tos
$\mathbf{h_6}$	CH	N	H	OH	H	$O(CH_2)_2O(CH_2)_2Tos$	Tos
$\mathbf{h_{6*}}$	CH	N	H	OH	H	$O(CH_2)_2O(CH_2)_2I$	I
$\mathbf{h_7}$	CH	N	H	OH	H	$O(CH_2)_2(O(CH_2)_2Tos$	Tos
$\mathbf{h_{7^\circ}}$	CH	N	H	OH	H	$O(CH_2)_2(O(CH_2)_2Cl$	Cl
$\mathbf{h_{7*}}$	CH	N	H	OH	H	$O(CH_2)_2(O(CH_2)_2I$	I
$\mathbf{h_8}$	N	N	H	OH	H	$O(CH_2)_2O(CH_2)_2Tos$	Tos
$\mathbf{h_9}$	N	CH	OH	OCH_3	$O(CH_2)_2O(CH_2)_2Tos$	OCH_3	Tos
$\mathbf{h_{10}}$	N	CH	F	OH	F	$O(CH_2)_2(O(CH_2)_2Tos$	Tos
$\mathbf{h_{10*}}$	N	CH	F	OH	F	$O(CH_2)_2(O(CH_2)_2I$	I
$\mathbf{h_{11}}$	CH	CH	H	OH	H	$O(CH_2)_2Tos$	Tos
$\mathbf{h_{12}}$	N	CH	H	OH	H	$O(CH_2)_2(O(CH_2)_2I$	I
$\mathbf{h_{13}}$	N	N	H	OH	H	$O(CH_2)_2(O(CH_2)_2I$	I
$\mathbf{h_{14}}$	CH	CH	OH	OCH_3	$O(CH_2)_2O(CH_2)_2I$	OCH_3	I

LG: leaving group, Tos: tosylate.

Scheme 4. Synthesis of precursors $\mathbf{h_4}$–$\mathbf{h_{14}}$ for one-step radiofluorination. The rate of these reactions primarily depends on the acidity of the –OH group and, to some extent, on the leaving group of the alkylating agent.

5.2.5.2.1 6-(4'-(5-(2-bromoethoxy)pyrimidin-2-yl)-[2,2'-bithiazol]-4-yl)-[1,3]dioxolo[4,5-b]pyridine, h_4

K_2CO_3 (5.41 mg, 0.02608 mmol, 1.5 mol. equiv.) was added to a 1 mL of DMF suspension of 10 mg (0.02608 mmol) of $\mathbf{d_{11}}$ in a 10 mL glass vial. The mixture was heated while stirring with a magnetic stirrer for 10 min at 80°C. Subsequently, 14.1 µL (0.04937 mmol, 2.1 mol. equiv) of TBAH (1M) was slowly added, and the mixture was stirred at rt until complete dissolution of $\mathbf{d_{11}}$. 14.9 µL (0.2340 mmol, 5 mol. equiv.) of 1,2-dibromoethane was added to the mixture and it was heated while stirring at 80°C. The reaction was stopped after the complete consumption of $\mathbf{d_{11}}$. 10 µL of 1N NaOH was added to the reaction mixture, which was then transferred to a 10 mL falcon tube. 10 mL of Milli-Q® water was added to the mixture, and it was left for 5 min at 4°C. 1 mL of MeOH was added to the mixture, and it was centrifuged at 6000 r.p.m for 10 min. Iterative washing of the sediments was carried out using 5 mL of MeOH, with 2 min sonication followed by centrifugation for 10 min at 6000 r.p.m at 10°C, yielding 99% HPLC purity. MeOH was completely evaporated in vacuo and $\mathbf{h_4}$ was obtained as a brown amorphous solid after lyophilization.

5.2.5.2.2 4-(benzo[d][1,3]dioxol-5-yl)-4'-(5-(2-bromoethoxy)pyrimidin-2-yl)-2,2'-bithiazole, h_5

K_2CO_3 (8.1 mg, 0.05883 mmol, 1.5 mol. equiv.) was added to a 1 mL DMF suspension of 15 mg (0.0392 mmol) of **d_{12}** in a 10 mL glass vial. The mixture was heated while stirring with a magnetic stirrer for 10 min at 80°C. Subsequently, 16 µL (0.05611 mmol, 1.4 mol. equiv) of TBAH (1M) was added to the mixture, followed by 17 µL (0.2340 mmol, 5 mol. equiv.) of 1,2-dibromoethane and it was heated while stirring at 80°C. The reaction was stopped after the complete consumption of **d_{12}**. Further workup follows as described in **5.2.5.2.1**. **h_5** was obtained as a yellowish-white amorphous solid after lyophilization.

5.2.5.2.3 2-((2-(4'-(benzo[d][1,3]dioxol-5-yl)-[2,2'-bithiazol]-4-yl)pyrimidin-5-yl)oxy)ethyl 4-methylbenzenesulfonate, h_{5*}

K_2CO_3 (3.61 mg, 0.02614 mmol, 1.5 mol. equiv.) was added to a 0.5 mL DMF suspension of 10 mg (0.0262 mmol) of **d_{12}** in a 10 mL glass vial. The mixture was heated while stirring with a magnetic stirrer for 10 min at 80°C. Subsequently, 9.6 µL (0.03654 mmol, 1.4 mol. equiv) of TBAH (1M) was added to the mixture followed by 19.4 mg (0.05230 mmol, 2 mol. equiv.) of ethyleneglycol tosylate in 200 µL of DMF was added to the mixture, and it was heated while stirring at 80°C. The reaction was stopped after the complete consumption of **d_{12}**. Further workup follows, as described in **5.2.5.2.1**. **h_{5*}** was obtained as a white, amorphous solid after lyophilization.

5.2.5.2.4 2-(2-((2-(4'-(benzo[d][1,3]dioxol-5-yl)-[2,2'-bithiazol]-4-yl)pyrimidin-5-yl)oxy)ethoxy)ethyl 4-methylbenzenesulfonate, h_6

K_2CO_3 (10.8 mg, 0.0784 mmol, 1.5 mol. equiv.) was added to a 0.8 mL DMF suspension of 20 mg (0.0523 mmol) of **d_{12}** in a 10 mL glass vial. The mixture was heated while stirring with a magnetic stirrer for 10 min at 80°C. Subsequently, 19.2 µL (0.07322 mmol, 1.4 mol. equiv) of TBAH (1M) was added to the mixture, followed by 65.0 mg (0.2978 mmol, 3 mol. equiv.) of diethylene glycol ditosylate was dissolved in 200 µL of DMF and added to the mixture, which heated while stirring at 80°C. The reaction was stopped after the complete consumption of **d_{12}**. Further workup follows, as described in **5.2.5.2.1**. **h_6** was obtained as an off-white amorphous solid after lyophilization.

5.2.5.2.5 4-(benzo[d][1,3]dioxol-5-yl)-4'-(5-(2-(2-iodoethoxy)ethoxy)pyrimidin-2-yl)-2,2'-bithiazole h_{6*}

K_2CO_3 (6.5 mg, 0.04704 mmol, 1.5 mol. equiv.) was added to a 0.5 mL DMF suspension of 12 mg (0.03138 mmol) of **d_{12}** in a 10 mL glass vial. The mixture was heated while stirring with a magnetic stirrer for 10 min at 80°C. Subsequently, 11.5 µL (0.04392 mmol, 1.4 mol. equiv) of TBAH (1M) was added to the mixture followed by 13.4 µL (0.09414 mmol, 3 mol. equiv.) of 1-iodo-2-(2-iodoethoxy)ethane and it was heated

while stirring at 80°C. The reaction was stopped after the complete consumption of **d_{12}**. Further workup follows, as described in **5.2.5.2.1**. **h_{6*}** was obtained as a light yellow amorphous solid after lyophilization.

5.2.5.2.6 2-(2-(2-((2-(4'-(benzo[d][1,3]dioxol-5-yl)-[2,2'-bithiazol]-4-yl)pyrimidin-5-yl)oxy)ethoxy)ethoxy)ethyl 4-methylbenzenesulfonate, h_7

K_2CO_3 (10.8 mg, 0.0784 mmol, 1.5 mol. equiv.) was added to a 0.5 mL DMF suspension of 20 mg (0.0523 mmol) of **d_{12}** in a 10 mL glass vial. The mixture was heated while stirring with a magnetic stirrer for 10 min at 80°C. Subsequently, 9.6 µL (0.03654 mmol, 1.4 mol. equiv) of TBAH (1M) was added to the mixture, followed by 71.8 mg (0.1564 mmol, 3 mol. equiv.) of triethylene glycol ditosylate was dissolved in 200 µL of DMF and was added to the mixture, which was heated while stirring at 80°C. The reaction was stopped after the complete consumption of **d_{12}**. Further workup follows, as described in **5.2.5.2.1**. **h_7** was obtained as an off-white amorphous solid after lyophilization.

5.2.5.2.7 4-(benzo[d][1,3]dioxol-5-yl)-4'-(5-(2-(2-(2-chloroethoxy)ethoxy)ethoxy)pyrimidin-2-yl)-2,2'-bithiazole, h_{7°

K_2CO_3 (5.4 mg, 0.03922 mmol, 1.5 mol. equiv.) was added to a 0.5 mL DMF suspension of 10 mg (0.0261 mmol) of **d_{12}** in a 10 mL glass vial. The mixture was heated while stirring with a magnetic stirrer for 5 min at 80°C. Subsequently, 9.6 µL (0.03654 mmol, 1.4 mol. equiv) of TBAH (1M) was added to the mixture, followed by 18.2 µL (0.0997 mmol, 4.45 mol. equiv.) of 1,2-bis(2-chloroethoxy)ethane. The mixture was heated while stirring at 80°C for 50 min, for 20 min at 85°C, for 20 min at 90°C, for 20 min at 94°C with 10 µL (0.04774 mmol) of TBAH (1 M) added each time to drive the reaction to completion. The reaction was stopped after the complete consumption of **d_{12}**. Further workup follows, as described in **5.2.5.2.1**. **h_{7°** was obtained as a yellowish-white amorphous solid after lyophilization.

5.2.5.2.8 4-(benzo[d][1,3]dioxol-5-yl)-4'-(5-(2-(2-(2-iodoethoxy)ethoxy)ethoxy)pyrimidin-2-yl)-2,2'-bithiazole, h_{7^*}

K_2CO_3 (5.4 mg, 0.03922 mmol, 1.5 mol. equiv.) was added to a 0.5 mL DMF suspension of 10 mg (0.0261 mmol) of **d_{12}** in a 10 mL glass vial. The mixture was heated while stirring with a magnetic stirrer for 5 min at 80°C. Subsequently, 9.6 µL (0.03654 mmol, 1.4 mol. equiv) of TBAH (1M) was added to the mixture, followed by 18.2 µL (0.0997 mmol, 4.45 mol. equiv.) of 1,2-bis(2-iodoethoxy)ethane. The reaction was stopped after the complete consumption of **d_{12}** (in 5 min). Further workup follows, as described in **5.2.5.2.1**. **h_{7^*}** was obtained as an off-white amorphous solid after lyophilization.

5.2.5.2.9 2-(2-((2-(4'-([1,3]dioxolo[4,5-b]pyridin-6-yl)-[2,2'-bithiazol]-4-yl)pyrimidin-5-yl)oxy)ethoxy)ethyl 4-methylbenzenesulfonate, h_8

K_2CO_3 (5.4 mg, 0.0391 mmol, 1.5 mol. equiv.) was added to a 0.5 mL DMF suspension of 10 mg (0.0261 mmol) of **d_{11}** in a 10 mL glass vial. The mixture was heated while stirring with a magnetic stirrer for 10 min at 80°C. Subsequently, 14.1 µL (0.04937 mmol, 2.1 mol. equiv) of TBAH (1M) was added, and the mixture was stirred at rt until complete dissolution of **d_{11}**. 32.4 mg (0.0782 mmol, 3 mol. equiv.) of diethylene glycol ditosylate was dissolved in 200 µL of DMF and was added to the mixture. It was heated while stirring at 80°C. The reaction was stopped after the complete consumption of **d_{11}**. Further workup follows, as described in **5.2.5.2.1**. **h_8** was obtained as an off-white amorphous solid after lyophilization.

5.2.5.2.10 2-(2-(5-(4'-([1,3]dioxolo[4,5-b]pyridin-6-yl)-[2,2'-bithiazol]-4-yl)-2-methoxyphenoxy)ethoxy)ethyl 4-methylbenzenesulfonate, h_9

K_2CO_3 (7.56 mg, 0.05469 mmol, 1.5 mol. equiv.) was added to a 0.8 mL DMF suspension of 15 mg (0.03646 mmol) of **d_3** in a 10 mL glass vial. The mixture was heated while stirring with a magnetic stirrer for 10 min at 80°C. Subsequently, 20.1 µL (0.07657 mmol, 2.1 mol. equiv) of TBAH (1M) was added to the mixture, followed 32.4 mg (0.0782 mmol, 2.5 mol. equiv.) of diethylene glycol ditosylate dissolved in 200 µL of DMF. The mixture was heated while stirring at 80°C. The reaction was stopped after the complete consumption of **d_3**. 10 µL of 1N NaOH was added to the mixture, and it was then transferred to a 10 mL falcon tube. 10 mL of Milli-Q® water was added to the mixture and left for 10 min at 4°C. 1 mL of MeOH was added to the mixture and it was centrifuged at 6000 r.p.m for 10 min. The sediment was redissolved in DMSO and purified using semiprep HPLC. SHP with an aqueous mixture of THF and MeOH solution (0.07%:30%), 0.1% TFA (solvent A) and MeCN, 0.1 % TFA (solvent B) with a flowrate of 5 mL/min and a gradient A/B: 65:35 to 15:85 in 17 min. The organic solvents were evaporated in vacuo followed by lyophilization to obtain a white amorphous **h_9** in ≥99% HPLC purity.

5.2.5.2.11 2-(2-(2-(4-(4'-([1,3]dioxolo[4,5-b]pyridin-6-yl)-[2,2'-bithiazol]-4-yl)-2-fluorophenoxy)ethoxy)ethoxy)ethyl 4-methylbenzenesulfonate, h_{10}

K_2CO_3 (10.4 mg, 0.07525 mmol, 1.5 mol. equiv.) was added to a 0.8 mL DMF suspension of 20 mg (0.0500 mmol) of **d_{13}** in a 10 mL glass vial. The mixture was heated while stirring with a magnetic stirrer for 5 min at 80°C. Subsequently, 14.2 µL (0.05010 mmol, 2 mol. equiv) of TBAH (1M) was added to the mixture, followed by 23.0 mg (0.1001 mmol, 2 mol. equiv.) of triethylene glycol ditosylate was dissolved in 200 µL of DMF. The mixture was then heated while stirring at 80°C. The reaction was stopped after the complete consumption of **d_{13}**. 10 µL of 1N NaOH was added to the mixture, which was then transferred to a 10 mL falcon tube. 10 mL of Milli-Q® water was added to the mixture and left for 10 min at 4°C. 1 mL of MeOH was added to the mixture, and it was centrifuged at 6000 r.p.m. for 10 min. The sediment was redissolved

in DMSO and purified using semiprep HPLC. SHP was with an aqueous mixture of THF and MeOH solution (0.1%:30%), 0.1% TFA (solvent A) and MeCN, 0.1 % TFA (solvent B) at a flow rate of 5 mL/min and a gradient A/B: 50:50 to 12:88 in 18 min. The organic solvents were evaporated in vacuo followed by lyophilization to obtain an off-white amorphous **h_{10}** with ≥99% HPLC purity.

5.2.5.2.12 6-(4'-(3-fluoro-4-(2-(2-(2-iodoethoxy)ethoxy)ethoxy)phenyl)-[2,2'-bithiazol]-4-yl)-[1,3]dioxolo[4,5-b]pyridine, h_{10*}

K_2CO_3 (5.4 mg, 0.03915 mmol, 1.5 mol. equiv.) was added to a 0.5 mL DMF suspension of 10 mg (0.0261 mmol) of **d_{13}** in a 10 mL glass vial. The mixture was heated while stirring with a magnetic stirrer for 5 min at 80°C. Subsequently, 7.1 µL (0.02501 mmol, 2 mol. equiv) of TBAH (1M) was added to the mixture, followed by 9.1 µL (0.08614 mmol, 2.0 mol. equiv.) of 1,2-bis(2-iodoethoxy)ethane. The mixture was then heated while stirring at 80°C. The reaction was stopped after the complete consumption of **d_{13}**. Further workup follows, as described in **5.2.5.2.1**. **h_{10*}** was obtained as a violet crystalline solid after lyophilization with ≥99% HPLC purity.

5.2.5.2.13 2-(4-(4'-(benzo[d][1,3]dioxol-5-yl)-[2,2'-bithiazol]-4-yl)phenoxy)ethyl 4-methylbenzenesulfonate, h_{11}

K_2CO_3 (10.9 mg, 0.07887 mmol, 1.5 mol. equiv.) was added to a 0.8 mL DMF suspension of 20 mg (0.05257 mmol) of **d_{14}** in a 10 mL glass vial. The mixture was heated while stirring with a magnetic stirrer for 5 min at 80°C. Subsequently, 19.3 µL (0.07360 mmol, 1.5 mol. equiv) of TBAH (1M) was added to the mixture, followed by 77.9 mg (0.2103 mmol, 4.0 mol. equiv.) of ethylene ditosylate dissolved in 200 uL of DMF. The mixture was heated while stirring at 80°C. The reaction was stopped after the complete consumption of **d_{14}**. Further workup follows, as described in **5.2.5.2.1**. **h_{11}** was obtained as an off-white solid after lyophilization with ≥99% HPLC purity.

5.2.5.2.14 6-(4'-(4-(2-(2-(2-iodoethoxy)ethoxy)ethoxy)phenyl)-[2,2'-bithiazol]-4-yl)-[1,3]dioxolo[4,5-b]pyridine, h_{12}

K_2CO_3 (5.40 mg, 0.03907 mmol, 1.5 mol. equiv.) was added to a 0.4 mL DMF suspension of 10 mg (0.02622 mmol) of **d_{15}** in a 10 mL glass vial. The mixture was heated while stirring with a magnetic stirrer for 5 min at 80°C. Subsequently, 13.7 µL (0.0524 mmol, 2 mol. equiv) of TBAH (1M) was added to the mixture, followed by 9.57 µL (0.05244 mmol, 2 mol. equiv.) of 1,2-bis(2-iodoethoxy)ethane. The mixture was heated while stirring at 80°C. The reaction was stopped after the complete consumption of **d_{15}**. Further workup follows, as described in **5.2.5.2.1**. **h_{12}** was obtained as an off-white solid after lyophilization with ≥99% HPLC purity.

5.2.5.2.15 6-(4'-(5-(2-(2-(2-iodoethoxy)ethoxy)ethoxy)pyrimidin-2-yl)-[2,2'-bithiazol]-4-yl)-[1,3]dioxolo[4,5-b]pyridine, h_{13}

K_2CO_3 (5.40 mg, 0. 03907 mmol, 1.5 mol. equiv.) was added to a 1 mL DMF suspension of 10 mg (0.02608 mmol) of **d_{11}** in a 10 mL glass vial. The mixture was heated while stirring with a magnetic stirrer for 10 min at 80°C. Subsequently, 14.1 µL (0.04937 mmol, 2.1 mol. equiv) of TBAH (1M) was added, and the mixture was stirred at rt until complete dissolution of the suspension. 9.5 µL (0.0522 mmol, 2.0 mol. equiv.) of 1,2-bis(2-iodoethoxy)ethane was added to the mixture, and it was heated while stirring at 80°C. The reaction was stopped after the complete consumption of **d_{11}**. Further workup follows, as described in **5.2.5.2.1**. **h_{13}** was obtained as an off-white solid after lyophilization. with ≥99% HPLC purity.

5.2.5.2.16 4-(benzo[d][1,3]dioxol-5-yl)-4'-(3-(2-(2-(2-iodoethoxy)ethoxy)ethoxy)-4-methoxyphenyl)-2,2'-bithiazole, h_{14}

K_2CO_3 (6.74 mg, 0.0487 mmol, 2.0 mol. equiv.) was added to a 0.5 mL DMF suspension of of 10 mg (0.02436 mmol) of **d_1** in a 10 mL glass vial. The mixture was heated while stirring with a magnetic stirrer for 10 min at 80°C. Subsequently, 12.5 µL (0.04871 mmol, 2.0 mol. equiv) of TBAH (1M) was added to the mixture, followed by 9.5 µL (0.04871 mmol, 2.0 mol. equiv.) of 1,2-bis(2-iodoethoxy)ethane was added to the mixture, and it was heated while stirring at 80°C. The reaction was stopped after the complete consumption of **d_1**. Further workup follows, as described in **5.2.5.2.1**. **h_{14}** was obtained as an off-white solid after lyophilization with ≥99% HPLC purity.

5.2.5.3 Synthesis of the Standard Compounds from the phenol and pyrimidinol DABTAs

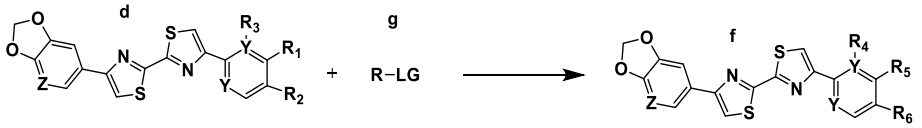

f	Z	Y	R_1	R_2	R_3	R_4	R_5	R_6	LG
f_4	N	N	H	OH	-	-	H	$O(CH_2)_2F$	Br
f_5	CH	N	H	OH	-	-	H	$O(CH_2)_2F$	Tos
f_6	CH	N	H	OH	-	-	H	$O(CH_2)_2O(CH_2)_2F$	Br
f_7	CH	N	H	OH	-	-	H	$O(CH_2)_2(O(CH_2)_2)_2F$	Br
f_8	N	N	H	OH	-	-	H	$O(CH_2)_2O(CH_2)_2F$	Br
f_9	N	CH	OH	OCH_3	H	H	$O(CH_2)_2O(CH_2)_2F$	OCH_3	Br
f_{10}	N	CH	F	OH	H	H	F	$O(CH_2)_2(O(CH_2)_2)_2F$	Br
f_{11}	CH	CH	H	OH	H	H	H	$O(CH_2)_2F$	Tos
f_{12}	N	CH	F	OH	H	H	H	$O(CH_2)_2(O(CH_2)_2)_2F$	Br
f_{13}	N	N	H	OH	-	-	H	$O(CH_2)_2(O(CH_2)_2)_2F$	Br
f_{14}	CH	CH	OH	OCH_3	H	H	$O(CH_2)_2(O(CH_2)_2)_2F$	OCH_3	Br
f_{15}	CH	N	H	OH	-	-	H	OCH_3	Tos
f_{16}	N	N	H	OH	-	-	H	OCH_3	Tos
f_{17}	N	CH	H	OH	H	H	OCH_3	OCH_3	I
f_{18}	N	CH	OH	OCH_3	H	OCH_3	H	OCH_3	I
f_{19}	N	CH	H	OH	OH	H	H	OCH_3	I

f_{20}	N	CH	H	OH	OH	$O(CH_2)_2O(CH_2)_2F$	H	$O(CH_2)_2O(CH_2)_2F$	Br

LG: leaving group, Tos: tosylate.

Scheme 5. Synthesis of the cold versions f_4-f_{20} of the tracers. The rate of these reactions primarily depends on the acidity of the –OH group and, to some extent, on the leaving group of the alkylating agent. The tosylate leaving group was generally avoided, when possible, as it showed a higher tendency to form side products.

5.2.5.3.1 6-(4'-(5-(2-fluoroethoxy)pyrimidin-2-yl)-[2,2'-bithiazol]-4-yl)-[1,3]dioxolo[4,5-b]pyridine, f_4

K_2CO_3 (7.2 mg, 0.0521 mmol, 2.0 mol. equiv.) was added to a 1 mL DMF suspension of 10 mg (0.0261 mmol) of **d_{11}** in a 10 mL glass vial. The mixture was heated while stirring with a magnetic stirrer for 10 min at 80°C. Subsequently, 14.1 µL (0.04937 mmol, 2.1 mol. equiv) of TBAH (1M) was added, and the mixture was stirred at rt until complete dissolution of the suspension. Subsequently, 2.5 µL (0.0339 mmol, 1.3 mol. equiv.) of 1-bromo-2-fluoroethane was added to the mixture, and it was heated while stirring at 80°C. The reaction was stopped after the complete consumption of **d_{11}**. 10 µL of 1N NaOH was added to the mixture, and it was then transferred to a 10 mL falcon tube. 10 mL of Milli-Q® water was added to the mixture, and it was left for 10 min at 4°C. 1 mL of MeOH was added to the mixture, and it was centrifuged at 6000 r.p.m for 10 min. Iterative washing of the sediments was carried out using 5 mL of MeOH, with 2 min sonication followed by centrifugation for 10 min (6000 r.p.m) yielding 99% HPLC purity. MeOH was completely evaporated in vacuo and **f_4** was obtained as a white amorphous solid with ≥99% HPLC purity.

5.2.5.3.2 4-(benzo[d][1,3]dioxol-5-yl)-4'-(5-(2-fluoroethoxy)pyrimidin-2-yl)-2,2'-bithiazole, f_5

K_2CO_3 (10.8 mg, 0.0784 mmol, 1.5 mol. equiv.) was added to a 1 mL DMF suspension of 20 mg (0.0523 mmol) of **d_{12}** in a 10 mL glass vial. The mixture was heated while stirring with a magnetic stirrer for 10 min at 80°C. Subsequently, 19.2 µL (0.03654 mmol, 1.4 mol. equiv) of TBAH (1M) was added to the mixture, followed by 13.4 µL (0.07844 mmol, 1.5 mol. equiv.) of 2-fluoroethyl 4-methylbenzenesulfonate. The mixture was heated while stirring at 80°C. The reaction was stopped after the complete consumption of **d_{12}**. Further workup follows as described in **5.2.5.3.1**. **f_5** was obtained as a white, waxy, amorphous solid with ≥99% HPLC purity.

5.2.5.3.3 4-(benzo[d][1,3]dioxol-5-yl)-4'-(5-(2-(2-fluoroethoxy)ethoxy)pyrimidin-2-yl)-2,2'-bithiazole, f_6

K_2CO_3 (10.8 mg, 0.0784 mmol, 1.5 mol. equiv.) was added to a 1 mL DMF suspension of 20 mg (0.0523 mmol) of **d_{12}** in a 10 mL glass vial. The mixture was heated while stirring with a magnetic stirrer for 10 min at 80°C. Then, 19.2 µL (0.03654 mmol, 1.4 mol. equiv) of TBAH (1M) was added to the mixture, followed by 7.8 µL (0.0362 mmol, 1.5 mol. equiv.) of 1-bromo-2-(2-fluoroethoxy)ethane. The mixture was heated

while stirring at 80°C. The reaction was stopped after the complete consumption of **d_{12}**. Further workup follows as described in **5.2.5.3.1**. **f_6** was obtained as a white, amorphous solid with ≥99% HPLC purity.

5.2.5.3.4 4-(benzo[d][1,3]dioxol-5-yl)-4'-(5-(2-(2-(2-fluoroethoxy)ethoxy)ethoxy)pyrimidin-2-yl)-2,2'-bithiazole, f_7

K_2CO_3 (10.8 mg, 0.0784 mmol, 1.5 mol. equiv.) was added to a 1 mL DMF suspension of 20 mg (0.0523 mmol) of **d_{12}** in a 10 mL glass vial. The mixture was heated while stirring with a magnetic stirrer for 10 min at 80°C. Subsequently, 19.2 µL (0.03654 mmol, 1.4 mol. equiv) of TBAH (1M) was added to the mixture, followed by 12.0 µL (0.0784 mmol, 2.0 mol. equiv.) of 1-bromo-2-(2-(2-fluoroethoxy)ethoxy)ethane. The mixture was heated while stirring at 80°C. The reaction was stopped after the complete consumption of **d_{12}**. Further workup follows as described in **5.2.5.3.1**. **f_7** was obtained as a yellowish-white amorphous solid with ≥99% HPLC purity.

5.2.5.3.5 6-(4'-(5-(2-(2-fluoroethoxy)ethoxy)pyrimidin-2-yl)-[2,2'-bithiazol]-4-yl)-[1,3]dioxolo[4,5-b]pyridine, f_8

K_2CO_3 (7.2 mg, 0.0521 mmol, 2.0 mol. equiv.) was added to a 1 mL DMF suspension of 10 mg (0.0261 mmol) of **d_{11}** in a 10 mL glass vial. The mixture was heated while stirring with a magnetic stirrer for 10 min at 80°C. Subsequently, 14.1 µL (0.04937 mmol, 2.1 mol. equiv) of TBAH (1M) was added, and the mixture was stirred at rt until complete dissolution of the suspension. Subsequently, 6.0 µL (0.05218 mmol, 2 mol. equiv.) of 1-bromo-2-(2-fluoroethoxy)ethane was added to the mixture, and it was heated while stirring at 80°C. The reaction was stopped after the complete consumption of **d_{11}**. Further workup follows, as described in **5.2.5.3.1**. **f_8** was obtained as an off-white amorphous solid with ≥99% HPLC purity.

5.2.5.3.6 6-(4'-(3-(2-(2-fluoroethoxy)ethoxy)-4-methoxyphenyl)-[2,2'-bithiazol]-4-yl)-[1,3]dioxolo[4,5-b]pyridine, f_9

K_2CO_3 (10.1 mg, 0.0729 mmol, 2 mol. equiv.) was added to a 1 mL DMF suspension of 15 mg (0.0364 mmol) of **d_3** in a 10 mL glass vial. The mixture was heated while stirring with a magnetic stirrer for 5 min at 80°C. Then, 22.9 µL (0.1017 mmol, 3 mol. equiv) of TBAH (1M) was added to the mixture, followed by 10 µL (0.1001 mmol, 2 mol. equiv.) of 1-bromo-2-(2-fluoroethoxy)ethane. The mixture was heated while stirring at 80°C. The reaction was stopped after the complete consumption of **d_3**. Further workup follows as described in **5.2.5.3.1**. **f_9** was obtained as an off-white amorphous solid with ≥99% HPLC purity.

5.2.5.3.7 6-(4'-(3-fluoro-4-(2-(2-(2-fluoroethoxy)ethoxy)ethoxy)phenyl)-[2,2'-bithiazol]-4-yl)-[1,3]dioxolo[4,5-b]pyridine, f_{10}

K_2CO_3 (10.4 mg, 0.07525 mmol, 1.5 mol. equiv.) was added to a 0.8 mL DMF suspension of 20 mg (0.0500 mmol) of **d_{13}** in a 10 mL glass vial. The mixture was heated while stirring with a magnetic stirrer for 5 min at 80°C. Subsequently, 14.2 µL (0.05010 mmol, 2 mol. equiv) of TBAH (1M) was added to the mixture, followed by 7.8 µL (0.0362 mmol, 1.5 mol. equiv.) of 1-bromo-2-(2-fluoroethoxy)ethane was dissolved in 200 µL of DMF. The mixture was then heated while stirring at 80°C. The reaction was stopped after the complete consumption of **d_{13}**. Further workup follows as described in **5.2.5.3.1**. **f_{10}** was obtained as an off-white amorphous solid with ≥99% HPLC purity.

5.2.5.3.8 4-(benzo[d][1,3]dioxol-5-yl)-4'-(4-(2-fluoroethoxy)phenyl)-2,2'-bithiazole, f_{11}

K_2CO_3 (10.9 mg, 0.07887 mmol, 1.5 mol. equiv.) was added to a 0.8 mL DMF suspension of 20 mg (0.05257 mmol) of **d_{14}** in a 10 mL glass vial. The mixture was heated while stirring with a magnetic stirrer for 5 min at 80°C. Afterward, 19.3 µL (0.07360 mmol, 1.5 mol. equiv) of TBAH (1M) was added to the mixture, followed by 16.7 µL (0.0592 mmol, 1.5 mol. equiv.) of 2-fluoroethyl 4-methylbenzenesulfonate. The mixture was heated while stirring at 80°C. The reaction was stopped after the complete consumption of **d_{14}**. Further workup follows as described in **5.2.5.3.1**. **f_{11}** was obtained as an off-white solid after lyophilization with ≥99% HPLC purity.

5.2.5.3.9 6-(4'-(4-(2-(2-(2-fluoroethoxy)ethoxy)ethoxy)phenyl)-[2,2'-bithiazol]-4-yl)-[1,3]dioxolo[4,5-b]pyridine, f_{12}

K_2CO_3 (5.4 mg, 0.03907 mmol, 1.5 mol. equiv.) was added to a 0.4 mL DMF suspension of 10 mg (0.02622 mmol) of **d_{15}** in a 10 mL glass vial. The mixture was heated while stirring with a magnetic stirrer for 5 min at 80°C. Subsequently, 13.7 µL (0.0524 mmol, 2 mol. equiv) of TBAH (1M) was added to the mixture, followed by 7.99 µL (0.0526 mmol, 2 mol. equiv.) of 1-bromo-2-(2-(2-fluoroethoxy)ethoxy)ethane. The mixture was heated while stirring at 80°C. The reaction was stopped after the complete consumption of **d_{15}**. Further workup follows as described in **5.2.5.3.1**. **f_{12}** was obtained as an off-white solid after lyophilization with ≥99% HPLC purity.

5.2.5.3.10 6-(4'-(5-(2-(2-(2-fluoroethoxy)ethoxy)ethoxy)pyrimidin-2-yl)-[2,2'-bithiazol]-4-yl)-[1,3]dioxolo[4,5-b]pyridine, f_{13}

K_2CO_3 (5.41 mg, 0.02608 mmol, 1.5 mol. equiv.) was added to a 1 mL DMF suspension of 10 mg (0.02608 mmol) of **d_{11}** in a 10 mL glass vial. The mixture was heated while stirring with a magnetic stirrer for 10 min at 80°C. Subsequently, 14.1 µL (0.04937 mmol, 2.1 mol. equiv) of TBAH (1M) was added, and the mixture was stirred at rt until complete dissolution of the suspension. 7.95 µL (0.0522 mmol, 2.0 mol. equiv.) of 1-bromo-2-(2-(2-fluoroethoxy)ethoxy)ethane was added to the mixture, and it was heated while stirring at

80°C. The reaction was stopped after the complete consumption of **d_{11}**. 10 mL of Milli-Q® water was added to the mixture, and it was left for 10 min at 4°C. 1 mL of MeOH was added to the mixture, and it was centrifuged at 6000 r.p.m for 10 min. Iterative washing of the precipitate was carried out using 5 mL of MeOH and acetone (5:1) with 1.7% glacial acetic acid was added to the resulting sediment with 2 min sonication, followed by centrifugation for 10 min (6000 r.p.m) at 10°C yielding 99% HPLC purity. MeOH was completely evaporated in vacuo and **f_{13}** was obtained as an off-white solid after lyophilization with ≥99% HPLC purity.

5.2.5.3.11 4-(benzo[d][1,3]dioxol-5-yl)-4'-(3-(2-(2-(2-fluoroethoxy)ethoxy)ethoxy)-4-methoxyphenyl)-2,2'-bithiazole, f_{14}

K_2CO_3 (6.74 mg, 0.0487 mmol, 2.0 mol. equiv.) was added to a 0.5 mL DMF suspension of 10 mg (0.02436 mmol) of **d_1** in a 10 mL glass vial. The mixture was heated while stirring with a magnetic stirrer for 10 min at 80°C. Subsequently, 12.5 µL (0.04871 mmol, 2.0 mol. equiv) of TBAH (1M) was added to the mixture, followed by 7.42 µL (0.04873 mmol, 2.0 mol. equiv.) of 1-bromo-2-(2-(2-fluoroethoxy)ethoxy)ethane. The mixture was heated while stirring at 80°C. The reaction was stopped after the complete consumption of **d_1**. Further workup follows as described in **5.2.5.3.1**. **f_{14}** was obtained as an off-white solid after lyophilization with ≥99% HPLC purity.

5.2.5.3.12 4-(benzo[d][1,3]dioxol-5-yl)-4'-(5-methoxypyrimidin-2-yl)-2,2'-bithiazole, f_{15}

K_2CO_3 (8.13 mg, 0.0588 mmol, 1.5 mol. equiv.) was added to a 1 mL DMF suspension of 15 mg (0.0262 mmol) of **d_{12}** in a 10 mL glass vial. The mixture was heated while stirring with a magnetic stirrer for 10 min at 80°C. Subsequently, 9.6 µL (0.03654 mmol, 1.4 mol. equiv) of TBAH (1M) was added to the mixture followed by 7.1 µL (0.04704 mmol, 1.2 mol. equiv.) of methyltosylate. The mixture was heated while stirring at 80°C. The reaction was stopped after the complete consumption of **d_{12}**. Further workup follows, as described in **5.2.5.3.1**. **f_{15}** was obtained as an off-white solid after lyophilization with ≥99% HPLC purity.

5.2.5.3.13 5-(4'-(5-methoxypyrimidin-2-yl)-[2,2'-bithiazol]-4-yl)-[1,3]dioxolo[4,5-b]pyridine, f_{16}

K_2CO_3 (5.41 mg, 0.02608 mmol, 1.5 mol. equiv.) was added to a 1 mL DMF suspension of 10 mg (0.02608 mmol) of **d_{11}** in a 10 mL glass vial. The mixture was heated while stirring with a magnetic stirrer for 10 min at 80°C. Subsequently, 14.1 µL (0.04937 mmol, 2.1 mol. equiv) of TBAH (1M) was added and the mixture was stirred at rt until complete dissolution of the suspension 5.1 µL (0.0339 mmol, 1.3 mol. equiv.) of methyltosylate was added to the mixture, and it was heated while stirring at 80°C. The reaction was stopped after the complete consumption of **d_{11}**. Further workup follows, as described in **5.2.5.3.1**. **f_{16}** was obtained as a brown waxy amorphous solid after lyophilization with ≥99% HPLC purity.

5.2.5.3.14 6-(4'-(4-methoxyphenyl)-[2,2'-bithiazol]-4-yl)-[1,3]dioxolo[4,5-b]pyridine, f_{17}

K_2CO_3 (5.4 mg, 0.03933 mmol, 1.5 mol. equiv.) was added to a 0.5 mL DMF suspension of 10 mg (0.02622 mmol) of **d_{15}** in a 10 mL glass vial. The mixture was heated while stirring with a magnetic stirrer for 5 min at 80°C. Subsequently, 13.7 µL (0.0524 mmol, 2 mol. equiv) of TBAH (1M) was added to the mixture, followed by 4.9 µL (0.07864 mmol, 2 mol. equiv.) of methyliodide. The mixture was heated while stirring at 80°C. The reaction was stopped after the complete consumption of **d_{15}**. Further workup follows, as described in **5.2.5.3.1**. **f_{17}** was obtained as an off-white solid after lyophilization with ≥99% HPLC purity.

5.2.5.3.15 6-(4'-(3,4-dimethoxyphenyl)-[2,2'-bithiazol]-4-yl)-[1,3]dioxolo[4,5-b]pyridine, f_{18}

K_2CO_3 (5.1 mg, 0.03645 mmol, 1.5 mol. equiv.) was added to a 1 mL DMF suspension of 10 mg (0.02430 mmol) of **d_3** in a 10 mL glass vial. The mixture was heated while stirring with a magnetic stirrer for 5 min at 80°C. Subsequently, 12.7 µL (0.04860 mmol, 2 mol. equiv) of TBAH (1M) was added to the mixture, followed by 4.5 µL (0.07290 mmol, 2 mol. equiv.) of methyiodide. The mixture was heated while stirring at 80°C. The reaction was stopped 1 hour when no further decrease in **d_3** was observed. The reaction mixture (suspension) was transferred to a 10 mL falcon tube and centrifuged. Iterative washing of the resulting sediment was carried out, first with 2 mL of DMF with 5 µL of TBAH (1M), then with 2 mL of only DMF, and finally with 5 mL of acetone. The sediment was sonicated with the above solvents for 5 min followed by centrifugation for 10 min (6000 r.p.m) yielding 99% HPLC purity. Acetone was completely evaporated in vacuo and **f_{18}** was obtained as an off-white amorphous solid with ≥99% HPLC purity.

5.2.5.3.16 6-(4'-(2,4-dimethoxyphenyl)-[2,2'-bithiazol]-4-yl)-[1,3]dioxolo[4,5-b]pyridine, f_{19}

K_2CO_3 (9.9 mg, 0.07171 mmol, 3.0 mol. equiv.) was added to 0.5 mL of DMF solution of **d_{22}** (9.5 mg, 0.0239 mmol) in a 10 mL glass vial. The mixture was heated while stirring with a magnetic stirrer for 5 min at 80°C. Subsequently, 18.8 µL (0.07168 mmol, 3.0 mol. equiv) of TBAH (1M) was added, followed by the addition of 6.0 µL (0.0956 mmol, 4 mol. equiv.) of methyliodide was added to the mixture, and it was heated while stirring at 80°C. The reaction was stopped after the complete consumption of **d_{22}**. Further workup follows as described in **5.2.5.3.1**. **f_{22}** was obtained as a dark brown amorphous solid with ≥99% HPLC purity.

5.2.5.3.17 6-(4'-(2,4-bis(2-(2-fluoroethoxy)ethoxy)phenyl)-[2,2'-bithiazol]-4-yl)-[1,3]dioxolo[4,5-b]pyridine, f_{20}

K_2CO_3 (7.0 mg, 0.05065 mmol, 2.0 mol. equiv.) was added to 1 mL of DMF, which contained a suspension of 10 mg (0.0216 mmol) of **d_{22}** in a 10 mL glass vial. The mixture was heated while stirring with a magnetic stirrer for 10 min at 80°C. Subsequently, 13.8 µL (0.05283 mmol, 2.1 mol. equiv) of TBAH (1M) was added, and the mixture was stirred at rt until complete dissolution of the suspension. Followed by the

addition of 12.2 µL (0.1006 mmol, 4 mol. equiv.) of 1-bromo-2-(2-fluoroethoxy)ethane was added to the mixture, and it was heated while stirring at 80°C. The reaction was stopped after the complete consumption of **d_{22}**. Further workup follows, as described in **5.2.5.3.1**. **f_{20}** was obtained as a dark brown amorphous solid with ≥99% HPLC purity.

5.3 Radiochemical synthesis

5.3.1 One-step radiofluorination

5.3.1.1 Ruthenium-mediated nucleophilic aromatic substitution (S_NAr) deoxyradiofluorination

The radiolabeling protocol for the radiosynthesis of [^{18}**F]d**$_2$ and **[**^{18}**F]d**$_4$ is identical except for a few minor deviations, which are detailed below.

Chromafix PS-HCO_3-^{18}F separation cartridge (45.0 mg, Product No. 731876 from ABX) was preconditioned by consecutively passing 3 mL of an aqueous $K_2C_2O_4$ (10 mg/mL) and 2 mL H_2O through the cartridge at a flow rate of 5 mL/min. Aqueous [^{18}F]fluoride solution was then loaded in the preconditioned Chromafix PS-HCO_3-^{18}F cartridge, followed by the removal of residual water by passing 1 mL of anhydrous MeCN through it. Subsequently, 2 mL of air was pushed through the cartridge. [^{18}F]Fluoride was eluted from the cartridge with a solution of 7 mg each of the ruthenium complexes of (**f_1**) and (**f_3**) (10 mmol) **Scheme 6**, and 14 mg of 2-chloro-1,3-bis(2,6-diisopropylphenyl)imidazolium chloride (g) (30 mmol, 3.0 equivalent) in 0.5 mL of MeCN into a 5 mL borosilicate vial (98% elution efficiency). MeCN was evaporated by heating at 80°C under a stream of nitrogen for about 5 min. Into the vial was added 0.45 mL of a mixture of veratrole, pivalonitrile, and ethanol (4:4:1, v:v:v). The reaction vial containing 0.45 mL of the reaction mixture was sealed with a Teflon-lined cap and was stirred at 130°C for 30 and 35 min for (**f_1**) and (**f_3**), respectively **Scheme 6**.

The reaction mixture was left to cool at rt, followed by the addition of 1 mL of 90% aqueous MeCN to the reaction mixture. The mixture was then promptly injected into the 2 mL loop of semiprep-HPLC. In-line HPLC detectors included a UV detector (Sykam) set at 254 nm and a radioactivity detector (Bioscan Flow-Count fitted with a PIN detector), equipped with a semiprep column Zorbax Bonus RP, 9.4 x 250 mm, 5.0 µm. **[**^{18}**F]d**$_2$ and **[**^{18}**F]d**$_4$ were eluted isocratically with aqueous MeCN solution (73 and 63%, respectively) containing 0.01% TBAH as the ion-pairing agent at retention times (T_R) 14.0 min and 15.3 min.

The >99% pure fractions obtained from the semiprep HPLC containing the ^{18}F-labeled tracers were diluted with Milli-Q® water (1:4.5) and fixed in a Sep-Pak C18 Classic Cartridge, 55–105 µm cartridge (pre-conditioned by passing 2 mL of ethanol through it, and thereafter 10 mL of Milli-Q® water). The cartridge was then washed with 4 mL of Milli-Q® water. Residual water was removed by passing nitrogen gas through

it. The radiolabeled products were then eluted with 96% ethanol. The ethanol eluate was tested for purity using the RP analytical HPLC. The identities of the radiolabeled tracers were confirmed by spiking with their respective cold versions **d**$_2$ and **d**$_4$.

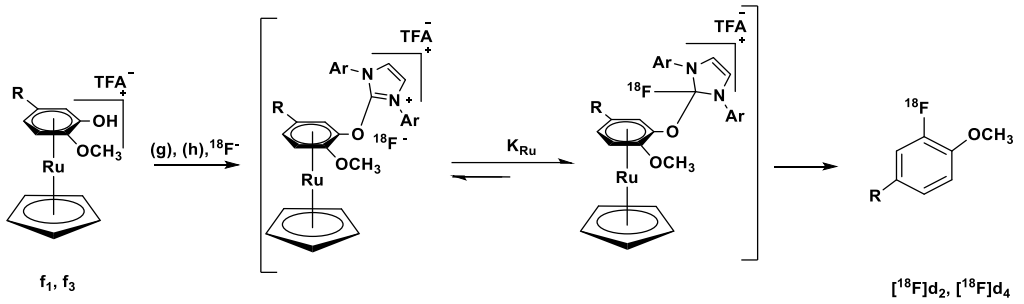

Scheme 6. Deoxyradiofluorination of the ruthenium complexes. Although the azeotropic drying step is skipped, the long reaction duration of 30 min somewhat diminishes this advantage. Nevertheless, contact with the radioactive reaction vial was reduced. TFA (counteranion obtained because of SHP with TFA-acidified solvents). For "R", see **Scheme 3**.

5.3.1.2 Halide-mediated S_NAr radiofluorination

A general protocol for the radiolabeling of **d**$_5$, **d**$_7$, **d**$_9$, **d**$_{16}$, **d**$_{18}$ and **d**$_{20}$ will be provided below, along with the quantity of the reagents used presented in **Table 1**.

For the radiosynthesis of **[^{18}F]d$_6$, [^{18}F]d$_8$, [^{18}F]d$_{10}$, [^{18}F]d$_{17}$, [^{18}F]d$_{19}$, and [^{18}F]d$_{21}$**, aqueous [^{18}F]fluoride solution was loaded in a pre-conditioned QMA (Sep-Pak Accell Plus QMA Carbonate Plus Light Cartridge, 130.0 mg sorbent per cartridge, 37-55 µm). The cartridge was pre-conditioned with 10 mL of Milli-Q® water that was slowly pushed through it. Then, with a mixture of kryptofix® 2.2.2 ($K_{2.2.2}$) and an aqueous solution of 1 M K_2CO_3 for **[^{18}F]d$_6$** and **[^{18}F]d$_{19}$**, and in combination with an aqueous solution of 1 M $KHCO_3$ for **[^{18}F]d$_8$**, **[^{18}F]d$_{17}$**, and **[^{18}F]d$_{21}$** or 1 M $K_2C_2O_4.H_2O$ for **[^{18}F]d$_{10}$**, [^{18}F]fluoride was eluted into a 5 mL borosilicate vial **Table 1**.

Table 1. Radiolabeling conditions of [^{18}F]d$_6$, [^{18}F]d$_8$, [^{18}F]d$_{17}$, [^{18}F]d$_{19}$, and [^{18}F]d$_{21}$

Tracer	Base						Kryptofix		Time, Temp.	Aq. MeCN/T_R [min]
	K_2CO_3		$KHCO_3$		$K_2C_2O_4.H_2O$					
	Vol., [µL]	A, [µmol]	Vol., [µL]	A, [µmol]	Vol., [µL]	A, [µmol]	Qty, [mg]	A, [µmol]		
[^{18}F]d$_6$	6.5	6.5	-	-	-	-	7.3	19.4	5 min, 180°C	71%, 14.8
[^{18}F]d$_8$	4.7	4.7	9.0	9.0	-	-	5.1	13.6	6 min, 190°C	63%, 11.9
[^{18}F]d$_{10}$	4.5	4.5	-	-	7.6	7.6	8.6	22.8	5 min, 150°C	60%, 13.0
[^{18}F]d$_{17}$	4.7	4.7	6.8	6.8	-	-	5.1	13.6	3 min, 140°C	63%, 17.0
[^{18}F]d$_{19}$	6.5	6.5	-	-	-	-	7.3	19.4	5 min, 180°C	69%, 16.5
[^{18}F]d$_{21}$	4.7	4.7	9.0	9.0	-	-	5.1	13.6	6 min, 190°C	62%, 11.9

Vol.: Volume. Qty: quantity of kryptofix used. A: amount of substance. Aq. MeCN: aqueous MeCN solution used for SHP. T_R: retention of time.

Water was removed azeotropically at 94°C, or 100°C (for **[^{18}F]d$_{10}$** only) with 0.5–1 mL anhydrous MeCN. Then, 2 mg of their precursors were suspended in 0.4 mL of DMSO and added to the borosilicate vial. The mixtures were heated for the duration and at the T°C given in **Table 1**, **Scheme 7** . Afterward, the reaction mixtures were allowed to cool down at rt and 1 mL of 90% aqueous MeCN was added to them. The resulting mixtures were injected into the semiprep HPLC. The rest follows, as already described in **5.3.1.1**. The identities of the tracers were confirmed by a spike injection with their already-characterized standards.

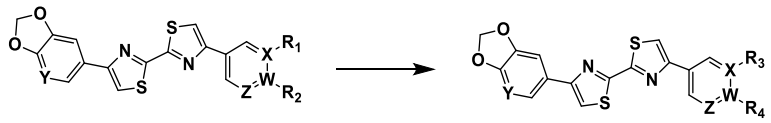

	W	X	Y	Z	R_1	R_2	R_3	R_4
[^{18}F]d$_6$	C	CH	CH	N	H	Br	H	^{18}F
[^{18}F]d$_8$	C	CH	N	N	H	Br	H	^{18}F
[^{18}F]d$_{10}$	C	N	N	N	-	-	-	^{18}F
[^{18}F]d$_{17}$	C	CH	N	CH	NO_2	Cl	NO_2	^{18}F
[^{18}F]d$_{19}$	N	C	CH	CH	Cl	-	^{18}F	-
[^{18}F]d$_{21}$	N	C	N	CH	Cl	-	^{18}F	-

Scheme 7. Radiosynthesis of the Csp2–[^{18}F]F DABTAs via their aryl/heteroaryl halide precursors. The radiosynthesis of the benzodioxole moiety-containing [^{18}F]d$_6$ and [^{18}F]d$_{19}$ was more straightforward, likely due to the relatively higher stability of their precursors at the basic pH used in the radiofluorination (see **7.2.1.2**), as well as the comparatively greater solubility of these tracers compared to the others.

5.3.1.3 Nucleophilic substitution (S_N2) radiofluorination

Radiosynthesis follows the same protocol described in **5.3.1.2** with some deviations. K_2CO_3 was the only base used for the elution of fluoride-18 from the QMA cartridge, MeCN was the reaction medium, the reaction temperature was always 120°C, and the flow rate for SHP was always 4 mL/min except for the elution of **[^{18}F]f$_4$**, **[^{18}F]f$_8$**, and **[^{18}F]f$_{13}$** (3 mL/min). The conditions specific to each of the radiolabeling are presented below in **Table 2**. 2 mg of the precursors were used for radiolabeling except for the radiosynthesis of **[^{18}F]f$_6$** via the iodide LG where just 1 mg of the precursor was used.

Table 2. Radiolabeling conditions for direct S_N2 radiofluorination of the DABTAs

Tracer	Base, K_2CO_3		Kryptofix		Time, Temp.	Aq. MeCN, T_R
	Vol., [µL]	A, [µmol]	Qty, [mg]	A, [µmol]		
[^{18}F]f$_4$	6.34	6.34	7.2	19.1	120°C, 7 min	54%, 7.4 min
[^{18}F]f$_5$	6.34	6.34	7.2	19.1	120°C, 7 min	55%, 13.6 min
[^{18}F]f$_6$	7.20 [a] 6.34 [b]	7.20 [a] 6.34 [b]	8.2 [a] 7.2 [b]	21.8 [a] 19.1 [b]	120°C, 6 min 120°C, 4 min	53%, 14.3 min 53%, 14.3 min
[^{18}F]f$_7$	6.69 [a] 6.34 [b*]	6.69 [a] 6.34 [b]	7.4 [a] 7.2 [b]	19.6 [a] 19.1 [b]	120°C, 6 min 120°C, 9 min	52%, 14.6 min 52%, 14.6 min
[^{18}F]f$_8$	7.15	7.15	6.7	17.8	120°C, 5 min	47%, 13.3 min

[^{18}F]f$_9$	7.16	7.16	7.8	20.8	120°C, 10 min	56%, 15.8 min
[^{18}F]f$_{10}$	9.80 [a] 6.34 [b]	9.80 [a] 6.34 [b]	11.1 [a] 7.2 [b]	29.4 [a] 19.1 [b]	120°C, 10 min 120°C, 9 min	60%, 14.0 min 60%, 14.0 min
[^{18}F]f$_{11}$	6.91	6.91	7.8	20.7	120°C, 9 min	66%, 16.5 min
[^{18}F]f$_{12}$	6.34	6.34	7.2	19.1	120°C, 7 min	57%, 17.3 min
[^{18}F]f$_{13}$	6.34	6.34	7.2	19.1	120°C, 7 min	50%, 10.0 min
[^{18}F]f$_{14}$	6.34	6.34	7.2	19.1	120°C, 9 min	63%, 18.0 min

Vol.: Volume. Qty: quantity of kryptofix used. A: amount of substance. Aq. MeCN: aqueous MeCN solution used for SHP. T_R: retention of time. [a] via the tosylate LG [b] via the iodide LG [*] with 1 mg of precursor.

The scheme of radiosynthesis of the tracers is presented in **Scheme 8** below:

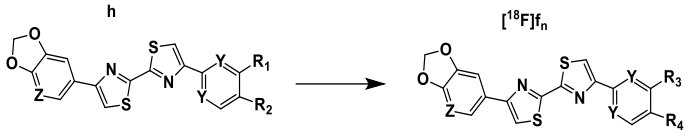

[^{18}F]f	**Z**	**Y**	**R$_1$**	**R$_2$**	**R$_3$**	**R$_4$**
[^{18}F]f$_4$	N	N	H	$O(CH_2)_2Br$	H	$O(CH_2)_2{}^{18}F$
[^{18}F]f$_5$	CH	N	H	$O(CH_2)_2Br$	H	$O(CH_2)_2{}^{18}F$
[^{18}F]f$_6$	CH	N	H	$(O(CH_2)_2)_2Tos$	H	$(O(CH_2)_2)_2{}^{18}F$
[^{18}F]f$_7$	CH	N	H	$(O(CH_2)_2)_3$(Tos or I)	H	$(O(CH_2)_2)_3{}^{18}F$
[^{18}F]f$_8$	N	N	H	$(O(CH_2)_2)_2Tos$	H	$(O(CH_2)_2)_2{}^{18}F$
[^{18}F]f$_9$	N	CH	$(O(CH_2)_2)_2Tos$	OCH_3	$(O(CH_2)_2)_2{}^{18}F$	OCH_3
[^{18}F]f$_{10}$	N	CH	F	$O(CH_2)_2)_3$(Tos or I)	F	$(O(CH_2)_2)_3{}^{18}F$
[^{18}F]f$_{11}$	CH	CH	H	$O(CH_2)_2Tos$	H	$O(CH_2)_2{}^{18}F$
[^{18}F]f$_{12}$	CH	CH	H	$(O(CH_2)_2)_3I$	H	$(O(CH_2)_2)_3{}^{18}F$
[^{18}F]f$_{13}$	N	N	H	$(O(CH_2)_2)_3I$	H	$(O(CH_2)_2)_3{}^{18}F$
[^{18}F]f$_{14}$	CH	CH	$(O(CH_2)_2)_3I$	OCH_3	$(O(CH_2)_2)_3{}^{18}F$	OCH_3

Tos: tosylate, I: iodide.

Scheme 8. Radiosynthesis of [^{18}F]f$_4$-[^{18}F]f$_{14}$ via radiofluorination. Compared to the radiosynthesis of the [^{18}F]arylfluorides (**5.3.1.2, 7.2.1.2**), the radiosynthesis of these tracers are uncomplicated, except for the synthesis of **[^{18}F]f$_5$** via the tosylate leaving group (see **7.2.1.3**).

5.3.2 Two-step radiolabeling

5.3.2.1 The first step of the two-step radiofluorination

This follows the same protocol as described in **5.3.1.2**, except that K_2CO_3 was the only base used for the elution of fluoride-18 from the QMA cartridge, and the reaction was conducted in the solvent MeCN. Radiosynthesis of the [^{18}F]fluoroethylated/PEGylated DABTAs was carried out via a radiofluorinated intermediate **[^{18}F]FETos**, **[^{18}F]FDETos**, and **[^{18}F]FTETos** with 8.5 mg of the precursors: ethylene glycol ditosylate, diethylene glycol ditosylate, or triethylene glycol ditosylate **Scheme 9a**. Both reagents and conditions of the reactions are presented in **Table 3**.

The reaction mixture was cooled at rt, after which 500 µL of 0.02 M acetic acid solution was added to it. The mixture was purified via semiprep purification. SHP was with an aqueous MeOH solution with neither an acidic nor a basic ion-pairing agent. The collected fraction was diluted with 3 times its volume with Milli-Q® water and loaded onto an already conditioned Strata X cartridge (33 µm, 30 mg/mL, Phenomenex). The Strata X cartridge was conditioned by passing 1 ml of MeOH through the cartridge, followed by 1 mL of Milli-Q® H_2O. The cartridge with the intermediate was dried by flushing it with a steady stream of nitrogen gas for 10 min at rt and 10 min at 55°C.

Table 3. Radiolabeling conditions for the first step of the two-step radiofluorination

Intermediate	Base, K_2CO_3		Kryptofix		Time, Temp.	Aq. MeOH, T_R
	Qty, [mg]	A, [µmol]	Qty, [mg]	A, [µmol]		
[^{18}F]FETos	4.7	34.0	15	39.8	75°C, 5 min	55%, 9.0 min
[^{18}F]FDETos	3.0	21.7	15	39.8	80°C, 5 min	55%, 8.7 min
[^{18}F]FTETos	2.7	19.5	15	39.8	75°C, 4 min	50%, 11.0 min

Vol.: Volume. Qty: quantity of kryptofix used. A: amount of substance. Aq. MeOH: aqueous MeOH solution used for SHP. T_R: retention of time.

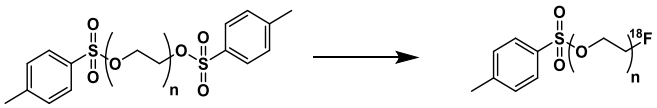

Scheme 9a. Radiosynthesis of the radiofluorinated intermediate in the first step of the two-step radiofluorination. For [^{18}F]FETos n = 1, [^{18}F]FDETos n = 2, [^{18}F]FTETos n = 3. The radiosynthesis of these intermediates is extensively described in the literature, but minor optimization was still needed, especially in the drying step before they were used in the subsequent step shown in **5.3.2.2**.

5.3.2.2 The second step of the two-step radiofluorination

2.5 mg of the DABTA precursors **d_3, d_{11}-$_{13}$** (**Scheme 2**, Step II) in 300 µL anhydrous DMF was added to a 5 mL borosilicate vial equipped with a magnetic stirrer. The required amount of TBAH (1M) in MeOH **Table 4a** was added to the vial. The vial was covered with a Teflon-lined cap and stirred at 115°C in a nitrogen atmosphere for 3 min. Afterward, the intermediate (**[^{18}F]FETos**, **[^{18}F]FDETos**, or **[^{18}F]FTETos)** was eluted from the Strata X with 1 mL of DMF into the vial.

Table 4a. Radiolabeling conditions for the second step of the two-step radiofluorination

Tracer	Precursor		Base, TBAH		Intermediate	Time, Temp.	Aq. MeCN*, T_R
	Qty, [mg]	A, [µmol]	Vol., [µL]	A, [µmol]			
[^{18}F]f_4	2.5	6.5	6.0	21.0	**[^{18}F]FETos**	115°C, 6 min	54%, 7.4 min
[^{18}F]f_5	2.5	6.5	3.0	10.5	**[^{18}F]FETos**	115°C, 4 min	56%, 15.6 min
[^{18}F]f_6	2.5	6.5	3.0	10.5	**[^{18}F]FDETos**	115°C, 4 min	55%, 14.2 min
[^{18}F]f_7	2.5	6.5	3.0	10.5	**[^{18}F]FTETos**	115°C, 6 min	55%, 14.3 min

[^{18}F]f$_9$	2.5	6.1	4.0	14.0	**[^{18}F]FDETos**	115°C, 5 min	59%, 15.8 min
[^{18}F]f$_{10}$	2.5	6.3	3.0	10.5	**[^{18}F]FTETos**	115°C, 5 min	61%, 12.3 min

Vol.: Volume. Qty: quantity of kryptofix used. A: amount of substance. Aq. MeCN: aqueous MeCN solution used for SHP. T_R: retention of time. * with 0.05% TBAH (1.4 N).

The reaction was carried out in an atmosphere of nitrogen gas for the required duration at 115°C. The rest followed the same protocol as was described in **5.3.1.1**. The scheme of radiosynthesis of the tracers is presented in **Scheme 8** below:

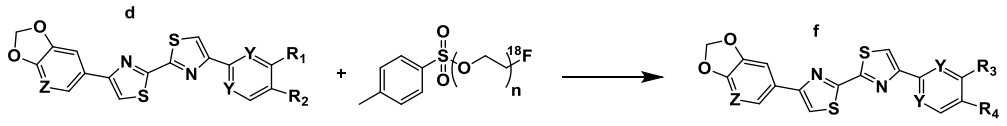

[^{18}F]f	Z	Y	R_1	R_2	R_3	R_4	n
[^{18}F]f$_4$	N	N	H	$O^-Bu_4N^+$	H	$O(CH_2)_2{}^{18}F$	1
[^{18}F]f$_5$	CH	N	H	$O^-Bu_4N^+$	H	$O(CH_2)_2{}^{18}F$	1
[^{18}F]f$_6$	CH	N	H	$O^-Bu_4N^+$	H	$(O(CH_2)_2)_2{}^{18}F$	2
[^{18}F]f$_7$	CH	N	H	$O^-Bu_4N^+$	H	$(O(CH_2)_2)_2{}^{18}F$	3
[^{18}F]f$_9$	N	CH	$O^-Bu_4N^+$	OCH_3	$(O(CH_2)_2)_2{}^{18}F$	OCH_3	2
[^{18}F]f$_{10}$	N	CH	F	$O^-Bu_4N^+$	F	$(O(CH_2)_2)_3{}^{18}F$	3

Scheme 9b. O-[^{18}F]fluoroalkylation/PEGylation via radiofluorinated intermediate of the phenol/pyrimidinol precursors. $O^-Bu_4N^+$ salt of the phenol/pyrimidinol DABTAs with TBAH (Bu = butyl). The radiofluorinated intermediate appeared to be fairly unstable in the presence of free TBAH; therefore, excess TBAH was removed by purging the reaction mixture with nitrogen gas through a hypodermic needle, while a ventilating hypodermic needle allowed the displaced TBAH to escape.

5.3.3 Carbon-11 radiolabeling

5.3.3.1 The first step of Carbon-11 radiolabeling: [^{11}C]CH_3I and [^{11}C]CH_3OTf production

[^{11}C]CO_2 (~103 GBq) is produced in the cyclotron (PETtrace 880^{TM}, GE HealthCare, Germany) via the $^{14}N[p,\alpha]^{11}C$ reaction after 15 min of irradiation at 60 µA. The [^{11}C]CO_2 is then transferred in a target gas stream to the TRACERlab FX2 MeI processing module, where ~63 GBq is trapped. The [^{11}C]CO_2 is captured by a molecular sieve in the methane oven at rt. [^{11}C]CO and other residues are diverted to the waste through an exhaust valve located after the oven.

[^{11}C]CO_2 is converted into [^{11}C]CH_4 by passing H_2 gas over a nickel-catalyst (Shimalite-Ni) support at 350°C. The oven outlet is then closed. The resulting [^{11}C]CH_4 is released into a liquid nitrogen-cooled methane trap for further purification and concentration. Afterward, the methane oven is subsequently turned off and allowed to cool down.

[^{11}C]CH_4 is converted to [^{11}C]CH_3I by passing it through a gas circulation system where it reacts with iodine at 720°C. The resulting [^{11}C]CH_3I is then passed through a separate NaOH trap to remove some impurities such as hydrogen iodide. The [^{11}C]CH_3I is subsequently extracted from circulation process using a Porapak trap at rt. Unconverted [^{11}C]CH_4 is returned to the circulation system to react further with iodine. The trapped

[^{11}C]CH_3I (20-30 GBq) is desorbed from the adsorbent by heating at 190°C and carried by a He-flow into the reactor of a separate synthesizer. The synthesis scheme is shown below in **Scheme 10a**.

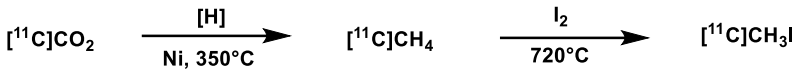

Scheme 10a. The synthesis of the [^{11}C]methyliodide via the gas phase method. Carbon-11 labeling was primarily conducted via methylation using [^{11}C]CH_3I. Attempts with [^{11}C]CH_3OTf (see **7.2.3**) resulted in much lower RCC compared to those observed with [^{11}C]CH_3I.

To obtain [^{11}C]methyltriflate [^{11}C]CH_3OTf, the synthesized [^{11}C]CH_3I was subsequently converted to [^{11}C]CH_3OTf by passing the [^{11}C]CH_3I through an α-alumina column impregnated with silver triflate (Ag OTf) at 190°C. The identity of the final product(s) was confirmed by co-injection with the corresponding standard compound.

5.3.3.2 The second step of carbon-11 radiolabeling: O-[^{11}C]methylation

The needed amount of the DABTA precursors **d_3, d_{11}, d_{12}, and d_{15}** (**Table 4b**) was weighed out in a 5 mL borosilicate vial equipped with a magnetic stirrer. 400 µL anhydrous DMF was added to the vial, followed by 4 µL of TBAH (1M) in MeOH. The vials were sealed with a Teflon-lined cap and stirred at 120°C in a nitrogen atmosphere for 3 min **Scheme 10b**. [^{11}C]CH_3I was bubbled into the DMF solution at room temperature. Except for the synthesis of **[^{11}C]f_{16}**, for which the reaction mixture was heated for 4 min, the rest of the [^{11}C]C-labeled tracers were synthesized by heating at 90°C for 5 min in a nitrogen atmosphere. SHP was conducted at a flow rate of 4 mL/min with different concentrations of TBAH (1.4 N) in the eluent **Table 4b**. The rest followed the same protocol as was described in **5.3.1.1**.

Table 4b. Radiolabeling conditions for the second step of the carbon-11 radiolabeling

Tracer	**Precursor**			**Base, TBAH**		**SHP**	
[^{11}C]f	**d**	**Qty, [mg]**	**A, [µmol]**	**Vol., [µL]**	**A, [µmol]**	**Aq. MeCN, T_R**	**TBAH, [%]**
[^{11}C]f_{15}	**d_{12}**	1.0	2.6	4.0	21.0	54%, 12.0 min	0.040
[^{11}C]f_{16}	**d_{11}**	2.0	5.2	4.0	10.5	45%, 8.0 min	0.005
[^{11}C]f_{17}	**d_{15}**	1.5	3.9	4.0	10.5	64%, 7.0 min	0.010
[^{11}C]f_{18}	**d_3**	1.5	3.6	4.0	10.5	60%, 8.5 min	0.010

Vol.: Volume. Qty: quantity of kryptofix used. A: amount of substance. Aq. MeCN: aqueous MeCN solution used for SHP. T_R: retention of time. TBAH, [%] concentration of TBAH in the eluents.

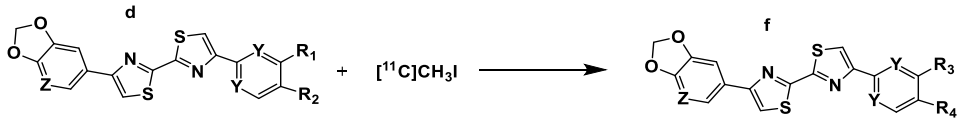

[^{11}C]f	**Z**	**Y**	**R_1**	**R_2**	**R_3**	**R_4**
[^{11}C]f_{15}	CH	N	H	$O^-Bu_4N^+$	H	$O^{11}CH_3$
[^{11}C]f_{16}	N	N	H	$O^-Bu_4N^+$	H	$O^{11}CH_3$
[^{11}C]f_{17}	N	CH	H	$O^-Bu_4N^+$	H	$O^{11}CH_3$

[^{11}C]f_{18}	N	CH	$O^-Bu_4N^+$	OCH_3	$O^{11}CH_3$	OCH_3

Scheme 10b. O-[^{11}C]methylation of d_{11}, d_{12}, d_{15}, and d_3 with TBAH (1 M) in DMF at 90°C. Where, Bu_4N^+ represents the TBAH cation (Bu = butyl). Since [^{11}C]CH_3I was also unstable in TBAH, the same precautions applied to the radiofluorinated intermediates was taken here as well (**Scheme 9b**).

5.3.4 Calculation of radiochemical yields (RCY)

RCY were calculated based on the amount of the decay-corrected pure tracer isolated after SHP. It was decay-corrected to the end of elution of [^{18}F]fluoride from the QMA cartridge and calculated as a percentage of the amount of activity eluted into the reaction vial (AAEV): %RCY = (pure eluate/AAEV)×100

For the two-step reactions. The amount of activity lost during fixation on the strata cartridge and during elution, with DMF into the second reaction vial is taken into consideration. For the carbon-11-labeled tracers, AAEV was taken to be the amount of radioactivity in the borosilicate vial measured immediately before synthesis was started.

5.3.5 Calculation of molar activity (A_m)

50 µL of tracers were collected from a known volume of an ethanol fraction of the respective tracers, and the amount of radioactivity contained in it was counted using a Capintec well ɣ-counter. The activity was subsequently decay-corrected until the end of radiosynthesis (until the end of the first-step synthesis for the two-step radiolabeled tracers). The radioactivity was left to decay, and it was injected into the analytical HPLC (the same volume injected for the preparation of the calibration curve). To determine the concentration associated with decay-corrected radioactivity of the injected aliquot, the HPLC-UV response was calculated based on a calibration curve prepared with the cold versions (**5.2.5.3**) of the tracers.

5.4 Other in vitro experiments

5.4.1 Determination of log D

A given volume of 0.5–1.0 MBq of octanol solution of the tracers was added to 1.5 mL Eppendorf vials containing 0.5 mL of PBS (pH 7.4). Octanol was added afterward to a final volume of 1.0 mL. To achieve a good distribution of the tracer(s), the vials were vigorously vortexed for 10 min. The vials were then centrifuged for 10 min at 13000 r.p.m. in a Heraus Biofuge 13 centrifuge to obtain a well-separated phase. 100 µL of aliquots were carefully taken both from the octanol and aqueous phases. The amount of activity in the samples was then measured using a gamma counter. Calculation of the log octanol/PBS values was then carried out. Three or more separate evaluations were carried out.

5.4.2 Plasma binding (ultrafiltration method)

0.5–1.0 MBq of the tracers was added to 450 µL of Seronorm™ Human Plasma (Invicon Gmbh, Germany) and incubated for 10 min. Then, the plasma was distributed in three ultrafiltration vials (150 µL each) (Centrifree YM-30, cutoff 30,000 MW, Millipore) and centrifuged for 10 min at 8 000 r.p.m. Equal volumes of the ultrafiltrate (C_{free}) and plasma (C_{total}) were measured with a gamma counter. The percentage of unbound tracers was calculated using the formula: $\%fp = C_{free}/C_{total}$ x 100%, (n = 3).

5.4.3 Plasma stability

8–10 MBq of each tracer was added to 300 µL of Seronorm™ Human Plasma (Invicon Gmbh, Germany), and incubated at 37°C. Aliquots were taken from the plasma at 30, 60, 90, and 120 min. To each aliquot, 100 µL of MeCN was added to precipitate plasma proteins, and the mixture was centrifuged at 13 000 rpm in a Heraeus Biofuge 13 centrifuge for 10 min. The supernatants were then analyzed using radio-HPLC (n = 3).

5.4.4 In vitro binding assays

5.4.4.1 Preparation of the amyloid protein aggregates

5.4.4.1.1 Preparation of recombinant α-syn fibrils

The incubation of purified recombinant α-synuclein monomer (10 mg/mL) obtained as described by Uzuegbunam et al [138] was carried out in PBS (pH 7.4) at 37°C. The solution was shaken at 900 r.p.m. in an Eppendorf Thermomixer for 84 hours. Determination of the concentration of the formed fibrils (α-syn), was carried out following the centrifugation of the reaction vial at 12 000 g for 5 min. The pellet obtained was washed thrice with 20 mM Tris-HCl pH 7.4. The supernatants from all three centrifugations carried out were combined, and the concentration of the non-aggregated monomer was determined using SDS-PAGE. Determination of the concentration of α-syn was carried out by subtracting the amount of α-synuclein monomer in the supernatant from the initially used amount.

5.4.4.1.2 Preparation of recombinant β-amyloid fibrils

1 mg β-amyloid$_{1–42}$ peptide (Abcam, United Kingdom) was dissolved in a mixture of 50 µL DMSO and 925 µL of Milli-Q® water. Finally, 25 µL of 1M Tris HCl, pH 7.4, was added to bring the final peptide concentration to 1 mg/mL. The mixture was then incubated at 37°C for 30 h with shaking at 900 r.p.m. To separate the non-aggregated monomers from the formed fibrils, the reaction mixture was centrifuged at 12 000 g for 5 min, and the resulting pellet was washed three times with 500 µL of 20 mM Tris HCl pH 7.4. The supernatants from the three centrifugation steps were combined, and the concentration of the monomer in the resulting supernatant was determined in a BCA assay (with a BSA standard curve). Determination of

the concentration of fibrils formed was carried out by subtracting the amount of β-amyloid$_{1–42}$ peptide monomer in the supernatant from the initially used amount.

5.4.4.1.3 Preparation of recombinant tau fibrils

Recombinant tau monomer (R&D Systems, U.S.A) was dissolved in 20 mM Tris HCl pH 8.0, 100 mM NaCl, 25 μM low MW heparin, and 0.5 mM dithiothreitol to a final concentration of 300 μg/mL. The mixture was incubated with shaking 900 r.p.m. at 37°C for 48 h. To separate the non-aggregated monomers from the formed fibrils, the reaction mixture was centrifuged at 12 000 g for 5 min and the resulting pellet was washed thrice with 500 μL of 20 mM Tris HCl pH 7.4. The supernatants from the three centrifugation steps were combined, and the concentration of the monomer in the resulting supernatant was determined in a BCA assay (with a BSA standard curve). Determination of the concentration of fibrils formed was carried out by subtracting the amount of tau peptide monomer in the supernatant from the initially used amount.

5.4.4.2 Preparation of α-synuclein, β-amyloid$_{1–42}$ and tau fibrils for competition binding assays

The pellets of the fibrils obtained above **5.4.4.1** were resuspended in 20 mM Tris-HCl pH 7.4 and diluted as needed for the binding assays.

5.4.4.3 Competition binding assays

The binding assays were carried out with both tritiated DCVJ ([^{3}H]DCVJ) and tritiated PiB ([^{3}H]PiB) **Figure 19**. [^{3}H]DCVJ binds to all the protein aggregates with high affinity: K_d for α-syn 4.4 nM, Aβ 8.9 nM, tau 15.6 nM. [^{3}H]PiB binds also with relatively high affinity to the fibrils [85,177–179]: K_d for α-syn 4.9 nM, Aβ 3.7 nM, tau 117.5 nM.

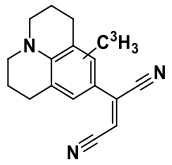

[^{3}H]DCVJ

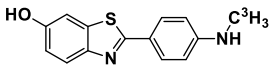

[^{3}H]PiB

Figure 19. The chemical structures of tritiated DCVJ and PiB. While PiB exhibits some affinity for in vitro–synthesized α-syn, its binding to LB in actual brains affected by dementia with DLB is negligible.

5.4.4.3.4 Competition binding assays with the α-syn fibrils

A fixed concentration of [^{3}H]DCVJ (10 nM) and α-synuclein aggregates (125 nM) prepared as described above **5.4.4.2** were used with different final concentrations of the standard compounds (**Figure 23** and **Figure 25**) from 0.01–100 nM. The experiment was carried out in quintuplicates for each concentration.

The mixture was incubated for 2 h in a final volume of 200 µL per well after dilution with 20 mM Tris HCl, pH 7.4. The incubated mixtures were filtered through a Perkin Elmer GF/B glass filter via a TOMTEC cell harvester and immediately washed thrice with 1 mL of deionized water. The filters containing the bound ligands were dried and afterward mixed with 3 mL of BetaPlate Scint solution (PerkinElmer Life Sciences) and left there for 2 h before counting in a Wallac 1450 MicroBeta TriLux Liquid Scintillation Counter (PerkinElmer Life Sciences). For the determination of the inhibition constants, data were analyzed using GraphPad Prism software (version 7.0) to obtain IC_{50} values by fitting the data to the equation Y = bottom+(top−bottom)/(1+10(x–log IC_{50})). K_i values were calculated from IC_{50} values using the equation K_i = IC_{50}/(1+[radioligand]/K_d). For assays with [^{3}H]PiB, a fixed concentration of [^{3}H]PiB (10 nM) and a 10 mM phosphate buffer (pH 7.4), 1 mM EDTA and 0.5% BSA (for incubation and washing) were used instead.

5.4.4.3.5 Competition binding assays for Aβ$_{1–42}$ and tau fibrils

Fixed concentrations (125 nM) of A$\beta_{1–42}$, tau aggregates, and [^{3}H]DCVJ (10 nM and 20 nM for the A$\beta_{1–42}$ and tau competition experiments, respectively) were used with different concentrations of the standard compounds from 1−1000 nM. The experiment was performed in quadruplicates for each concentration. Further procedures followed the same already described in **5.4.4.3.4**.

For assays with [^{3}H]PiB, fixed concentrations (125 nM) of A$\beta_{1–42}$, tau aggregates, and [^{3}H]PiB (10 nM and 200 nM for the A$\beta_{1–42}$ and tau competition experiments, respectively) with 10 mM phosphate buffer (pH 7.4) that contained 1 mM EDTA and 0.5% BSA (for incubation and washing) were used instead.

5.4.5 In vitro autoradiography

5.4.5.1 With brain tissue from mice injected with pre-formed α-synuclein fibrils (PFF)

Cryoprotected brain tissue sections (30 µm) stored in antifreeze from wild-type mice (WT:C57Bl/6J; Stock JAX:000664, the Jackson Laboratory, USA) injected with pre-formed α-synuclein fibrils (PFF) were washed twice in saline and fixed onto SuperFrost Plus™ slides and stored at -20°C prior to use. The brain slices included sections of the hippocampal and brain regions. Before use, the slices were thawed at rt and preincubated in the incubation buffer for 20 min. For total binding and non-specific binding experiments, the brain slices were incubated in 50 mM Tris HCl buffer for 60 min with 1.2 MBq/mL of **[^{18}F]$\mathbf{d_4}$** and **[^{18}F]$\mathbf{d_6}$** of A_m (47.8−60.0 GBq/µmol). For non-specific binding, the standard compound was added to a final concentration of 3.8 µM to block non-specific binding. After incubation, the slices were incubated in a 70% aqueous ethanol solution for 1 min and then incubated thrice for 2 min each in 3 different 50% aqueous ethanol solutions, with a final 3-sec dip in Milli-Q® water.

5.4.5.2 With brain tissue from transgenic mice

Fresh frozen tissues were obtained from the following transgenic mice models of α-synucleinopathy (A53T), β-amyloidopathy (ArcAβ), and tauopathy (P301S) and cut into 20 µm slices and fixed onto SuperFrost Plus™ slides and stored at -20°C prior to use. The slices were pre-incubated in 100% MeOH and incubated for 60 min in 50 mM of Tris pH 7.4, with 1.2 MBq/mL of [^{18}F]**$\mathbf{d_6}$** of A_m (28.7−50.0 GBq/µmol). The rest followed as described in **5.4.5.1**.

5.4.5.3 With postmortem human brain tissue

Paraffinated diseased PHBT sections (LBD, MSA, β-amyloidopathy, tauopathy, and AD) and non-diseased PHBT sections (control) were provided by Neurobiobank Munich [180]. The LBD sections included: LB/LN-containing cingulate gyrus, fusiform and entorhinal cortices. MSA sections - GCI-containing anterior striatum, pons, pons at the level of locus coeruleus, cerebellum, anterior striatum basal ganglia at the level of pallidum, cerebellar hemisphere with dentate nucleus, cerebellar hemisphere with dentate nucleus. β-amyloidopathy (Aβ without tau fibrils): inferior parietal lobulus and cingulate gyrus. Tauopathy: hippocampus at the level of the cornu ammmonis. AD: cortex and subcortical white matter of the middle frontal gyrus, occipital cortex (area striata, peri- and parastriata), and hippopcampus (Ammon's horn) with parahippocampus. The control: undiseased hippocampus at thelevel of cornu ammmonis. Each tracer was tested once with each of the PHBT.

Paraffinated PHBT slices (5 µm), were deparaffinized and rehydrated as described below: the slides with the paraffinated slices were incubated thrice for 15 min in fresh xylene (Sigma-Aldrich, Germany). Then, the samples were incubated once for 15 min in each of the next steps: 100% isopropanol, 96% ethanol, 70% ethanol, 50% ethanol, and finally in Milli-Q®water. The deparaffinated brain slices were preincubated for 20 min in the incubation buffer containing 50 mM Tris-base (Roth, Germany) buffer (pH 7.4) and 1.0 % bovine serum albumin (BSA) (Biowest, USA) for 20 min at rt. After which, the sections were incubated for 60 min (40 min for the carbon-11 labeled tracers) at rt in the incubation buffer which contained 0.2 MBq/mL (0.5 MBq/mL for the carbon-11 labeled tracers) of the tracers prepared in 15–40 µL of ethanol (final concentration 0.038–0.1%).

At 60 min, the slices were transferred and incubated in a 1% BSA solution for 2 min, followed by two 3-min incubations in 50% aqueous ethanol, and then incubated in a 70% aqueous ethanol solution for 1 min. For the carbon-11-labeled tracers, the slices were incubated in a 1% aqueous BSA solution for 1 min, then for 30 sec in a 50% aqueous ethanol solution, and for 10 sec in a 70% aqueous ethanol solution. Finally, the sections were dipped for 3 sec in Milli-Q® water and left to dry at rt. The air-dried brain sections were then exposed overnight to phosphorimaging plates (Fujifilm, Tokyo, Japan). The read-out of the plate was performed with a Phosphor-Imager (CR35 BIO, Dürr-Biomedical, Miami, FL, USA) at 25 µm resolution mode. Subsequent processing and data analysis were carried out with the AIDA Image Analyzer software.

5.5 Ex vivo and in vivo experiments.

All animal experiments were approved by local authorities (animal license: 55.2-1-54-2532-216-15) and conducted in accordance with guidelines for the welfare and use of animals in experimental procedures.

5.5.1 Biodistribution experiments

The ethanol solutions containing the tracers obtained as described in **5.3.1.1** were diluted with DMSO, Tween-20, and saline added consecutively to achieve a final concentration of 2.4%, 2.4%, and 0.4% of ethanol, DMSO, and Tween-20, respectively. The pH was adjusted to 7.4 with a 0.05 N aqueous NaOH solution. 3−4 MBq of the tracers prepared in the above solvent mixture were administered to the mice via the caudal vein under isoflurane anesthesia (initiation of which takes place in a low-stress anesthesia box with 3−5% isoflurane with 2 L/min oxygen as required; it is thereafter maintained via a nasal mask with 1−3% isoflurane with 2 L oxygen/min, with the eyes of the mice protected from drying using Bepanthen eye ointment (Bayer, Germany)). The mice were sacrificed at 5, 60, and 120 min p.i. The following organs and tissues were extracted: blood, heart, lung, liver, stomach, pancreas, colon, small intestine, kidney, muscle, bone, tail, and brain. The radioactivity in the pre-weighed tissue samples was determined using a γ-counter. Data are expressed as a percent of the injected dose per gram tissue (%ID/g, mean ± sd, n = 3).

5.5.2 Metabolite experiments

The tracers **[^{18}F]$\mathbf{d_6}$**, **[^{18}F]$\mathbf{d_8}$**, **[^{18}F]$\mathbf{f_4}$**, **[^{18}F]$\mathbf{f_5}$**, **[^{18}F]$\mathbf{f_6}$**, **[^{18}F]$\mathbf{f_7}$**, and **[^{18}F]$\mathbf{f_8}$** were prepared as already described in **5.3.1.1**. 50–70 MBq of each tracer was injected via the caudal vein in the mice (n = 3 per tracer; **[^{18}F]$\mathbf{f_4}$** (n = 1)). At 20 min p.i., the animals were euthanized, and the needed tissues extracted and placed on dry ice. To separate plasma from the blood cells, the blood samples were first centrifuged at 13000 r.p.m. for 10 min, then MeCN acidified with 1% TFA (10 min, 4°C) was added to the centrifugate to precipitate the plasma proteins, followed by another centrifugation as already described, and ultrafiltration using ultrafiltration tubes (Centrifree YM-30; cutoff 30,000 MW; Millipore). 10 μL 1 M-DMSO solution of their cold versions was added to the centrifugate, which was subsequently analyzed by RP-HPLC. The brain was frozen in liquid nitrogen and homogenized with a ball mill. A mixture of MeCN and DMSO (5:1) with 1% TFA containing the cold version of the tracers was added to the homogenate and mixed. The suspension was centrifuged. The supernatant was then filtered using ultrafiltration tubes as already described, and the resulting filtrate was subsequently analyzed by RP-HPLC.

5.5.3 In vivo PET-MRI dynamic scan with biodistribution

For PET imaging, [^{18}F]$\mathbf{d_6}$ and [^{18}F]$\mathbf{d_8}$ were prepared as described in **5.3.1.1**, and 11.8 ± 0.70 MBq (n = 6) was injected via the caudal vein in the mice (n = 3 for each tracer). PET was recorded on nanoScan®

PET/MRI (Mediso Medical Imaging System) under isoflurane anesthesia, as described in 2.5.1. PET was recorded in list mode for 120 min and consisted of 36 frames (1×60 s; 30×10 s; 1×600 s; 1×900 s; 3×1800 s). Data were reconstructed using Nucline nanoScan 3.00.021.0000 software, employing an OSEM3D algorithm without scatter and attenuation correction. Tissue time-activity curves (TACs) were obtained by projecting the defined ROI onto all frames of the dynamic PET scans. After the PET dynamic scan, the mice were promptly euthanized, and the rest of the protocol followed as described in **5.5.1**.

MRI scan was a fast-spin echo 2D (FSE2D) scan, T2-weighted with coronal orientation, 23 slices with a slice thickness of 1.0 mm and a 0.2 mm slice gap. Frequency resolution was 0.391 mm, and the phase resolution was 0.198 mm. The number of excitations and of repetition time (TR) shots was 2 and 1 respectively. TR was 3000 msec, and echo time was 60.6 msec. Field of view (FOV) (frequency) 100 mm, FOV (phase) 38 mm, frequency encoding 256, phase encoding 192, echo train length 8, and echo spacing 7.58 msec.

6. RESULTS

6.1 Chemical yields

The overall yields **Table 5** of the compounds were dependent on the success of the first step of the synthesis as well as the number of times it was carried out. Repeated synthesis with improved purification strategies enabled the product (b) to be obtained at higher yields. The chemical yields of the compounds obtained in Step I were provided in the descriptions in **5.2.2**.

In most cases, the compounds were produced in moderate to high yields **Table 5**. The lowest yields were seen for the 2-halopyrimidine compounds $\mathbf{d_9}$ and $\mathbf{d_{10}}$. This was owing to the poor solubility of their step II predecessors, $\mathbf{b_8}$ and $\mathbf{b_9}$, respectively, in the eluents used for the SHP. Furthermore, it seemed that the compounds interacted strongly with the ionized residual silanol groups residing on the C18 silica stationary phase, which led to the retention of the compounds in the column. Moreover, their syntheses were carried out once; hence, optimization of their HPLC purification was not affected. The interaction with the stationary phase observed in $\mathbf{b_8}$ and $\mathbf{b_9}$ was worse in their cases but was not unusual for the mono-heteroarylthiazole compounds, especially those without a hydroxyl group, as were $\mathbf{b_8}$ and $\mathbf{b_9}$. The synthesis of $\mathbf{f_{17}}$ was not very successful as well via tosylate LG (methyltosylate). The reaction failed to go to completion with only ~41% (analytical HPLC) at 10 min of heating. No further increment in yield was observed even after 60 min of heating. Heating to 85°C just resulted in the formation of side products instead.

Table 5. Chemical yields (STEP II and Overall)

№	DABTA	Step I/II (overall), [%]	Step III, [%]	Overall yield, [%]
1.	$\mathbf{d_1}$	57.4 ± 0.91, (n = 2)	-	57.4 ± 0.91, (n = 2)
2.	$\mathbf{d_2}$	47.7 (n = 1)	-	47.7 (n = 1)
3.	$\mathbf{d_3}$	47.7 ± 3.23, (n = 3)	-	47.7 ± 3.23, (n = 3)
4.	$\mathbf{d_4}$	43.4, (n = 1)	-	43.4, (n = 1)
5.	$\mathbf{d_5}$	56.7 ± 6.62, (n = 3)	-	56.7 ± 6, (n = 3)
6.	$\mathbf{d_6}$	57.0, (n = 1)	-	57.0, (n = 1)
7.	$\mathbf{d_7}$	33.7 ± 2.38, (n = 4)	-	33.7 ± 2.38, (n = 4)
8.	$\mathbf{d_8}$	70.9 ± 1.63, (n = 3)	-	70.9 ± 1.63, (n = 3)
9.	$\mathbf{d_9}$	20.4, (n = 1)	-	20.4, (n = 1)
10.	$\mathbf{d_{10}}$	15.6, (n = 1)	-	15.6, (n = 1)
11.	$\mathbf{d_{11}}$	47.3 ± 3.11, (n = 2)	-	47.3 ± 2.28, (n = 2)
12.	$\mathbf{d_{12}}$	59.5 ± 2.28, (n = 8)	-	59.5 ± 2.28, (n = 8)
13.	$\mathbf{d_{13}}$	55.5, (n = 1)	-	55.5, (n = 1)
14.	$\mathbf{d_{14}}$	44.0, (n = 1)	-	44.0, (n = 1)
15.	$\mathbf{d_{15}}$	30.5, (n = 1)	-	30.5, (n = 1)
16.	$\mathbf{d_{16}}$	39.8, (n = 1)	-	39.8, (n = 1)
17.	$\mathbf{d_{18}}$	76.0, (n = 1)	-	76.0, (n = 1)

18.	**d_{20}**	72.1, (n = 1)	-	72.1, (n = 1)
17.	**d_{22}**	63.5, (n = 1)	-	63.5, (n = 1)
18.	**f_1**	57.4 ± 0.91, (n = 2)	58.0, (n = 1)	33.3, (n = 1)
19.	**f_3**	47.7 ± 3.23, (n = 3)	58.0, (n = 1)	27.7, (n = 1)
20.	**f_4**	47.3 ± 2.28, (n = 2)	85.9 ± 15.56, (n = 2)	40.6 ± 7.37, (n = 2)
21.	**f_5**	59.5 ± 2.28, (n = 8)	89.3, (n = 1)	53.1, (n = 1)
22.	**f_6**	59.5 ± 2.28, (n = 8)	77.5 ± 24.81, (n = 2)	46.7 ± 14.98, (n = 2)
23.	**f_7**	59.5 ± 2.28, (n = 8)	84.9 ± 0.71, (n = 2)	51.2 ± 0.43, (n = 2)
24.	**f_8**	47.3 ± 2.28, (n = 2)	82.0, (n = 1)	38.8, (n = 1)
25.	**f_9**	47.7 ± 3.23, (n = 3)	54.3 ± 1.03, (n = 2)	25.9 ± 0.49, (n = 2)
26.	**f_{10}**	55.2, (n = 1)	66.3 ± 4.94, (n = 2)	36.6 ± 2.72, (n = 2)
27.	**f_{11}**	42.0, (n = 1)	91.1, (n = 1)	38.3, (n = 1)
28.	**f_{12}**	30.5, (n = 1)	80.0, (n = 1)	24.5, (n = 1)
29.	**f_{13}**	47.3 ± 2.28, (n = 2)	57.0, (n = 1)	27.0, (n = 1)
30.	**f_{14}**	57.4 ± 0.91, (n = 2)	91.2, (n = 1)	52.3, (n = 1)
31.	**f_{15}**	59.5 ± 2.28, (n = 8)	85.5, (n = 1)	50.9, (n = 1)
32.	**f_{16}**	57.4 ± 0.91, (n = 2)	77.2, (n = 1)	44.3, (n = 1)
33.	**f_{17}**	30.5, (n = 1)	96.4, (n = 1)	29.4, (n = 1)
34.	**f_{18}**	47.7 ± 3.23, (n = 3)	87.0, (n = 1)	41.4, (n = 1)
35.	**f_{19}**	63.5, (n = 1)	98.3, (n = 1)	62.4, (n = 1)
36.	**f_{20}**	63.5, (n = 1)	95.2, (n = 1)	60.1, (n = 1)
37.	**h_4**	47.3 ± 2.28, (n = 2)	80.0, (n = 1)	37.8, (n = 1)
39.	**h_5**	59.5 ± 2.28, (n = 8)	72.8 ± 13.10, (n = 2)	43.9 ± 7.89, (n = 2)
40.	**h_5**	59.5 ± 2.28, (n = 8)	25.0, (n = 1)	14.9, (n = 1)
41.	**h_6**	59.5 ± 2.28, (n = 8)	63.7 ± 19.30, (n = 2)	38.4 ± 11.66, (n = 2)
42.	**h_{6*}**	59.5 ± 2.28, (n = 8)	88.7, (n = 1)	52.8, (n = 1)
43.	**h_7**	59.5 ± 2.28, (n = 8)	83.9 ± 5.47, (n = 2)	50.6 ± 3.31, (n = 2)
44.	**h_{7°**	59.5 ± 2.28, (n = 8)	53.8, (n = 1)	32.0, (n = 1)
45.	**h_{7*}**	59.5 ± 2.28, (n = 8)	74.1, (n = 1)	44.0, (n = 1)
46.	**h_8**	47.3 ± 2.28, (n = 2)	86.3, (n = 1)	40.8, (n = 1)
47.	**h_9**	47.7 ± 3.23, (n = 3)	79.3, (n = 1)	37.8, (n = 1)
48.	**h_{10}**	55.2, (n = 1)	74.2, (n = 1)	40.9, (n = 1)
49.	**h_{10*}**	55.2, (n = 1)	75.9, (n = 1)	41.9, (n = 1)
50.	**h_{11}**	42.4, (n = 1)	90.0, (n = 1)	37.8, (n = 1)
51.	**h_{12}**	30.5, (n = 1)	75.0, (n = 1)	22.4, (n = 1)
52.	**h_{13}**	47.3 ± 2.28, (n = 2)	80.7, (n = 1)	38.2, (n = 1)
53.	**h_{14}**	57.4 ± 0.91, (n = 2)	86.8, (n = 1)	49.8, (n = 1)

n: number of times the synthesis was carried out.

6.2 Radiochemical yields (RCY)

The RCY reported in **Table 6** are those that resulted from the descriptions provided in **5.3**. The RCY obtained during the optimization were not included in the calculations.

Some tracers, the most notable being **[^{18}F]d_8**, owing to their promising attributes, were more extensively optimized, details of which will be provided in the discussion section **7.2**. For **[^{18}F]d_{10}**, the optimization was

carried out in order to afford a more stable tracer for the biodistribution studies, since the tracer was barely promising. Radiolabeling via ruthenium-mediated radiofluorination (**[^{18}F]d$_2$** and **[^{18}F]d$_4$)** was also not further optimized after the biodistribution studies; the same went for **[^{18}F]f$_8$**. Tracers, which were developed just for the determination of their potency in *in vitro* autoradiography experiments, were also not considerably optimized. This includes such tracers as **[^{18}F]d$_{19}$** and **[^{18}F]d$_{21}$**, both structural isomers of **[^{18}F]d$_6$** and **[^{18}F]d$_8$**, respectively, which followed the same radiolabeling protocols already prepared for their respective isomers without optimization. **[^{18}F]d$_{17}$**, which followed a slightly optimized radiolabeling protocol for **[^{18}F]d$_8$**. The rest of the tracers obtained via one-step radiofluorination from the outset gave moderate to high RCY; hence, the radiolabeling conditions were not further optimized.

For the two-step radiolabeling, the conditions for **[^{18}F]f$_5$** were considerably optimized. This was done to afford enough RCY for further experiments since its synthesis takes nearly two half-lives of fluorine-18 (110 min). It was also not possible to start with a high amount of radioactivity to lower the risk of radioactive contamination, since radiosyntheses were done manually. For the carbon-11 radiolabeling, less optimization was needed; experience from the two-step radiofluorination was readily applied to moderate to high RCY.

The RCY of the [^{18}F]fluoroalkylated/PEGylated pyrimidinol tracers that bear the [1,3]dioxolo[4,5-b]pyridine ring, such as **[^{18}F]f$_4$**, **[^{18}F]f$_8$**, **[^{18}F]f$_{13}$**, and **[^{11}C]f$_{16}$** were affected by their interaction with the sorbent in the C-18 HPLC column at a basic pH. This resulted in the tailing of peaks and consequently led to a lower RCY. This could be improved by carefully adjusting the pH of the eluent(s), since very acidic pH was also largely unsuccessful. Recovery of these tracers after fixation in the Sep-Pak C18 Classic Cartridge with ethanol was also difficult, especially for **[^{18}F]f$_{13}$**. Up to 35% of the tracer was always retained in the cartridge; using 2 mL of absolute ethanol did not improve the outcome.

Table 6. Radiochemical yield (RCY)

Tracer	**One-step radiofluorination, [%]**			**Two-step radiofluorination, [%]**	
	Ru-mediated S_NAr	**Hal-mediated S_NAr**	**Hal/tosylate-mediated S_N2**	**First step[c]**	**Second step**
[^{18}F]d$_2$	13.8 ± 1.0, (n = 9)	-	-	-	-
[^{18}F]d$_4$	14.5 ± 2.8, (n = 3)	-	-	-	-
[^{18}F]d$_6$	-	24.7 ± 7.4, (n = 9)	-	-	-
[^{18}F]d$_8$	-	17.8 ± 3.9, (n = 9)	-	-	-
[^{18}F]d$_{10}$	-	8.6 ± 0.8, (n = 3)	-	-	-
[^{18}F]d$_{17}$	-	5.0 ± 0.7, (n = 2)	-	-	-
[^{18}F]d$_{19}$	-	6.1[d],	-	-	-

		(n = 1)			
[^{18}F]d$_{21}$	-	7.0 [b], (n = 1)	-	-	-
[^{18}F]f$_4$	-	-	42.4 ± 11.7, (n = 2)	58.8 ± 8.7, (n = 17)	10.4, (n = 1)
[^{18}F]f$_5$	-	-	50.4 ± 17.7, (n = 3)	58.8 ± 8.7, (n = 17)	15.8 ± 3.7, (n = 4)
[^{18}F]f$_6$	-	-	37.4 ± 9.28 [a], (n = 6) 34.4 ± 7.50 [b], (n = 2) [1]	56.7 ± 6.81, (n =3)	12.8 ± 4.04, (n = 2)
[^{18}F]f$_7$	-	-	24.9 ± 15.83 [a], (n = 3) 34.7 ± 8.60 [b], (n = 3)	52.6 ± 2.01, (n = 2)	32.8, (n = 1)
[^{18}F]f$_8$	-	-	22.4 ± 3.17, (n = 2)	-	-
[^{18}F]f$_9$	-	-	30.8 ± 8.75, (n= 3)	56.7 ± 6.81, (n = 3)	37.5, (n = 1)
[^{18}F]f$_{10}$	-	-	36.7 ± 17.00 [a], (n = 2) 32.7 ± 1.86 [b] (n = 2)	52.6 ± 2.01, (n = 2)	34.8, (n = 1)
[^{18}F]f$_{11}$	-	-	19.6 ± 0.79, (n = 2)	-	-
[^{18}F]f$_{12}$	-	-	19.1, (n =1)	-	-
[^{18}F]f$_{13}$	-	-	25.3, (n =1)	-	-
[^{18}F]f$_{14}$	-	-	28.6, (n =1)	-	-
[^{11}C]f$_{15}$	-	-	-	-	26.7 ± 1.60, (n = 3)
[^{11}C]f$_{16}$	-	-	-	-	19.0 ± 9.28 [e], (n = 3)
[^{11}C]f$_{17}$	-	-	-	-	72.4, (n = 1)
[^{11}C]f$_{18}$	-	-	-	-	67.0, (n = 1)

Ru: Ruthenium. **Hal:** halogen. [a] via the tosylate LG. [b] via the I-LG. [c] the results of the first step were calculated based on all the synthesis done with the corresponding glycol ditosylate. [d] RCY was up to 13.8% when the **[^{18}F]d$_{19}$** retained in the column was washed out [e] RCY improved with optimized SHP. n: number of times synthesis was carried out. [1] radiolabeling with only 1 mg of precursor. The RCY of [^{11}C]CH_3I was 41.6−49.3% (decay-corrected); the calculation of the RCY of the carbon-11 labeled tracers was based on this RCY.

6.3 Molar activity (A_m)

As with the RCY, the molar activities (A_m) reported in **Table 7** were those that resulted from the descriptions provided in **5.3.** The A_m of the DABTAs were moderate to high. The lowest consistent A_m was observed in **[^{18}F]f$_{10}$**, and was expected owing to the presence of fluorine-19 in its precursor (**d$_{13}$**). Due to the importance

of high A_m in the in vivo imaging of α-syn, efforts will be made in the future to improve the A_m of the eventual lead DABTAs.

Table 7. Molar activity (A_m) obtained via different LGs

Tracer	One-step radiofluorination, [GBq/µmol]			Two-step radiolabeling, [GBq/µmol]
	Ru-mediated S_NAr	Hal-mediated S_NAr	Hal/tosylate-mediated S_N2	Second step
[^{18}F]d$_2$	85.9 ± 22.6, (n = 3)	-	-	-
[^{18}F]d$_4$	145.9 ± 37.3, (n = 3)	-	-	-
[^{18}F]d$_6$	-	65.8 ± 19.1, (n = 6)	-	-
[^{18}F]d$_8$	-	58.5 ± 24.0, (n = 13)	-	-
[^{18}F]d$_{10}$	-	ND	-	-
[^{18}F]d$_{17}$	-	ND	-	-
[^{18}F]d$_{19}$	-	ND	-	-
[^{18}F]d$_{21}$	-	ND	-	-
[^{18}F]f$_4$	-	-	30.2 [a]	ND
[^{18}F]f$_5$	-	-	69.5 ± 11.9, (n = 4)	113.8 ± 63.2, (n = 2)
[^{18}F]f$_6$	-	-	59.9 ± 81.9, (n = 6) 20.2 ± 2.2 [b] (n = 2)	56.4 [a]
[^{18}F]f$_7$	-	-	25.3 ± 8.5 [c], (n = 3) 27.8 ± 8.1 [d], (n = 2)	100 [a]
[^{18}F]f$_8$	-	-	10.9 ± 12.0, (n = 2)	-
[^{18}F]f$_9$	-	-	56.3 ± 8.4, (n = 2)	70.8 [a]
[^{18}F]f$_{10}$	-	-	31.5 ± 20.1, (n = 2) 16.5 ± 3.1, (n = 2)	71.3 [a]
[^{18}F]f$_{11}$	-	-	32.0 ± 30.0, (n = 2)	-
[^{18}F]f$_{12}$	-	-	28.9 [a]	-
[^{18}F]f$_{13}$	-	-	23.5 [a]	-
[^{18}F]f$_{14}$	-	-	61.4 [a]	-
[^{11}C]f$_{15}$	-	-	-	131.6 ± 32.8, (n = 3)
[^{11}C]f$_{16}$	-	-	-	52.5 [a]
[^{11}C]f$_{17}$	-	-	-	107.8 [a]
[^{11}C]f$_{18}$	-	-	-	85.7 [a]

Ru: Ruthenium. **Hal:** halogen. **ND**: not determined. [a] determined only once. [b] 1 mg of $\mathbf{h_{7*}}$ used for radiosynthesis, [c] via the tosylate LG. [d] via the I-LG. n: number of times A_m was determined.

6.4 In vitro experiments

6.4.1 Binding assays, log D and free plasma fraction

As expected of good brain tracers, all the DABTA tracers were lipophilic, with log D between 3.1 and 2.0. As also expected, the tracers with the [1,3]dioxolo[4,5-b]pyridine ring were less lipophilic than their benzodioxole-ring-bearing counterparts **Table 8**: **[^{18}F]$\mathbf{d_4}$/[^{18}F]$\mathbf{d_2}$**, **[^{18}F]$\mathbf{d_8}$/[^{18}F]$\mathbf{d_6}$**, **[^{18}F]$\mathbf{d_{21}}$/[^{18}F]$\mathbf{d_{19}}$**, **[^{18}F]$\mathbf{f_4}$/[^{18}F]$\mathbf{f_5}$**, **[^{18}F]$\mathbf{f_8}$/[^{18}F]$\mathbf{f_6}$**, **[^{18}F]$\mathbf{f_{13}}$/[^{18}F]$\mathbf{f_7}$**, and **[^{11}C]$\mathbf{f_{15}}$/[^{11}C]$\mathbf{f_{16}}$**. Being dependent on lipophilicity, the free plasma fraction (*fp*) of the tracers correlated with their log D; the more lipophilic the tracer, the lower the *fp* **Table 8**. However, the presence of some functional groups, such as the methoxy group as in **[^{18}F]$\mathbf{d_2}$**, may reduce the affinity of the tracers for blood protein **Table 8**, since the log D values of **[^{18}F]$\mathbf{d_2}$** and **[^{18}F]$\mathbf{f_5}$** quite similar. Additionally, the tracers showed 100% stability in plasma at 30, 60, 90, and 120 min. Since the chromatograms of all the tracers looked the same in this experiment, only exemplary chromatograms were shown **Figure 22**.

Apparently, the presence of [1,3]dioxolo[4,5-b]pyridine improved affinity to α-syn as well as selectivity in most cases (**Table 8**, **Figure 20** and **Figure 21**). The only tracer with subnanomolar affinity to α-syn without a [1,3]dioxolo[4,5-b]pyridine ring was **[^{18}F]$\mathbf{f_6}$**, a finding that indicates the potential influence of the fluoroethylethoxy functional group it contains. Owing to their low solubility in the incubation buffer, binding assays with $\mathbf{f_8}$ and $\mathbf{f_{16}}$ were nearly impossible. In the case of the former, at least its affinity to α-syn was determined, but for the latter, this was not possible.

Table 8. In vitro properties of the DABTAs

Tracer	log D	*fp*, [%]	K_i, [nM]			Selectivity	
			α-syn	Aβ	tau	Aβ/α-syn	tau/α-syn
[^{18}F]$\mathbf{d_2}$	3.2 ± 0.09	0.25 ± 0.01	1.22*	241.7*	>1000*	198.0	>1000
[^{18}F]$\mathbf{d_4}$	3.0 ± 0.04	0.45 ± 0.03	0.66*	275.3*	>1000*	417.0	>1000
[^{18}F]$\mathbf{d_6}$	2.8 ± 0.09	0.14 ± 0.02	1.21*	237.2*	966*	196.0	798.0
[^{18}F]$\mathbf{d_8}$	2.6 ± 0.09	0.85 ± 0.02	0.10*	386.3*	>1000*	3863.0	>1000
[^{18}F]$\mathbf{d_{10}}$	2.3 ± 0.14	ND	1.36*	406.8*	>1000*	299.1	>735.3
[^{18}F]$\mathbf{d_{17}}$	2.3 ± 0.03	ND	ND	ND	ND	ND	ND
[^{18}F]$\mathbf{d_{19}}$	2.8 ± 0.08	ND	ND	ND	ND	ND	ND
[^{18}F]$\mathbf{d_{21}}$	2.7 ± 0.05	ND	ND	ND	ND	ND	ND
[^{18}F]$\mathbf{f_4}$	2.7 ± 0.08	1.18 ± 0.02	0.99*	250.6*	464.9*	253.1	469.6
[^{18}F]$\mathbf{f_5}$	3.0 ± 0.09	0.06 ± 0.01	2.27*	133.7*	515.2*	58.9	227.0
[^{18}F]$\mathbf{f_6}$	2.5 ± 0.05	0.17 ± 0.02	0.50*	197.8*	437.2*	397.2	877.9

[^{18}F]f$_7$	2.7 ± 0.09	0.11 ± 0.03	1.17 1.51*	76.4 ND	242.1 ND	65.3 ND	206.9 ND
[^{18}F]f$_8$	2.5 ± 0.04	0.90 ± 0.04	2.30	ND	ND	ND	ND
^{a}[^{18}F]f$_9$	2.7 ± 0.07	0.36 ± 0.01	0.96 0.84*	47.6 ND	1130 ND	51.2 ND	1215.1 ND
[^{18}F]f$_{10}$	2.8 ± 0.04	0.33 ± 0.02	0.93 1.00*	37.3 ND	615.0 ND	40.1 ND	661.3 ND
[^{18}F]f$_{11}$	3.2 ± 0.04	0.05 ± 0.01	3.71	99.6	498.7	26.8	134.4
[^{18}F]f$_{12}$	2.7 ± 0.04	0.24 ± 0.07	0.92	38.7	983.0	42.1	1068.5
[^{18}F]f$_{13}$	2.2 ± 0.03	0.94 ± 0.08	0.38	46.6	120.0	122.6	315.8
[^{18}F]f$_{14}$	2.8 ± 0.03	0.34 ± 0.06	1.74	210.2	662.2	120.8	380.6
[^{11}C]f$_{15}$	3.1 ± 0.04	ND	2.45	59.3	707	24.0	288.6
^{a}[^{11}C]f$_{16}$	2.0 ± 0.05	ND	ND	ND	ND	ND	ND
[^{11}C]f$_{17}$	3.1 ± 0.02	0.35 ± 0.06	2.45	59.3	707.0	24.0	288.6
^{a}[^{11}C]f$_{18}$	3.0 ± 0.05	ND	4.99	ND	ND	ND	ND
[^{11}C]f$_{19}$	ND	ND	1.35	148.7	671.3	110.1	497.2
[^{18}F]f$_{20}$	ND	ND	1.31	221.2	814.6	170.2	621.8
[^{124}I]h$_{13}$	ND	ND	1.17	ND	ND	ND	ND

NB, the cold version of the tracers were used for the competitive binding experiments. *fp* free plasma fraction. *[^{3}H]DCVJ was used; otherwise [^{3}H]PiB was used. **^{a}** Low solubility prevented further experiments with Aβ and tau fibrils and in the case of **f$_{16}$** for α-syn as well.

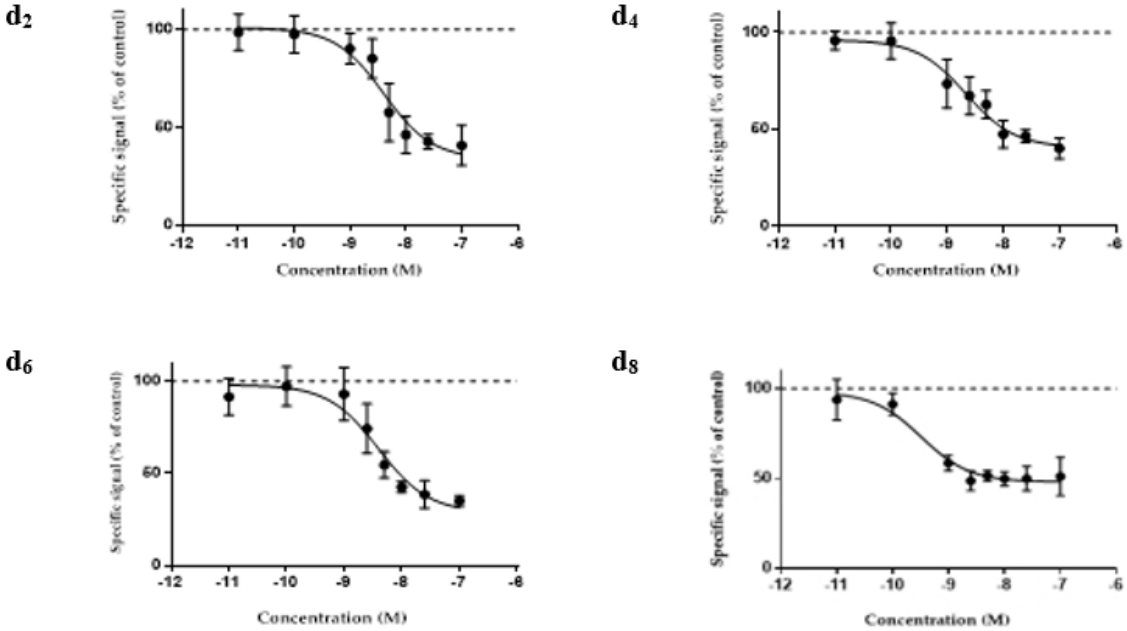

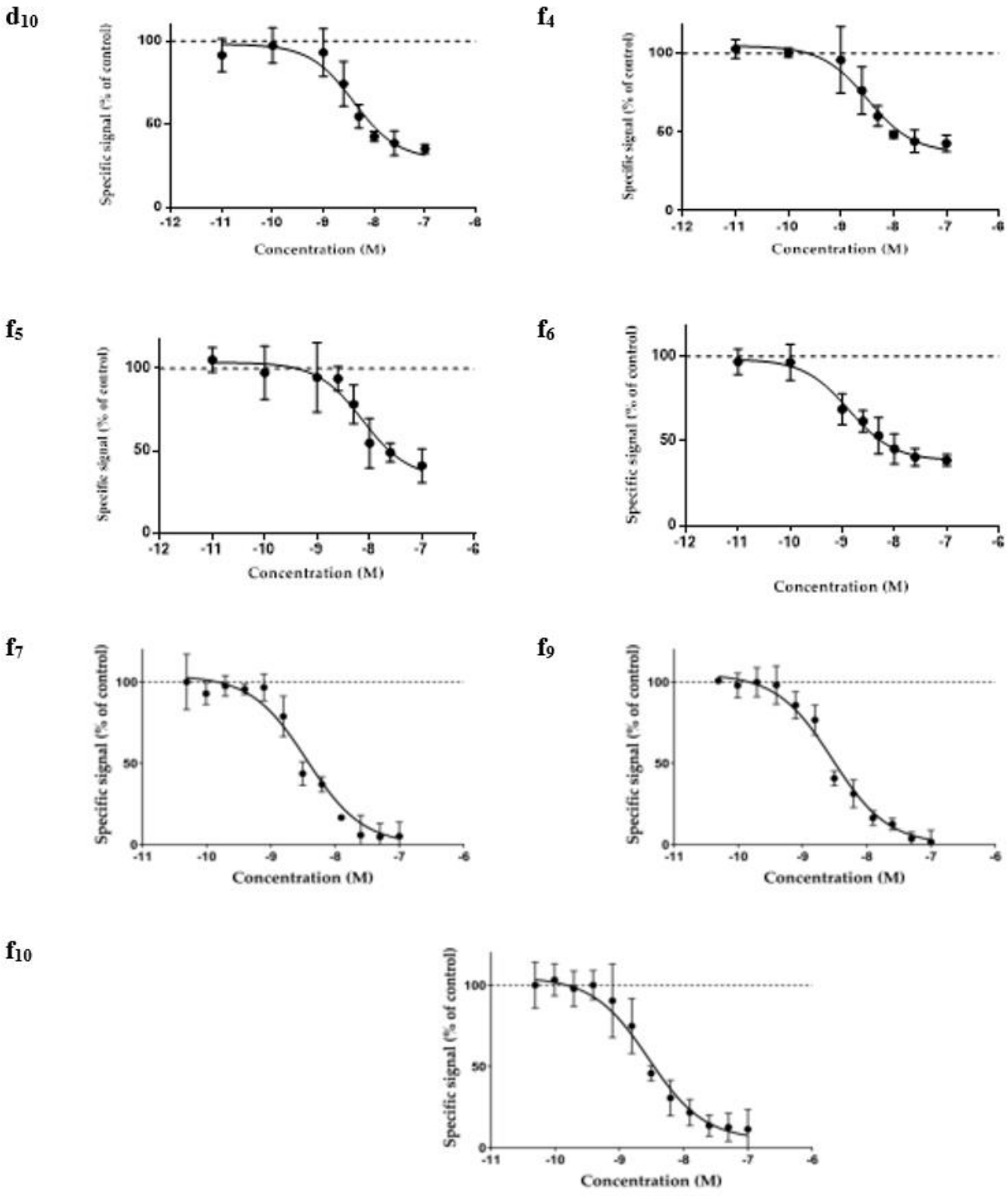

Figure 20a. α-Syn displacement binding curves of standard compounds of DABTAs against [^{3}H]DCVJ. The standard compounds were used in a concentration from 0.01−100 nM, with a fixed concentration of α-syn (125 nM). [^{3}H]DCVJ was used in fixed concentration of 10 nM.

d_2

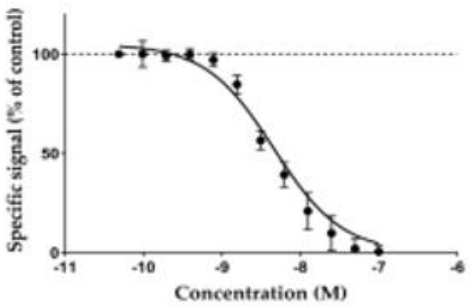

d_4

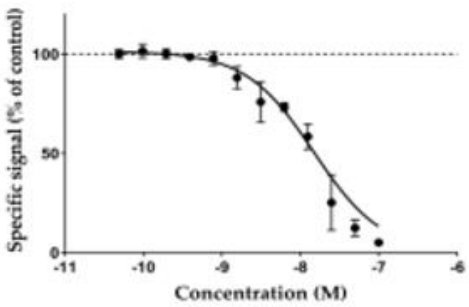

d_6

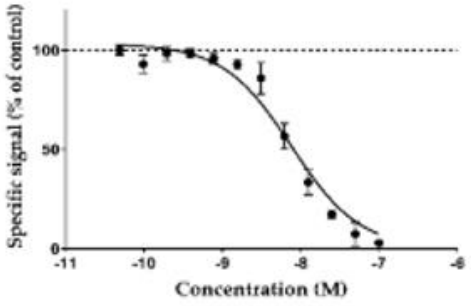

d_8

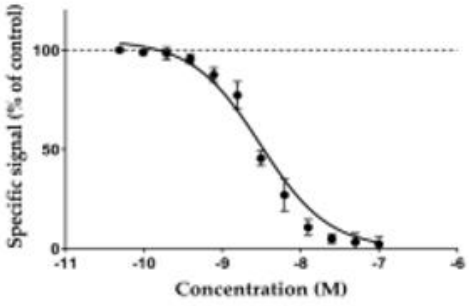

d_{10}

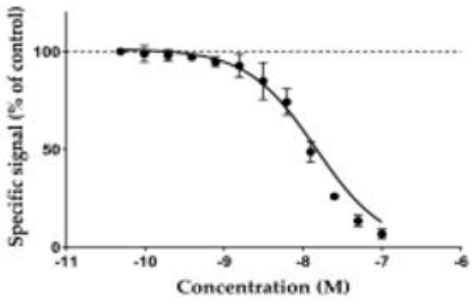

f_4

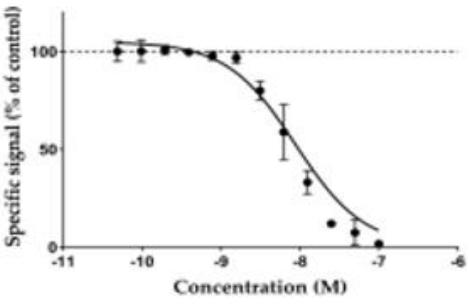

f_5

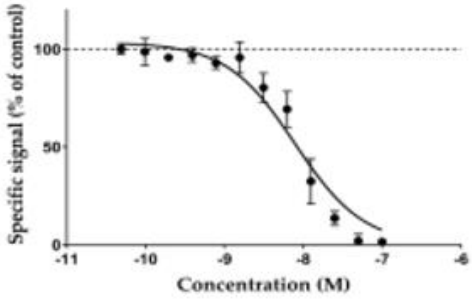

f_6

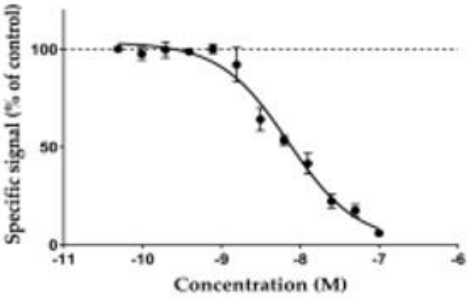

f_7

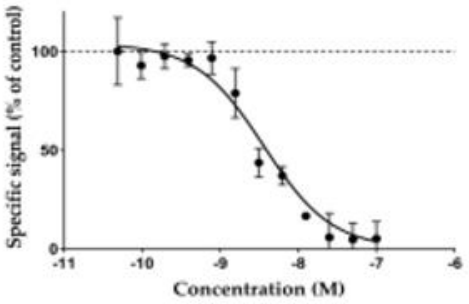

f_8

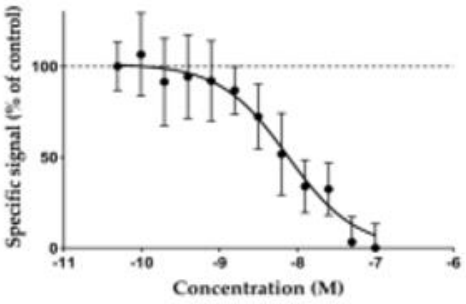

f_9

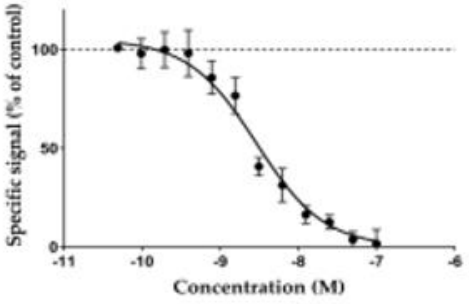

f_{10}

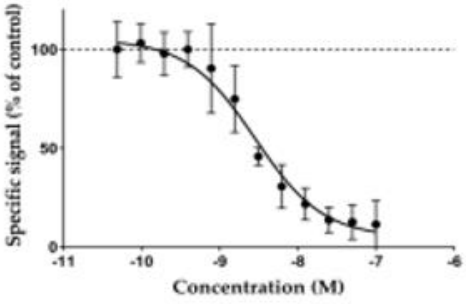

f_{11}

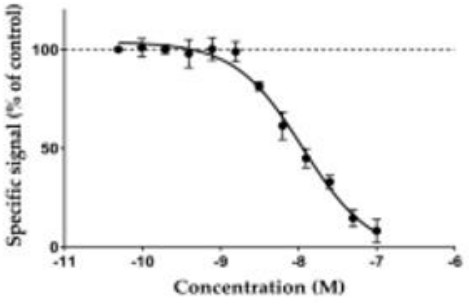

f_{12}

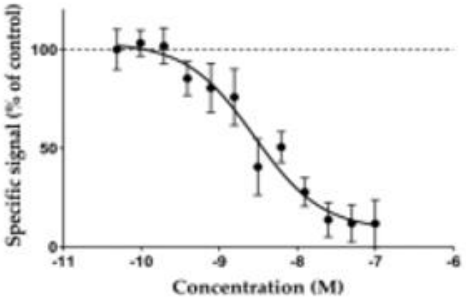

f_{13}

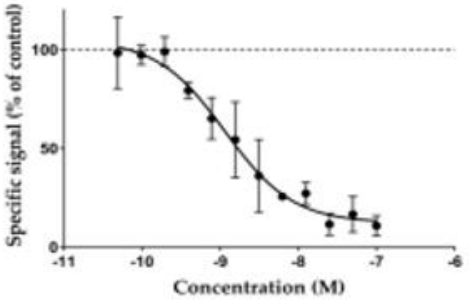

f_{14}

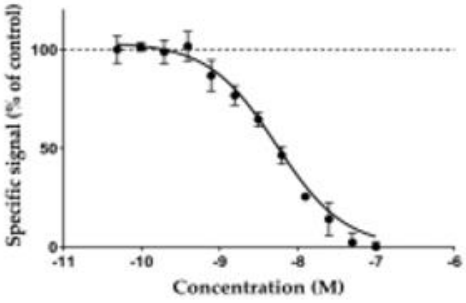

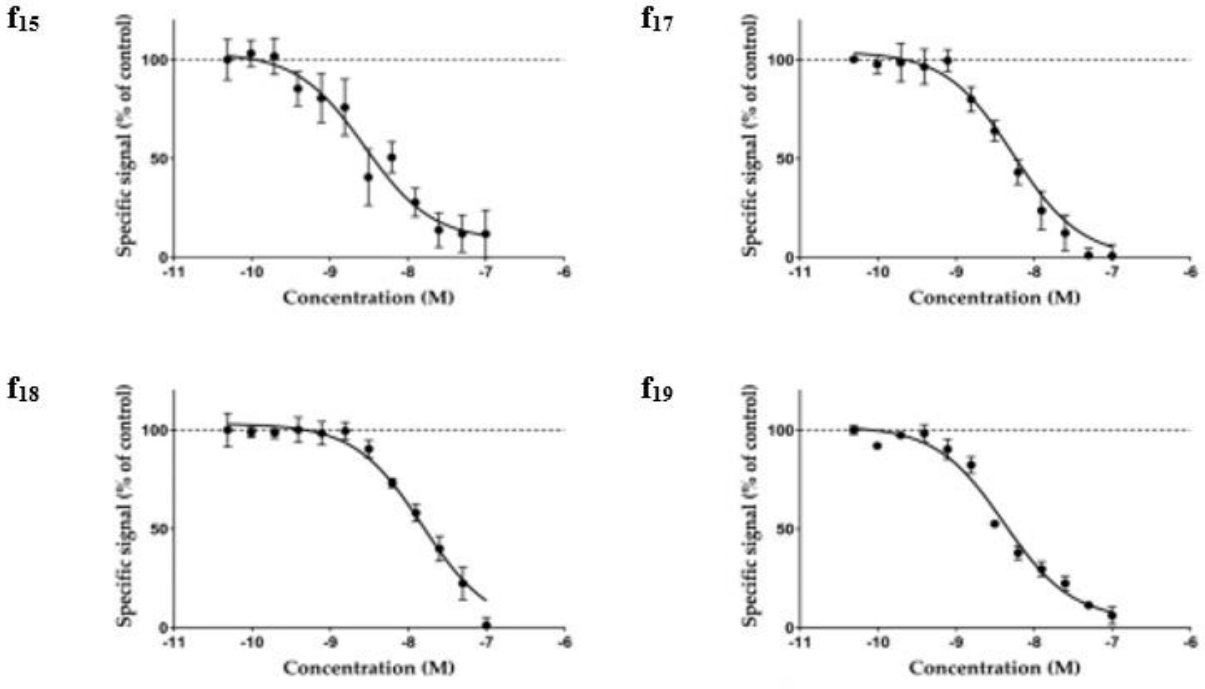

Figure 20b. α-Syn displacement binding curves of standard compounds of DABTAs against [^{3}H]PiB.
The standard compounds were used in a concentration from 0.01−100 nM, with a fixed concentration of α-syn (125 nM). [^{3}H]PiB were also used in fixed concentration of 10 nM.

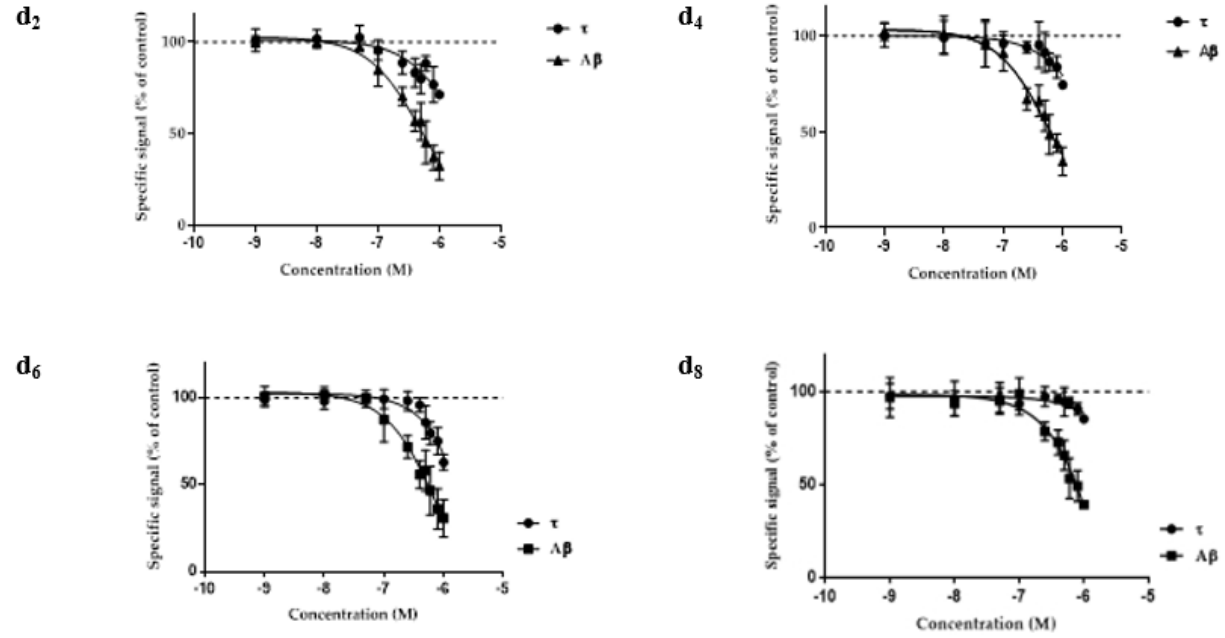

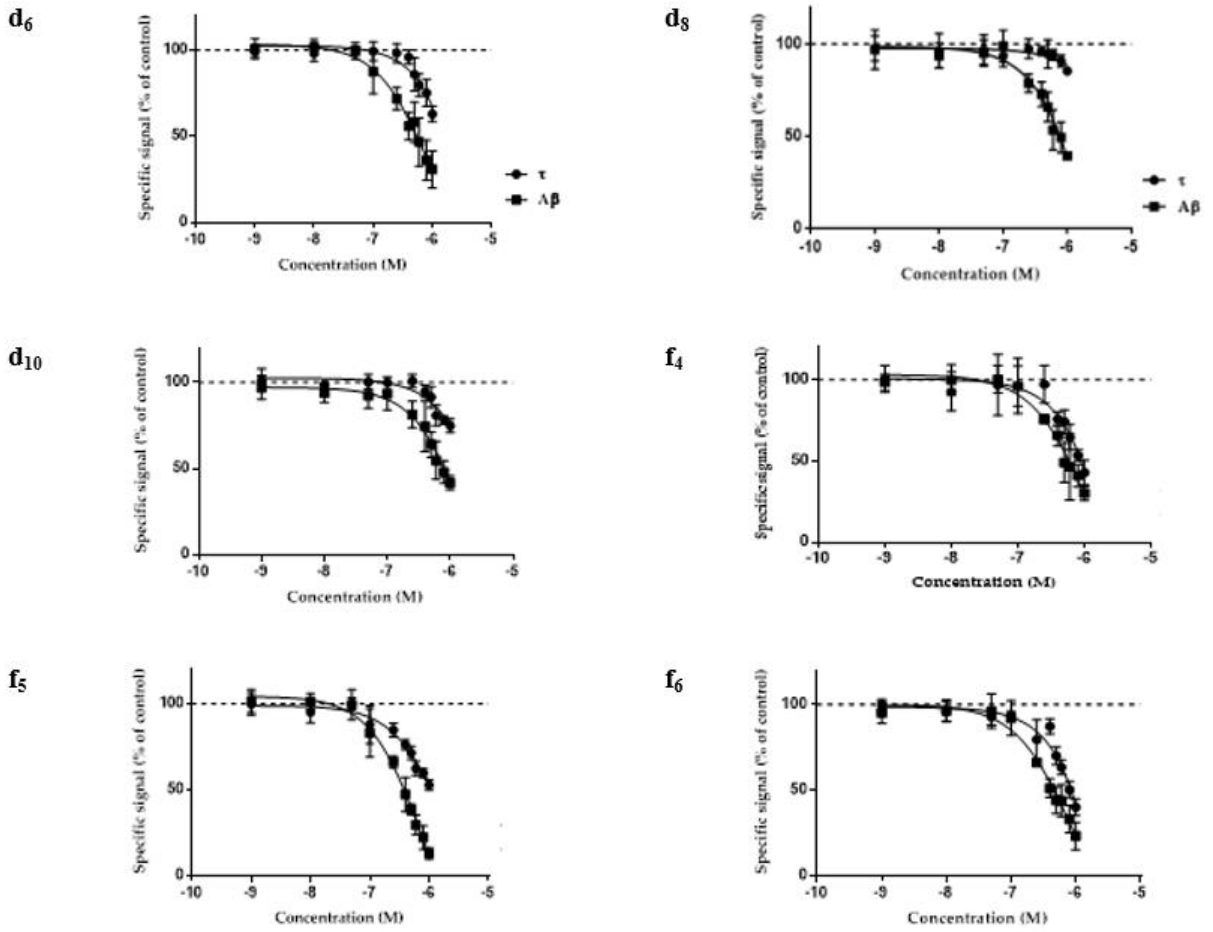

Figure 21a. Aβ and tau displacement binding curves of standard compounds of DABTAs against [^{3}H]DCVJ. The standard compounds were used in a concentration from 1−1000 nM, with a fixed concentration of $A\beta_{1-42}$ and tau (125 nM). 10 nM and 20 nM of [^{3}H]DCVJ was used in a fixed concentration for the determination of affinity against $A\beta_{1-42}$ and tau respectively.

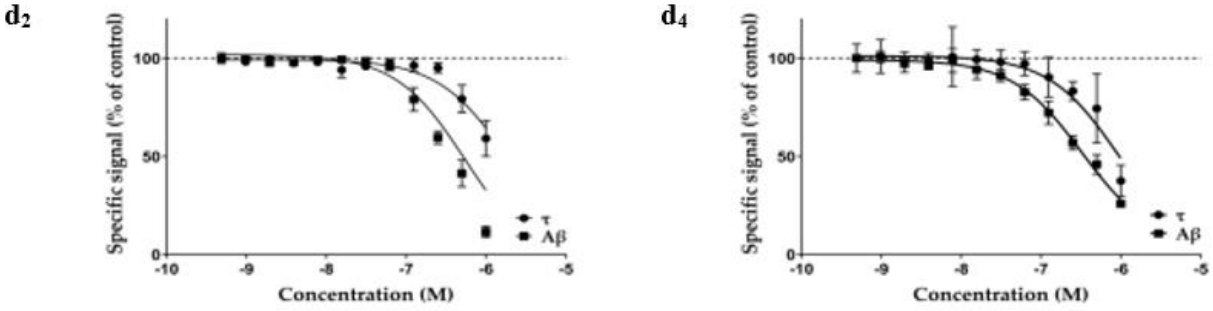

d_6

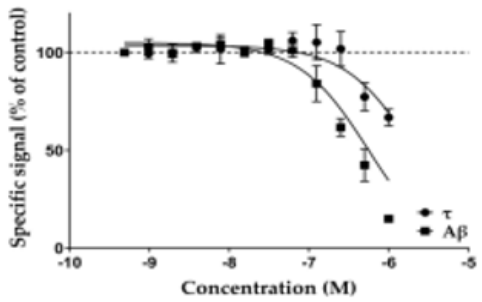

d_8

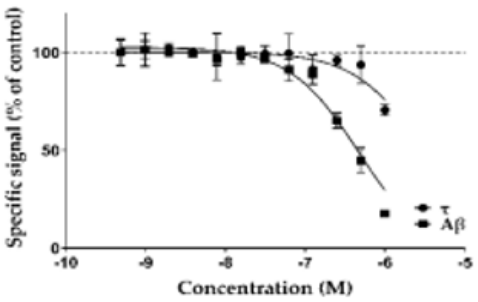

d_{10}

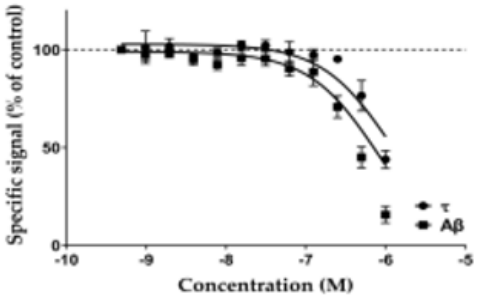

f_4

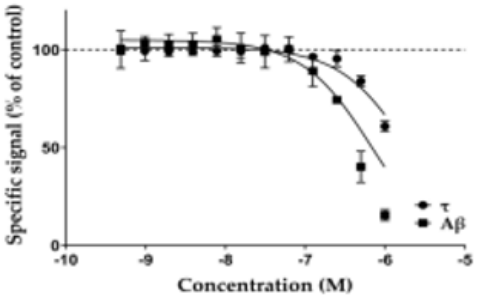

f_5

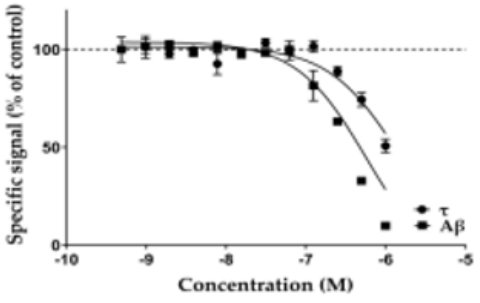

f_6

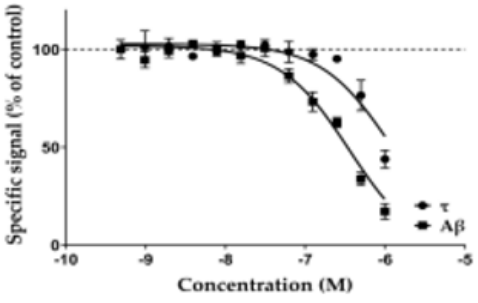

f_7

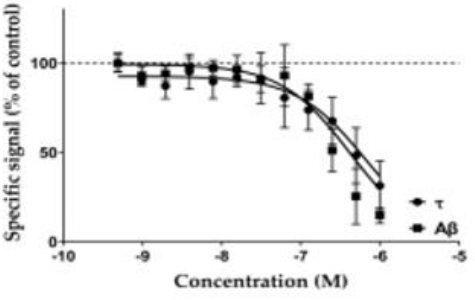

f_9

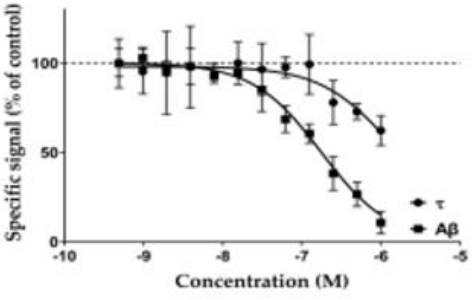

f_{10}

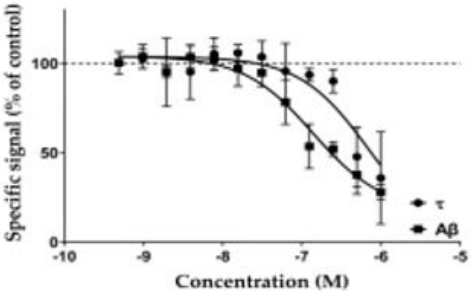

f_{11}

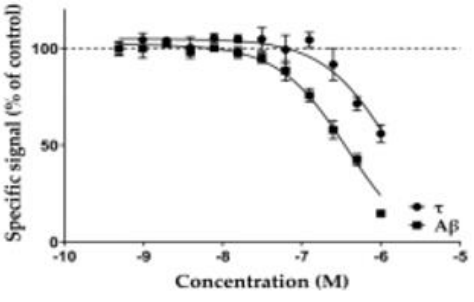

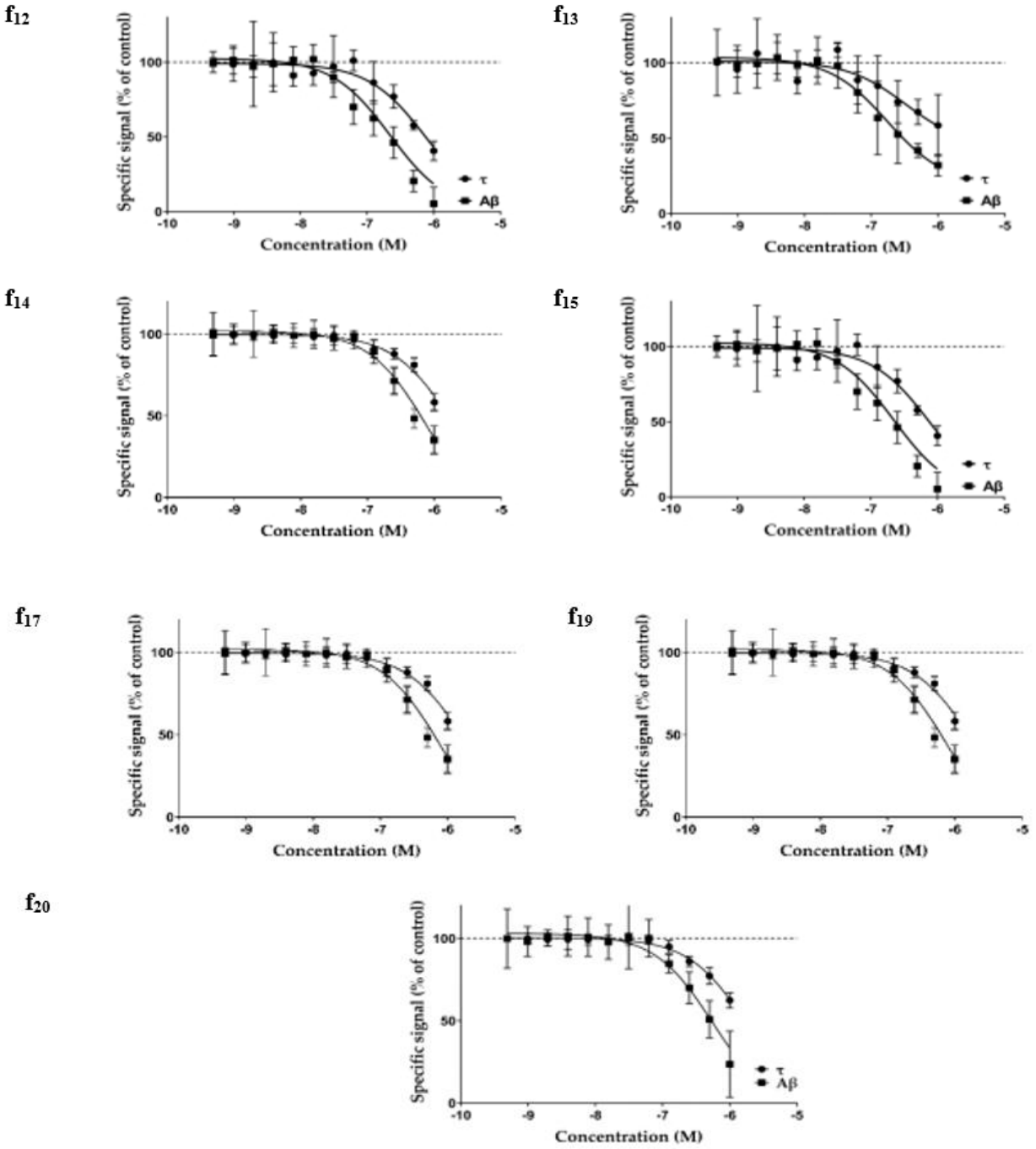

Figure 21b. Tau and Aβ displacement binding curves of standard compounds of DABTAs against [^{3}H]DCVJ and [^{3}H]PiB. The standard compounds were used in a concentration from 1−1000 nM, with a fixed concentration of $A\beta_{1-42}$ and tau (125 nM). 10 nM and 200 nM of [^{3}H]PiB was also used in a fixed concentration for the determination of affinity against $A\beta_{1-42}$ and tau respectively.

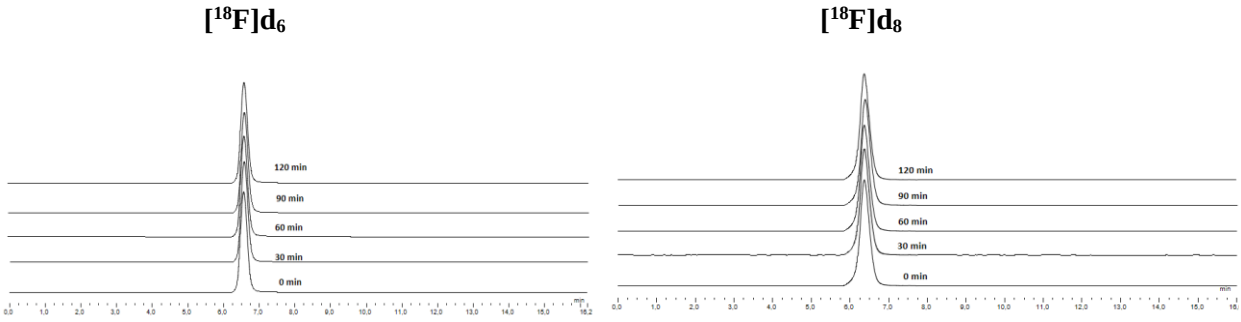

Figure 22. Exemplary plasma stability chromatograms of [^{18}F]d_6 and [^{18}F]d_8. Since all the tracers showed the same results in vitro, only two exemplary chromatograms were presented.

6.4.2 In vitro autoradiography

6.4.2.1 PFF mice brain tissue

Autoradiography experiments conducted on PFF brain tissue showed no signal in the region of injection of the PFF (shown with red circles) **Figure 23** for both **[^{18}F]d_4** and **[^{18}F]d_6**.

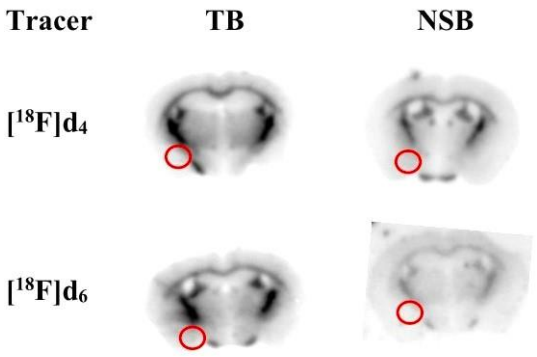

Figure 23. Diagram of the autoradiography experiments with PFF mice brain tissue. The presented autoradiograms are a result of overnight exposure, after incubation of the brain slices with the radiotracers at 1.2 MBq/mL. The red circles indicate the points from which specific signals were expected.

6.4.2.2 Transgenic mice brain tissue

This experiment was carried out only with **[^{18}F]d_8**. This was because the tissues were in short supply and **[^{18}F]d_8** had proven to be the most promising tracer based on its binding affinity **Table 8** and brain pharmacokinetics. **[^{18}F]d_8** unfortunately showed binding only to Aβ **Figure 24**. There were no specific signals from the A53T mice brain tissue compared to the control. The signals seen in the tau brain were apparently from artifacts resulting from tissue breakdown and did not correlate with the known distribution of tau in the brain of the P301S tg mice.

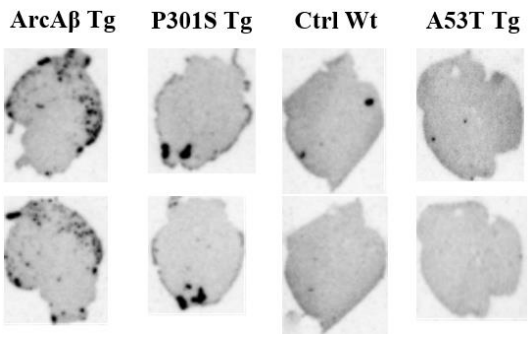

Figure 24. Diagram of the autoradiogram of the autoradiography experiments with transgenic mouse brain tissue. Here is shown areas of specific staining in the ArcAβ mice cortical brain regions of the brain sections with none in the control sections, A53T mice brain sections and P301S brain sections (artifacts located towards the cerebellum) after incubation with 1.2 MBq/mL of **[^{18}F]d$_8$**.

6.4.2.3 Postmortem human brain tissue (PHBT)

All the tracers except [^{18}F]d$_2$ and ^{18}F]d$_{10}$ were tested on diseased PHBT. However, the results for [^{18}F]d$_{19}$ were not shown, since they were visually similar to those of its structural isomer [^{18}F]d$_6$ (**Figure 25a**). The results of [^{11}C]f$_{16}$ were also not displayed, since it showed the same staining properties as [^{18}F]f$_8$.

The tracers were grouped and presented based on their defining characteristics. In **Figure 25a** were shown tracers that bear either only a Csp2–[^{18}F]F bond or were carbon-11 labeled without a fluorine atom in the tracer. In **Figure 25b** were presented the [^{18}F]fluoroalkylated/PEGylated pyrimidinol DABTA derivatives. In **Figure 25c** were displayed the [^{18}F]fluoroPEGylated phenol DABTA derivatives.

Compared to the controls, that is the non-diseased brain regions (middle and superior temporal gyri, amygdala, and hippocampus at the level of cornu ammonis), all the DABTAs stained the GCIs in the MSA PHBT with varying intensities either in the anterior striatum, cerebellar hemisphere with dentate nucleus, pons at level of the locus coeruleus, or basal ganglia at the level of pallidum. However, not all of them stained LBs in the DLB PHBT in the regions of the anterior hippocampus, cingulate gyrus, fusiform cortex, entorhinal cortex, or amygdala. With the exception of [^{18}F]d$_4$ in **Figure 25a**, none of the other tracers in this group showed convincing staining of LBs. Apart from [^{18}F]f$_8$, the most intense staining was observed for the DABTAs in **Figure 25b**, in the fusiform cortex, the entorhinal cortex and amygdala for [^{18}F]f$_7$ and in the cingulate gyrus and neighboring gyrus for the rest of the tracers. The DABTAs in **Figure 25c** also stained LBs but not as intensely as the **Figure 25b** DABTAs, particularly in the cingulate gyrus and neighboring gyrus. Nevertheless, more intense staining was observed in the anterior hippocampus.

None of the tracers showed any staining in the tau PHBT, suggesting specific uptake in the hippocampus at the level of cornu ammonis. Less pronounced staining of Aβ in the β-amyloidopathy-only brain sections

and Alzheimer's disease (AD) were more evident in the tracers which bore the [1,3]dioxolo[4,5-b]pyridine ring, that is, **[^{18}F]f$_4$**, **[^{18}F]f$_8$**, **[^{18}F]f$_9$**, **[^{18}F]f$_{10}$**, **[^{18}F]f$_{12}$**, and **[^{18}F]f$_{13}$** which are collectively referred to as the [1,3]dioxolo[4,5-b]pyridine fluoroethylated/PEGylated (DPFPD) tracers. The same was displayed by the tracers in **Figure 25a** DABTAs (except for [^{18}F]**d$_4$**) regardless of the moiety borne, be it [1,3]dioxolo[4,5-b]pyridine ring or the benzodioxole ring. The benzodioxole fluoroethylated/PEGylated (BFPD) tracers **[^{18}F]f$_5$**, **[^{18}F]f$_6$**, **[^{18}F]f$_7$**, and **[^{18}F]f$_{11}$**, with the exception of **[^{18}F]f$_{14}$**, stained Aβ in the inferior parietal lobules (Aβ only sections) and the occipital striate cortex regions in the AD sections **Figure 25c**.

The images presented in **Figure 25a−c** were unfortunately not devoid of artifacts (black spots), which are not uncommon in paraffinated tissue sections.

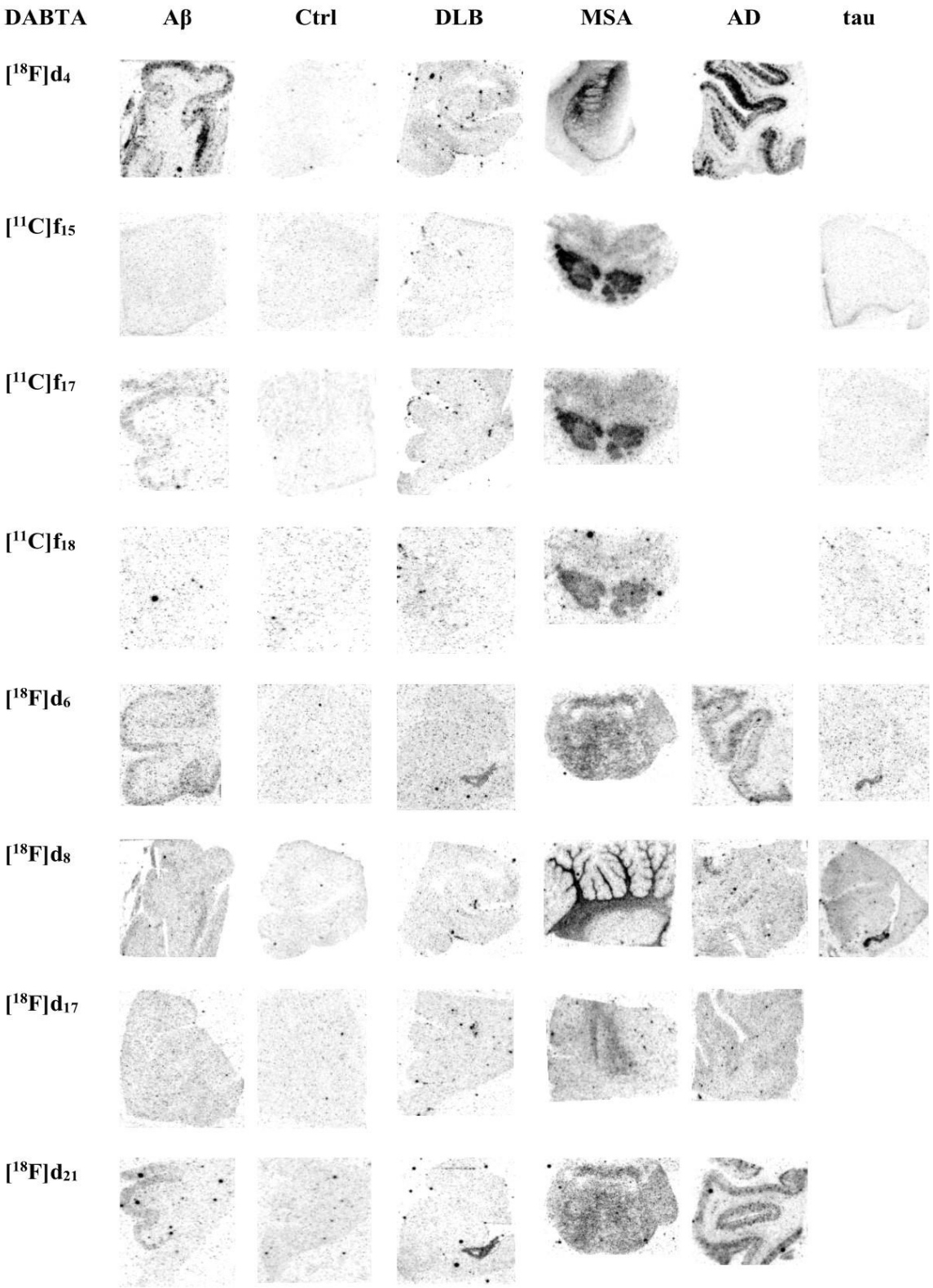

Figure 25a. Diagram of the autoradiogram of autoradiography experiments on PHBT of the carbon-11 labeled DABTAs and DABTAs with Csp2–[^{18}F]F bond. Note: the random bold black spots are artifacts.

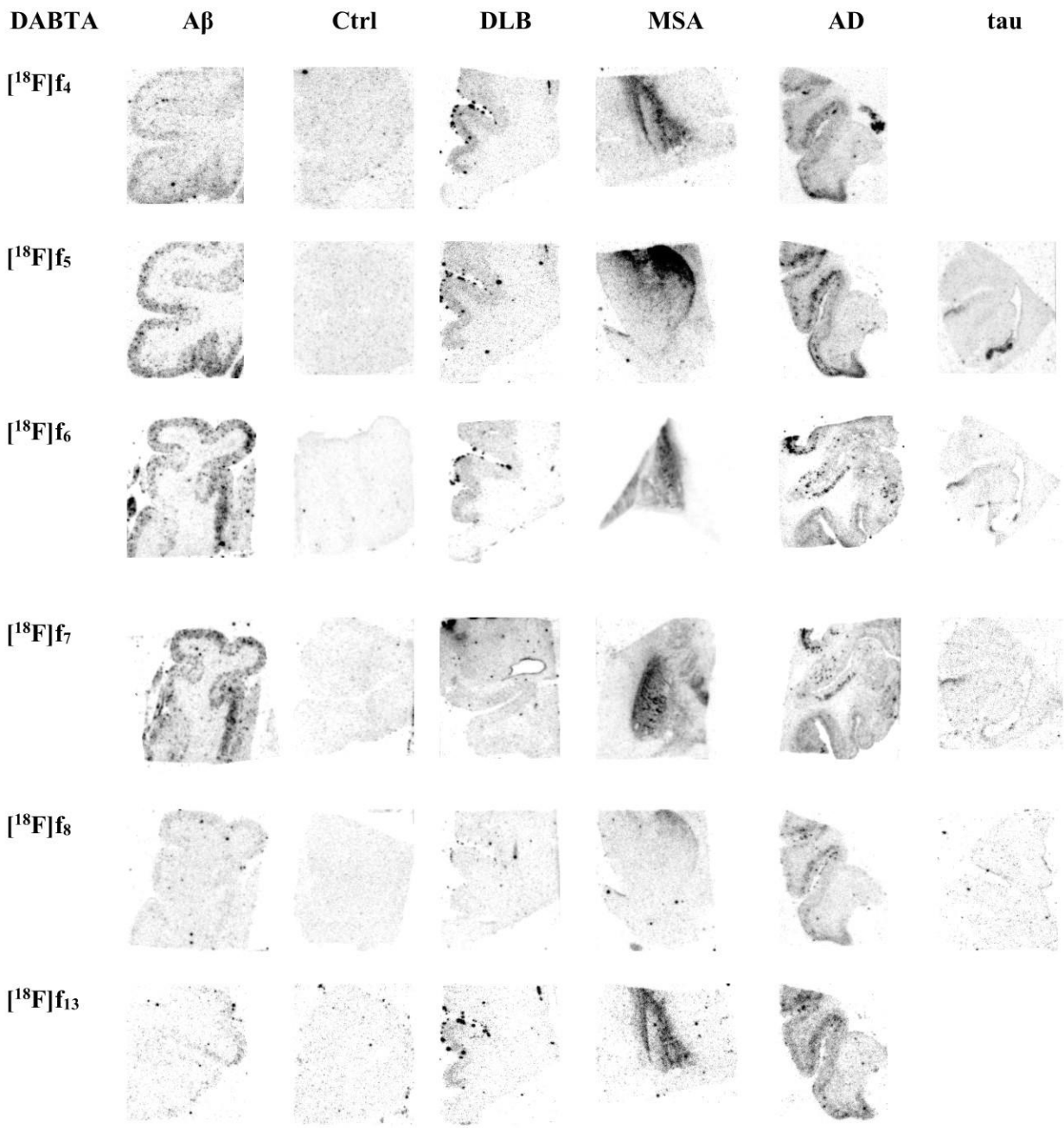

Figure 25b. Diagram of the autoradiogram of autoradiography experiments on postmortem human brain tissues (PHBT) of the [^{18}F]fluoroalkylated/PEGylated pyrimidinol DABTA derivatives. Note: the random bold black spots are artifacts.

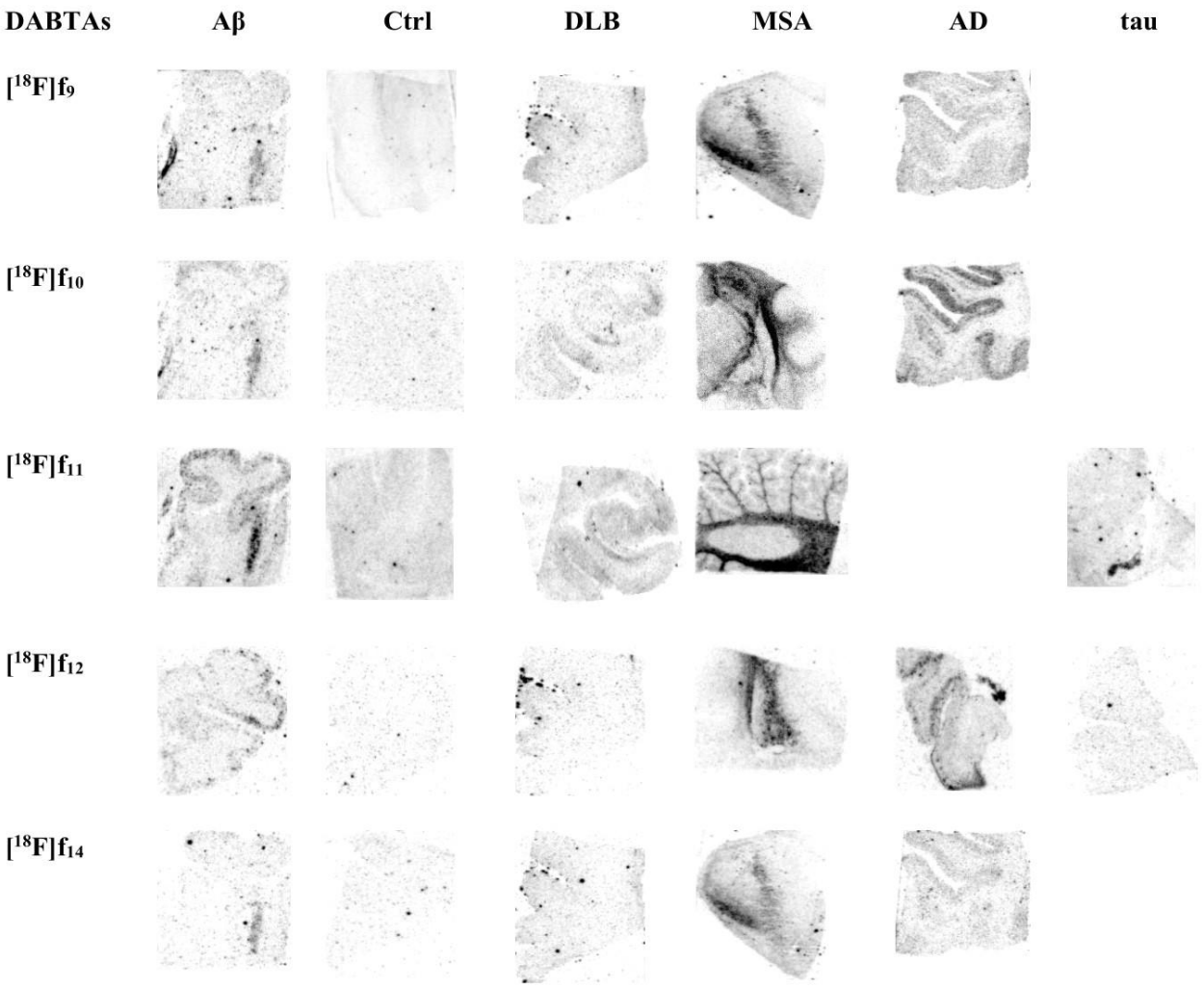

Figure 25c. Diagram of the autoradiogram of autoradiography experiments on postmortem human brain tissues (PHBT) of the [^{18}F]FfluoroPEGylated phenol DABTA derivatives. **Figure 25a-c** show the staining intensity of PHBT with DLB, AD, MSA tau, and β-amyloidopathy compared to the control (Crtl) after incubation with 0.2 MBq/mL of the presented [^{18}F]fluorine-labeled and 0.5 MBq of the [^{11}C]carbon-labeled tracers. Note: the random bold black spots are artifacts.

6.5 Ex vivo experiments

6.5.1 Biodistribution experiments

Biodistribution studies enabled the determination of brain uptake of the tracers (the location of the target α-syn) and the in vivo stability of the tracers **Figure 26**. In vivo stability was indirectly assessed by the bone uptake (compact bone, trabecular bone, and bone marrow) of free [^{18}F]fluoride and radiometabolites such as [^{18}F]fluoroethanol, [^{18}F]fluoroethoxyethanol and [^{18}F]fluorodiethoxyethanol, which result from the metabolism of the fluoroethylated/PEGylated tracers (**[^{18}F]f$_{4\text{-}10}$**). The highest brain uptake was observed with the BFPD tracers (**[^{18}F]f$_{5\text{-}7}$**). Low brain uptake may not only be attributed to low lipophilicity but also to other physicochemical properties, as demonstrated by the tracers **[^{18}F]f$_4$** and **[^{18}F]f$_8$**, which exhibited high pulmonary retention.

Low brain uptake was nonetheless observed with **[^{18}F]d$_2$**, which is one of the most lipophilic tracers listed in **Table 8**. Brain clearance, another important parameter, was also determined in biodistribution studies and improved with decreasing lipophilicity. Good examples include the following pairs: **[^{18}F]d$_8$** > **[^{18}F]d$_6$** and **[^{18}F]f$_7$** > **[^{18}F]f$_6$** > **[^{18}F]f$_5$**.

For **[^{18}F]f$_4$** and **[^{18}F]f$_8$**, the lung uptake was very high, hence these values were not included in their graphs in **Figure 26**, but presented in **Table 9**.

Table 9. The lung uptake of tracers [^{18}F]f$_4$ and [^{18}F]f$_8$

Tracers	5 min	60 min
[^{18}F]f$_4$	63.8 ± 4.6	1.9 ± 0.4
[^{18}F]f$_8$	140.9 ± 72.9	131.6 ± 77.4

[^{18}F]d$_2$

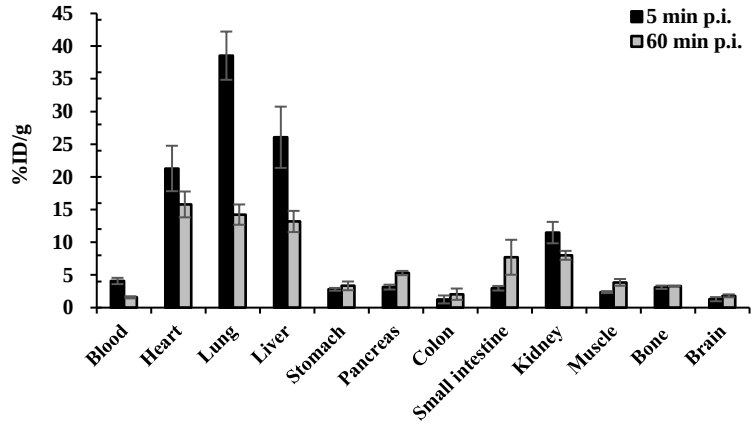

[^{18}F]d$_4$

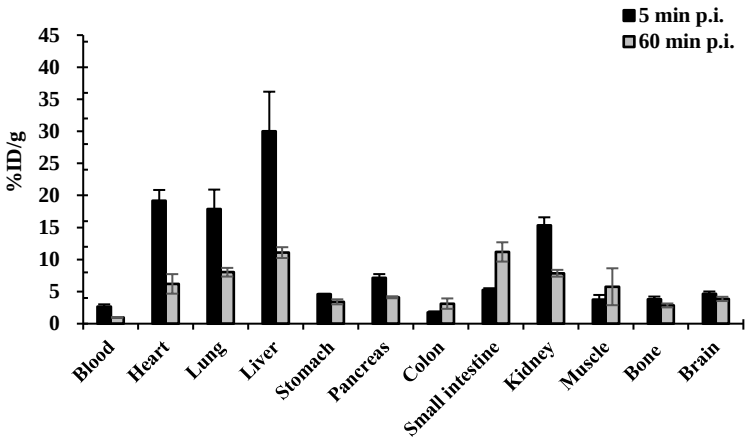

[^{18}F]d$_6$

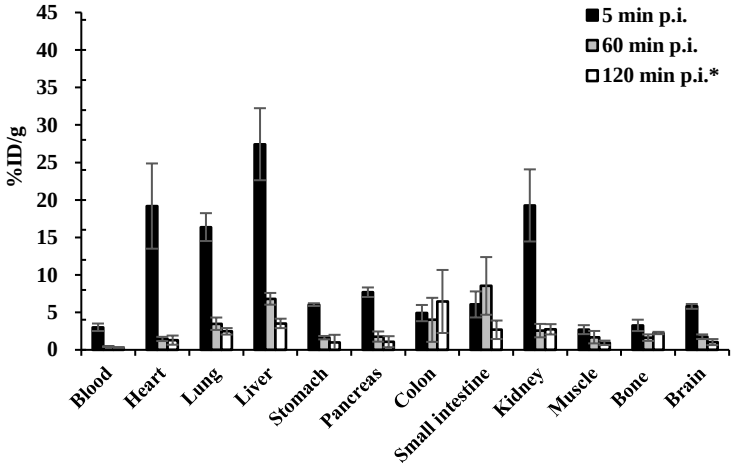

[^{18}F]d$_8$

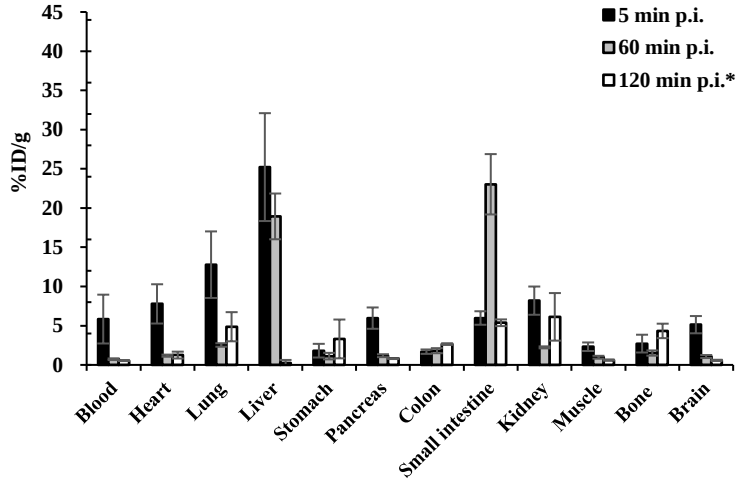

[^{18}F]d_{10}

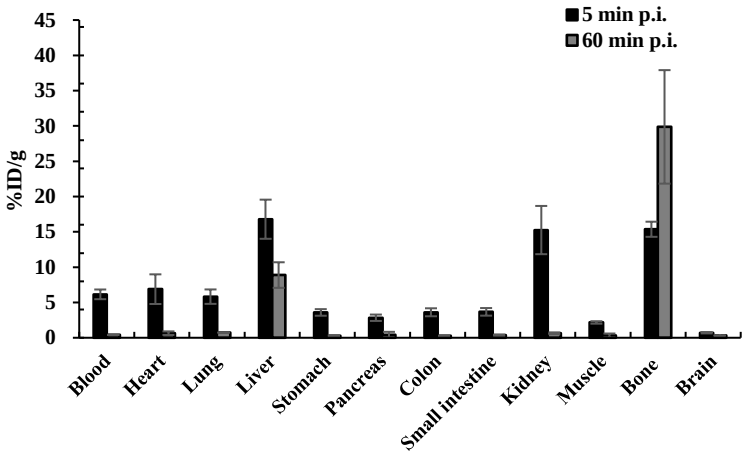

[^{18}F]f_4

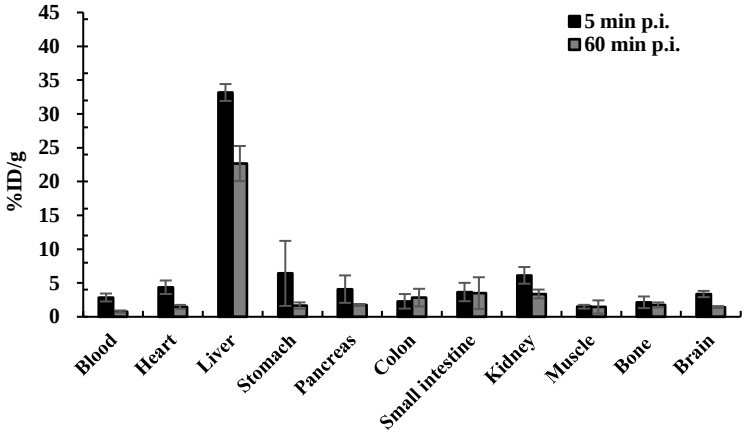

[^{18}F]f_5

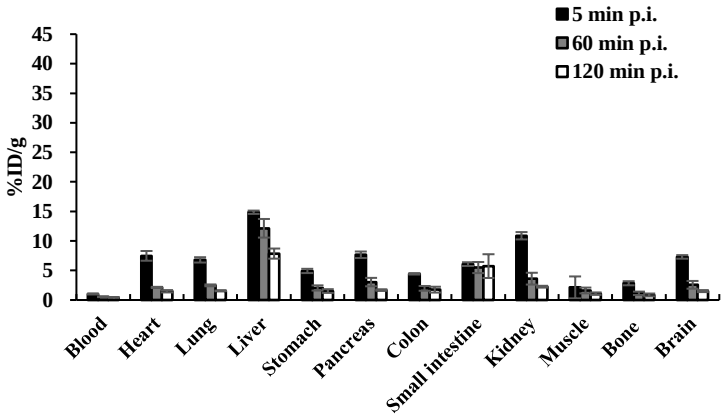

[^{18}F]f$_6$

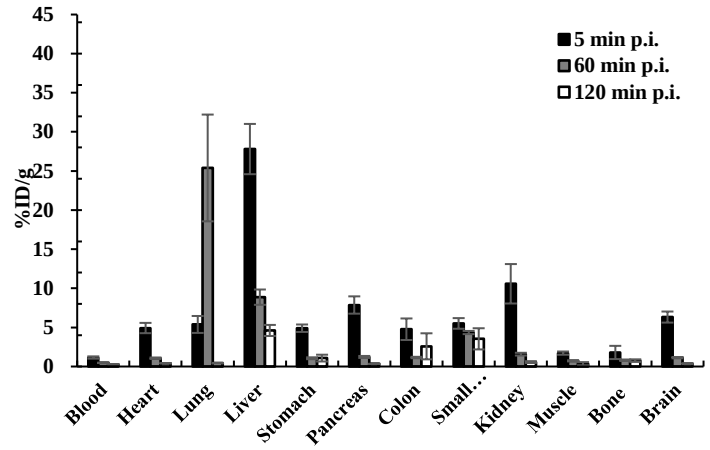

[^{18}F]f$_7$

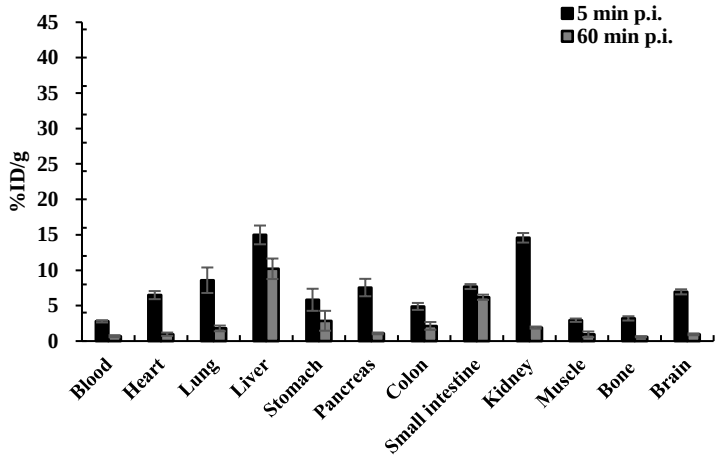

[^{18}F]f$_8$

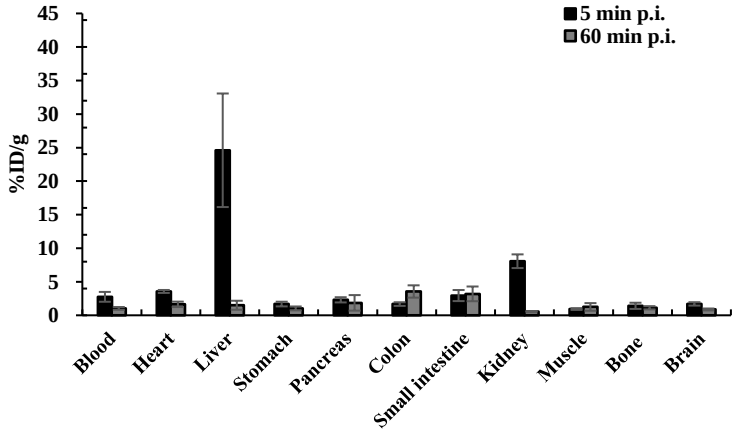

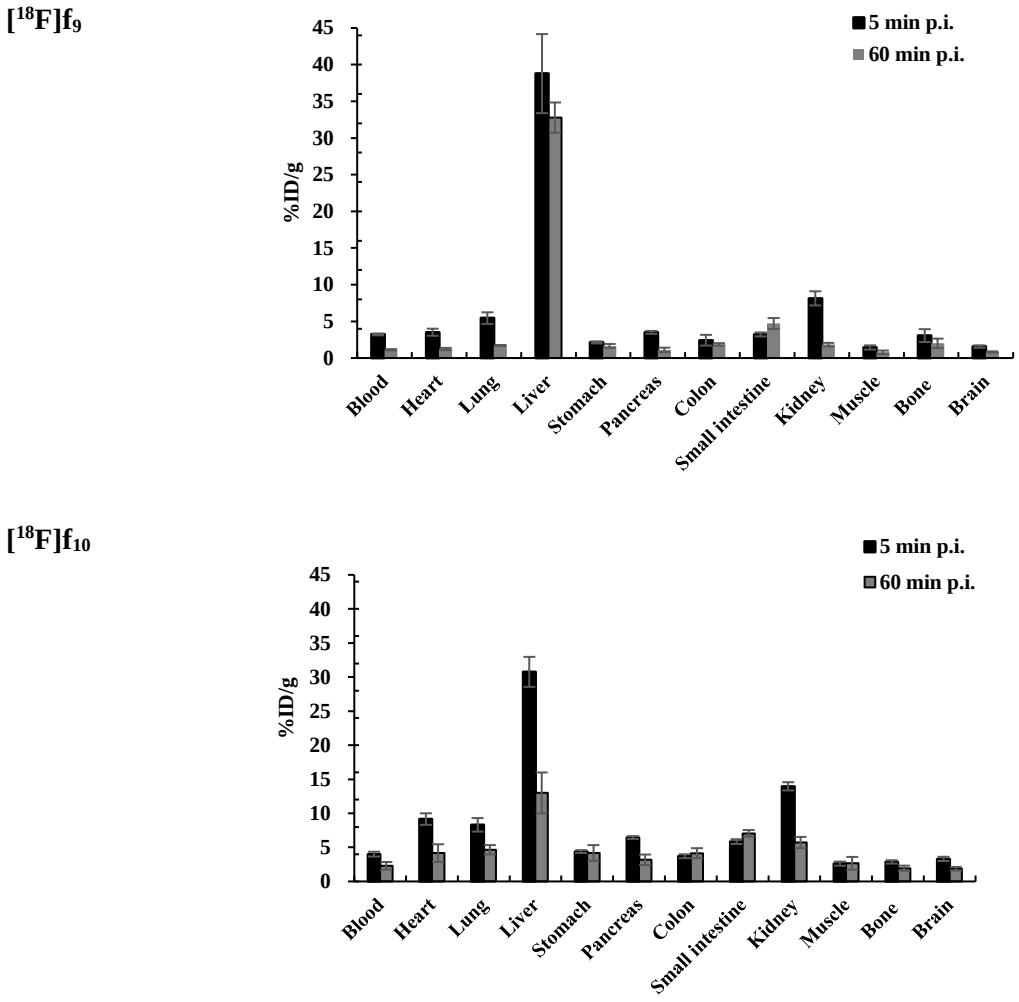

Figure 26. Biodistribution experiments of DABTAs in healthy C57BL/6J mice (n = 3) at 5 min, 60 min, and 120 min for [^{18}F]d_6, [^{18}F]d_8, [^{18}F]f_5, and [^{18}F]f_6. The graph shows the tracer uptake in the organs of interest at the time points given above. * 120 min time point obtained from biodistribution after PET dynamic scans.

6.5.2 Metabolite experiment

Biodistribution experiments showed the brain uptake of the radiofluorinated tracers; however, the observed signals could be not only from the parent tracers injected but also from the [^{18}F]radiometabolites that made it across the BBB. The metabolite experiments enabled the identification of the brain content of the [^{18}F]F-labeled species at 20 min p.i., be the signals from the parent tracers or the radiometabolites. The tracers (**[^{18}F]d_6** and **[^{18}F]d_8**) with Csp2–[^{18}F]F bonds showed no visible brain radiometabolites; however, tracers (**[^{18}F]$f_{4\text{-}7}$**) with Csp3–[^{18}F]F bonds showed <2% of the brain radiometabolites. **[^{18}F]f_9** showed the highest brain radiometabolite (4%) of the evaluated tracers. In vivo plasma stability was also moderate to high **Figure 27** and correlated closely with lipophilicity, except for **[^{18}F]f_9** which showed a high degree of what was believed to be O-defluoroPEGylation.

The chromatograms of the tracers extracted as described in **5.5.2**, after the euthanasia of the healthy C57BL/6J mice at 20 min are presented below **Figure 27**.

Tracers	Plasma	Brain
$[^{18}F]d_6$	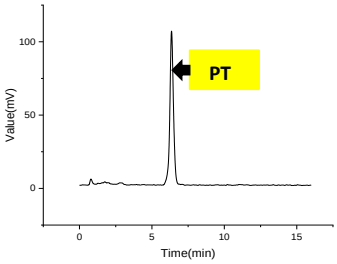	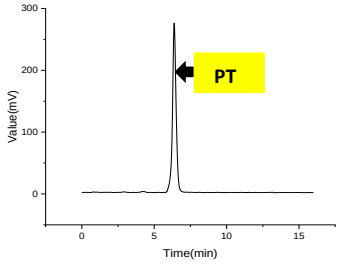
% of PT	**90.4 ± 5.6**	**100.0 ± 0.0**
$[^{18}F]d_8$	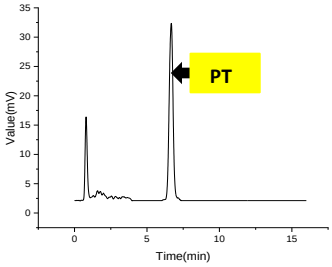	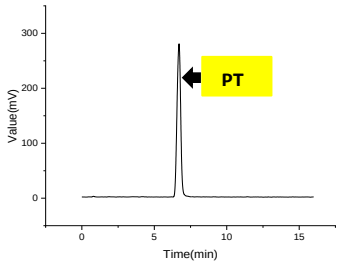
% of PT	**71.4 ± 2.6**	**100.0 ± 0.0**
$[^{18}F]f_4$	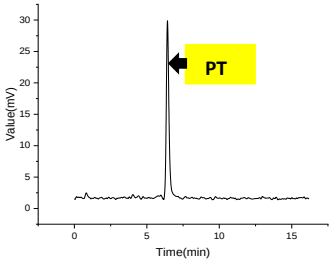	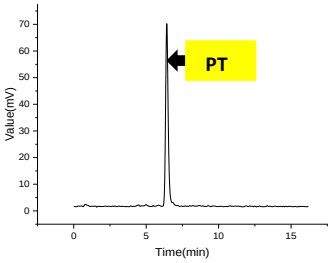
% of PT	**92.9**	**97.6**
$[^{18}F]f_5$	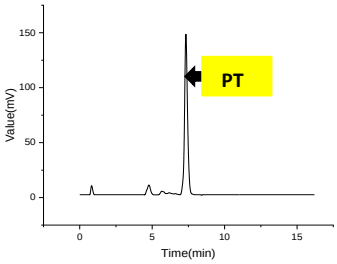	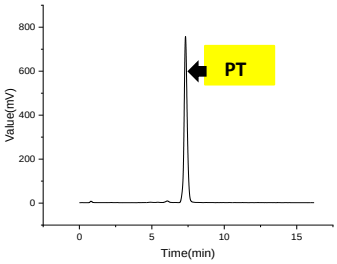
% of PT	**83.9 ± 5.2**	**99.1 ± 0.4**

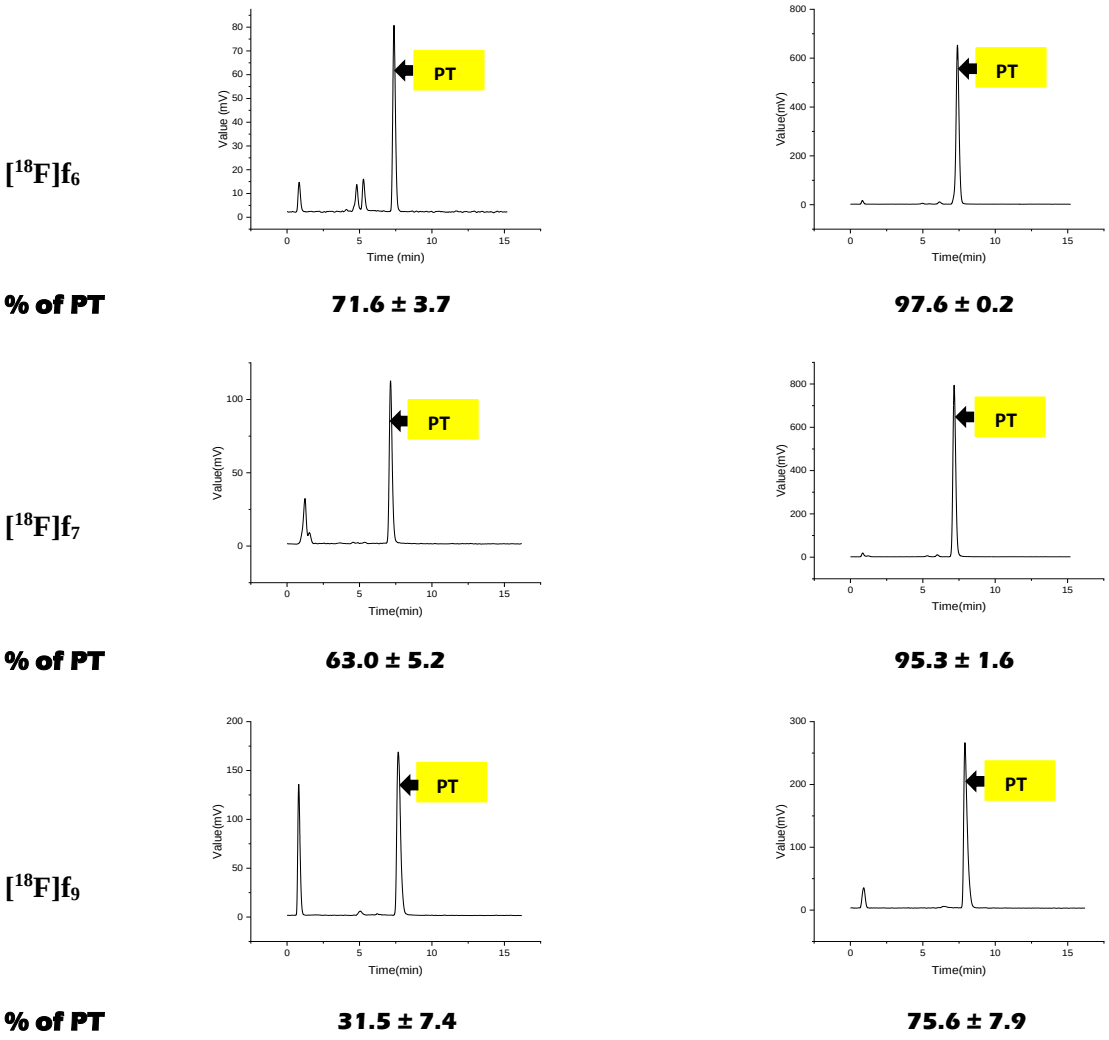

Figure 27. Representative HPLC chromatograms of the plasma and brain extract of healthy C57BL/6J mice (n = 3) injected with the **[^{18}F]d_6**, [^{18}F]d_8, [^{18}F]f_4, [^{18}F]f_5, [^{18}F]f_6, [^{18}F]f_7 and [^{18}F]f_9. (PT parent tracer, n = 3 except for [^{18}F]f_4 (n =1)).

6.6 In vivo experiments

6.6.1 PET-MRI dynamic scans

PET-based biodistribution showed time-dependent brain pharmacokinetics of the two tracers (**[^{18}F]d_6** and **[^{18}F]d_8**) evaluated. The brain uptake of the less lipophilic **[^{18}F]d_8** peaked within the first 15 mins p.i., and there was a faster brain clearance with time compared to the more lipophilic **[^{18}F]d_6**, which showed a slower brain uptake and clearance (**Figure 28** and **Figure 29**).

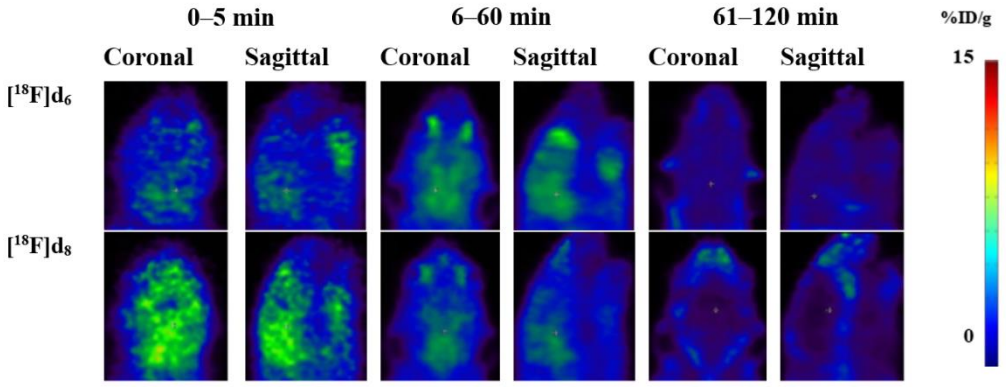

Figure 28. Representative averaged coronal and sagittal PET images of the brain accumulation of [^{18}F]d_6 and [^{18}F]d_8 displayed as %ID/g in healthy C57BL/6J mice (n = 3). PET was recorded in list mode for 120 min and consisted of 36 frames (1×60 s; 30×10 s; 1×600 s; 1×900 s; 3×1800 s).

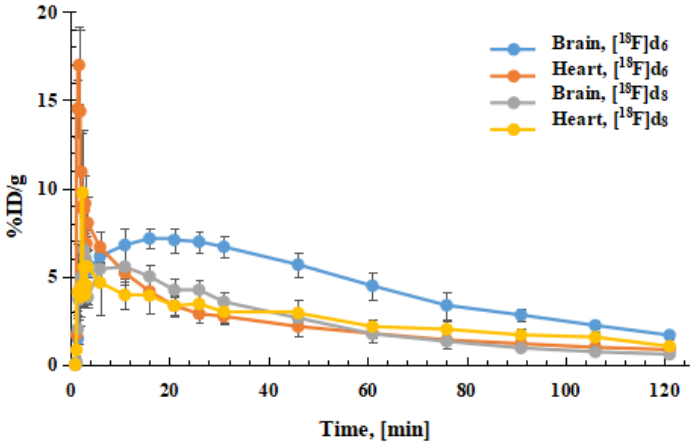

Figure 29. Time-activity curves (TACs) of [^{18}F]d_6 and [^{18}F]d_8 obtained from the brain and heart tissues of healthy C57BL/6J mice PET was recorded in list mode for 120 min and consisted of 36 frames (1×60 s; 30×10 s; 1×600 s; 1×900 s; 3×1800 s).

7. DISCUSSION

7.1 Cold chemistry

The first and second steps in the synthesis of the DABTAs are based on a modified Hantzsch method of thiazole synthesis. The mechanism of the reaction **Scheme 11** [181,182] involves two nucleophilic attacks. Firstly, by either of the highly nucleophilic sulfur atoms of the dithiooxamide molecule on the α-carbon of the bromoketone of the phenacyl/heteroacylbromide molecule. This is followed by another nucleophilic attack, this time, of the imine nitrogen on the carbonyl carbon. Subsequently, condensation/dehydration to form the corresponding 4-arylthiazole-2-carbothioamide takes place. In the second step, the reaction mechanism is repeated with the corresponding phenacyl/heteroacylbromide.

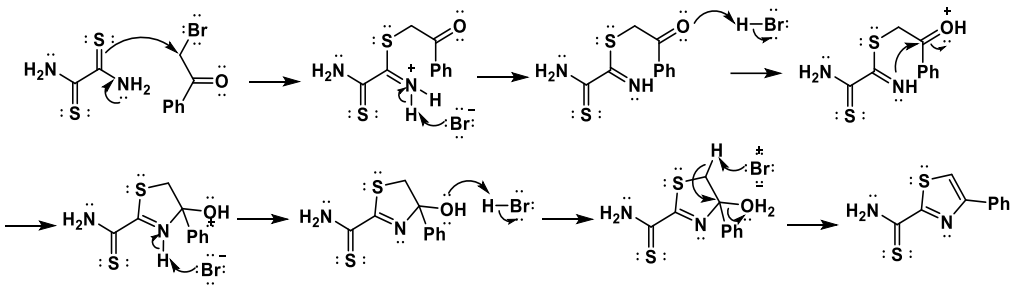

Scheme 11. The proposed reaction mechanism for the formation of the 4-aryl/heteroarylthiazole-2-carbothioamides, b. Where Ph represents the substituted phenyl/heteroaryl moiety. The same reaction takes place in the Step II of the chemical synthesis.

The reagent dithiooxamide used in Step I (see **5.2.1**) of the reactions was typically used in 1.5 molar equivalents of the phenacyl/heteroacylbromide. No observable difference was observed when higher molar equivalents were used. This may be due to the loss of the product in the course of purification, owing to the added difficulty in the removal of dithiooxamide.

The reactions were carried out in DMF due to its more selective dissolution of the 4-arylthiazole-2-carbothioamides over the symmetric DABTAs formed in Step I. The latter tends to be poorly soluble in DMF, which allows them to be easily separated (over 95%) from the 4-arylthiazole-2-carbothioamides and unreacted dithiooxamide. Dithiooxamide was subsequently removed via semiprep HPLC in the minimal presence of the symmetric DABTAs that are usually too hydrophobic for the semiprep HPLC. The 4-arylthiazole-2-carbothioamides are also soluble in DMSO; however, the sulfoxide group in DMSO (pK_a 35) initiates a nucleophilic attack on the α-carbon in phenacyl/heteroacyl)bromide with the eventual release of the foul-smelling dimethylsulfide **Scheme 12** [183,184] and blackening of the reaction solution.

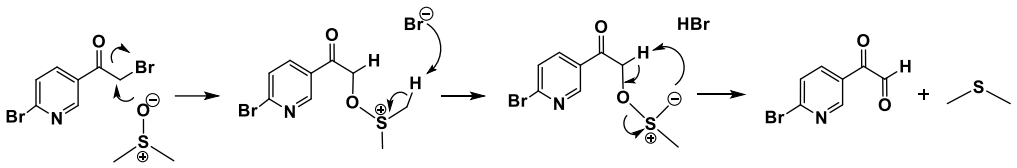

Scheme 12. The proposed reaction mechanism of the formation of a glyoxal and dimethylsulfide from an α-bromoketone and DMSO. DMF lacks the sulfur-oxygen bond found in DMSO. It contains a carbonyl group (C=O), but this group does not have the same oxidative potential as the sulfoxide in DMSO.

The side-reaction depicted in **Scheme 12** may also occur in DMF (pk_a -0.3), but it proceeds at a slower rate. In DMF, the nitrogen atom's lone pair is delocalized through resonance with the carbonyl group, which reduces its electron density and makes it a less effective nucleophile compared to the sulfur atom in DMSO. However, in the presence of the more basic heteroacylbromide, 1-([1,3]dioxolo[4,5-b]pyridin-6-yl)-2-bromoethan-1-one –from which $\mathbf{d_7}$ (Step II, **Scheme 2**) and other compounds were synthesized—the synthesis of $\mathbf{d_7}$ was unsuccessful. Fortunately, the addition of glacial acetic acid was able to quench possible side reactions likely caused by the basic reactant. Therefore, all reactions involving 1-([1,3]dioxolo[4,5-b]pyridin-6-yl)-2-bromoethan-1-one were conducted in a strongly acetic acid medium to minimize side reactions.

One-pot synthesis, although possible, was avoided since the unreacted dithiooxamide from Step I **Scheme 1**, could still react with the phenacyl/heteroacylbromide used in Step II **Scheme 2** to give the corresponding 4-aryl/heteroarylthiazole-2-carbothioamide and symmetric DABTA as in Step I **Figure 23**. Since the asymmetric DABTAs obtained from Step II are also hydrophobic, in the end, present in the reaction mixture are two hydrophobic symmetric DABTAs and an asymmetric DABTAs with no easy means to separate them. Even when the symmetric DABTA from Step I is removed via decantation, there always remains some dissolved symmetric DABTA. Therefore, it is more practical to begin Step II with the corresponding pure (≥ 99% purity) 4-aryl/heteroarylthiazole-2-carbothioamide.

To obtain the 4-arylthiazole-2-carbothioamides in high purity, purification using the semiprep HPLC is the most preferable method. However, due to solubility problems encountered when purifying with just MeCN (solvent B) and water (solvent A), MeOH (20–40%) is usually added to solvent A to prevent the precipitation of the compounds in the tubes and columns. Aqueous tetrahydrofuran solution can also be used; however, it causes tailing of the analyte peaks when used at high concentrations, in addition to other technical limitations [185]. Therefore, it was used at low concentrations (0.2–2%) in the aqueous MeOH solution, at which it prevents peak tailing instead. This solvent mixture prevents the analytes from precipitating and clogging the system. Moreover, the tailing of the product peaks is better controlled, especially for the 4-heteroarylthiazole-2-carbothioamides (**Scheme 1**), which, due to a secondary analyte

interaction between the protonated basic ring nitrogen and the incompletely deionized silanol groups in the column, tended to tail more.

The purification of the asymmetric DABTAs obtained in Step II is relatively easier when the 4-aryl/heteroarylthiazole-2-carbothioamides used for the synthesis are pure. The asymmetric DABTAs are usually purified via trituration, which allows, getting rid of the unreacted 4-aryl/heteroarylthiazole-2-carbothioamide and phenacyl/heteroacylbromide using MeOH or acetone, which dissolves the compounds, leaving behind the pure asymmetric DABTAs. Although time-consuming, $\mathbf{d_1}$ was purified using semiprep HPLC; $\mathbf{d_{14}}$ could also be thus purified. The others, which contain pyridine and pyrimidine rings, counterintuitively showed less solubility even in strong organic solvents such as DMSO; hence, were best purified via trituration.

For the phenol/pyrimidinol-containing DABTAs, an additional third step (**Scheme 4** and **Scheme 5**) was required both for the synthesis of the standard compounds and the precursors that facilitate one-step radiolabeling. The reactions were carried out in DMF at 80°C with the corresponding reagents (**5.2.5.2** and **5.2.5.3**). The DABTAs were deprotonated using K_2CO_3. 1 M TBAH, an organic base, was added in some cases to quicken the reaction. The third step was made possible via the tosylate and halide LGs (bromide and iodide). However, the halide LGs afforded cleaner and faster synthesis, especially the iodide LG.

Some phenol/pyrimidinol DABTAs needed a specific LG for the Step III synthesis to be carried out. The synthesis of the tosylate precursor $\mathbf{h_{5*}}$ with ethyleneglycol ditosylate proved to be more difficult in the conditions described for the synthesis of the other tosylate precursors, such as $\mathbf{h_6}$, $\mathbf{h_7}$, and $\mathbf{h_{11}}$ (**7.2.1.3**), and eventually gave a hard-to-dissolve compound, a trait uncharacteristic of DABTAs bearing the benzodioxole ring. Although this property is not uncommon for the DABTAs ($\mathbf{d_7}$, for example), it might have played a role in the radiolabeling of this precursor, which gave uncharacteristically low RCC (this will be further examined in **7.2.1.2**). The bromo precursor ($\mathbf{h_5}$) was synthesized relatively easily and was more amenable to radiofluorination with high RCC. Surprisingly, the synthesis of a bromo-precursor ($\mathbf{h_{11*}}$) from $\mathbf{d_{14}}$ with the same bromoalkylating agent (dibromoethane) was not possible in the same conditions described for the synthesis of $\mathbf{h_4}$ and $\mathbf{h_5}$; in contrast, the reaction with ethyleneglycol ditosylate proceeded without much difficulty and was relatively cleaner.

The reason why the reaction of $\mathbf{d_{14}}$ with dibromoethane was unsuccessful might have been a result of insufficient acidity of the $\mathbf{d_{14}}$ phenol. Being a better LG, the tosylate LG might have compensated for this inadequacy. This, however, does not explain why $\mathbf{d_{12}}$ reacted with difficulty with ethyleneglycol ditosylate, although it is a stronger acid than $\mathbf{d_{14}}$ (**Figure 30**), and the tosylate is a better LG than the bromide. Being relatively less acidic than the pyrimidinol DABTAs ($\mathbf{d_{11}}$ and $\mathbf{d_{12}}$), the O-methylation of $\mathbf{d_{15}}$ via

methyltosylate was not as successful as its pyrimidinol counterparts. Only around 41% chemical conversion was observed during the synthesis of **f_{17}** via a tosylate LG at 80°C for 20 min. An increment in temperature from 80°C to 85°C and a longer duration led to increased side products. However, O-methylation using methyl iodide proceeded more facilely, negating the hypothesis that the tosylate LG makes up for the low acidity of the phenols. Apart from the above observations, the modification of the phenol-containing DABTAs was carried out without much event.

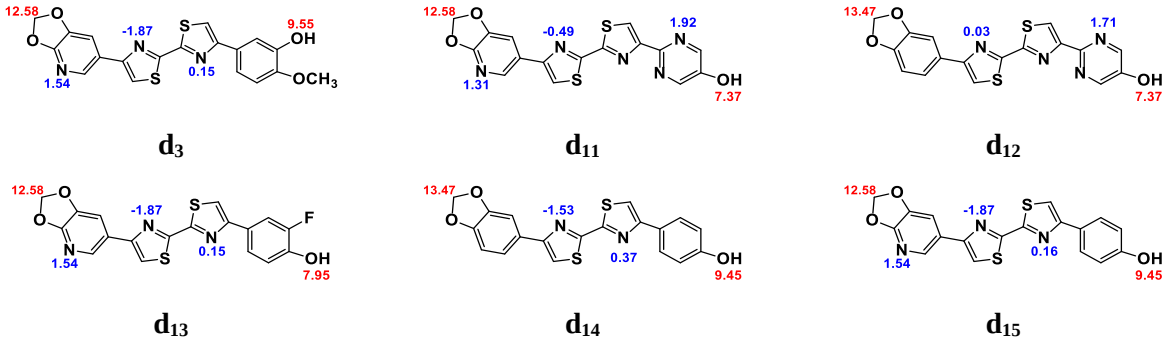

Figure 30. Comparison of the basicity of the phenol-DABTAs. Color blue: basic pKa, color red: acidic pKa. In most of the cases, the more acidic the hydrogen in the hydroxyl group, the faster the reaction proceeded.

The optimization (Step III, **5.2.5.2**) described above enabled the radiosynthesis of the corresponding (**[^{18}F]f_{4-14}**) tracers via Csp3–bonded LGs in S_N2 reaction. For the tracers **[^{18}F]d_6**, **[^{18}F]d_8**, **[^{18}F]d_{10}**, **[^{18}F]d_{17}**, **[^{18}F]d_{19}**, and **[^{18}F]d_{21}** radiofluorination was facilitated via Csp3–bonded LGs in S_NAr reactions. However, for **[^{18}F]d_2** and **[^{18}F]d_4**, where the LG (-OH group) is a bad LG, optimization of their precursors via ruthenium complexation was performed. This transformed the –OH group into a good LG, which facilitated the incorporation of fluorine-18 via S_NAr.

Ruthenium complexation involves the complexation of the guaiacol rings contained in both **d_1** and **d_3** with ruthenium metal via a reaction with (η^5-Cyclopentadienyl)(η^6-naphthalene)ruthenium(1+) trifluoromethanesulfonate in the low-coordinating solvent dichloroethane with MeCN as a catalyst **Scheme 3**. The ruthenium-mediated deoxyradiofluorination of electron-rich arenes was first reported by the Ritter group and it played a significant role in the radiosynthesis of **[^{18}F]d_2** and **[^{18}F]d_4**. This process is described in greater detail in a publication by the same author [138]. In summary, ruthenium, being electropositive, acts as an electron sink, and drains the electron-rich guaiacol rings of electrons, rendering them electron deficient, thus making them susceptible to nucleophilic attack.

7.2 Radiochemistry

Radiochemistry is the bedrock of nuclear medicine, and the DABTAs were radiolabeled using various methods shown in detail above in **5.3**.

The majority of the DABTAs were [^{18}F]F-labeled. Although radiolabeling with carbon-11 is also feasible, its short half-life of 20.4 minutes [186] makes it less desirable. In contrast, fluorine-18, which has a longer half-life of 110 minutes, is preferred whenever possible. Both **[^{18}F]d$_2$** and **[^{18}F]d$_4$** can also be labeled with carbon-11 (C-11); however, to enhance stability, they were instead labeled with fluorine-18 (F-18) [187]. Furthermore, considering the lipophilicity of DABTAs, which necessitates longer PET scans to achieve a good signal-to-noise ratio (SNR), a long-lived radioisotope like fluorine-18 is advantageous. Nevertheless, some DABTAs (**5.3.3**) were labeled with C-11. Other long-lived positron-emitting radiohalogens were avoided for biological reasons. Iodine-124 (4.2 days) [167] and bromine-76 (16.2 hours) [188] would have increased the steric bulk (MW) of the DABTAs due to their atomic weights (AW) of 124 and 76, respectively, compared to fluorine-18, which is a bioisosteric alternative to hydrogen and has an AW of 18 [189] **Figure 31**. Additionally, Iodine-124 and bromine-76 would further increase the lipophilicity of the already considerably lipophilic DABTAs **Figure 31**.

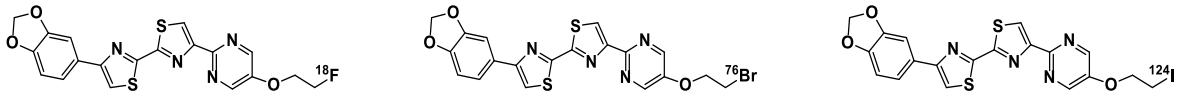

MW 427.46, Clog P 4.04 MW 485.38, Clog P 4.52 MW 533.36, Clog P 4.91

Figure 31. The effect of different positron-emitting radiohalogens on the MW and the lipophilicity a DABTAs. While the other radiohalogens have longer half-lives than fluorine-18, they exhibit less clean decay profiles and increase the lipophilicity and MW of the DABTAs—properties that are detrimental to their in vivo potency.

In terms of decay profiles, F-18 has the cleanest decay profile among the radiohalogens, comparable to that of C-11 (99.8% of the time via positron emission and 0.2% via electron capture). F-18 decays 97% of the time through positron emission and 3% through EC. In comparison, Br-76 and I-124 decay by 57% and 23%, respectively, via positron emission, with the rest usually being via gamma emissions and EC accompanied by gamma emissions. The PET scanner cannot differentiate between true coincidences resulting from positron-electron annihilation and non-annihilation gamma emissions, particularly when they are close in energy. This generates background PET activity similar to scattered coincidences. High positron energies produced by these radioisotopes (maximum kinetic energies of 3980 keV and 2138 keV) compared to the 634 keV observed in F-18 rresult in a loss of spatial resolution [168,188,190,191]. Furthermore, the distance traveled by the positron before annihilation contributes to blurring in the PET image. Lower energy emitters like F-18 and C-11 travel a relatively shorter distance (0.7 mm) compared to higher energy emitters like Br-76 (5.3 mm) before annihilation [188].

Lastly, preliminary binding assays indicated that the introduction of a fluorine atom in DABTAs enhances their affinity for α-syn and improves the lipophilicity of the ligand. For instance, O-fluoroethylation of **d$_{14}$** to obtain **[^{18}F]f$_{11}$** (Ki 3 nM, Clog P 5.70) instead of merely O-ethylating it (Ki 10 nM, Clog P 5.98) not only improved the ligand's affinity for α-syn but also reduced its lipophilicity **Figure 32** [176].

Figure 32. The influence of fluorine-18 on the affinity of the DABTAs to α-syn. The O-fluoroethylation (**f$_{11}$**) and O-ethylation of **d$_{14}$** resulted in compounds with different binding properties and lipophilic profiles.

7.2.1 One-step radiofluorination

7.2.1.1 Ruthenium-mediated S_NAr deoxyradiofluorination

The majority of the DABTAs were radiolabeled with fluorine-18 using various reaction mechanisms, the most notable of which was the ruthenium-mediated deoxyradiofluorination of the electron-rich arenes **d$_1$** and **d$_3$** [138]. Based on the results obtained from biodistribution experiments conducted with the tracers **[^{18}F]d$_2$** and **[^{18}F]d$_4$** (**Figure 26**), which were derived from the precursors **d$_1$** and **d$_3$**, respectively, further optimization of the radiolabeling conditions was not deemed necessary. An advantage of this method of radiofluorination is the elimination of azeotropic drying of the fluoride ion (**5.3.1.1**); however, with a reaction time of up to 35 minutes, this advantage is somewhat diminished. Nevertheless, the operator is spared the radiation exposure that occurs during azeotropic drying.

7.2.1.2 Halide-mediated S_NAr radiofluorination

Among the two promising 6-fluoropyridine tracers, **[^{18}F]d$_6$** and **[^{18}F]d$_8$**, the radiosynthesis of **[^{18}F]d$_8$** required significant optimization **Table 10**. In contrast, **[^{18}F]d$_6$** was readily obtained with high to moderate RCY from the outset. The initial radiosynthesis of **[^{18}F]d$_8$** using only K_2CO_3, resulted in inconsistent yields at 180°C for 7 minutes. Thus, it was concluded that the [1,3]dioxolo[4,5-b]pyridine ring in its precursor, **d$_7$**, likely played a role, as it shares the same 6-bromopyridine ring with the precursor **d$_5$** of **[^{18}F]d$_6$**. The presence of the [1,3]dioxolo[4,5-b]pyridine ring may have increased the overall basicity of **d$_7$**, making it more sensitive to the basic medium used for radiofluorination. While other unknown factors may also be involved, the most apparent issue—namely, the increased basicity of the precursor—was addressed. The results of efforts to reduce the basicity of the reaction medium are presented in **Table 10**.

Initial trials with less basic potassium salts ($KHCO_3$ and $K_2C_2O_4$) also yielded low RCC. However, it was observed that reducing kryptofix with these weaker basic salts allowed for heating the reaction mixtures to higher temperatures, which resulted in increased RCC. Although both $KHCO_3$ (pK_b 7.6) and $K_2C_2O_4$ (pK_b 10) gave sufficiently high RCC when used alone, eluting fluoride-18 from the QMA cartridge proved challenging due to their weaker basicity. A combination of 4.5 µmol of K_2CO_3 (pK_b 3.8) with either of the weaker bases enhanced the elution of fluoride-18, increasing elution efficiency by 76%. This combination also reduced the loss of fluoride-18 as H[^{18}F]F, particularly when using the relatively acidic $K_2C_2O_4$.

Table 10. Optimization of the radiosynthesis of [^{18}F]d_8 with K_2CO_3, $K_2C_2O_4$, and $KHCO_3$ in DMSO

№	K_2CO_3, (mol. equiv. d_7)	$K_2C_2O_4$, (mol. equiv. d_7)	$KHCO_3$, (mol. equiv. d_7)	K_{222}, (mol. equiv. bases)	T°C/Rtn duration, [min]	RCC, [%]
1.	2.00	-	-	2.00	180/3	22.1
					180/4	39.0
					180/5	50.9
					180/6	58.6
					180/7	71.7–39.5
2.	0.01[a]	-	-	2.70	150/4	85.1
3.	0.01	-	-	2.70	150/4	16.0
4.	1.00	-	-	3.10	180/5	54.6/60.0
					180/10	50.0
5.	1.00	1.70	-	2.00	150/5	42.8
					150/7	52.2
					150/10	47.5
6.	1.00	1.70	-	2.00	180/3	34.6
					180/5	71.1–71.6
					180/6	47.5
					180/7	48.7–63.7
7.	1.00	1.70	-	2.00	200/3	49.2–67.8
					200/5	59.0–67.3
					200/7	47.0–74.9
					200/11	48.4
8.	-	-	2.00	1.50	140/3	6.6
					140/4	14.0
					140/5	20.8
9.	-	-	2.00	1.50	150/3	10.1
					150/4	28.7
					150/5	26.1
10.	-	-	2.00[b]	1.50	150/2	2.2
					150/4	12.0
					150/5	29.2
11.	-	-	2.00	1.50	180/1	43.9
					180/2	57.6
					180/3	71.1
12.	1.00	-	2.00	1.00	180/5	56.1
					180/6	63.8
					180/7	78.9
					180/8	64.2
					180/9	63.1
13.	0.94	-	2.00	1.00	180/5	44.53
					180/6	58.86
					180/7	60.4
					180/8	60.5
					180/9	70.8
14.	1.00	-	2.00	1.00	185/5	36.1
					185/6	63.0
					185/7	62.4

					185/8	77.6
					185/9	60.6
					190/5	53.3–80.0
					190/6	68.2–90.0
					190/7	75.3–75.6
					190/8	68.1–79.8
					190/9	68.1–80.0
					193/5	57.0
					193/6	55.2
					193/7	51.0
					193/8	50.0
					193/9	44.1
15.	1.00[c]	-	2.00	1.00	150/5	2.1
					150/7	2.6
					150/9	4.6
					150/11	4.9

[a] Isotopic exchange. [b] Reaction in DMF. [c]Reaction in MeCN. T°C temperature**.** Rtn reaction. RCC radiochemical conversion.

The radiosynthesis of **[^{18}F]d$_{19}$** and **[^{18}F]d$_{21}$** was conducted following the established protocol of their structural isomers, **[^{18}F]d$_6$** and **[^{18}F]d$_8$**, without any optimization. Although both **d$_{18}$** and **d$_{20}$** featured a superior LG (in S_NAr), that is, the chloride LG, the protocols developed for the bromo-bearing **d$_6$** and **d$_7$** could not be effectively used for the radiosynthesis of **[^{18}F]d$_{19}$** and **[^{18}F]d$_{21}$**. Nevertheless, the radiosynthesis protocol was not further optimized since they poorly stained α-syn in the autoradiography experiments **Figure 25a** when compared to **[^{18}F]d$_6$** and **[^{18}F]d$_8$**. Furthermore, their precursors are more hydrophilic than the bromo-precursors of **[^{18}F]d$_6$** and **[^{18}F]d$_8$** complicating the separation of the tracers from their precursors via SHP. This necessitated a reduction in the organic component of their SHP eluents to prevent co-elution with their precursors. This consequently led to increased retention times and and subsequently higher losses due to column retention; up to 44% of **[^{18}F]d$_{19}$** was recovered during column cleaning. They may also display slower brain clearance compared to their structural isomers. A spike injection of **[^{18}F]d$_{19}$** and **[^{18}F]d$_{21}$** with the cold versions (**d$_6$** and **d$_8$**) of their structural isomers **[^{18}F]d$_6$** and **[^{18}F]d$_8$**, showed they were eluted ~0.3 min after the cold versions compared to the ~0.2 min observed for **[^{18}F]d$_6$** and **[^{18}F]d$_8$**.

The same conditions used for the radiosynthesis of **[^{18}F]d$_8$** were applied for the radiosynthesis of **[^{18}F]d$_{17}$**, albeit at a lower temperature (135°C) and for a shorter duration (3 min). At higher temperatures (≥160°C) and longer durations, there was a decrease in RCC accompanied by the formation of side products, which complicated its SHP. **[^{18}F]d$_{17}$** is more lipophilic **Table 21** than **[^{18}F]d$_6$**; it was radiosynthesized to evaluate the effect of the $–NO_2$ group on the potency of the DABTAs in vitro autoradiography with PHBT. Based on the results obtained **Figure 25a** further optimization of its radiofluorination was not pursued.

The radiosynthesis of **[^{18}F]d$_{10}$** using only K_2CO_3 was significantly more successful than that of **[^{18}F]d$_8$**. This may be attributed to two factors: first, the chloride LG is a better LG in S_NAr than the bromide LG. Second, the LG is situated between two electron-withdrawing nitrogen atoms in the pyrimidine ring **Scheme 7**. Consequently, it is possible that the rate of decomposition of the precursor and the tracer **[^{18}F]d$_{10}$** was counterbalanced by a faster rate of incorporation of fluorine-18 into the molecule. However, the precarious position of the fluorine-18 atom at the electron-deficient carbon, exacerbated by the highly electronegative fluorine atom–which is also an effective LG–rendered the Csp2–[^{18}F]F carbon high susceptible to nucleophilic attack even by the weakly nucleophilic ethanol used in the preparation of the tracer. Fortunately, utilizing the minimum amount of K_2CO_3 in conjunction with $K_2C_2O_4$ at a lower temperature **Table 11** slowed down breakdown rate of the tracer, even after 120 min in plasma at 37°C. |Nevertheless, the tracer proved unstable in the biodistribution experiment **Figure 26**.

Table 11.Optimization of the radiosynthesis of d_{10} with K_2CO_3 and $K_2C_2O_4$

№	K_2CO_3, (mol. equiv. d_9)	$K_2C_2O_4$, (mol. equiv. d_9)	K_{222}, (mol. equiv. bases)	T°C/Rtn duration, [min]	RCC, [%]
1.	1.21	-	3.11	140/4	55.2
2.	1.41	-	3.02	140/8	60.7
3.	1.45	-	3.02	140/4	62.7–84.4
4.	0.91	1.05	2.64	150/4	44.6
5.	0.91	1.53	2.20	150/4	88.0
7.	0.60	1.02	2.20	140/4	51.3
8.	0.60	1.05	2.64	150/5	28.4
9.	0.45	1.36	3.61	140/8 150/5	46.8 57.3
10.	0.45	0.79	5.03	150/5	75.2
11.	0.005	1.53	3.01	140/2	54.7

Rtn: reaction. RCC: radiochemical conversion.

7.2.1.3 Halide/tosylate-mediated S_N2 radiofluorination

Except for a few exceptions, namely the synthesis of **[^{18}F]f$_5$**, **[^{18}F]f$_7$**, and **[^{18}F]f$_{11}$** using the tosylate LG, radiofluorination via S_N2 reactions proceeded quite smoothly.

The radiosynthesis of **[^{18}F]f$_5$** via the tosylate LG was initially attempted, resulting in low RCC **Table 12**. Notably, the precursor (**h$_{5*}$**) was markedly resistant to dissolution in DMSO. While resistance to dissolution is a common characteristic of DABTAs, particularly among those containing halopyridine or pyrimidine moieties, DABTAs with the O-ethyl/PEG groups typically demonstrate at least slight solubility in DMSO. **h$_{5*}$** could only be dissolved at 180°C in DMSO during radiosynthesis and immediately precipitated after heating, complicating the SHP of **[^{18}F]f$_5$**. In contrast, the O-ethylbromide precursor (**h$_5$**) was more soluble.

It yielded **[^{18}F]f$_5$** in moderate to high RCY in both DMSO and MeCN, without the need for further optimization of the radiolabeling conditions **Table 12**.

Table 12. Radiosynthesis of [^{18}F]f$_5$ via the tosylate LG (h$_{5*}$) and bromide LG (h$_5$)

№	LG	Precursor/ Solvent	K_2CO_3, (mol. equiv. precursor)	$K_2C_2O_4$, (mol. equiv. h$_{5*}$)	K_{222}, (mol. equiv. base)	T°C/Rtn duration, [min]	RCC, [%]
1.	**Tosylate**	**h$_{5*}$/DMSO**	2.09	-	3.03	120/4 150/4 180/3	3.2 4.0 7.1
2.		**h$_{5*}$/DMSO**	2.09	2.62	1.44	180/3 180/4	10.5 8.5
3.		**h$_{5*}$/DMSO**	0.48	1.12	5.35	180/2 180/5	1.82 2.17
4.	**Bromide**	**h$_5$/DMSO**	2.07	-	2.93	150/3	79.4
5.		**h$_5$/DMSO**	1.55	-	2.97	150/3	68.8
6.		**h$_5$/DMSO**	1.55	-		120/5 120/7 120/10	99.1 97.8 95.8
7.		**h$_5$/MeCN**	1.55	-	3.01	120/5	96.5–99.3

Rtn: reaction. RCC: radiochemical conversion.

The radiosynthesis of **[^{18}F]f$_{11}$** using the tosylate LG fared better than that of its pyrimidine analog **[^{18}F]f$_5$**, which also employed the tosylate LG. The RCC was nevertheless not very impressive **Table 13**. Notably, the RCC was higher in MeCN compared to DMSO. Unfortunately, **[^{18}F]f$_{11}$** could not be radiosynthesized via the bromide-LG. The O-bromoethylation of its phenolic precursor (**d$_{14}$**) was unsuccessful.

Table 13. Optimization of the radiosynthesis of [^{18}F]f$_{11}$ via the tosylate LG (h$_{11}$)

№	K_2CO_3, (mol. equiv. h$_{11}$)	K_{222}, (mol. equiv. base)	Solvent	T°C/Rtn duration, [min]	RCC, [%]
1.	2.24	3.01	MeCN	120/4 120/5 120/7 120/9 120/10	39.1 40.0 34.3 52.1 35.8
2.	2.00	3.00	MeCN	120/7 120/9	33.0 41.4
3.	1.80	2.91	MeCN	120/5 120/7 120/9	33.2 35.1 44.1
4.	2.00	3.00	DMSO	120/2 120/3 120/4 120/5 120/7	10.2 14.7 17.2 17.1 17.8

Rtn reaction. RCC radiochemical conversion.

The radiosynthesis of **[^{18}F]f$_6$** via the tosylate LG was less eventful than its predecessor, [**^{18}F]f$_5$**. The conditions outlined in **5.3.1.3** consistently performed well in both DMSO and MeCN. Since the only

difference between their tosylate precursors (**h_{5*}** and **h_6**) was the exchange of the O-ethyltosylate moiety with the longer O-ethoxyethyltosylate, it is possible that there was an interaction between the tosylate and the pyrimidine ring in **h_{5*}**. This interaction might not have been possible in **h_6**, owing to the slightly increased distance between the tosylate and the pyrimidine ring. Furthermore, the radiosynthesis of the **[^{18}F]f_6** was achievable with just 1 mg of the precursor **h_{6*}**.

The exact conditions employed for the radiosynthesis of **[^{18}F]f_6** did not successfully translate to the radiosynthesis of **[^{18}F]f_8**, despite their similarities, with the only difference being the presence of a pyridine ring in place of the benzene ring in **[^{18}F]f_8**. A slight increase in K_2CO_3 **Table 14** resulted in modest improvement in RCY. However, further increases in both K_2CO_3 and Kryptofix diminished the RCC **Table 14**. Solubility in the reaction medium may have influenced these results, as **h_8** exhibited poor solubility in MeCN compared to **h_6**, the precursor of **[^{18}F]f_6**. Further optimization in DMSO pursued due to the tracer's poor in vivo performance (**Table 9**, **Figure 26**).

Table 14. Optimization of the radiosynthesis of [^{18}F]f_8 via the tosylate LG (h_8)

№	K_2CO_3, (mol. equiv. h_8)	K_{222}, (mol. equiv. base)	T°C/Rtn duration, [min]	RCC, [%]
1.	1.88	2.49	120/5 120/7 120/10	54.9 39.9 26.2
2.	2.24	2.49	120/5 120/7 120/10	66.0–78.0 65.0 70.4–84.3
3.	2.26	3.02	120/7	67.6

Rtn: reaction. RCC: radiochemical conversion.

Obtaining [**^{18}F]f_7** in good RCY was also challenging via the tosylate LG (**h_7**). The RCCs **Table 15** were not as consistent as those observed for its direct predecessor, [**^{18}F]f_6** via the same LG.

Despite the inconsistencies in RCCs, some trends were noted: MeCN proved to be a better solvent than DMSO, and heating at 120°C in MeCN consistently resulted in higher RCC; longer heating durations also correlated with higher RCC, although this was usually accompanied by lower A_m. Higher RCC (**Table 15**, № 3, and 9) appeared to correlate with elevated base concentrations, a phenomenon peculiar to DABTAs with the tosylate-LG (**Table 14**, **Table 15**, **Table 16** and **Table 17**). However, this must be done with caution; otherwise, the RCC may decrease. For instance, the radiosynthesis of [**^{18}F]f_6** with K_2CO_3 (3.4 times mol. equiv. to the precursor (**h_6**)) and 2.5 times of kryptofix (mol. equiv. to the base) at 120°C for 5 min resulted in approximately a 55% reduction in RCC.

Table 15. Optimization of the radiosynthesis of of [^{18}F]f_7 via the tosylate (h_7), iodide (h_{7*}) and chloride ($h_{7°}$) LG

№	LG	Precursor	K_2CO_3, (mol. equiv. precursor)	K_{222}, (mol. equiv. base)	T°C/Rtn duration, [min]	RCC, [%]
1.	**Tosylate**	**h_7**	3.36[a]	3.00	150/5 150/7 150/9	27.9 28.1 28.4
2.			3.36	3.00	120/5 120/7 120/9	96.8 95.7 95.7
3.			3.36	3.00	120/4	43.8
4.			3.36	2.93	120/4	29.5
5.			3.36	2.93	100/3 100/4 100/5 100/7 100/8 100/10	19.8 18.0 23.6 23.1 24.1 25.7
3.			2.50	3.00	120/5 118/5	30.6 37.0
4.			2.44	2.50	120/4 120/5 120/7 120/10	26.0 27.4 26.9 27.4
5.			2.24	2.93	120/10	80.0
6.			2.24	2.93	120/6 120/7	28.6 43.3
7.	**Chloride**	**$h_{7°}$**	3.38	3.01	120/5 120/7 120/9	1.86 3.32 3.82
8.	**Iodide**	**h_{7*}**	3.96	3.01	120/5 120/7 120/9	39.2 46.8 52.2
9.			1.98	3.01	120/5 120/7 120/9	73.7 74.2 79.8–94.0

[a] in DMSO. Rtn: reaction. RCC: radiochemical conversion.

As a promising tracer, other readily available LGs were also examined, such as iodide (**h_{7*}**) and chloride (**$h_{7°}$**) **Table 15**. The same challenges encountered during the chemical synthesis of **$h_{7°}$** were also observed when it was used for the radiosynthesis of [^{18}**F]f_7**. The inability of the chloride LG to "leave" was evident in both the chemical synthesis of **$h_{7°}$**—where the reaction was forced to completion by heating from 80°C-94°C over the course of an hour—and in the radiosynthesis of [^{18}**F]f_7** using this LG.

Conversely, both the chemical synthesis of **h_{7*}** and its radiolabeling were relatively straightforward. Its chemical synthesis was completed in just 5 min at 80°C. As anticipated, the RCC via the I-LG **Table 15** was more than ten times higher compared to the Cl-LG. RCY via the I-LG was also greater than that of the tosylate LG, with a 39.5% increase in RCY was observed **Table 6**, along with a 9.9% increase in A_m **Table**

7. Unfortunately, the radiosynthesis of **[^{18}F]f$_5$** via the I-LG was not feasible, as the chemical synthesis of its precursor was unsuccessful.

The solvent effect on the radiofluorination of LG-alkylated/pegylated DABTAs was most pronounced in the radiosynthesis of **[^{18}F]f$_9$** (**Table 20**). Even at the same temperature (**Table 16**, № 1 and 3), radiosynthesis conducted in DMSO yielded < 20% RCC. It is noteworthy that, although two DABTAs have similar functional groups, the physicochemical properties of the entire molecule significantly influence the outcome of their radiolabeling. For example, **h$_6$** and **h$_9$** both contain the O-2,2′-oxydiethyl tosylate group **Scheme 4**.

Table 16. Optimization of the radiosynthesis of of [^{18}F]f$_9$ via the tosylate LG (h$_9$)

№	K_2CO_3, (mol. equiv. h$_9$)	K_{222}, (mol. equiv. base)	Solvent	T°C/Rtn duration, [min]	RCC, [%]
1.	2.34	2.91	DMSO	120/4	10.2
				120/5	11.7
				120/6	14.1
				120/7	17.0
2.	3.36	2.91	MeCN	80/5	5.3
				80/7	11.3
				80/9	16.4
				80/11	26.3
				100/5	58.4
				100/10	48.7
				120/5	75.4
				120/10	83.7–91.3
3.	2.25	3.02	MeCN	120/5	76.7

Rtn: reaction. RCC: radiochemical conversion.

Preliminary radiosyntheses of **[^{18}F]f$_{10}$** via the tosylate LG yielded similarly poor results in DMSO as observed in the radiosynthesis of **[^{18}F]f$_7$**, but showed improvement in MeCN **Table 17**. The inconsistency observed in the RCC of **[^{18}F]f$_7$** via the tosylate LG was also observed: № 3 **Table 17** yielded an isolated RCY of 51.3%, while № 4 gave only 24.7%. In contrast, the RCY of **[^{18}F]f$_{10}$** via the I-LG was more consistent, averaging 32.6 ± 1.9% (n = 2), although A_m was lower **Table 7**.

Table 17. Optimization of the radiosynthesis of [^{18}F]f$_{10}$ via the tosylate (h$_{10}$) and iodide (h$_{10*}$) LG

№	LG	Precursor	K_2CO_3, (mol. equiv. precursor)	K_{222}, (mol. equiv. base)	T°C/Rtn duration, [min]	RCC, [%]
1.	**Tosylate**	**h$_{10}$**	3.36 [a]	2.22	120/4	19.0
2.			3.36 [a]	3.00	120/4	37.0
3.			3.36	3.00	120/5	73.0
					120/7	80.6
					120/10	81.9
4.			3.36	3.00	120/10	48.0
5.	**Iodide**	**h$_{10*}$**	3.36	3.00	120/5	66.1
					120/7	71.0
					120/9	81.9–89.6

[a] in DMSO. Rtn reaction. RCC radiochemical conversion.

Both iodide and bromide LGs for radiofluorination via the S_N2 mechanism resulted in a higher RCY than the tosylate LG; the opposite is typically observed in organic chemistry. As previously concluded, this may not stem from the intrinsic properties of the LG, but rather from their potential interactions with the DABTA scaffold. Additionally, the halogen LGs provided more consistent RCY compared to the tosylate LG. Furthermore, their chemical syntheses produced minimal side products, facilitating a simpler purification process for the precursor. Compared to the DABTAs bearing the tosylate LG, those bearing the halogen LG were more easily dissolved in DMSO, which enhanced their characterization through NMR. For the tracers **[^{18}F]f$_{12}$**, **[^{18}F]f$_{13}$**, and **[^{18}F]f$_{14}$**, radiosynthesis was carried out via the iodide-LG to decent RCY as reported in **Table 6**.

7.2.2 Two-step radiofluorination

This was only achievable with the DABTAs containing the hydroxyl functional group. However, it was not attempted for all the tracers due to the time-consuming nature of the process, which takes nearly three hours of radiosynthesis—nearly two half-lives of fluorine-18. To compensate for this, radiosynthesis must be started with high radioactivity, which in turn increases exposure to radioactivity (**5.3.2**), especially if the radiosynthesis is done manually.

Nevertheless, this synthesis method could be beneficial for producing radiotracers for patient use, as the SHP carried out in both the first and second steps may help eliminate the toxic phase-transfer catalyst, kryptofix used in the first step [190]. In the first step, the precursors ethyleneglycol-, diethyleneglycol- and triethyleneglycol ditosylate were used selected due to their ease of preparation, low volatility, relatively high reactivity, and stability [192].

The second step of the two-step radiosynthesis involved converting the phenol/pyrimidinol DABTAs into their conjugate base forms using a base to facilitate a nucleophilic attack on the carbon bearing the LG in the radiofluorinated intermediate tracer **Scheme 9b**. Various bases are discussed in the literature [192]. However, for the DABTAs, only sodium hydride (NaH) and the nucleophilic base TBAH were tested.

Table 18. Optimization of the second step of the radiosynthesis of [^{18}F]f$_4$ and [^{18}F]f$_5$ with sodium hydride (NaH)

№	Tracer	Qty of precursor, (mg)	NaH		T°C/Rtn duration, [min]	RCC, [%]
			Qty, (mg)	mol. equiv. to precursor		

1.	**[^{18}F]f$_4$**	3.5	2.0	9.1	80/5 80/10 80/15	1.9 3.7 5.5
2.	**[^{18}F]f$_5$**	3.5	4.0*	18.2	90/1	1.0

* Sodium hydride was not removed. Rtn: reaction. RCC: radiochemical conversion. Qty quantity.
Note: Reaction was terminated once **[^{18}F]FETos** was completely used up.

NaH yielded unsatisfactory results **Table 18** for the two-step synthesis of **[^{18}F]f$_4$** and **[^{18}F]f$_5$**; therefore, it was not pursued further. However, it was used as follows: the precursors **d$_{11}$** and **d$_{12}$** were deprotonated with NaH in DMF for 2 min at 80°C and via centrifugation, the unreacted NaH was removed. The deprotonated DABTAs were then reacted with **[^{18}F]FETos**, as illustrated in **Scheme 9b**.

The use of the organic base tetrabutylammonium hydroxide (TBAH) has also been described in literature [193–196]. Since it was readily available, efforts were made to enhance the RCYs with it. Some of the conditions outlined in the referenced articles were replicated **Table 19**.

Table 19. Optimization of the second step of the radiosynthesis [^{18}F]f$_5$ with TBAH (1M)

№	**d$_{12}$, (mg)**	**TBAH (1M)**		**T°C/Rtn duration, [min]**	**RCC, [%]**
		V, (µL)	**mol. equiv. to precursor)**		
1.	2.5	68.0	56.9	140/5	16.0
2.	4.0	14.3	4.8	120/3	12.1
3.	2.5	6.5*	3.5	120/3	1.0
4.	2.0	4.0	2.7	115/4 120/3	43.3 28.7
5.	2.5	4.0	2.2	115/4	49.3
6.	2.0	3.0	2.0	115/4	35.7
7.	2.5	3.0	1.6	115/4	35.8–45.8

* 1.4 M TBAH. Reaction was terminated once [^{18}F]FETos was completely used up.

Although an improved RCY was observed with TBAH compared to NaH (**Table 19**, № 1–3) according to protocols reported in the literature, it was not until additional efforts were made to simultaneously evaporate surplus TBAH during the reaction that the RCC increased remarkably (**Table 19**, № 4–7). The participation of **[^{18}F]FETos** in side reactions was reduced under these improved conditions, which included a decrease in temperature. Other bases were not tested; instead, efforts focused on optimizing the conditions for the direct radiosynthesis of the tracers described above. The two-step radiolabeling of the other phenol/pyrimidinol DABTAs followed the same established protocol outlined in **Table 19**.

7.2.3 Carbon-11 labeling

The first step of carbon-11 labeling was carried out as described in **5.3.3.1**, following a radiosynthesis procedure already established by the facility and was not optimized by the author.

For the second step of carbon-11 labeling of the pyrimidinol DABTAs **d_{11}** and **d_{12}**, both NaH and TBAH (1M) were evaluated for their efficacy in O-[^{11}C]methylation of the pyrimdinols using [^{11}C]CH_3I. TBAH proved to be more reliable, as longer reaction times increased the RCC, whereas the opposite trend was observed with NaH. This discrepancy may be partly attributed to the smaller amount of the deprotonated species used in the radiosynthesis with NaH. The procedure for labeling with NaH involved deprotonation at room temperature, which typically yields a nearly clear solution. However, after centrifugation, **d_{11}** was found in the sediment, indicating incomplete deprotonation. Consequently, the supernatant contained less than the intended amount of the sodium salt of **d_{11}**. In contrast, with TBAH (**5.3.3.2**), **d_{11}** completely dissolved in the base and was not removed prior to the O-[^{11}C]methylation reaction.

Conducting the reaction in a nitrogen atmosphere, as described in **5.3.3.2**, significantly increased the yield of **[^{11}C]f_{16}** substantially **Table 20**. Initially, this method was avoided to prevent laboratory contamination due to the volatility of [^{11}C]CH_3I (Bp 42°C) compared to [^{18}F]fluoroethyl tosylate (Bp 140°C). However, contamination proved to be minimal and was further minimalized by performing the reaction without withdrawing samples from the vial at three time points, as was done when NaH was used.

Interestingly, halving the amount of **d_{11}** also resulted in a reduction of RCC by more than half. Such a noticeable reduction in RCC was not observed for **[^{18}F]f_{15}**. The synthesis of **[^{18}F]f_{17}** and **[^{18}F]f_{18}** proceeded smoothly using the already established protocol.

Table 20. Optimization of the second step of the [^{11}C]methylation of [^{18}F]f_{15} and [^{18}F]f_{16} in DMF via [^{11}C]CH_3I

№	Tracer	d_{11}, (mg)	d_{12}, (mg)	NaH, (mol. equiv. to precursor)	TBAH (1M)		T°C/Rtn duration, [min]	RCC, [%]
					V, (µL)	mol. equiv. to precursor		
1.	**[^{18}F]f_{16}**	2.0	-	79.9	-	-	90/3 90/5 90/7	32.5 6.35 2.62
2.	**[^{18}F]f_{16}**	2.0	-	95.9	-	-	90/3 90/4 90/5	15.2 4.69 2.42
3.	**[^{18}F]f_{16}**	2.0*	-	16.0	-	-	60,80,90,100/3	0.34–0.00
4.	**[^{18}F]f_{16}**	2.0	-	16.0	-	-	90/3	28.6
5.	**[^{18}F]f_{16}**	2.0*	-	-	3.0	2.0	60,80,90,100/3	0.50–0.00
6.	**[^{18}F]f_{16}**	2.0	-	-	3.0	2.0	90/3 90/5	34.3 37.8
7.	**[^{18}F]f_{16}**	2.0	-	-	4.0	2.7	90/5	68.1–85.0

8.	**[^{18}F]f$_{16}$**	1.0	-	-	3.0	4.0	90/4	21.7
9.	**[^{18}F]f$_{15}$**	-	2.0	-	4.0	2.7	90/5	88.0
10.	**[^{18}F]f$_{15}$**	-	1.0	-	3.0	4.0	90/5	72.9–89.9
* via [^{11}C]CH_3Otf. Reaction was terminated depending on the observed decrease of the tracer peak.								

7.2.4 Factors that influenced the quantity of precursors used in radiolabeling and conditions for semipreparative purification

The decision to use 2 mg of the precursor in the radiosyntheses was partly influenced by the tendency of the DABTAs to precipitate in aqueous solvent mixtures. Additionally, the conservation of the precursors was a significant consideration, as some building blocks required custom synthesis. The former posed challenges for the SHP of the reaction mixture, as clogging of the tubes during the purification occurred with higher quantities of the precursor. Consequently, after some trials, a quantity of 2 mg was selected, particularly for the halopyridine/pyrimidine DABTAs, which exhibited low solubility in aqueous solvent mixtures. For the two-step radiofluorination, the use of 2.0–2.5 mg of the precursors was necessitated by the fact that these precursors, as indicated by the UV channel during SHP, co-elute with the radiotracer fractions when employed in larger quantities. These phenol/pyrimidinol precursors are sufficiently lipophilic to cross the BBB and saturate binding sites, especially considering the moderate A_m observed for the tracers. Furthermore, they may have unknown biological effects in vivo.

To facilitate the removal of the phenol/pyrimidinol precursors, the basic ion-pairing reagent TBAH (0.01%) was employed: it ionizes them, reduces their retention time, and prevents their co-elution with the tracers. Additionally, it facilitated the removal of unreacted fluoride-18 and other acidic side-products of oxidation and hydrolysis by forming soluble organic salts. This condition was also applied to the non-phenolic DABTAs, which were previously pre-purified before semiprep purification to enhance the RCP of the tracers. This entailed diluting the reaction mixture with water, fixing it in a C-18 cartridge, and subsequently eluting the semi-pure tracer, which was then further purified via SHP. The tracers were typically obtained in high purity but with low RCY. Moreover, certain tracers, such as **[^{18}F]d$_8$** and **[^{18}F]d$_{10}$**, were poorly retained in the cartridge leading to losses during pre-purification. Interestingly, the retained tracers were unexpectedly difficult to elute with MeCN from the cartridge after fixation, leading to further losses. Elution with DMSO or THF resulted in poorly resolved peaks. Pre-purification also led to prolonged exposure to radioactivity. The transition from the acidic ion-pairing reagent TFA to TBAH resulted in approximately double the RCY.

TBAH, of course, has its drawbacks [197], which must be considered when the tracer is intended for patient use. However, the concentration (91 mg/L) at which the base is used is lower than the oral LD50 in rats (500 mg/kg). Given its solubility in water, the concentration is further reduced when the cartridge is rinsed

with water. Interestingly, the ethanol eluate of the tracers obtained from the cartridges thereafter showed a pH ~ 5.5. Although the reason is unclear, this suggests the absence of TBAH in the eluate.

7.3 Binding experiments

7.3.1 In vitro binding assays with recombinant fibrils

In vitro binding experiments using protein aggregates derived from recombinant protein monomers are currently regarded as a high-throughput method for the preliminary screening of α-syn ligands. This approach primarily allows to determine whether the ligands exhibit greater affinity for α-syn or Aβ or tau. Other conclusions are generally avoided, as some tracers that demonstrated high binding affinity to recombinant α-syn may not replicate this potency with human-derived α-syn (**6.4.2.3**) [10]. For instance, **[^{18}F]d_8**, based on the autoradiography experiments (**6.4.2.3**) failed to translate its potency from recombinant α-syn to human-derived DLB α-syn. Nevertheless, due to a scarcity of human brain materials for such binding affinity experiments, the use of recombinant protein aggregates remains a cornerstone for selecting lead α-syn tracers.

Competitive in vitro binding assays were conducted following an established protocol using the tritiated fluorescent probe 4-(dicyanovinyl)julolidine (DCVJ). DCVJ is a pan-amyloid tracer binding to α-syn, Aβ, and tau with nearly equal high affinity (K_d α-syn 4.42 nM, Aβ 8.9 nM, tau 15.6 nM). This characteristic limits its use for selective labeling of α-syn; however, it proves to be a valuable tracer for competitive in vitro binding assays. Its high affinity for these amyloid fibrils allows for the use of lower volumes of the tritiated ligand, thereby minimizing tritium waste. [^{3}H]DCVJ was employed at twice its K_d for the binding experiments with the respective amyloid fibrils (potential adsorption, and pipetting losses were factored in). Due to the limited availability of [^{3}H]DCVJ, the Aβ tracer [^{3}H]PiB was also utilized.

The physicochemical properties of the DABTAs that may have influenced their binding affinity are discussed in greater details in this paper [138]. Therefore, a more concise summary will be provided here. The varying binding binding affinities of the DABTAs to recombinant α-syn, Aβ, and tau can be attributed to the intrinsic effects of the functional groups present in the DABTAs and their electronic effects on the DABTA scaffold (**Table 21**).

Certain conclusions were drawn from the observations made based on the binding affinity (K_i) of the ligands to α-syn, Aβ, and tau aggregates [138] using [^{3}H]DCVJ. However, some of these theories were not upheld when [^{3}H]PiB was used. Unlike the binding assays conducted with [^{3}H]DCVJ, additional components were introduced into the incubation medium for the assays involving [^{3}H]PiB. The effects of these components on the binding affinity of the ligands remain unknown.

i. The methylenedioxy functional group is essential to binding affinity for α-syn, which explains why all the DABTAs in this project contain this moiety.

ii. The presence of EWG substituents directly correlates with a higher binding affinity for α-syn and perhaps with selectivity as well. A notable example is **d_4** and **f_9** (**Table 8**). There was nearly a 1.3-fold reduction in affinity when the fluorine atom in **d_4** was replaced with the fluoroPEG in **f_9** (**Figure 33**). This may also be attributed to the increased tPSA of **f_9**, which facilitates more H-bonding with the aqueous medium and the consequent price of desolvation during binding to α-syn.

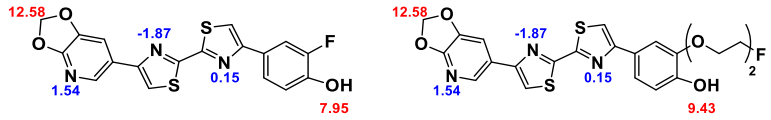

nor-d_4 **nor-f_9**

Figure 33. Illustration of the mesomeric effects of the ortho substituents on the phenyl ring using nor-d_4 and f_9. Color blue: basic pKa, color red: acidic pKa. The K_i of the above compounds were not determined; however, the effects of EWG (nor-**d_4**) and EDG (nor-**f_9**) are better demonstrated by their influence on the acidity of the -OH group.

iii. The positive role of H-bond acceptors in the DABTAs was also recognized, as was the negative role that H-bond donors may have play in diminishing selectivity over Aβ and tau **Figure 34**. For example, **d_1** (K_i 9.0 nM, 12 nM, and 7.0 nM to α-syn, Aβ, and tau, respectively) is not a good α-syn ligand compared to **d_2** (K_i 1.2 nM, >1000 nM, and 241.7 nM to α-syn, Aβ, and tau, respectively). Additionally, the electronic effects of the highly electronegative fluorine functional group should not be overlooked.

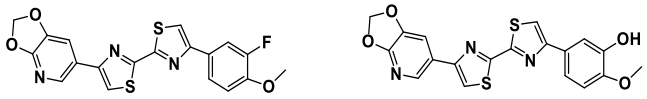

d_2 **d_1**

Figure 34. The effect of a H-bond donor on the binding affinity and selectivity of the DABTAs as shown by d_2 and d_1. It is possible that the -OH groups can form H-bonds with multiple targets, leading to non-specific interactions and reduced selectivity.

iv. In some cases, H-bond acceptors compensated for weaker π–π interactions [198,199]. This was the case for **d_2**, which features a phenyl ring substituted with a methoxy group and a fluorine atom. It exhibited a K_i value for α-syn that was nearly identical to that of **d_6**. In contrast, **d_6** contains a heterocyclic pyridine ring, which is believed to facilitate stronger π–π interactions.

v. The greater the number of heteroaromatic rings a ligand possesses, the higher its affinity for α-syn. Notable examples include **d_2** and **d_4**; **d_6** and **d_8**; **f_4** and **f_5**; **f_7** and **f_{13}** (**Table 8**), likely due to enhanced π–π interactions. Moreover, the protonated [1,3]dioxolo[4,5-b]pyridine at pH 7.4 may participate in

ionic bonding in addition to forming stronger hydrogen bonds. The inability of **d_{10}** and **f_8** to behave like the others may be due to their relatively low solubility in the incubation buffer.

7.3.2 In vitro autoradiography

In vitro autoradiography using diseased (α-synucleinopathies) PHBT is currently a reliable method for evaluating the efficacy of α-syn tracers [10]. While established transgenic rodent models, such as the A53T, A30P, and E46K, exist [200], studies have yet to determine whether the α-syn loads in these models are sufficient for in vivo PET imaging. For example, in **Figure 24**, brain slices obtained from the A53T model showed no distinct binding of **[^{18}F]d_8**. However, since **[^{18}F]d_8** also demonstrated no distinct labeling in the DLB PHBT **Figure 25a**, the prospects for **[^{18}F]d_8** as an α-syn tracer appear bleak.

The inconsistent potency of [^{18}F]d_8 is not uncommon and is actually reminiscent of many published α-syn tracers [10], such as **[^{11}C]MODAG-001** [160], which also displayed exceptional binding affinity to recombinant α-syn as well but none to human-derived α-syn. This descrepancy may be attributed to the previously mentioned PTM [170]. Unlike **[^{11}C]MODAG-001**, [^{18}F]d_8 displayed almost no binding to human-derived Aβ [160] **Figure 25a**. As previously noted, the Aβ load in β-amyloidopathies is at least ≥ 10-fold that of α-syn in the brains of individuals with LBD and MSA, resulting in a higher binding potential [151,152]. Furthermore, a PET study conducted by Fodero-Tavoletti et al revealed that Aβ occupies an area that is two-fold larger in AD subjects compared to those with dementia with DLB. Image quantification of PET images from DLB-Aβ subjects corroborated this finding, suggesting that LB occupy an area that is 30 times smaller than that of Aβ. It is reassuring to note that, based on ELISA analysis, the Aβ concentration in DLB-Aβ subjects is two-fold lower than in AD brain homogenates [201].

Therefore, it is not surprising that even the tracers **[^{18}F]f_5**, **[^{18}F]f_6**, **[^{18}F]f_7**, and **[^{18}F]f_{11}**, which stained α-syn in the PHBT, also stained Aβ in amyloidopathies. However, these tracers were also used at relatively high concentrations (0.2–0.5 MBq/mL) due to the moderate A_m at the time of incubation **Table 7**. This increased the likelihood of non-selective binding to the Aβ plaques. Due to a lack of data on the relative densities of α-syn, Aβ, and tau in PD and other parkinsonism-causing NDD [118], it is currently challenging to determine how these tracers would perform in terms of selectivity in vivo. Fortunately, no binding to tau aggregates was observed.

All the evaluated DABTAs stained GCIs with varying intensities; however, of the twenty-one tracers assessed, only twelve stained LBs in the DLB PHBT. These twelve tracers share a common characteristic: the simultaneous presence of a fluorine atom in the immediate vicinity of an alkoxy group, be it ortho to each other as in **[^{18}F]d_4** or two carbons apart, as in **[^{18}F]f_4** to **[^{18}F]f_{14}**. There is reason to believe that these groups contribute to the potency of the tracers, as those lacking both functional groups did not significantly

stain the DLB PHBT. For instance, **[^{18}F]$\mathbf{d_8}$**, contains only a fluorine atom without an alkoxy group, and **[^{11}C]$\mathbf{f_{15}}$** (an analog of **[^{18}F]$\mathbf{f_5}$**) has a methoxy group but lack a proximate fluorine atom.

The synergistic role of the fluorine atom and the alkoxy group was initially attributed solely to H-bond formation. However, the lack of noticeable LBs binding of **[^{11}C]$\mathbf{f_{18}}$** (an analog of **[^{18}F]$\mathbf{d_4}$**), which contains two H-bond-accepting methoxy group ortho position, dispelled this hypothesis; the additional methoxy group rather diminished binding to LBs **Figure 25a**. Given that the fluorine atom in **[^{18}F]$\mathbf{d_4}$** is a poorer H-bond acceptor than the corresponding methoxy group in **[^{11}C]$\mathbf{f_{18}}$**, this supports our theory regarding the combined effect of the alkoxy group and the fluorine atom on affinity for human-derived LBs. This synergy could potentially be enhanced by other functional groups, such as the pyrimidine and pyridine rings, which strengthen π–π interactions (**[^{18}F]$\mathbf{f_4}$** to **[^{18}F]$\mathbf{f_{13}}$** (**Figure 25b**) compared to **[^{18}F]$\mathbf{f_{14}}$** (**Figure 25c**)), contribute to ionic bonding, and serve as H-bond acceptors. Additionally, the ability of the tracer to be well-solvated in biological media plays a significant role. The poorly soluble **[^{18}F]$\mathbf{f_8}$** ((**Figure 25b**) and **[^{11}C]$\mathbf{f_{16}}$** were unsuccessful, despite containing promising promising functional groups **Table 21**.

The weaker signals observed for **[^{18}F]$\mathbf{f_9}$**, **[^{18}F]$\mathbf{f_{10}}$**, and **[^{18}F]$\mathbf{f_{12}}$** may be partly attributed to the absence of a pyrimidine moiety, which results in a lack of ionic bonding, reduced H-bonding and fewer π–π interactions. In contrast, **[^{18}F]$\mathbf{f_{11}}$** (**Figure 25c**), which lacks both a pyridine and a pyrimidine ring visibly stained the α-syn-containing cingulate gyrus compared to **[^{18}F]$\mathbf{f_{10}}$** (**Figure 25c**). This may be partially explained by the tracer's lipophilicity, which enhances hydrophobic interactions. On the other hand, **[^{18}F]$\mathbf{f_{11}}$**, a more hydrophilic analog (log D 2.8) performed worse than both **[^{18}F]$\mathbf{f_{11}}$** and **[^{18}F]$\mathbf{f_{10}}$** (**Figure 25c**) probably because it lacks either a pyridine or a pyrimidine ring and is insufficiently lipophilic to take advantage of hydrophobic interactions. Nonetheless, it would be intriguing to investigate the impact of double fluoroPEGylation of **[^{18}F]$\mathbf{f_{20}}$** (**Table 21**) on its affinity for LBs versus Aβ compared to **[^{18}F]$\mathbf{f_{10}}$**.

Moreover, extending the length of the fluoroPEG substituent beyond n = 2 may be detrimental to their binding affinity to the fibrils, particularly to the GCIs. This was most evident in the pyrimidine-containing DABTAs **[^{18}F]$\mathbf{f_4}$/[^{18}F]$\mathbf{f_{13}}$** and **[^{18}F]$\mathbf{f_6}$/[^{18}F]$\mathbf{f_7}$**. An increase in polar groups could result in enhanced hydration (solvation) of the molecules. Before these molecules can bind to their respective sites, they must first undergo desolvation. When combined with the energy required to desolvate their solvated α-syn binding sites, the total energy expended in desolvation may be less than the stabilization energy gained from the binding interaction between the tracers and their target sites [202]. Since the fluoroalkoxy group appears to be crucial for the binding of the DABTAs to LBs, making it more polar might adversely affect binding interactions with LBs. Nevertheless, it would be interesting to investigate the effect of the stronger H-bond-accepting iodine atom on the affinity of the DABTAs to LBs when it replaces the fluorine atom, provided

that the larger size of the iodine atom does not present a hindrance. It is planned that **h_{13}**, an analog of **[^{18}F]f_{13}**, will be labeled with either iodine-123 or iodine-124 for SPECT and PET imaging, respectively.

The synergistic impact of the fluorine atom and the alkoxy group appears to have a lesser impact on the interaction of the tracers with the GCIs compared to LBs, as all the tracers stained the former. In this context, other types of interactions may predominate, such as π–π interactions, ionic bonding, or hydrophobic interactions. Furthermore, MSA-extracted α-synuclein filaments are comparatively thicker and exhibit more twists than DLB-extracted ones, suggesting an increased surface area available for tracer binding [203]. Additionally, the quantity of α-synuclein filaments extracted from an MSA brain is greater than that extracted from a DLB brain [204], indicating a higher availability of α-syn for tracer binding, as demonstrated by the autoradiography experiments in **Figure 25a–c**.

On the other hand, it appears that the fluorine atom, alkoxy group, and pyrimidine ring also synergistically enhance the interaction of the tracers with Aβ. This effect was more pronounced in the BFPD tracers, that is, the DABTAs containing a benzodioxole moiety, such as **[^{18}F]f_5**, **[^{18}F]f_6**, and **[^{18}F]f_7**, with the exception of **[^{18}F]f_{11}** and **[^{18}F]f_{14}**. Both **[^{18}F]f_{11}** and **[^{18}F]f_{14}** lack the pyrimidine ring, which may have resulted in reduced staining of Aβ. Moreover, the combination of the methoxy and fluoroPEG groups may have played a role in the case of **[^{18}F]f_{14}** through unknown mechanisms, although increased steric bulk is suspected, which may have hindered the tracer´s ability to fit into its Aβ binding sites. This steric bulk, which was absent in **[^{18}F]d_4**, may explain the observed intense staining of Aβ **Figure 25a**, despite containing the [1,3]dioxolo[4,5-b]pyridine moiety, which seemingly diminished an effective interaction of the DPFPD tracers with Aβ. This phenomenon was also observed with **[^{18}F]f_4**, **[^{18}F]f_{13}**, **[^{18}F]f_{10}**, **[^{18}F]f_9**, **[^{18}F]f_{12}**, and **[^{18}F]f_8**. It could be possible that the protonation of the pyridine moiety in these tracers diminishes the interaction of the [1,3]dioxolo[4,5-b]pyridine moiety with its binding site in Aβ. Interestingly, all the tracers lacking the fluorine atom and alkoxy group combination also displayed reduced staining of Aβ in the Aβ PHBT regardless of the moiety present, whether it was benzodioxole or [1,3]dioxolo[4,5-b]pyridine **Figure 25a**. Thus, the pyrimidine ring may be the main culprit in this case.

The differentiation protocol (**5.4.5.3**) utilized for minimizing non-specific binding was extensively optimized for the fluorine-18 labeled tracers and was modified to accommodate the carbon-11 labeled tracers. This resulted mostly in images with good SNR. However, the conditions must be adjusted based on the physicochemical properties of the specific to ensure that specific binding is not washed away.

Even with a good SNR, partial volume effects (PVE) affected the images due to the spillover of radioactivity. Although fluorine-18 is a low-energy emitter compared to the other positron-emitting radiohalogens bromine-76 and iodine-124 [188,205], its emission energy (634 KeV) is still sufficiently high to cause PVE. This phenomenon was most pronounced in the GCI-laden MSA brain tissues. Nonetheless,

for future in vitro autoradiography, there are plans to radiolabel the most promising tracers with tritium, which has an emission energy of 18.6 keV, to minimize PVE.

Unfortunately, it is not currently possible to confirm the sources of these signals using IHC. However, it is reassuring to note that the signals observed in the autoradiography experiments correlate with the known distribution of the LBs and GCIs in these pathologies.

7.4 In vivo and ex vivo experiments

7.4.1 Biodistribution and in vivo experiments

Even though high binding affinity and selectivity are important parameters in the development of DABTAs, their in vivo pharmacokinetics ultimately determine their clinical utility. The first ever reported DABTA[206], **FS3-1** (**[^{18}F]f$_{11}$**), showed promise as a potential α-syn tracer, demonstrating statistically significant differences between E46K rats and control subjects. Unfortunately, the tracer exhibited pharmacokinetics best described by a three-compartment model (3-TCM) in NHP, due to its relatively high lipophilicity [207]. There was an unexpected slight increase in brain uptake at later time points p.i. This prompted the optimization of the lipophilicity of the DABTAs **Table 8** and **Table 21** in order to achieve optimal brain clearance while maintaining high intial brain uptake. Brain clearance of α-syn tracers is particularly crucial due to the low concentration of the target, especially in the DLB cases **Figure 25a–c**. This necessitates a high SNR, which is essential for uncomplicated kinetic modeling, more accurate quantification, and reproducibility.

The direct pyrimidine analog of **[^{18}F]f$_{11}$**, namely **[^{18}F]f$_5$**, was not easily accessible due to the unavailability of the pyrimdinol building block. Consequently, **[^{18}F]d$_2$**, which features a Csp2–[^{18}F]F bond [208] was synthesized and tested, as it showed reduced Clog P and decreased MW (**Table 8** and **Table 18**), along with potentially improved in vivo stability. Despite these enhancements, **[^{18}F]d$_2$** displayed brain pharmacokinetics reminiscent of **[^{18}F]f$_{11}$**. The other DABTAs containing a Csp2–[^{18}F]F bond (**[^{18}F]d$_4$**, **[^{18}F]d$_6$**, and **[^{18}F]d$_8$**) demonstrated progressively improved brain pharmacokinetics that correlated directly with their lipophilicity **Table 8** and **Table 21** [138] with the exception of **[^{18}F]d$_{10}$**. **[^{18}F]d$_{10}$** displayed generally poor pharmacokinetics due to significant in vivo defluorination **Figure 26** making difficult to ascertain whether it would have exhibited favorable brain pharmacokinetics if this were not the case.

Despite the poor in vivo stability of **[^{18}F]d$_{10}$**, it ignited interest in the pyrimidine ring as a useful moiety in the DABTAs. Tracers **[^{18}F]f$_{4\text{-}8}$** and **[^{18}F]f$_{13}$** contain the pyrimidine ring, but in another position compared to **[^{18}F]d$_{10}$**. The OH group is in a meta position relative to the heterocyclic nitrogen atoms, a set-up that prevents tautomerization. Furthermore, in this position, the pyrimidine nitrogen atoms are sterically hindered, which

inhibits their participation in N-alkylation during both chemical synthesis (**Scheme 4** and **Scheme 5**) and two-step radiofluorination **Scheme 9b.** The OH group in these tracers could also be substituted with [^{18}F]F through ruthenium-mediated deoxyfluorination. This prospective tracer would likely be more stable than **[^{18}F]d$_{10}$** owing to the more favorable meta position of the fluorine atom relative to both nitrogen atoms. However, the feasibility of synthesizing the ruthenium complex was uncertain, as the pyrimidine ring is electron deficient compared to the guaiacol ring in **d$_1$** and **d$_3$**. Thus, more reliable, and cost-effective alternatives were explored, specifically O-fluoroethylation and O-fluoro(oligo)PEGylation of **d$_{11}$** and **d$_{12}$**. This approach facilitated a gradual optimization of the physicochemical properties of the tracers, resulting in the development of eight distinct tracers **Table 21**.

The [^{18}F]fluoroethylated DABTA **[^{18}F]f$_5$** mirrored the brain pharmacokinetics of **[^{18}F]d$_6$**, surpassing it in terms of brain uptake **Figure 26** and **Figure 35**; however, the brain clearance was slower. In contrast, **[^{18}F]f$_4$** failed to replicate the brain uptake observed for **[^{18}F]d$_8$**. It turned out that this might have been caused by the accumulation of the tracer in the lungs at 5 min p.i (**6.5.1**, **Table 9**). Similarly, **[^{18}F]f$_8$** exhibited an even greater tendency for lung accumulation. Both **[^{18}F]f$_4$** and **[^{18}F]f$_8$** share the same core structure suggesting that this core may possess a high affinity for pulmonary tissue, an affinity modulated by the substituents at the –OH group. Hence, it is likely that the low brain uptake is attributable to the significant pulmonary sequestration of the tracers.

[^{18}F]f$_6$, a [^{18}F]fluoroPEGylated (n = 2) derivative of **[^{18}F]f$_5$**, demonstrated improved brain clearance compared to its predecessor, **[^{18}F]f$_5$**, although it exhibited decreased yet still optimal brain uptake **Figure 26**. Conversely, no improvement in brain pharmacokinetics was observed for **[^{18}F]f$_8$**, the [^{18}F]fluoroPEGylated (n = 2) derivative of **[^{18}F]f$_4$** as it was markedly retained in the lungs. To further enhance brain clearance, **[^{18}F]f$_6$** was further derivatized by extending its fluoroPEG chain (to 2-(2-(2-fluoroethoxy)ethoxy)ethyl) to obtain **[^{18}F]f$_7$**. **[^{18}F]f$_7$** exhibited interesting in vitro properties: an unexpected decrease in *fp* and increased log D 2.7 compared to the 2.5 observed for **[^{18}F]f$_6$** (**Table 8**), which was the contrary to their Clog P **Table 21**. Although the accuracy of the log D of **[^{18}F]f$_7$** was initially questioned, a biodistribution study with the tracer confirmed its accuracy, revealing a higher brain uptake of **[^{18}F]f$_7$** compared to its predecessor **[^{18}F]f$_6$** (**Figure 26** and **Figure 35**).

These properties exhibited by **[^{18}F]f$_7$** can be ascribed to its extended [^{18}F]fluoroPEG-chain (n = 3). The additional lipophilic ethyl component enhances brain uptake, while the oxygen atom increased the hydrophilicity of the tracer. This combination results in reduced uptake in peripheral tissues, hence increased brain bioavailability of the tracer and faster brain clearance. It is suspected that the brain uptake of **[^{18}F]f$_5$** may have been higher if peripheral uptake had been minimal, since it has also has a lower MW than **[^{18}F]f$_7$**

Table 21 [209]. Despite the seemingly contradictory properties of **[^{18}F]f$_7$**, it displayed faster brain kinetics than **[^{18}F]f$_5$** and **[^{18}F]f$_6$** as anticipated.

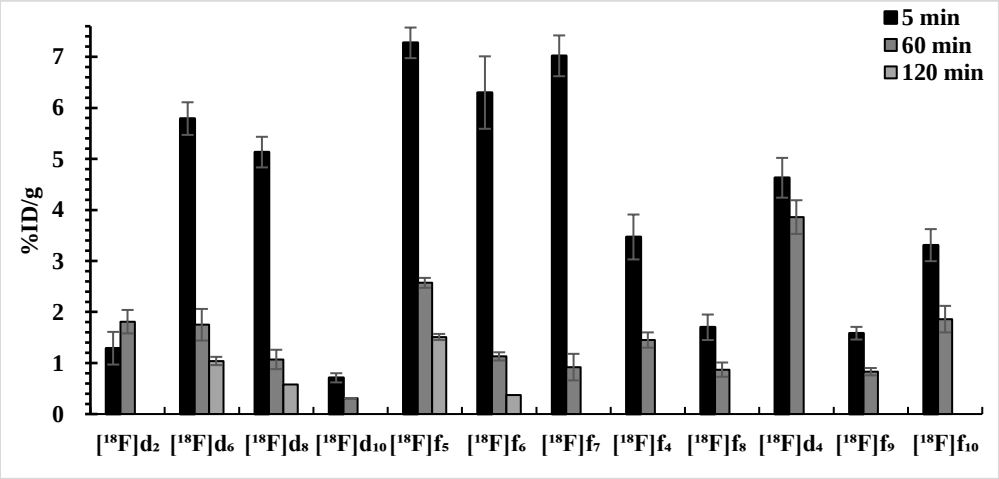

Figure 35. The brain pharmacokinetics of the DABTAs. The low brain bioavailability displayed by **[^{18}F]d$_{10}$** was mainly due to its overall instability and not due to uptake in peripheral tissues.

The success of **[^{18}F]f$_7$** led to the [^{18}F]fluoroPEGylation of the suboptimal **[^{18}F]d$_4$** and its guaiacol precursor **d$_3$** resulting in the tracers **[^{18}F]f$_{10}$** and **[^{18}F]f$_9$**. However, this endeavor yielded only minimal success. Compared to their predecessor **[^{18}F]d$_4$**, both tracers exhibited lower brain uptake. **[^{18}F]d$_4$**, **[^{18}F]f$_9$**, and **[^{18}F]f$_{10}$** serve as prime examples of the interplay between MW, log D, and tPSA on the brain pharmacokinetics of the DABTAs. Brain uptake at 5 min p.i. increased with increasing lipophilicity, following the order [**^{18}F]f$_9$** < **[^{18}F]f$_{10}$** < **[^{18}F]d$_4$**. The higher brain uptake of the larger **[^{18}F]f$_{10}$** compared to **[^{18}F]f$_9$** could be attributed to their phenyl ring substituents, since both contain the same amount of H-bond-accepting oxygen atoms.

However, **[^{18}F]f$_{10}$** contains an additional small hydrophobic C(sp2)F-bonded fluorine atom [210], which may have facilitated its diffusion across the BBB. The celerity of brain clearance, on the other hand, correlated with the tPSA of the tracers, with the order being **[^{18}F]d$_4$** ≪ **[^{18}F]f$_{10}$ < [^{18}F]f$_9$**. Among the three tracers, **[^{18}F]f$_{10}$** remains a candidate for optimization to enhance its brain pharmacokinetics.

Generally, increased polarity negatively impacts the ability of ligands to permeate the BBB, particularly when combined with higher MW. However, these principles are conditional and depend on the specific ligand, including the position of the polar group and the spatial arrangement of the molecule in terms of size. Despite its large size, **[^{18}F]f$_7$**, may have been able to cross the BBB using its benzodioxole moiety rather than relying on its fluoroPEGylated (n = 3) pyrimidine ring for brain uptake. The latter may have instead played a major role in the brain clearance of **[^{18}F]f$_7$** and its reduced peripheral accumulation. This rationale informed the development of **[^{18}F]f$_{13}$**, despite the unfavorable pharmacokinetics displayed by its predecessor, **[^{18}F]f$_8$**.

Table 21. Comparison of the DABTAs based on their MW, tPSA and Clog P

№	Tracer	Structure (with the pK_a of the heterocyclic nitrogen shown)	MW [g/mol]	tPSA	Clog P
1.	**[^{18}F]d$_2$**	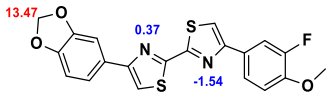	412.5	52.4	5.47
2.	**[^{18}F]d$_4$**	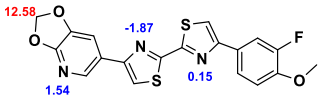	413.5	64.8	4.78
3.	**[^{18}F]d$_6$**	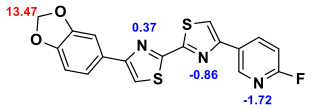	383.4	55.5	4.19
4.	**[^{18}F]d$_8$**	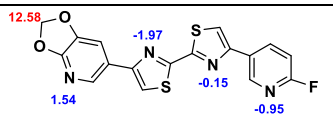	384.4	67.9	3.50
5.	**[^{18}F]d$_{10}$**	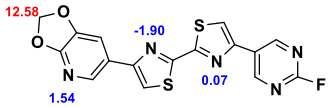	385.4	80.4	2.50
6.	**[^{18}F]d$_{17}$**	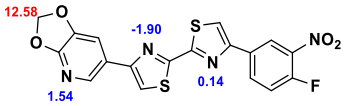	428.4	107.4	4.34
7.	**[^{18}F]d$_{19}$**	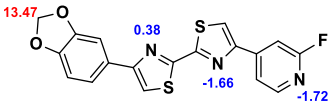	383.4	55.5	4.19
8.	**[^{18}F]d$_{21}$**	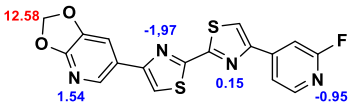	384.4	67.9	3.50
9.	**[^{18}F]f$_4$**	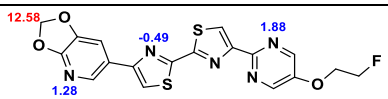	429.4	89.5	3.35
10	**[^{18}F]f$_5$**	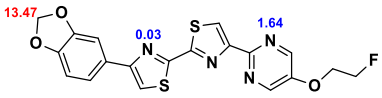	428.5	77.1	4.04
11.	**[^{18}F]f$_6$**	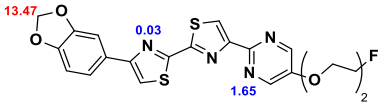	472.5	86.4	3.79
12.	**[^{18}F]f$_7$**	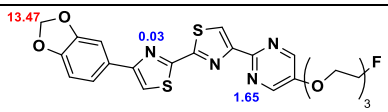	515.6	95.6	3.61
13.	**[^{18}F]f$_8$**	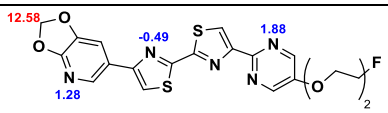	472.5	98.7	3.10
14.	**[^{18}F]f$_9$**	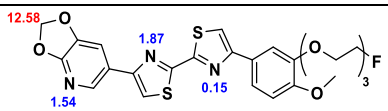	500.6	83.2	4.48

15.	**[^{18}F]f$_{10}$**	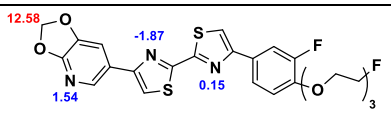	532.6	83.2	4.61
16.	**[^{18}F]f$_{11}$**	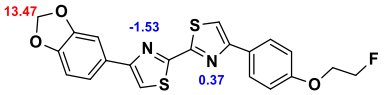	426.5	52.4	5.70
17.	**[^{18}F]f$_{12}$**	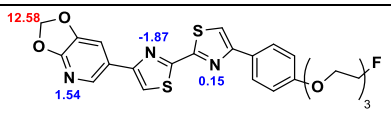	515.6	83.2	4.59
18.	**[^{18}F]f$_{13}$**	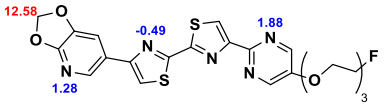	517.3	108.0	2.93
19.	**[^{18}F]f$_{14}$**	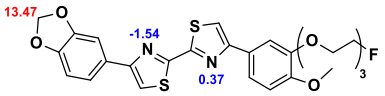	514.6	88.1	4.99
20.	**[^{11}C]f$_{15}$**	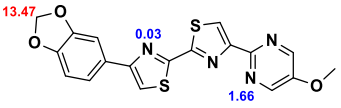	396.4	77.1	3.78
21.	**[^{11}C]f$_{16}$**	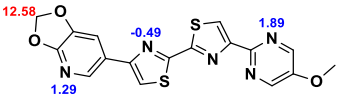	397.4	89.5	3.10
22.	**[^{11}C]f$_{17}$**	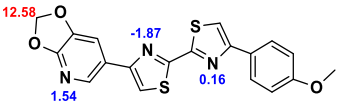	395.5	64.8	4.76
23.	**[^{11}C]f$_{18}$**	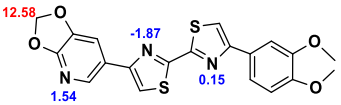	425.48	74.0	4.48
24.	**[^{11}C]f$_{19}$**	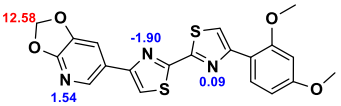	425.5	74.0	4.27
25.	**[^{18}F]f$_{20}$**	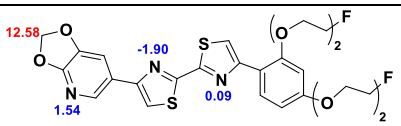	577.6	92.5	4.27

Some of the tracers supported the hypothesis, which posits that the DABTAs partition across the BBB primarily using their most lipophilic moiety, when the overall hydrophilicity of the tracer increases. The tracer **[^{18}F]d$_8$** exhibited a brain uptake of 5.13 %ID/g, nearly equivalent to that of **[^{18}F]d$_6$**, which had a brain uptake of 5.79 %ID/g, despite containing the [1,3]dioxolo[4,5-b]pyridine moiety. This moiety appears to hinder the performance of other [1,3]dioxolo[4,5-b]pyridine tracers probably due to H-bond formation. This suggests that **[^{18}F]d$_8$** may have predominantly partitioned via its fluoropyridine moiety that features a minimally basic nitrogen atom, whose tendency to protonate at physiological pH is reduced along with its H-bonding capabilities. In contrast, **[^{18}F]d$_4$** contains a -OCH_3 group with a relatively higher H-bond-forming ability (4.63 %ID/g). The presence of the [1,3]dioxolo[4,5-b]pyridine ring in both **[^{18}F]d$_2$** and **[^{18}F]d$_6$** likely

reduced the peripheral uptake of these tracers compared to their respective predecessors, **[^{18}F]d$_2$** and **[^{18}F]d$_6$**, resulting in enhanced brain uptake. This also explains why the brain uptake of **[^{18}F]f$_{10}$** surpassed that of **[^{18}F]f$_9$**; the substituted phenyl ring in **[^{18}F]f$_{10}$** is more lipophilic. **[^{18}F]f$_{14}$**, which contains a benzodioxole moiety, may display a higher brain uptake than **[^{18}F]f$_{10}$**, but with similar or worse brain clearance.
For the remaining unevaluated tracers, their brain pharmacokinetics can be predicted based on the evaluated tracers with similar functional groups or lipophilic profiles **Table 21**. The brain uptake of **[^{18}F]d$_{17}$** may be inferior to that of **[^{18}F]d$_4$**, due to the charge on the nitro group. If it crosses the BBB, brain clearance is expected to be faster compared to **[^{18}F]d$_4$** owing to its higher tPSA. **[^{18}F]d$_{19}$** and **[^{18}F]d$_{21}$** are expected to replicate the brain pharmacokinetics of their structural isomers **[^{18}F]d$_6$** and **[^{18}F]d$_8$**, respectively. **[^{18}F]f$_{12}$** may exhibit superior brain pharmacokinetics compared to its Csp2–F-containing predecessor, **[^{18}F]f$_{10}$**, which is more lipophilic and relatively heavier.

The carbon-11-labeled tracers (**[^{11}C]f$_{15}$**, **[^{11}C]f$_{16}$**, **[^{11}C]f$_{17}$**, and **[^{11}C]f$_{18}$**) will benefit from possessing a relatively lower MW **Table 21**, which could enhance brain penetrance. Furthermore, **[^{11}C]f$_{16}$** may also be susceptible to pulmonary retention as **[^{18}F]f$_8$** due to its low solubility. Lacking a fluorine atom, the role of the fluorine atom in the pulmonary accumulation of the tracers with the **d$_{11}$** core structure (**[^{18}F]f$_4$** and **[^{18}F]f$_8$**) can be evaluated using **[^{11}C]f$_{16}$**. The brain uptake of **[^{11}C]f$_{15}$** may be lower than that of its [^{18}F]fluoroalkylated derivative **[^{18}F]f$_5$** due to the absence of the hydrophobic [^{18}F]fluoroethyl group. The same applies to **[^{11}C]f$_{16}$** in comparison to **[^{18}F]f$_4$** (**Scheme 2**).

7.4.2 In vivo stability

All the tracers displayed minimal defluorination except for **[^{18}F]d$_{10}$**. This was revealed by the high bone signal observed in the biodistribution experiments **Figure 26** and **Figure 36** The ortho-position of [^{18}F]F between the pyrimidine nitrogen atoms was detrimental to its in vivo stability. This indicates that although the Csp2–F bond is one of the strongest bonds in organic chemistry, a ring substituent could, via mesomeric and inductive effects, affect its stability, as was the case for **[^{18}F]d$_{10}$**. The rest of the evaluated DABTAs showed <5%ID/g bone uptake. Even the tracers with the relatively weaker Csp3–F bonds, that is, the fluoroethylated/PEGylated DABTAs exhibited in vivo resistance to defluorination.

In ex vivo metabolite experiments conducted on healthy mice (**5.5.2**), the objective of which was to determine the source of the signals obtained in the biodistribution experiments, be it from the injected tracers or their radiometabolites. The results indicated that there were no detectable radiometabolites (<<1%) from the 6-fluoropyridine DABTAs (**[^{18}F]d$_6$** and **[^{18}F]d$_8$**) that crossed the blood-brain barrier (BBB). In contrast, the [^{18}F]fluoroethylated/PEGylated tracers exhibited minimal brain radiometabolites (<4%) for the promising candidates evaluated, namely**[^{18}F]f$_4$**, **[^{18}F]f$_5$**, **[^{18}F]f$_6$**, and **[^{18}F]f$_7$**. The brain radiometabolites are

suspected to be products of O-[^{18}F]defluoroethylation/PEGylation, based on their retention times in the chromatograms **Figure 27**. O-[^{18}F]defluoroethylation has been documented in the literature as one of the metabolic pathways for tracers such as **[^{18}F]f$_4$** and **[^{18}F]f$_5$** [208,211].

O-[^{18}F]defluoroethylation is followed by the oxidation of the 2-[^{18}F]fluoroethanol to form the corresponding aldehyde (2-[^{18}F]fluoroacetaldehyde), which is subsequently converted to the carboxylic acid 2-[^{18}F]fluoroacetate. The metabolic is ultimately transformed into 2-[^{18}F]fluoroacetyl-CoA **Scheme 13**. 2-[^{18}F]fluoroacetyl-CoA remains trapped within the cell and subsequently enters the tricarboxylic acid cycle [93,211,212].

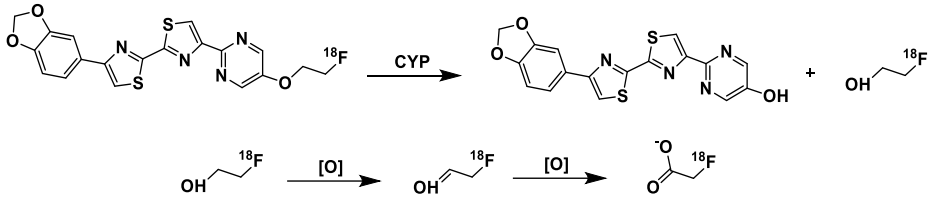

Scheme 13. Scheme of the O-de[^{18}F]fluoroalkylation of the [^{18}F]fluoroethylated DABTAs. O-de[^{18}F]fluoroalkylation was significant for **[^{18}F]f$_9$**, which bears an EDG (-OCH$_3$) that apparently activates the ring toward electrophilic substitution reactions facilitated by CYP enzymes.

It was reported by Pan et al. that 2-[^{18}F]fluoroethanol significantly crosses the BBB [211], suggesting that the more lipophilic 2-[^{18}F]fluoroacetaldehyde also crosses the BBB. Since these radiometabolites are highly brain-penetrant, their brain uptake is dependent on the susceptibility of the tracers to biotransformation and the turnover rate of the radiometabolites. It is suspected that the [^{18}F]fluoroPEGylated tracers also undergo such biotransformation resulting in the formation of the corresponding alcohol, aldehyde, and carboxylic acid **Scheme 13**. An examination of the brain chromatograms in **6.5.2**, **Figure 27**, indicates that the [^{18}F]fluoroPEGylated DABTAs are likely more susceptible to O-de[^{18}F]fluoroPEGylation than the [^{18}F]fluoroethylated tracers. O-de[^{18}F]fluoroPEGylation was most pronounced in **[^{18}F]f$_9$**, reaching up to 10% at 20 min p.i. The electron-donating fluoroPEG, positioned ortho to methoxy group, appears to reduce the strength of the O-CH$_3$ bond[213]. Biotransformation via O-demethylation is also possible for the methoxy containing **[^{18}F]d$_2$**, **[^{18}F]d$_8$**, **[^{18}F]f$_{14}$**, and all the carbon-11-labeled tracers.

Bearing the methylenedioxy group, all the DABTAs are also susceptible to O-demethylation **Scheme 14** [214,215]. This results in the formation of catechol radiometabolite and either formic acid or carbon monoxide, depending on the metabolic way. It is suspected that the more lipophilic radiometabolites, which eluted shortly before the parent tracer **Figure 27**, as shown in the chromatograms of the O-[^{18}F]fluoroethylated/pegylated tracers, may be the catechol radiometabolites.

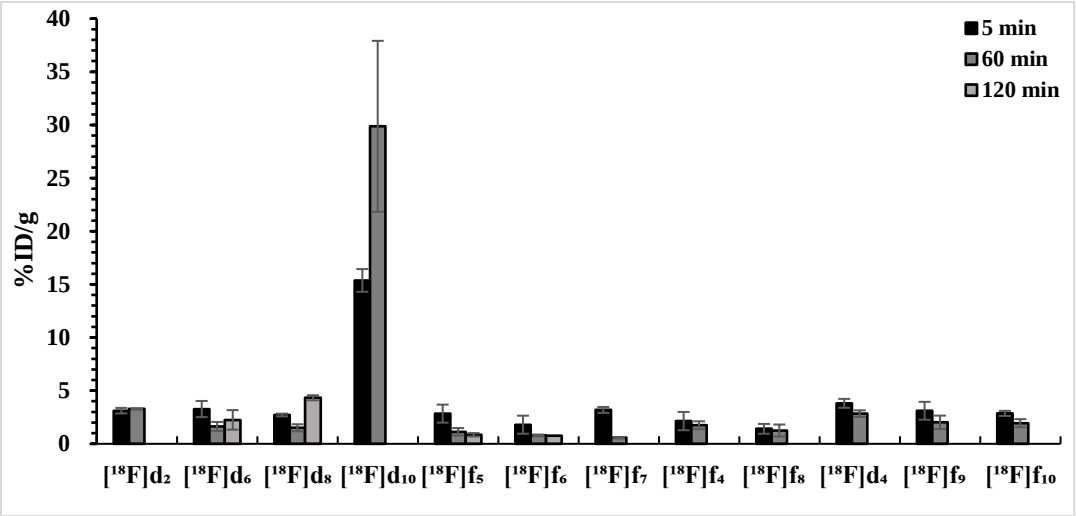

Figure 36. De[^{18}F]fluorination as shown by the bone-uptake of fluorine-18. [^{18}F]d$_{10}$ was the only DABTA that showed significant in vivo defluorination due to the precarious position of fluorine-18 in the molecule.

Their brain penetration should be minimal since they are highly polar alongside the also polar O-[^{18}F]fluoroethylated/pegylated pyrimidinyl and phenyl moieties. The absence of the 6-[^{18}F]fluoropyridine tracers ((**[^{18}F]d$_6$** and **[^{18}F]d$_8$**) in the brain may indicate that these tracers underwent de[^{18}F]fluorination prior to O-demethylation. Alternatively, it could suggest that the O-[^{18}F]fluoroethylated/pegylated groups in **[^{18}F]f$_4$**, **[^{18}F]f$_5$**, **[^{18}F]f$_6$**, **[^{18}F]f$_7$**, and **[^{18}F]f$_9$** enhanced brain uptake.

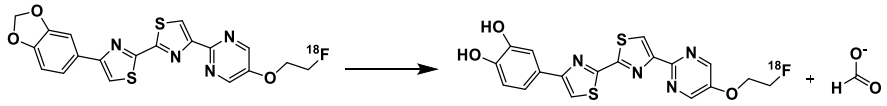

Scheme 14. The O-demethylation of the DABTAs via the methylenedioxy group. As with O-de[^{18}F]fluoroalkylation, the tracers bearing the electron-rich benzodioxole moiety are more susceptible to O-demethylation than those containing the electron-deficient pyridyldioxole moiety.

Apart from the two metabolic pathways described above, there may be additional biotransformation pathways for the DABTA tracers that lead to the formation of brain-permeable radiometabolites. Regardless of the metabolic pathway, the majority of the assessed DABTAs showed optimal plasma stability. More than 60–80% of the parent tracers remained unchanged in the plasma at 20 min p.i. with the exception of **[^{18}F]f$_9$**. **[^{18}F]f$_9$** appeared to be unstable to O-de[^{18}F]fluoroPEGylation at 20 min p.i.; only 45% of the parent tracer was found in the plasma. This corroborates the hypothesis that the quantity of brain radiometabolites found in the brain is a function of their turnover in the periphery. Notably, of all the evaluated tracers, **[^{18}F]f$_9$** is the only one thus far to display up to 6% brain radiometabolites.

8. CONCLUSION

The challenges associated with developing suitable α-syn tracers were discussed in **4.5.5**. Some of these challenges were addressed by designing our tracers based on a 4,4'-diaryl-2,2'-bithiazole (DABTA) scaffold. The DABTA scaffold consists of planar, hydrophobic aromatic rings. These properties facilitate interaction with binding sites: planarity enables stacking over aromatic amino acid residues, while hydrophicity promotes hydrophobic interaction. The π systems in the aromatic rings—regions of diffuse high electron density—can serve as effective hydrogen bond acceptors in binding sites containing strong H-bond donors, such as protonated lysine residues. Additionally, hydrophobicity facilitates the partitioning of the tracers across the BBB to reach the α-syn target. The thiazole rings also contain hydrogen bond acceptors, including the nitrogen atom and the less effective sulfur atom. The next step involved fine-tuning these intrinsic properties to develop tracers with optimal binding affinity for α-syn, selectivity over Aβ and tau, as well as optimal pharmacokinetics.

By meticulously modifying the physicochemical properties of the DABTAs, guided by *in silico* modeling, various functional groups were incorporated into the molecules. This approach led to the development of DABTAs with optimal pharmacokinetics, as well as high affinity and selectivity. The project began with the chemical synthesis of both the precursors and the standard compounds. For the most promising tracers, precursor synthesis was optimized, resulting in higher chemical yields (CY) **Table 5**. Although optimizing chemical synthesis was time-consuming, the primary bottleneck was the acquisition of the building blocks. Some building blocks were not readily available and had to be custom-synthesized, which required considerable time. This represented one of the unavoidable challenges in brain tracer development.

Even though established protocols exist for radiofluorination and carbon-11 labeling, each precursor and tracer possesses unique physicochemical properties that requires optimization of radiosynthesis parameters such as T°C, pH, solvent, and reaction duration. The optimization of pH and T°C was particularly important in the radiosynthesis of **[^{18}F]d$_8$** and **[^{18}F]d$_{10}$** (**Table 10** and **Table 11**). The radiosynthesis of some tracers compelled a solvent change from DMSO to MeCN (**Table 16** and **Table 17**). Notable examples include tracers obtained via direct S_N2 reactions, like **[^{18}F]f$_9$** and **[^{18}F]f$_{10}$**. Others required changing the leaving group, as seen with **[^{18}F]f$_5$** and **[^{18}F]f$_7$** (**Table 12** and **Table 15**). Both the second steps of two-step radiofluorination and [^{11}C]carbon labeling also required optimization of pH (base) and T°C. Nonetheless, some tracers, such as **[^{18}F]d$_6$** and **[^{18}F]f$_6$**, were synthesized easily without extensive optimization.

Other factors influencing the realization of the tracers in high RCY were also optimized, including the amount of precursor used in the radiosynthesis and SHP. The former is preferably increased only when adjustments to other parameters prove ineffective, as high quantities of hydrophobic precursors complicate

SHP. Typically, 1.0–2.5 mg of the precursors was used in this project, except for the ruthenium complexes, which required 7 mg. Fortunately, the ruthenium complexes are soluble salts, and did not complicate the purification process. For the carbon-11 labeling of **[^{11}C]f$_{15}$**, the amount of the lipophilic precursor **d$_{12}$** used was reduced to 1 mg to improve its separation from **[^{11}C]f$_{15}$**. Additionally, SHP was optimized by using the base-pairing agent TBAH in the eluents in most cases, instead of the commonly used acid-pairing agent TFA, to enhance the separation of the tracers from their precursors.

The optimization of radiosynthesis resulted in moderate to high RCY for both the direct (over 40% was possible) and two-step (reaching up to 72%) radiofluorination **Table 6**. The A_m were also high in some cases **Table 7**, particulary for the ruthenium-mediated S_NAr obtained tracers [^{18}F]**d$_2$** and **[^{18}F]d$_4$** (>85 GBq/μmol)**.** For the other tracers, it was moderate, reaching >45 GBq/μmol. Two-step radiolabeling afforded higher A_m than their one-step counterparts. This difference was most pronounced in **[^{18}F]f$_{10}$**, which contains fluoride-19 in its precursor; the one-step radiofluorination of **[^{18}F]f$_{10}$** resulted in molar activities that were half those obtained via the two-step method.

In vitro competitive binding assays with recombinant fibrils, conducted using established protocols, proceeded relatively smoothly except for the dissolution of some standard compounds in DMSO. **f$_8$** and **f$_{16}$** were notably more difficult to dissolve compared to other hard-to-dissolve standards such as **d$_8$** and **d$_{10}$**, which also exhibited a lower tendency to dissolve. Consequently, accurate in vitro competitive binding experiments could not be performed with these compounds. his difficulty may also explain their poor autoradiography results with MSA and DLB PHBT **Figure 25b** compared to their analogs **[^{18}F]f$_4$** and **[^{18}F]f$_{13}$** **Figure 27**, as well as their suboptimal in vivo pharmacokinetics **Figure 26**.

All the evaluated standards demonstrated high binding affinity to α-syn and selectivity over Aβ and tau. Although some failed to faithfully translate this potency to human-derived fibrils in in vitro autoradiography experiments, the results remained encouraging. In vitro autoradiography with PHBT further aided in identifying DABTAs such as **[^{18}F]d$_8$**, **[^{18}F]f$_4$**, **[^{18}F]f$_5$**, **[^{18}F]f$_6$**, **[^{18}F]f$_7$**, and **[^{18}F]f$_{13}$** as promising candidates for further evaluation in animal models of α-synucleinopathy. This approach also underscored the importance of certain functional groups including the alkoxy group, the fluorine atom, and the [1,3]dioxolo[4,5-b]pyridine ring in the DABTAs. The tritiation of **[^{18}F]f$_7$** and **[^{18}F]f$_6$** is planned to facilitate more accurate quantification of signals in future in vitro autoradiography experiments.

Another important parameter evaluated was the in vivo pharmacokinetics of the tracers in healthy mice (**6.5.1**). This was primarily assessed through ex vivo biodistribution studies. Additional in vivo PET-based biodistribution studies were conducted for **[^{18}F]d$_6$** and **[^{18}F]d$_8$**. Since it was impossible to inject all the mice simultaneously and harvest the required organs at the necessary time points during the biodistribution

studies, it was essential to obtain the tracers with a high radiochemical yield (RCY) to compensate for the time loss. This necessity drove the extensive optimization of the radiosynthesis for some of the tracers; the short half-life of fluorine-18 also contributed to this decision. Furthermore, solubilizing these lipophilic tracers in the injection solution was crucial, as some were prone to precipitation in aqueous solutions. This may likely not be due to the tracers themselves, which are usually in less than femtomolar concentrations, but rather the unlabeled impurities that co-elute with the tracers during SHP. Thus, PBS was avoided because it caused the precipitation of these impurities. Instead, saline solution was used, together with solubilizers such as DMSO and Tween-20 to prevent precipitation.

Biodistribution studies were conducted to evaluate the blood-brain barrier (BBB) permeability of the tracers. Some of the tracers demonstrated impressive brain uptake (3.5–7.3%ID/g) at 5 min p.i., in the following order: **[^{18}F]f$_{10}$** < **[^{18}F]f$_4$** < **[^{18}F]d$_4$** < **[^{18}F]d$_8$** < **[^{18}F]d$_6$** < **[^{18}F]f$_6$** < **[^{18}F]f$_7$** < **[^{18}F]f$_5$**. High SNR is crucial for accurate quantification of α-syn in the brain and helps avoid complex kinetic modeling; therefore, brain clearance was also an important parameter assessed in this study. Among the tracers, **[^{18}F]f$_7$** was the most notable, exhibiting a high brain uptake of 7.0 %ID/g at 5 minutes p.i. and achieving up to 86.9% brain clearance at 60 minutes p.i. Other tracers, such as [**^{18}F]d$_8$** and **[^{18}F]f$_6$** achieved similar results only after 120 minutes p.i. These results indicate that introducing fluorine-18 via the hydroxyl group ([^{18}F]fluoroethylation/PEGylation) provides sufficient flexibility to modify the physicochemical properties of the DABTAs without significantly affecting their binding affinity for α-syn. From an economic perspective, this method is also more cost-effective than modifying the molecular scaffold itself.

The introduction of fluorine-18 via [^{18}F]fluoroethylation/PEGylation has also its drawbacks. Two of the most promising [^{18}F]fluoroethylated tracers, **[^{18}F]f$_7$** and **[^{18}F]f$_6$**, showed brain radiometabolites, although minimal (< 3%) at 20 min p.i. **Figure 27**, compared to [**^{18}F]d$_6$** and **[^{18}F]d$_8$**, which showed none at the same time point. To ensure accurate quantification of specific signals, tracers are expected to show little to no radiometabolites in the brain. In humans, who have a relatively slower metabolism compared to mice, the turnover rate of radiometabolites may also be slower. Bone (skull) uptake of free [^{18}F]fluorides, resulting from in vivo de[^{18}F]fluorination, can also lead to inaccurate signal quantification. This uptake was minimal for all the tracers (< 5%ID/g) except for **[^{18}F]d$_{10}$** (**Figure 36**).

In conclusion, during the project, it was possible to modify the pharmacokinetics of the DABTAs along with their binding affinity to develop tracers suitable for the in vivo detection of α-synuclein in patients with α-synucleinopathies.

9. REFERENCES

1. Lekoubou, A.; Echouffo-Tcheugui, J.B.; Kengne, A.P. Epidemiology of neurodegenerative diseases in sub-Saharan Africa: a systematic review. *BMC Public Health* **2014**, *14*, 653, doi:10.1186/1471-2458-14-653.
2. Neurodegenerative diseases - Latest research and news | Nature. Available online: https://www.nature.com/subjects/neurodegenerative-diseases (accessed on 6 March 2022).
3. JPND | Neurodegenerative Disease Research. What? | JPND. Available online: https://www.neurodegenerationresearch.eu/what/ (accessed on 6 March 2022).
4. Jackson, W.S. Selective vulnerability to neurodegenerative disease: the curious case of Prion Protein. *Dis. Model. Mech.* **2014**, *7*, 21–29, doi:10.1242/dmm.012146.
5. Moussaud, S.; Jones, D.R.; Moussaud-Lamodière, E.L.; Delenclos, M.; Ross, O.A.; McLean, P.J. Alpha-synuclein and tau: teammates in neurodegeneration? *Mol. Neurodegener.* **2014**, *9*, 43, doi:10.1186/1750-1326-9-43.
6. Alafuzoff, I.; Hartikainen, P. Alpha-synucleinopathies. *Handb. Clin. Neurol.* **2017**, *145*, 339–353, doi:10.1016/B978-0-12-802395-2.00024-9.
7. Brás, I.C.; Dominguez-Meijide, A.; Gerhardt, E.; Koss, D.; Lázaro, D.F.; Santos, P.I.; Vasili, E.; Xylaki, M.; Outeiro, T.F. Synucleinopathies: Where we are and where we need to go. *J. Neurochem.* **2020**, *153*, 433–454, doi:10.1111/jnc.14965.
8. Galvin, J.E.; Lee, V.M.; Trojanowski, J.Q. Synucleinopathies: clinical and pathological implications. *Arch. Neurol.* **2001**, *58*, 186–190, doi:10.1001/archneur.58.2.186.
9. Braak, H.; Del Tredici, K.; Rüb, U.; Vos, R.A.I. de; Jansen Steur, E.N.H.; Braak, E. Staging of brain pathology related to sporadic Parkinson's disease. *Neurobiology of Aging* **2003**, *24*, 197–211, doi:10.1016/S0197-4580(02)00065-9.
10. Korat, Š.; Bidesi, N.S.R.; Bonanno, F.; Di Nanni, A.; Hoàng, A.N.N.; Herfert, K.; Maurer, A.; Battisti, U.M.; Bowden, G.D.; Thonon, D.; et al. Alpha-Synuclein PET Tracer Development-An Overview about Current Efforts. *Pharmaceuticals (Basel)* **2021**, *14*, doi:10.3390/ph14090847.
11. Spillantini, M.G.; Goedert, M. The alpha-synucleinopathies: Parkinson's disease, dementia with Lewy bodies, and multiple system atrophy. *Ann. N. Y. Acad. Sci.* **2000**, *920*, 16–27, doi:10.1111/j.1749-6632.2000.tb06900.x.
12. Parkinson Disease: Practice Essentials, Background, Anatomy. Available online: https://emedicine.medscape.com/article/1831191-overview#a3 (accessed on 17 April 2022).
13. Wichmann, T. Deep-Brain Stimulation for Neurologic and Neuropsychiatric Disorders. In *Handbook of basal ganglia structure and function*, Second edition; Steiner, H., Tseng, K.-Y., Eds.; Academic Press: Amsterdam, 2017; pp 971–995, ISBN 9780128022061.
14. Forno, L.S. Neuropathology of Parkinson's disease. *J. Neuropathol. Exp. Neurol.* **1996**, *55*, 259–272, doi:10.1097/00005072-199603000-00001.
15. Mandel, S.A.; Morelli, M.; Halperin, I.; Korczyn, A.D. Biomarkers for prediction and targeted prevention of Alzheimer's and Parkinson's diseases: evaluation of drug clinical efficacy. *EPMA J.* **2010**, *1*, 273–292, doi:10.1007/s13167-010-0036-z.
16. Halliday, G.; Murphy, K. Pathology of Parkinson's Disease. In *Movement disorders 4*; Fahn, S., Lang, A.E., Schapira, A.H.V., Eds.; Saunders/Elsevier: Philadelphia, Pa., 2010; pp 132–154, ISBN 9781416066415.
17. Zafar, S.; Yaddanapudi, S.S. *StatPearls*: *Parkinson Disease;* Treasure Island (FL), 2022.
18. Deleidi, M.; Maetzler, W. Protein clearance mechanisms of alpha-synuclein and amyloid-Beta in lewy body disorders. *Int. J. Alzheimers. Dis.* **2012**, *2012*, 391438, doi:10.1155/2012/391438.
19. McKeith, I.; Mintzer, J.; Aarsland, D.; Burn, D.; Chiu, H.; Cohen-Mansfield, J.; Dickson, D.; Dubois, B.; Duda, J.E.; Feldman, H.; et al. Dementia with Lewy bodies. *The Lancet Neurology* **2004**, *3*, 19–28, doi:10.1016/S1474-4422(03)00619-7.
20. Outeiro, T.F.; Koss, D.J.; Erskine, D.; Walker, L.; Kurzawa-Akanbi, M.; Burn, D.; Donaghy, P.; Morris, C.; Taylor, J.-P.; Thomas, A.; et al. Dementia with Lewy bodies: an update and outlook. *Mol. Neurodegener.* **2019**, *14*, 5, doi:10.1186/s13024-019-0306-8.
21. Haider, A.; Spurling, B.C.; Sánchez-Manso, J.C. *StatPearls*: *Lewy Body Dementia;* Treasure Island (FL), 2022.
22. Lewy Body Dementia: Practice Essentials, Background, Etiology. Available online: https://emedicine.medscape.com/article/1135041-overview#a3 (accessed on 18 April 2022).

23. Fillenbaum, G.G.; van Belle, G.; Morris, J.C.; Mohs, R.C.; Mirra, S.S.; Davis, P.C.; Tariot, P.N.; Silverman, J.M.; Clark, C.M.; Welsh-Bohmer, K.A.; et al. Consortium to Establish a Registry for Alzheimer's Disease (CERAD): the first twenty years. *Alzheimers. Dement.* **2008**, *4*, 96–109, doi:10.1016/j.jalz.2007.08.005.
24. Mayo, M.C.; Bordelon, Y. Dementia with Lewy bodies. *Semin. Neurol.* **2014**, *34*, 182–188, doi:10.1055/s-0034-1381741.
25. Nazarko, L. Dementia: prevalence and pathophysiology. *British Journal of Healthcare Assistants* **2019**, *13*, 266–270, doi:10.12968/bjha.2019.13.6.266.
26. Klein, J.C.; Eggers, C.; Kalbe, E.; Weisenbach, S.; Hohmann, C.; Vollmar, S.; Baudrexel, S.; Diederich, N.J.; Heiss, W.D.; Hilker, R. Neurotransmitter changes in dementia with Lewy bodies and Parkinson disease dementia in vivo. *Neurology* **2010**, *74*, 885–892, doi:10.1212/WNL.0b013e3181d55f61.
27. Ransmayr, G. Dementia with Lewy bodies: prevalence, clinical spectrum and natural history. *J. Neural Transm. Suppl.* **2000**, 303–314, doi:10.1007/978-3-7091-6301-6_21.
28. Nagahama, Y.; Okina, T.; Suzuki, N.; Matsuda, M. Neural correlates of psychotic symptoms in dementia with Lewy bodies. *Brain* **2010**, *133*, 557–567, doi:10.1093/brain/awp295.
29. Claassen, D.O.; Lowe, V.J.; Peller, P.J.; Petersen, R.C.; Josephs, K.A. Amyloid and glucose imaging in dementia with Lewy bodies and multiple systems atrophy. *Parkinsonism Relat. Disord.* **2011**, *17*, 160–165, doi:10.1016/j.parkreldis.2010.12.006.
30. Monzio Compagnoni, G.; Di Fonzo, A. Understanding the pathogenesis of multiple system atrophy: state of the art and future perspectives. *Acta Neuropathol. Commun.* **2019**, *7*, 113, doi:10.1186/s40478-019-0730-6.
31. Multiple System Atrophy: Background, Etiology and Pathophysiology, Epidemiology. Available online: https://emedicine.medscape.com/article/1154583-overview#a4 (accessed on 25 April 2022).
32. Fanciulli, A.; Stankovic, I.; Krismer, F.; Seppi, K.; Levin, J.; Wenning, G.K. Multiple system atrophy. *Int. Rev. Neurobiol.* **2019**, *149*, 137–192, doi:10.1016/bs.irn.2019.10.004.
33. Jellinger, K.A. Pathogenesis of Multiple System Atrophy - Recent Developments. *Int J Neurol Neurother* **2015**, *2*, doi:10.23937/2378-3001/2/1/1022.
34. Stemberger, S.; Scholz, S.W.; Singleton, A.B.; Wenning, G.K. Genetic players in multiple system atrophy: unfolding the nature of the beast. *Neurobiology of Aging* **2011**, *32*, 1924.e5-14, doi:10.1016/j.neurobiolaging.2011.04.001.
35. Jellinger, K.A. Multiple System Atrophy: An Oligodendroglioneural Synucleinopathy1. *J. Alzheimers. Dis.* **2018**, *62*, 1141–1179, doi:10.3233/JAD-170397.
36. Kwon, K.-Y.; Choi, C.G.; Kim, J.S.; Lee, M.C.; Chung, S.J. Diagnostic value of brain MRI and 18F-FDG PET in the differentiation of Parkinsonian-type multiple system atrophy from Parkinson's disease. *Eur. J. Neurol.* **2008**, *15*, 1043–1049, doi:10.1111/j.1468-1331.2008.02235.x.
37. Tanner, C.M.; Goldman, S.M. EPIDEMIOLOGY OF PARKINSON'S DISEASE. *Neurologic Clinics* **1996**, *14*, 317–335, doi:10.1016/S0733-8619(05)70259-0.
38. Collier, T.J.; Kanaan, N.M.; Kordower, J.H. Ageing as a primary risk factor for Parkinson's disease: evidence from studies of non-human primates. *Nat. Rev. Neurosci.* **2011**, *12*, 359–366, doi:10.1038/nrn3039.
39. Savica, R.; Grossardt, B.R.; Rocca, W.A.; Bower, J.H. Parkinson disease with and without Dementia: A prevalence study and future projections. *Mov. Disord.* **2018**, *33*, 537–543, doi:10.1002/mds.27277.
40. Hirsch, L.; Jette, N.; Frolkis, A.; Steeves, T.; Pringsheim, T. The Incidence of Parkinson's Disease: A Systematic Review and Meta-Analysis. *Neuroepidemiology* **2016**, *46*, 292–300, doi:10.1159/000445751.
41. Haaxma, C.A.; Bloem, B.R.; Borm, G.F.; Oyen, W.J.G.; Leenders, K.L.; Eshuis, S.; Booij, J.; Dluzen, D.E.; Horstink, M.W.I.M. Gender differences in Parkinson's disease. *J. Neurol. Neurosurg. Psychiatry* **2007**, *78*, 819–824, doi:10.1136/jnnp.2006.103788.
42. Dahodwala, N.; Shah, K.; He, Y.; Wu, S.S.; Schmidt, P.; Cubillos, F.; Willis, A.W. Sex disparities in access to caregiving in Parkinson disease. *Neurology* **2018**, *90*, e48-e54, doi:10.1212/WNL.0000000000004764.
43. Cerri, S.; Mus, L.; Blandini, F. Parkinson's Disease in Women and Men: What's the Difference? *J. Parkinsons. Dis.* **2019**, *9*, 501–515, doi:10.3233/JPD-191683.
44. Dorsey, E.R.; Constantinescu, R.; Thompson, J.P.; Biglan, K.M.; Holloway, R.G.; Kieburtz, K.; Marshall, F.J.; Ravina, B.M.; Schifitto, G.; Siderowf, A.; et al. Projected number of people with Parkinson disease in the most populous nations, 2005 through 2030. *Neurology* **2007**, *68*, 384–386, doi:10.1212/01.wnl.0000247740.47667.03.

45. Marras, C.; Beck, J.C.; Bower, J.H.; Roberts, E.; Ritz, B.; Ross, G.W.; Abbott, R.D.; Savica, R.; van den Eeden, S.K.; Willis, A.W.; et al. Prevalence of Parkinson's disease across North America. *NPJ Parkinsons. Dis.* **2018**, *4*, 21, doi:10.1038/s41531-018-0058-0.
46. Parkinson's Foundation. Statistics. Available online: https://www.parkinson.org/Understanding-Parkinsons/Statistics (accessed on 8 March 2022).
47. Hogan, D.B.; Fiest, K.M.; Roberts, J.I.; Maxwell, C.J.; Dykeman, J.; Pringsheim, T.; Steeves, T.; Smith, E.E.; Pearson, D.; Jetté, N. The Prevalence and Incidence of Dementia with Lewy Bodies: a Systematic Review. *Can. J. Neurol. Sci.* **2016**, *43 Suppl 1*, S83-95, doi:10.1017/cjn.2016.2.
48. Boot, B.P.; Orr, C.F.; Ahlskog, J.E.; Ferman, T.J.; Roberts, R.; Pankratz, V.S.; Dickson, D.W.; Parisi, J.; Aakre, J.A.; Geda, Y.E.; et al. Risk factors for dementia with Lewy bodies: a case-control study. *Neurology* **2013**, *81*, 833–840, doi:10.1212/WNL.0b013e3182a2cbd1.
49. Sturm, E.; Stefanova, N. Multiple system atrophy: genetic or epigenetic? *Exp. Neurobiol.* **2014**, *23*, 277–291, doi:10.5607/en.2014.23.4.277.
50. Shadrin, A.A.; Mucha, S.; Ellinghaus, D.; Makarious, M.B.; Blauwendraat, C.; Sreelatha, A.A.K.; Heras-Garvin, A.; Ding, J.; Hammer, M.; Foubert-Samier, A.; et al. Shared Genetics of Multiple System Atrophy and Inflammatory Bowel Disease. *Mov. Disord.* **2021**, *36*, 449–459, doi:10.1002/mds.28338.
51. Sklerov, M.; Waters, C. Understanding Multiple System Atrophy—Could Genetics Lead the Way? *US Neurology* **2016**, *12*, 110, doi:10.17925/USN.2016.12.02.110.
52. Katzeff, J.S.; Phan, K.; Purushothuman, S.; Halliday, G.M.; Kim, W.S. Cross-examining candidate genes implicated in multiple system atrophy. *Acta Neuropathol. Commun.* **2019**, *7*, 117, doi:10.1186/s40478-019-0769-4.
53. Durcan, T.M.; Fon, E.A. The three 'P's of mitophagy: PARKIN, PINK1, and post-translational modifications. *Genes Dev.* **2015**, *29*, 989–999, doi:10.1101/gad.262758.115.
54. Keeney, P.M.; Xie, J.; Capaldi, R.A.; Bennett, J.P. Parkinson's disease brain mitochondrial complex I has oxidatively damaged subunits and is functionally impaired and misassembled. *J. Neurosci.* **2006**, *26*, 5256–5264, doi:10.1523/JNEUROSCI.0984-06.2006.
55. Thomas, B.; Beal, M.F. Parkinson's disease. *Hum. Mol. Genet.* **2007**, *16 Spec No. 2*, R183-94, doi:10.1093/hmg/ddm159.
56. Klein, C.; Schlossmacher, M.G. The genetics of Parkinson disease: Implications for neurological care. *Nat. Clin. Pract. Neurol.* **2006**, *2*, 136–146, doi:10.1038/ncpneuro0126.
57. Lücking, C.B.; Dürr, A.; Bonifati, V.; Vaughan, J.; Michele, G. de; Gasser, T.; Harhangi, B.S.; Meco, G.; Denèfle, P.; Wood, N.W.; et al. Association between early-onset Parkinson's disease and mutations in the parkin gene. *N. Engl. J. Med.* **2000**, *342*, 1560–1567, doi:10.1056/NEJM200005253422103.
58. Klein, C.; Westenberger, A. Genetics of Parkinson's disease. *Cold Spring Harb. Perspect. Med.* **2012**, *2*, a008888, doi:10.1101/cshperspect.a008888.
59. Giasson, B.I.; Covy, J.P.; Bonini, N.M.; Hurtig, H.I.; Farrer, M.J.; Trojanowski, J.Q.; van Deerlin, V.M. Biochemical and pathological characterization of Lrrk2. *Ann. Neurol.* **2006**, *59*, 315–322, doi:10.1002/ana.20791.
60. Haugarvoll, K.; Wszolek, Z.K. PARK8 LRRK2 parkinsonism. *Curr. Neurol. Neurosci. Rep.* **2006**, *6*, 287–294, doi:10.1007/s11910-006-0020-0.
61. Vergouw, L.J.M.; van Steenoven, I.; van de Berg, W.D.J.; Teunissen, C.E.; van Swieten, J.C.; Bonifati, V.; Lemstra, A.W.; Jong, F.J. de. An update on the genetics of dementia with Lewy bodies. *Parkinsonism Relat. Disord.* **2017**, *43*, 1–8, doi:10.1016/j.parkreldis.2017.07.009.
62. Savica, R.; Grossardt, B.R.; Bower, J.H.; Boeve, B.F.; Ahlskog, J.E.; Rocca, W.A. Incidence of dementia with Lewy bodies and Parkinson disease dementia. *JAMA Neurol.* **2013**, *70*, 1396–1402, doi:10.1001/jamaneurol.2013.3579.
63. Ubhi, K.; Low, P.; Masliah, E. Multiple system atrophy: a clinical and neuropathological perspective. *Trends Neurosci.* **2011**, *34*, 581–590, doi:10.1016/j.tins.2011.08.003.
64. Klein, C.; Lohmann-Hedrich, K. Impact of recent genetic findings in Parkinson's disease. *Curr. Opin. Neurol.* **2007**, *20*, 453–464, doi:10.1097/WCO.0b013e3281e6692b.
65. Polymeropoulos, M.H.; Higgins, J.J.; Golbe, L.I.; Johnson, W.G.; Ide, S.E.; Di Iorio, G.; Sanges, G.; Stenroos, E.S.; Pho, L.T.; Schaffer, A.A.; et al. Mapping of a gene for Parkinson's disease to chromosome 4q21-q23. *Science* **1996**, *274*, 1197–1199, doi:10.1126/science.274.5290.1197.

66. Polymeropoulos, M.H.; Lavedan, C.; Leroy, E.; Ide, S.E.; Dehejia, A.; Dutra, A.; Pike, B.; Root, H.; Rubenstein, J.; Boyer, R.; et al. Mutation in the alpha-synuclein gene identified in families with Parkinson's disease. *Science* **1997**, *276*, 2045–2047, doi:10.1126/science.276.5321.2045.
67. Cooper, A.A.; Gitler, A.D.; Cashikar, A.; Haynes, C.M.; Hill, K.J.; Bhullar, B.; Liu, K.; Xu, K.; Strathearn, K.E.; Liu, F.; et al. Alpha-synuclein blocks ER-Golgi traffic and Rab1 rescues neuron loss in Parkinson's models. *Science* **2006**, *313*, 324–328, doi:10.1126/science.1129462.
68. Orme, T.; Guerreiro, R.; Bras, J. The Genetics of Dementia with Lewy Bodies: Current Understanding and Future Directions. *Curr. Neurol. Neurosci. Rep.* **2018**, *18*, 67, doi:10.1007/s11910-018-0874-y.
69. Miller, D.W.; Hague, S.M.; Clarimon, J.; Baptista, M.; Gwinn-Hardy, K.; Cookson, M.R.; Singleton, A.B. Alpha-synuclein in blood and brain from familial Parkinson disease with SNCA locus triplication. *Neurology* **2004**, *62*, 1835–1838, doi:10.1212/01.wnl.0000127517.33208.f4.
70. Kurreck, J.; Stein, C.A. *Molecular medicine*: *An introduction / Jens Kurreck, Cy Aaron Stein*, 1st; Wiley-VCH: Weinheim, 2015, ISBN 9783527675074.
71. Federoff, M.; Jimenez-Rolando, B.; Nalls, M.A.; Singleton, A.B. A large study reveals no association between APOE and Parkinson's disease. *Neurobiol. Dis.* **2012**, *46*, 389–392, doi:10.1016/j.nbd.2012.02.002.
72. Perez, F.; Helmer, C.; Dartigues, J.F.; Auriacombe, S.; Tison, F. A 15-year population-based cohort study of the incidence of Parkinson's disease and dementia with Lewy bodies in an elderly French cohort. *J. Neurol. Neurosurg. Psychiatry* **2010**, *81*, 742–746, doi:10.1136/jnnp.2009.189142.
73. Guerreiro, R.; Escott-Price, V.; Darwent, L.; Parkkinen, L.; Ansorge, O.; Hernandez, D.G.; Nalls, M.A.; Clark, L.; Honig, L.; Marder, K.; et al. Genome-wide analysis of genetic correlation in dementia with Lewy bodies, Parkinson's and Alzheimer's diseases. *Neurobiology of Aging* **2016**, *38*, 214.e7-214.e10, doi:10.1016/j.neurobiolaging.2015.10.028.
74. Brooks, D.J. Dopamine agonists: their role in the treatment of Parkinson's disease. *J. Neurol. Neurosurg. Psychiatry* **2000**, *68*, 685–689, doi:10.1136/jnnp.68.6.685.
75. Guerreiro, R.; Ross, O.A.; Kun-Rodrigues, C.; Hernandez, D.G.; Orme, T.; Eicher, J.D.; Shepherd, C.E.; Parkkinen, L.; Darwent, L.; Heckman, M.G.; et al. Investigating the genetic architecture of dementia with Lewy bodies: a two-stage genome-wide association study. *The Lancet Neurology* **2018**, *17*, 64–74, doi:10.1016/S1474-4422(17)30400-3.
76. Richardson, J.R.; Quan, Y.; Sherer, T.B.; Greenamyre, J.T.; Miller, G.W. Paraquat neurotoxicity is distinct from that of MPTP and rotenone. *Toxicol. Sci.* **2005**, *88*, 193–201, doi:10.1093/toxsci/kfi304.
77. Vila, M. Neuromelanin, aging, and neuronal vulnerability in Parkinson's disease. *Mov. Disord.* **2019**, *34*, 1440–1451, doi:10.1002/mds.27776.
78. Mastroberardino, P.G.; Hoffman, E.K.; Horowitz, M.P.; Betarbet, R.; Taylor, G.; Cheng, D.; Na, H.M.; Gutekunst, C.-A.; Gearing, M.; Trojanowski, J.Q.; et al. A novel transferrin/TfR2-mediated mitochondrial iron transport system is disrupted in Parkinson's disease. *Neurobiol. Dis.* **2009**, *34*, 417–431, doi:10.1016/j.nbd.2009.02.009.
79. Maroteaux, L.; Campanelli, J.T.; Scheller, R.H. Synuclein: a neuron-specific protein localized to the nucleus and presynaptic nerve terminal. *J. Neurosci.* **1988**, *8*, 2804–2815, doi:10.1523/JNEUROSCI.08-08-02804.1988.
80. Uéda, K.; Fukushima, H.; Masliah, E.; Xia, Y.; Iwai, A.; Yoshimoto, M.; Otero, D.A.; Kondo, J.; Ihara, Y.; Saitoh, T. Molecular cloning of cDNA encoding an unrecognized component of amyloid in Alzheimer disease. *Proc. Natl. Acad. Sci. U. S. A.* **1993**, *90*, 11282–11286, doi:10.1073/pnas.90.23.11282.
81. Jakes, R.; Spillantini, M.G.; Goedert, M. Identification of two distinct synucleins from human brain. *FEBS Letters* **1994**, *345*, 27–32, doi:10.1016/0014-5793(94)00395-5.
82. Goedert, M.; Jakes, R.; Spillantini, M.G. The Synucleinopathies: Twenty Years On. *J. Parkinsons. Dis.* **2017**, *7*, S51-S69, doi:10.3233/JPD-179005.
83. George, J.M. The synucleins. *Genome Biol.* **2002**, *3*, REVIEWS3002, doi:10.1186/gb-2001-3-1-reviews3002.
84. Brás, I.C.; Outeiro, T.F. Alpha-Synuclein: Mechanisms of Release and Pathology Progression in Synucleinopathies. *Cells* **2021**, *10*, 375, doi:10.3390/cells10020375.
85. Uzuegbunam, B.C.; Librizzi, D.; Hooshyar Yousefi, B. PET Radiopharmaceuticals for Alzheimer's Disease and Parkinson's Disease Diagnosis, the Current and Future Landscape. *Molecules* **2020**, *25*, doi:10.3390/molecules25040977.

86. Kawahata, I.; Finkelstein, D.I.; Fukunaga, K. Pathogenic Impact of α-Synuclein Phosphorylation and Its Kinases in α-Synucleinopathies. *Int. J. Mol. Sci.* **2022**, *23*, doi:10.3390/ijms23116216.
87. Bendor, J.T.; Logan, T.P.; Edwards, R.H. The function of α-synuclein. *Neuron* **2013**, *79*, 1044–1066, doi:10.1016/j.neuron.2013.09.004.
88. Fernández-Chacón, R.; Wölfel, M.; Nishimune, H.; Tabares, L.; Schmitz, F.; Castellano-Muñoz, M.; Rosenmund, C.; Montesinos, M.L.; Sanes, J.R.; Schneggenburger, R.; et al. The Synaptic Vesicle Protein CSPα Prevents Presynaptic Degeneration. *Neuron* **2004**, *42*, 237–251, doi:10.1016/S0896-6273(04)00190-4.
89. Chandra, S.; Gallardo, G.; Fernández-Chacón, R.; Schlüter, O.M.; Südhof, T.C. Alpha-synuclein cooperates with CSPalpha in preventing neurodegeneration. *Cell* **2005**, *123*, 383–396, doi:10.1016/j.cell.2005.09.028.
90. Nakamura, K.; Nemani, V.M.; Azarbal, F.; Skibinski, G.; Levy, J.M.; Egami, K.; Munishkina, L.; Zhang, J.; Gardner, B.; Wakabayashi, J.; et al. Direct membrane association drives mitochondrial fission by the Parkinson disease-associated protein alpha-synuclein. *J. Biol. Chem.* **2011**, *286*, 20710–20726, doi:10.1074/jbc.M110.213538.
91. Kamp, F.; Exner, N.; Lutz, A.K.; Wender, N.; Hegermann, J.; Brunner, B.; Nuscher, B.; Bartels, T.; Giese, A.; Beyer, K.; et al. Inhibition of mitochondrial fusion by α-synuclein is rescued by PINK1, Parkin and DJ-1. *EMBO J.* **2010**, *29*, 3571–3589, doi:10.1038/emboj.2010.223.
92. Oeckl, P.; Metzger, F.; Nagl, M.; Arnim, C.A.F. von; Halbgebauer, S.; Steinacker, P.; Ludolph, A.C.; Otto, M. Alpha-, Beta-, and Gamma-synuclein Quantification in Cerebrospinal Fluid by Multiple Reaction Monitoring Reveals Increased Concentrations in Alzheimer's and Creutzfeldt-Jakob Disease but No Alteration in Synucleinopathies. *Mol. Cell. Proteomics* **2016**, *15*, 3126–3138, doi:10.1074/mcp.M116.059915.
93. Andrew Parkinson, Brian W. Ogilvie, David B. Buckley, Faraz Kazmi and Oliver Parkinson. *Chapter 6: Biotransformation of Xenobiotics*: *Klaassen, Curtis D.; Casarett, Louis J. Toxicology. Casarett & Doull's toxicology*. The basic science of poisons / editor, Curtis D. Klaassen, Ninth edition; McGraw-Hill Education: New York, 2019, ISBN 9781259863745.
94. Kim, T.-E.; Newman, A.J.; Imberdis, T.; Brontesi, L.; Tripathi, A.; Ramalingam, N.; Fanning, S.; Selkoe, D.; Dettmer, U. Excess membrane binding of monomeric alpha-, beta- and gamma-synuclein is invariably associated with inclusion formation and toxicity. *Hum. Mol. Genet.* **2021**, *30*, 2332–2346, doi:10.1093/hmg/ddab188.
95. Du, X.-Y.; Xie, X.-X.; Liu, R.-T. The Role of α-Synuclein Oligomers in Parkinson's Disease. *Int. J. Mol. Sci.* **2020**, *21*, doi:10.3390/ijms21228645.
96. González, N.; Arcos-López, T.; König, A.; Quintanar, L.; Menacho Márquez, M.; Outeiro, T.F.; Fernández, C.O. Effects of alpha-synuclein post-translational modifications on metal binding. *J. Neurochem.* **2019**, *150*, 507–521, doi:10.1111/jnc.14721.
97. Brás, I.C.; Xylaki, M.; Outeiro, T.F. Mechanisms of alpha-synuclein toxicity: An update and outlook. *Prog. Brain Res.* **2020**, *252*, 91–129, doi:10.1016/bs.pbr.2019.10.005.
98. Cuervo, A.M.; Stefanis, L.; Fredenburg, R.; Lansbury, P.T.; Sulzer, D. Impaired degradation of mutant alpha-synuclein by chaperone-mediated autophagy. *Science* **2004**, *305*, 1292–1295, doi:10.1126/science.1101738.
99. Menozzi, E.; Macnaughtan, J.; Schapira, A.H.V. The gut-brain axis and Parkinson disease: clinical and pathogenetic relevance. *Ann. Med.* **2021**, *53*, 611–625, doi:10.1080/07853890.2021.1890330.
100. Jan, A.; Gonçalves, N.P.; Vaegter, C.B.; Jensen, P.H.; Ferreira, N. The Prion-Like Spreading of Alpha-Synuclein in Parkinson's Disease: Update on Models and Hypotheses. *Int. J. Mol. Sci.* **2021**, *22*, doi:10.3390/ijms22158338.
101. Braak, H.; Vos, R.A.I. de; Bohl, J.; Del Tredici, K. Gastric alpha-synuclein immunoreactive inclusions in Meissner's and Auerbach's plexuses in cases staged for Parkinson's disease-related brain pathology. *Neurosci. Lett.* **2006**, *396*, 67–72, doi:10.1016/j.neulet.2005.11.012.
102. Wakabayashi, K.; Takahashi, H.; Takeda, S.; Ohama, E.; Ikuta, F. Parkinson's disease: the presence of Lewy bodies in Auerbach's and Meissner's plexuses. *Acta Neuropathol.* **1988**, *76*, 217–221, doi:10.1007/BF00687767.
103. Shannon, K.M.; Keshavarzian, A.; Mutlu, E.; Dodiya, H.B.; Daian, D.; Jaglin, J.A.; Kordower, J.H. Alpha-synuclein in colonic submucosa in early untreated Parkinson's disease. *Mov. Disord.* **2012**, *27*, 709–715, doi:10.1002/mds.23838.

104. Liu, B.; Fang, F.; Pedersen, N.L.; Tillander, A.; Ludvigsson, J.F.; Ekbom, A.; Svenningsson, P.; Chen, H.; Wirdefeldt, K. Vagotomy and Parkinson disease: A Swedish register-based matched-cohort study. *Neurology* **2017**, *88*, 1996–2002, doi:10.1212/WNL.0000000000003961.
105. Lu, H.-T.; Shen, Q.-Y.; Xie, D.; Zhao, Q.-Z.; Xu, Y.-M. Lack of association between appendectomy and Parkinson's disease: a systematic review and meta-analysis. *Aging Clin. Exp. Res.* **2020**, *32*, 2201–2209, doi:10.1007/s40520-019-01354-9.
106. Mulak, A.; Bonaz, B. Brain-gut-microbiota axis in Parkinson's disease. *World J. Gastroenterol.* **2015**, *21*, 10609–10620, doi:10.3748/wjg.v21.i37.10609.
107. Savica, R.; Carlin, J.M.; Grossardt, B.R.; Bower, J.H.; Ahlskog, J.E.; Maraganore, D.M.; Bharucha, A.E.; Rocca, W.A. Medical records documentation of constipation preceding Parkinson disease: A case-control study. *Neurology* **2009**, *73*, 1752–1758, doi:10.1212/WNL.0b013e3181c34af5.
108. Killinger, B.A.; Madaj, Z.; Sikora, J.W.; Rey, N.; Haas, A.J.; Vepa, Y.; Lindqvist, D.; Chen, H.; Thomas, P.M.; Brundin, P.; et al. The vermiform appendix impacts the risk of developing Parkinson's disease. *Sci. Transl. Med.* **2018**, *10*, doi:10.1126/scitranslmed.aar5280.
109. Rey, N.L.; Steiner, J.A.; Maroof, N.; Luk, K.C.; Madaj, Z.; Trojanowski, J.Q.; Lee, V.M.-Y.; Brundin, P. Widespread transneuronal propagation of α-synucleinopathy triggered in olfactory bulb mimics prodromal Parkinson's disease. *J. Exp. Med.* **2016**, *213*, 1759–1778, doi:10.1084/jem.20160368.
110. Rey, N.L.; George, S.; Steiner, J.A.; Madaj, Z.; Luk, K.C.; Trojanowski, J.Q.; Lee, V.M.-Y.; Brundin, P. Spread of aggregates after olfactory bulb injection of α-synuclein fibrils is associated with early neuronal loss and is reduced long term. *Acta Neuropathol.* **2018**, *135*, 65–83, doi:10.1007/s00401-017-1792-9.
111. Uemura, N.; Uemura, M.T.; Lo, A.; Bassil, F.; Zhang, B.; Luk, K.C.; Lee, V.M.-Y.; Takahashi, R.; Trojanowski, J.Q. Slow Progressive Accumulation of Oligodendroglial Alpha-Synuclein (α-Syn) Pathology in Synthetic α-Syn Fibril-Induced Mouse Models of Synucleinopathy. *J. Neuropathol. Exp. Neurol.* **2019**, *78*, 877–890, doi:10.1093/jnen/nlz070.
112. Halliday, G.M.; Holton, J.L.; Revesz, T.; Dickson, D.W. Neuropathology underlying clinical variability in patients with synucleinopathies. *Acta Neuropathol.* **2011**, *122*, 187–204, doi:10.1007/s00401-011-0852-9.
113. Guo, J.L.; Covell, D.J.; Daniels, J.P.; Iba, M.; Stieber, A.; Zhang, B.; Riddle, D.M.; Kwong, L.K.; Xu, Y.; Trojanowski, J.Q.; et al. Distinct α-synuclein strains differentially promote tau inclusions in neurons. *Cell* **2013**, *154*, 103–117, doi:10.1016/j.cell.2013.05.057.
114. Peelaerts, W.; Bousset, L.; van der Perren, A.; Moskalyuk, A.; Pulizzi, R.; Giugliano, M.; van den Haute, C.; Melki, R.; Baekelandt, V. α-Synuclein strains cause distinct synucleinopathies after local and systemic administration. *Nature* **2015**, *522*, 340–344, doi:10.1038/nature14547.
115. Nuccio, F. de; Kashyrina, M.; Serinelli, F.; Laferrière, F.; Lofrumento, D.D.; Giorgi, F. de; Ichas, F. Oligodendrocytes Prune Axons Containing α-Synuclein Aggregates In Vivo: Lewy Neurites as Precursors of Glial Cytoplasmic Inclusions in Multiple System Atrophy? *Biomolecules* **2023**, *13*, doi:10.3390/biom13020269.
116. Atik, A.; Stewart, T.; Zhang, J. Alpha-Synuclein as a Biomarker for Parkinson's Disease. *Brain Pathol.* **2016**, *26*, 410–418, doi:10.1111/bpa.12370.
117. Ganguly, U.; Singh, S.; Pal, S.; Prasad, S.; Agrawal, B.K.; Saini, R.V.; Chakrabarti, S. Alpha-Synuclein as a Biomarker of Parkinson's Disease: Good, but Not Good Enough. *Front. Aging Neurosci.* **2021**, *13*, 702639, doi:10.3389/fnagi.2021.702639.
118. Bagchi, D.P.; Yu, L.; Perlmutter, J.S.; Xu, J.; Mach, R.H.; Tu, Z.; Kotzbauer, P.T. Binding of the radioligand SIL23 to α-synuclein fibrils in Parkinson disease brain tissue establishes feasibility and screening approaches for developing a Parkinson disease imaging agent. *PLoS One* **2013**, *8*, e55031, doi:10.1371/journal.pone.0055031.
119. Bae, Y.J.; Kim, J.-M.; Sohn, C.-H.; Choi, J.-H.; Choi, B.S.; Song, Y.S.; Nam, Y.; Cho, S.J.; Jeon, B.; Kim, J.H. Imaging the Substantia Nigra in Parkinson Disease and Other Parkinsonian Syndromes. *Radiology* **2021**, *300*, 260–278, doi:10.1148/radiol.2021203341.
120. Chougar, L.; Pyatigorskaya, N.; Degos, B.; Grabli, D.; Lehéricy, S. The Role of Magnetic Resonance Imaging for the Diagnosis of Atypical Parkinsonism. *Front. Neurol.* **2020**, *11*, 665, doi:10.3389/fneur.2020.00665.
121. Heim, B.; Krismer, F.; Marzi, R. de; Seppi, K. Magnetic resonance imaging for the diagnosis of Parkinson's disease. *J. Neural Transm. (Vienna)* **2017**, *124*, 915–964, doi:10.1007/s00702-017-1717-8.

122. Davis, K.M.; Ryan, J.L.; Aaron, V.D.; Sims, J.B. PET and SPECT Imaging of the Brain: History, Technical Considerations, Applications, and Radiotracers. *Semin. Ultrasound CT MR* **2020**, *41*, 521–529, doi:10.1053/j.sult.2020.08.006.
123. Rahmim, A.; Zaidi, H. PET versus SPECT: strengths, limitations and challenges. *Nucl. Med. Commun.* **2008**, *29*, 193–207, doi:10.1097/MNM.0b013e3282f3a515.
124. *Biomedical engineering in gastrointestinal surgery;* Schneider, A.; Feussner, H., Eds.; Academic Press: Amsterdam, 2017, ISBN 9780128032305.
125. Masahiro Fumita, Robert, B. Innis. *In vivo molecular imaging: ligand development and research applications*, 2000.
126. Bhidayasiri, R. How useful is (123I) beta-CIT SPECT in the diagnosis of Parkinson's disease? *Rev. Neurol. Dis.* **2006**, *3*, 19–22.
127. Mak, E.; Su, L.; Williams, G.B.; O'Brien, J.T. Neuroimaging characteristics of dementia with Lewy bodies. *Alzheimer's Research & Therapy* **2014**, *6*, 18, doi:10.1186/alzrt248.
128. Lim, S.M.; Katsifis, A.; Villemagne, V.L.; Best, R.; Jones, G.; Saling, M.; Bradshaw, J.; Merory, J.; Woodward, M.; Hopwood, M.; et al. The 18F-FDG PET cingulate island sign and comparison to 123I-beta-CIT SPECT for diagnosis of dementia with Lewy bodies. *J. Nucl. Med.* **2009**, *50*, 1638–1645, doi:10.2967/jnumed.109.065870.
129. Juh, R.; Pae, C.-U.; Lee, C.-U.; Yang, D.; Chung, Y.; Suh, T.; Choe, B. Voxel based comparison of glucose metabolism in the differential diagnosis of the multiple system atrophy using statistical parametric mapping. *Neurosci. Res.* **2005**, *52*, 211–219, doi:10.1016/j.neures.2005.03.010.
130. Taniwaki, T.; Nakagawa, M.; Yamada, T.; Yoshida, T.; Ohyagi, Y.; Sasaki, M.; Kuwabara, Y.; Tobimatsu, S.; Kira, J.-i. Cerebral metabolic changes in early multiple system atrophy: a PET study. *Journal of the Neurological Sciences* **2002**, *200*, 79–84, doi:10.1016/S0022-510X(02)00151-X.
131. Otsuka, M.; Ichiya, Y.; Kuwabara, Y.; Hosokawa, S.; Sasaki, M.; Yoshida, T.; Fukumura, T.; Kato, M.; Masuda, K. Glucose metabolism in the cortical and subcortical brain structures in multiple system atrophy and Parkinson's disease: a positron emission tomographic study. *Journal of the Neurological Sciences* **1996**, *144*, 77–83, doi:10.1016/S0022-510X(96)00172-4.
132. Lewis, S.J.; Pavese, N.; Rivero-Bosch, M.; Eggert, K.; Oertel, W.; Mathias, C.J.; Brooks, D.J.; Gerhard, A. Brain monoamine systems in multiple system atrophy: a positron emission tomography study. *Neurobiol. Dis.* **2012**, *46*, 130–136, doi:10.1016/j.nbd.2011.12.053.
133. Das, S.; Gordián-Vélez, W.J.; Ledebur, H.C.; Mourkioti, F.; Rompolas, P.; Chen, H.I.; Serruya, M.D.; Cullen, D.K. Innervation: the missing link for biofabricated tissues and organs. *NPJ Regen. Med.* **2020**, *5*, 11, doi:10.1038/s41536-020-0096-1.
134. Taïeb, D.; Hicks, R.J.; Hindié, E.; Guillet, B.A.; Avram, A.; Ghedini, P.; Timmers, H.J.; Scott, A.T.; Elojeimy, S.; Rubello, D.; et al. European Association of Nuclear Medicine Practice Guideline/Society of Nuclear Medicine and Molecular Imaging Procedure Standard 2019 for radionuclide imaging of phaeochromocytoma and paraganglioma. *Eur. J. Nucl. Med. Mol. Imaging* **2019**, *46*, 2112–2137, doi:10.1007/s00259-019-04398-1.
135. Brumberg, J.; Schröter, N.; Blazhenets, G.; Frings, L.; Volkmann, J.; Lapa, C.; Jost, W.H.; Isaias, I.U.; Meyer, P.T. Differential diagnosis of parkinsonism: a head-to-head comparison of FDG PET and MIBG scintigraphy. *NPJ Parkinsons. Dis.* **2020**, *6*, 39, doi:10.1038/s41531-020-00141-y.
136. Meyer, P.T.; Frings, L.; Rücker, G.; Hellwig, S. 18F-FDG PET in Parkinsonism: Differential Diagnosis and Evaluation of Cognitive Impairment. *J. Nucl. Med.* **2017**, *58*, 1888–1898, doi:10.2967/jnumed.116.186403.
137. *Imaging in Clinical Oncology;* Hsiao-Chun Cheng, Christina M. Ulane,Robert E. Burke, Ed.; Springer International Publishing: Cham, 2018, ISBN 978-3-319-68872-5.
138. Uzuegbunam, B.C.; Li, J.; Paslawski, W.; Weber, W.; Svenningsson, P.; Ågren, H.; Yousefi, B.H. Toward Novel 18FFluorine-Labeled Radiotracers for the Imaging of α-Synuclein Fibrils. *Front. Aging Neurosci.* **2022**, *14*, 830704, doi:10.3389/fnagi.2022.830704.
139. Kotzbauer, P.T.; Tu, Z.; Mach, R.H. Current status of the development of PET radiotracers for imaging alpha synuclein aggregates in Lewy bodies and Lewy neurites. *Clin Transl Imaging* **2017**, *5*, 3–14, doi:10.1007/s40336-016-0217-4.
140. Volkova, K.D.; Kovalska, V.B.; Balanda, A.O.; Losytskyy, M.Y.; Golub, A.G.; Vermeij, R.J.; Subramaniam, V.; Tolmachev, O.I.; Yarmoluk, S.M. Specific fluorescent detection of fibrillar α-synuclein using mono- and

trimethine cyanine dyes. *Bioorganic & Medicinal Chemistry* **2008**, *16*, 1452–1459, doi:10.1016/j.bmc.2007.10.051.
141. Celej, M.S.; Jares-Erijman, E.A.; Jovin, T.M. Fluorescent N-arylaminonaphthalene sulfonate probes for amyloid aggregation of alpha-synuclein. *Biophys. J.* **2008**, *94*, 4867–4879, doi:10.1529/biophysj.107.125211.
142. Kovalska, V.B.; Losytskyy, M.Y.; Tolmachev, O.I.; Slominskii, Y.L.; Segers-Nolten, G.M.J.; Subramaniam, V.; Yarmoluk, S.M. Tri- and pentamethine cyanine dyes for fluorescent detection of α-synuclein oligomeric aggregates. *J. Fluoresc.* **2012**, *22*, 1441–1448, doi:10.1007/s10895-012-1081-x.
143. Volkova, K.D.; Kovalska, V.B.; Yu Losytskyy, M.; Veldhuis, G.; Segers-Nolten, G.M.J.; Tolmachev, O.I.; Subramaniam, V.; Yarmoluk, S.M. Studies of interaction between cyanine dye T-284 and fibrillar alpha-synuclein. *J. Fluoresc.* **2010**, *20*, 1267–1274, doi:10.1007/s10895-010-0678-1.
144. Krebs, M.R.H.; Bromley, E.H.C.; Donald, A.M. The binding of thioflavin-T to amyloid fibrils: localisation and implications. *J. Struct. Biol.* **2005**, *149*, 30–37, doi:10.1016/j.jsb.2004.08.002.
145. Neal, K.L.; Shakerdge, N.B.; Hou, S.S.; Klunk, W.E.; Mathis, C.A.; Nesterov, E.E.; Swager, T.M.; McLean, P.J.; Bacskai, B.J. Development and screening of contrast agents for in vivo imaging of Parkinson's disease. *Mol. Imaging Biol.* **2013**, *15*, 585–595, doi:10.1007/s11307-013-0634-y.
146. Yu, L.; Cui, J.; Padakanti, P.K.; Engel, L.; Bagchi, D.P.; Kotzbauer, P.T.; Tu, Z. Synthesis and in vitro evaluation of α-synuclein ligands. *Bioorganic & Medicinal Chemistry* **2012**, *20*, 4625–4634, doi:10.1016/j.bmc.2012.06.023.
147. Kikuchi, A.; Takeda, A.; Okamura, N.; Tashiro, M.; Hasegawa, T.; Furumoto, S.; Kobayashi, M.; Sugeno, N.; Baba, T.; Miki, Y.; et al. In vivo visualization of alpha-synuclein deposition by carbon-11-labelled 2-2-(2-dimethylaminothiazol-5-yl)ethenyl-6-2-(fluoro)ethoxybenzoxazole positron emission tomography in multiple system atrophy. *Brain* **2010**, *133*, 1772–1778, doi:10.1093/brain/awq091.
148. Fodero-Tavoletti, M.T.; Mulligan, R.S.; Okamura, N.; Furumoto, S.; Rowe, C.C.; Kudo, Y.; Masters, C.L.; Cappai, R.; Yanai, K.; Villemagne, V.L. In vitro characterisation of BF227 binding to alpha-synuclein/Lewy bodies. *Eur. J. Pharmacol.* **2009**, *617*, 54–58, doi:10.1016/j.ejphar.2009.06.042.
149. Verdurand, M.; Levigoureux, E.; Lancelot, S.; Zeinyeh, W.; Billard, T.; Quadrio, I.; Perret-Liaudet, A.; Zimmer, L.; Chauveau, F. Amyloid-Beta Radiotracer 18FBF-227 Does Not Bind to Cytoplasmic Glial Inclusions of Postmortem Multiple System Atrophy Brain Tissue. *Contrast Media Mol. Imaging* **2018**, *2018*, 9165458, doi:10.1155/2018/9165458.
150. Kudo, Y.; Okamura, N.; Furumoto, S.; Tashiro, M.; Furukawa, K.; Maruyama, M.; Itoh, M.; Iwata, R.; Yanai, K.; Arai, H. 2-(2-2-Dimethylaminothiazol-5-ylethenyl)-6- (2-fluoroethoxy)benzoxazole: a novel PET agent for in vivo detection of dense amyloid plaques in Alzheimer's disease patients. *J. Nucl. Med.* **2007**, *48*, 553–561, doi:10.2967/jnumed.106.037556.
151. Mathis, C.A.; Lopresti, B.J.; Ikonomovic, M.D.; Klunk, W.E. Small-molecule PET Tracers for Imaging Proteinopathies. *Seminars in Nuclear Medicine* **2017**, *47*, 553–575, doi:10.1053/j.semnuclmed.2017.06.003.
152. Eberling, J.L.; Dave, K.D.; Frasier, M.A. α-synuclein imaging: a critical need for Parkinson's disease research. *J. Parkinsons. Dis.* **2013**, *3*, 565–567, doi:10.3233/JPD-130247.
153. Josephson, L.; Stratman, N.; Liu, Y.; Qian, F.; Liang, S.H.; Vasdev, N.; Patel, S. The Binding of BF-227-Like Benzoxazoles to Human α-Synuclein and Amyloid β Peptide Fibrils. *Mol. Imaging* **2018**, *17*, 1536012118796297, doi:10.1177/1536012118796297.
154. Verdurand, M.; Levigoureux, E.; Zeinyeh, W.; Berthier, L.; Mendjel-Herda, M.; Cadarossanesaib, F.; Bouillot, C.; Iecker, T.; Terreux, R.; Lancelot, S.; et al. In Silico, in Vitro, and in Vivo Evaluation of New Candidates for α-Synuclein PET Imaging. *Mol. Pharm.* **2018**, *15*, 3153–3166, doi:10.1021/acs.molpharmaceut.8b00229.
155. Jérôme Molette; Emanuele Gabellieri; Vincent Darmency. US20190071450A1 - Bicyclic compounds for diagnosis and therapy - Google Patents. Available online: https://patents.google.com/patent/US20190071450A1/en (accessed on 11 July 2022).
156. Maruyama, M.; Shimada, H.; Suhara, T.; Shinotoh, H.; Ji, B.; Maeda, J.; Zhang, M.-R.; Trojanowski, J.Q.; Lee, V.M.-Y.; Ono, M.; et al. Imaging of tau pathology in a tauopathy mouse model and in Alzheimer patients compared to normal controls. *Neuron* **2013**, *79*, 1094–1108, doi:10.1016/j.neuron.2013.07.037.
157. Koga, S.; Ono, M.; Sahara, N.; Higuchi, M.; Dickson, D.W. Fluorescence and autoradiographic evaluation of tau PET ligand PBB3 to α-synuclein pathology. *Mov. Disord.* **2017**, *32*, 884–892, doi:10.1002/mds.27013.

158. Miranda-Azpiazu, P.; Svedberg, M.; Higuchi, M.; Ono, M.; Jia, Z.; Sunnemark, D.; Elmore, C.S.; Schou, M.; Varrone, A. Identification and in vitro characterization of C05-01, a PBB3 derivative with improved affinity for alpha-synuclein. *Brain Res.* **2020**, *1749*, 147131, doi:10.1016/j.brainres.2020.147131.
159. Sylvain Routier, Franck Suzenet, Sylvie Chalon, Frederic Buron, Johnny Vercouillie, Ronald Mellki, Liliana Bioaryna,Denis Guilloteau, Laura Pieri. US10906900B2 - Compounds for using in imaging and particularly for the diagnosis of neurodegenerative diseases - Google Patents. Available online: https://patents.google.com/patent/US10906900B2/en (accessed on 11 July 2022).
160. Kuebler, L.; Buss, S.; Leonov, A.; Ryazanov, S.; Schmidt, F.; Maurer, A.; Weckbecker, D.; Landau, A.M.; Lillethorup, T.P.; Bleher, D.; et al. 11CMODAG-001-towards a PET tracer targeting α-synuclein aggregates. *Eur. J. Nucl. Med. Mol. Imaging* **2021**, *48*, 1759–1772, doi:10.1007/s00259-020-05133-x.
161. Wagner, J.; Krauss, S.; Shi, S.; Ryazanov, S.; Steffen, J.; Miklitz, C.; Leonov, A.; Kleinknecht, A.; Göricke, B.; Weishaupt, J.H.; et al. Reducing tau aggregates with anle138b delays disease progression in a mouse model of tauopathies. *Acta Neuropathol.* **2015**, *130*, 619–631, doi:10.1007/s00401-015-1483-3.
162. Raval, N.R.; Nasser, A.; Madsen, C.A.; Beschorner, N.; Beaman, E.E.; Juhl, M.; Lehel, S.; Palner, M.; Svarer, C.; Plavén-Sigray, P.; et al. An in vivo Pig Model for Testing Novel Positron Emission Tomography Radioligands Targeting Cerebral Protein Aggregates. *Front. Neurosci.* **2022**, *16*, 847074, doi:10.3389/fnins.2022.847074.
163. The Michael J. Fox Foundation for Parkinson's Research | Parkinson's Disease. Preclinical Testing of a Novel Tracer for Imaging Alpha-synuclein Aggregates. Available online: https://www.michaeljfox.org/grant/preclinical-testing-novel-tracer-imaging-alpha-synuclein-aggregates (accessed on 13 July 2022).
164. Ono, M.; Doi, Y.; Watanabe, H.; Ihara, M.; Ozaki, A.; Saji, H. Structure–activity relationships of radioiodinated diphenyl derivatives with different conjugated double bonds as ligands for α-synuclein aggregates. *RSC Adv.* **2016**, *6*, 44305–44312, doi:10.1039/C6RA02710E.
165. Borroni, E.; Gobbi, L.; Honer, M.; Martin Edelmann, Dale Mitchell, David Hardick, Wolfgang Schmidt, Christopher Steele, Mushtaq Mulla. US20200316232A1 - Radiolabeled compounds - Google Patents. Available online: https://patents.google.com/patent/US20200316232A1/en (accessed on 13 July 2022).
166. Lengyel-Zhand, Z.; Ferrie, J.J.; Janssen, B.; Hsieh, C.-J.; Graham, T.; Xu, K.-Y.; Haney, C.M.; Lee, V.M.-Y.; Trojanowski, J.Q.; Petersson, E.J.; et al. Synthesis and characterization of high affinity fluorogenic α-synuclein probes. *Chem. Commun. (Camb)* **2020**, *56*, 3567–3570, doi:10.1039/c9cc09849f.
167. Kuker, R.; Sztejnberg, M.; Gulec, S. I-124 Imaging and dosimetry. *Mol. Imaging Radionucl. Ther.* **2017**, *26*, 66–73, doi:10.4274/2017.26.suppl.07.
168. Rault, E.; Vandenberghe, S.; van Holen, R.; Beenhouwer, J. de; Staelens, S.; Lemahieu, I. Comparison of image quality of different iodine isotopes (I-123, I-124, and I-131). *Cancer Biother. Radiopharm.* **2007**, *22*, 423–430, doi:10.1089/cbr.2006.323.
169. Irwin, D.J.; Grossman, M.; Weintraub, D.; Hurtig, H.I.; Duda, J.E.; Xie, S.X.; Lee, E.B.; van Deerlin, V.M.; Lopez, O.L.; Kofler, J.K.; et al. Neuropathological and genetic correlates of survival and dementia onset in synucleinopathies: a retrospective analysis. *The Lancet Neurology* **2017**, *16*, 55–65, doi:10.1016/S1474-4422(16)30291-5.
170. Barrett, P.J.; Timothy Greenamyre, J. Post-translational modification of α-synuclein in Parkinson's disease. *Brain Res.* **2015**, *1628*, 247–253, doi:10.1016/j.brainres.2015.06.002.
171. van der Perren, A.; Gelders, G.; Fenyi, A.; Bousset, L.; Brito, F.; Peelaerts, W.; van den Haute, C.; Gentleman, S.; Melki, R.; Baekelandt, V. The structural differences between patient-derived α-synuclein strains dictate characteristics of Parkinson's disease, multiple system atrophy and dementia with Lewy bodies. *Acta Neuropathol.* **2020**, *139*, 977–1000, doi:10.1007/s00401-020-02157-3.
172. Shahnawaz, M.; Mukherjee, A.; Pritzkow, S.; Mendez, N.; Rabadia, P.; Liu, X.; Hu, B.; Schmeichel, A.; Singer, W.; Wu, G.; et al. Discriminating α-synuclein strains in Parkinson's disease and multiple system atrophy. *Nature* **2020**, *578*, 273–277, doi:10.1038/s41586-020-1984-7.
173. Strohäker, T.; Jung, B.C.; Liou, S.-H.; Fernandez, C.O.; Riedel, D.; Becker, S.; Halliday, G.M.; Bennati, M.; Kim, W.S.; Lee, S.-J.; et al. Structural heterogeneity of α-synuclein fibrils amplified from patient brain extracts. *Nat. Commun.* **2019**, *10*, 5535, doi:10.1038/s41467-019-13564-w.

174. Espa, E.; Clemensson, E.K.H.; Luk, K.C.; Heuer, A.; Björklund, T.; Cenci, M.A. Seeding of protein aggregation causes cognitive impairment in rat model of cortical synucleinopathy. *Mov. Disord.* **2019**, *34*, 1699–1710, doi:10.1002/mds.27810.
175. Thakur, P.; Breger, L.S.; Lundblad, M.; Wan, O.W.; Mattsson, B.; Luk, K.C.; Lee, V.M.Y.; Trojanowski, J.Q.; Björklund, A. Modeling Parkinson's disease pathology by combination of fibril seeds and α-synuclein overexpression in the rat brain. *Proc. Natl. Acad. Sci. U. S. A.* **2017**, *114*, E8284-E8293, doi:10.1073/pnas.1710442114.
176. US20170157274A1 - Compounds binding to neuropathological aggregates - Google Patents. Available online: https://patents.google.com/patent/US20170157274A1/en (accessed on 27 May 2022).
177. Mathis, C.A.; Wang, Y.; Holt, D.P.; Huang, G.-F.; Debnath, M.L.; Klunk, W.E. Synthesis and evaluation of 11C-labeled 6-substituted 2-arylbenzothiazoles as amyloid imaging agents. *J. Med. Chem.* **2003**, *46*, 2740–2754, doi:10.1021/jm030026b.
178. Ye, L.; Velasco, A.; Fraser, G.; Beach, T.G.; Sue, L.; Osredkar, T.; Libri, V.; Spillantini, M.G.; Goedert, M.; Lockhart, A. In vitro high affinity alpha-synuclein binding sites for the amyloid imaging agent PIB are not matched by binding to Lewy bodies in postmortem human brain. *J. Neurochem.* **2008**, *105*, 1428–1437, doi:10.1111/j.1471-4159.2008.05245.x.
179. Klunk, W.E.; Wang, Y.; Huang, G.-F.; Debnath, M.L.; Holt, D.P.; Shao, L.; Hamilton, R.L.; Ikonomovic, M.D.; DeKosky, S.T.; Mathis, C.A. The Binding of 2-(4′-Methylaminophenyl)Benzothiazole to Postmortem Brain Homogenates Is Dominated by the Amyloid Component. *J. Neurosci.* **2003**, *23*, 2086–2092, doi:10.1523/JNEUROSCI.23-06-02086.2003.
180. Neurobiobank München - Zentrum für Neuropathologie und Prionforschung - LMU München. Available online: https://www.neuropathologie.med.uni-muenchen.de/neurobiobank_muenchen/index.html (accessed on 31 May 2022).
181. Hantzsch, A.; Weber, J.H. Ueber Verbindungen des Thiazols (Pyridins der Thiophenreihe). *Ber. Dtsch. Chem. Ges.* **1887**, *20*, 3118–3132, doi:10.1002/cber.188702002200.
182. Mishra, C.B.; Kumari, S.; Tiwari, M. Thiazole: a promising heterocycle for the development of potent CNS active agents. *Eur. J. Med. Chem.* **2015**, *92*, 1–34, doi:10.1016/j.ejmech.2014.12.031.
183. Imperial College London; Chemical Engineering. Spiral: An Experimental Study on the Effects of Solvents on the Rate and Selectivity of Organic Reactions. Available online: https://spiral.imperial.ac.uk/handle/10044/1/24807 (accessed on 27 September 2021).
184. Kornblum, N.; Powers, J.W.; Anderson, G.J.; Jones, W.J.; Larson, H.O.; Levand, O.; Weaver, W.M. A NEW AND SELECTIVE METHOD OF OXIDATION. *J. Am. Chem. Soc.* **1957**, *79*, 6562, doi:10.1021/ja01581a057.
185. PubChem. Tetrahydrofuran. Available online: http://aquila.tversu.ru/LIB/Book/ComprehensiveHClBE.pdf (accessed on 6 June 2022).
186. Goud, N.S.; Bhattacharya, A.; Joshi, R.K.; Nagaraj, C.; Bharath, R.D.; Kumar, P. Carbon-11: Radiochemistry and Target-Based PET Molecular Imaging Applications in Oncology, Cardiology, and Neurology. *J. Med. Chem.* **2021**, *64*, 1223–1259, doi:10.1021/acs.jmedchem.0c01053.
187. Dollé, F. Carbon-11 and fluorine-18 chemistry devoted to molecular probes for imaging the brain with positron emission tomography. *J. Labelled Comp. Radiopharm.* **2013**, *56*, 65–67, doi:10.1002/jlcr.3037.
188. Ribeiro, M.J.; Almeida, P.; Strul, D.; Ferreira, N.; Loc'h, C.; Brulon, V.; Trébossen, R.; Mazière, B.; Bendriem, B. Comparison of fluorine-18 and bromine-76 imaging in positron emission tomography. *Eur. J. Nucl. Med.* **1999**, *26*, 758–766, doi:10.1007/s002590050447.
189. Tietz, O.; Dzandzi, J.; Bhardwaj, A.; Valliant, J.F.; Wuest, F. Design and synthesis of (125)IPyricoxib: A novel (125)I-labeled cyclooxygenase-2 (COX-2) inhibitors. *Bioorg. Med. Chem. Lett.* **2016**, *26*, 1516–1520, doi:10.1016/j.bmcl.2016.02.029.
190. Sandström, M.; Tolmachev, V.; Kairemo, K.; Lundqvist, H.; Lubberink, M. Performance of coincidence imaging with long-lived positron emitters as an alternative to dedicated PET and SPECT. *Phys. Med. Biol.* **2004**, *49*, 5419–5432, doi:10.1088/0031-9155/49/24/002.
191. Beattie, B.J.; Finn, R.D.; Rowland, D.J.; Pentlow, K.S. Quantitative imaging of bromine-76 and yttrium-86 with PET: a method for the removal of spurious activity introduced by cascade gamma rays. *Med. Phys.* **2003**, *30*, 2410–2423, doi:10.1118/1.1595599.

192. Kniess, T.; Laube, M.; Brust, P.; Steinbach, J. 2-[18 F]Fluoroethyl tosylate – a versatile tool for building 18 F-based radiotracers for positron emission tomography. *Med. Chem. Commun.* **2015**, *6*, 1714–1754, doi:10.1039/C5MD00303B.
193. Hocke, C.; Prante, O.; Salama, I.; Hübner, H.; Löber, S.; Kuwert, T.; Gmeiner, P. 18F-Labeled FAUC 346 and BP 897 derivatives as subtype-selective potential PET radioligands for the dopamine D3 receptor. *ChemMedChem* **2008**, *3*, 788–793, doi:10.1002/cmdc.200700327.
194. Tietze, R.; Hocke, C.; Löber, S.; Hübner, H.; Kuwert, T.; Gmeiner, P.; Prante, O. Syntheses and radiofluorination of two derivatives of 5-cyano-indole as selective ligands for the dopamine subtype-4 receptor. *J Label Compd Radiopharm* **2006**, *49*, 55–70, doi:10.1002/jlcr.1026.
195. Khanapur, S.; Paul, S.; Shah, A.; Vatakuti, S.; Koole, M.J.B.; Zijlma, R.; Dierckx, R.A.J.O.; Luurtsema, G.; Garg, P.; van Waarde, A.; et al. Development of 18F-labeled pyrazolo4,3-e-1,2,4- triazolo1,5-cpyrimidine (SCH442416) analogs for the imaging of cerebral adenosine A2A receptors with positron emission tomography. *J. Med. Chem.* **2014**, *57*, 6765–6780, doi:10.1021/jm500700y.
196. Wilson, A.A.; DaSilva, J.N.; Houle, S. [18F]fluoroalkyl analogues of the potent 5-HT1A antagonist WAY 100635: Radiosyntheses and in vivo evaluation. *Nuclear Medicine and Biology* **1996**, *23*, 487–490, doi:10.1016/0969-8051(96)00026-1.
197. Thermo Fischer Scientific. Safety data sheet of Tetrabutylammonium hydroxide.
198. Khavasi, H.R.; Mir Mohammad Sadegh, B. Influence of N-heteroaromatic π-π stacking on supramolecular assembly and coordination geometry; effect of a single-atom change in the ligand. *Dalton Trans.* **2015**, *44*, 5488–5502, doi:10.1039/c4dt03518f.
199. Huber, R.G.; Margreiter, M.A.; Fuchs, J.E.; Grafenstein, S. von; Tautermann, C.S.; Liedl, K.R.; Fox, T. Heteroaromatic π-stacking energy landscapes. *J. Chem. Inf. Model.* **2014**, *54*, 1371–1379, doi:10.1021/ci500183u.
200. Konnova, E.A.; Swanberg, M. *Parkinson's Disease: Pathogenesis and Clinical Aspects*: *Animal Models of Parkinson's Disease;* Brisbane (AU), 2018, ISBN 9780994438164.
201. Fodero-Tavoletti, M.T.; Smith, D.P.; McLean, C.A.; Adlard, P.A.; Barnham, K.J.; Foster, L.E.; Leone, L.; Perez, K.; Cortés, M.; Culvenor, J.G.; et al. In vitro characterization of Pittsburgh compound-B binding to Lewy bodies. *J. Neurosci.* **2007**, *27*, 10365–10371, doi:10.1523/JNEUROSCI.0630-07.2007.
202. Patrick, G.L. *An introduction to medicinal chemistry*, Fifth edition; Oxford University Press: Oxford, 2013, ISBN 9780199697397.
203. Holec, S.A.M.; Woerman, A.L. Evidence of distinct α-synuclein strains underlying disease heterogeneity. *Acta Neuropathol.* **2021**, *142*, 73–86, doi:10.1007/s00401-020-02163-5.
204. Goedert, M.; Jakes, R.; Anthony Crowther, R.; Grazia Spillantini, M. Parkinson's Disease, Dementia with Lewy Bodies, and Multiple System Atrophy as α-Synucleinopathies. *Methods Mol. Med.* **2001**, *62*, 33–59, doi:10.1385/1-59259-142-6:33.
205. Emond, E.C.; Groves, A.M.; Hutton, B.F.; Thielemans, K. Effect of positron range on PET quantification in diseased and normal lungs. *Phys. Med. Biol.* **2019**, *64*, 205010, doi:10.1088/1361-6560/ab469d.
206. Hooshyar Yousefi, B.; Shi, K.; Arzberger, T.; Wester, H.J.; Schwaiger, M.; Yakushev, I.; Weber, W. Translational study of a novel alpha-synuclein PET tracer designed for first-in-human investigating. In *57. Jahrestagung der Deutschen Gesellschaft für Nuklearmedizin.* NuklearMedizin 2019, Bremen, 4/3/2019 - 4/6/2019; Georg Thieme Verlag KG, 2019.
207. Alber, J.; Alladi, S.; Bae, H.-J.; Barton, D.A.; Beckett, L.A.; Bell, J.M.; Berman, S.E.; Biessels, G.J.; Black, S.E.; Bos, I.; et al. White matter hyperintensities in vascular contributions to cognitive impairment and dementia (VCID): Knowledge gaps and opportunities. *Alzheimer's & Dementia: Translational Research & Clinical Interventions* **2019**, *5*, 107–117, doi:10.1016/j.trci.2019.02.001.
208. Kuchar, M.; Mamat, C. Methods to Increase the Metabolic Stability of (18)F-Radiotracers. *Molecules* **2015**, *20*, 16186–16220, doi:10.3390/molecules200916186.
209. Lipinski, C.A. Lead- and drug-like compounds: the rule-of-five revolution. *Drug Discov. Today Technol.* **2004**, *1*, 337–341, doi:10.1016/j.ddtec.2004.11.007.
210. Howard, J.A.K.; Hoy, V.J.; O'Hagan, D.; Smith, G.T. How good is fluorine as a hydrogen bond acceptor? *Tetrahedron* **1996**, *52*, 12613–12622, doi:10.1016/0040-4020(96)00749-1.
211. Pan, J.; Pourghiasian, M.; Hundal, N.; Lau, J.; Bénard, F.; Dedhar, S.; Lin, K.-S. f-18Ffluoroethanol and 3-18Ffluoropropanol: facile preparation, biodistribution in mice, and their application as nucleophiles in the

synthesis of 18Ffluoroalkyl aryl ester and ether PET tracers. *Nuclear Medicine and Biology* **2013**, *40*, 850–857, doi:10.1016/j.nucmedbio.2013.04.009.
212. Weeks, A.M.; Coyle, S.M.; Jinek, M.; Doudna, J.A.; Chang, M.C.Y. Structural and biochemical studies of a fluoroacetyl-CoA-specific thioesterase reveal a molecular basis for fluorine selectivity. *Biochemistry* **2010**, *49*, 9269–9279, doi:10.1021/bi101102u.
213. Suryan, M.M.; Kafafi, S.A.; Stein, S.E. Dissociation of substituted anisoles: substituent effects on bond strengths. *J. Am. Chem. Soc.* **1989**, *111*, 4594–4600, doi:10.1021/ja00195a011.
214. Anders, M.W.; Sunram, J.M.; Wilkinson, C.F. Mechanism of the metabolism of 1,3-benzodioxoles to carbon monoxide. *Biochem. Pharmacol.* **1984**, *33*, 577–580, doi:10.1016/0006-2952(84)90310-1.
215. Wilkinson, C.F.; Hicks, L.J. Microsomal metabolism of the 1,3-benzodioxole ring and its possible significance in synergistic action. *J. Agric. Food Chem.* **1969**, *17*, 829–836, doi:10.1021/jf60164a009.

10. APPENDIX

10.1 Abbreviations, Acronyms, Symbols

%ID/g	Percent of the injected radioactivity per gram tissue.
[^{123}I]FP-CIT	N-ω-fluoropropyl- 2β-carbomethoxy- 3β-(4-[^{123}Iiodophenyl) nortropane or [^{123}IIoflupane
[^{123}I]Iofetamine	N-isopropyl-p-[^{123}I]iodoamphetamine
[^{123}I]MIBG	[^{123}I]metaiodobenzylguanidine
[^{123}I]β-CIT	2β-carbomethoxy-3β-(4-[^{123}I]iodophenyl)tropane
[^{18}F]FDETos	2-(2-[^{18}F]fluoroethoxy)ethyl 4-methylbenzenesulfonate
[^{18}F]FETos	2-([^{18}F]fluoro-)ethyl 4-methylbenzenesulfonate
[^{18}F]FTETos	2-(2-(2-[^{18}F]fluoroethoxy)ethoxy)ethyl 4-methylbenzenesulfonate
[^{99m}Tc]ECD	^{99m}Tc-ethyl cysteinate dimer
[^{99m}Tc]HMPAO	^{99m}Tc-hexamethylpropyleneamineoxime
^{13}C-NMR	Carbon-13 NMR
^{1}H-NMR	Proton NMR
2,6-ANS	2-Anilinonaphthalene-6-sulfonic acid
2,6-TNS	6-(p-tolylamino)naphthalene-2-sulfonic acid
ACh	Acetylcholine
AD	Alzheimer's disease
ALS	Amyotrophic lateral sclerosis
A_m	Molar activity previously known as specific activity
ANS	Autonomic nervous system
APOE	Apolipoprotein E
ATP	Adenosine triphosphate
Aβ	Beta-amyloid plaques/fibrils/aggregates
BFPD	Benzodioxole fluoroethylated/PEGylated DABTAs
CBD	Corticobasal dementia
CERAD	Consortium to establish a registry for Alzheimer's disease
Cl	Chloride
Clog P	Calculated log P
CNS	Central nervous system
COQ_2	Coenzyme-Q2
CP	Cerebellar peduncle
CSF	Cerebrospinal fluid
CSPα	Cysteine string protein-α
CT	Computed tomography
CY	Chemical yield
DABTA	4,4'-Disarylbisthiazole
DAT	Dopamine transporter
DCT1	Divalent cation transporter 1
DIP	Drug-induced parkinsonism
DJ-1	Protein deglycase DJ-1, also known as Parkinson disease protein-7
DLB	Dementia with Lewy bodies
DMF	Dimethylformamide
DMSO	Dimethylsulfoxide
DMV	Dorsal motor nucleus of the vagus
DN	Dopaminergic neurons
DTO	Dithiooxamide
EC	Electron capture

EDG	Electron-donating group
ET	Essential tremor
EOPD	Early-onset Parkinson's disease
ER	Endoplasmic reticulum
ESI-MS	Electrospray Ionisation Mass Spectrometry
EWG	Electron withdrawing group
FDG	2-deoxy-2-fluoro-D-glucose
F-dopa	Fluorodopa
fp	Free plasma fraction, i.e. fraction of the radiotracer that is not bound to plasma proteins.
GBA-1	Glucocerebrosidase (gene 1)
GBq	GigaBequerel
GCI	Glial cytoplasmic inclusions
GFAP	Glial fibrillary acidic protein
GPe	External segment of the globus pallidus
HPLC	High pressure liquid chromatography
I	Iodine
DPFPD	[1,3]dioxolo[4,5-b]pyridine fluoroethylated/PEGylated DABTAs
IHC	Immunohistochemistry
$K_2C_2O_4.H_2O$	Potassium oxalate monohydrate
K_2CO_3	Potassium carbonate
$KHCO_3$	Potassium hydrogen carbonate
LB	Lewy bodies
LBD	Lewy body dementia
LC	Locus coeruleus
LC-MS	Liquid chromatography-mass spectrometry
L-dopa	Levodopa
LG	Leaving group
LN	Lewy neurites
log D	Logarithm of the octanol-water distribution coefficient at pH 7.4
log P	Logarithm of the partition co-efficient
LRRK2	Leucine-rich repeat kinase 2 also known as dardarin and Parkinson disease protein-8
MBP	Myelin basic protein
MBq	MegaBecquerel
MeCN	Acetonitrile
MeOH	Methanol
MEWN	Midbrain Edinger-Westphal nucleus
MM/GBSA	Molecular mechanics generalized Born model and solvent accessibility
MP4A	N-[^{11}C]-methyl-4-piperidyl acetate
MP4P	N-[^{11}C]-methyl-4-piperidyl propionate
MPP	1-methyl-4-phenylpyridinium
MPTP	1-methyl-4-phenyl-1,2,3,6-tetrahydropyridine
MRI	Magnetic resonance imaging
mRNA	Messenger ribonucleic acid
MRS	Magnetic resonance spectroscopy
MSA	Multiple system atrophy
MW	Molecular weight
NAC	Non-amyloid-component
NaOH	Sodium hydroxide
NBM	Nucleus basalis of Meynert

NCI	Neuronal cytoplasmic inclusions
NDD	Neurodegenerative diseases
NFTs	Neurofibrillary tangles
NHP	Non-human primates
NM	Neuromelanin
NMR	Nuclear magnetic resonance
OPC	Olivopontocerebellar
OPCA	Olivopontocerebellar atrophy
OSEM3D	Three dimensional ordered subsets expectation maximization
PHBT	Postmortem human brain tissues (diseased)
PD	Parkinson's disease
PDD	Parkinson's disease dementia
PET	Positron emission tomography
PFF	Preformed α-synuclein fibrils (from recombinant monomers)
PiB	Pittsburg compound
PNS	Peripheral nervous system
PPS	Parkinson-plus syndrome
PSP	Progressive supranuclear palsy
PTM	Post-translation modification
RCC	Radiochemical conversions
RCP	Radiochemical purity
RCY	Radiochemical yield
REM	Rapid eye movement
RMD	Rapid eye movement sleep behavior disorder
RP	Reversed phase
rt	Room temperature
Rtn	Reaction
SCP	Superior cerebellar peduncle
Semiprep	Semipreparative
SHP	Semipreparative high-pressure liquid chromatograpy (HPLC) purification
SN	Substantia nigra
SNARE	Soluble N-ethylmaleimide-Sensitive Factor Attachment Proteins receptor
SNCA	Alpha-synuclein gene
SNP	Single nucleotide polymorphism
SNpc	Substantia nigra par compacta
SNR	Signal-to-noise ratio
SPECT	Single-photon emission computer tomography
TBAH	Tetrabutyammonium hydroxide
Tc	Technetium
THF	Tetrahydrofuran
ThS	Thioflavin S
ThT	Thioflavin T
TFA	Trifluoroacetic acid
TPSO	Topological surface area
T°C	Temperature
VD	Vascular dementia
VP	Vascular parkinsonism
α-syn	α-synuclein aggregates/fibrils

10.2 Figures and Legends

10.3 Tables

10.4 Reaction schemes

10.5 Characterization of the DABTAs

Nuclear Magnetic Resonance (NMR) and Mass Spectrometry (MS) Characterization

DABTA		**IUPAC Nomenclature**
b_1		**4-(benzo[d][1,3]dioxol-5-yl)thiazole-2-carbothioamide**
NMR	^{1}H	(DMSO-d_6) δ 6.07 (s, 2H), 7.00 (d, J = 5.5 Hz, 1H), 7.61 (dd, J = 4.3, 8.3 Hz, 1H), 7.69 (s, 1H), 8.27 (s, 1H), 9.94 (s, 1H), 10.19 (s, 1H).
	^{13}C	DMSO-d_6) δ 39.02, 39.19, 39.35, 39.52, 39.69, 39.85, 40.02, 101.30, 106.77, 108.55, 120.25, 121.60, 127.98, 147.54, 147.86, 155.27, 167.64, 186.46
ESI-MS	[M+1]	265.0
b_3		**4-(3-hydroxy-4-methoxyphenyl)thiazole-2-carbothioamide**
NMR	^{1}H	(DMSO-d_6) δ 3.82 (s, 3H), 7.00 (d, J = 5.6 Hz, 1H), 7.33 – 7.59 (m, 2H), 8.16 (s, 1H), 9.05 (s, 1H), 9.87 (s, 1H), 10.18 (s, 1H).
	^{13}C	(DMSO-d_6) δ 55.68, 112.05, 113.71, 117.69, 121.19, 126.74, 146.57, 148.18, 155.85, 167.71, 186.62
ESI-MS	[M+1]	267.0
b_4		**4-(3-fluoro-4-methoxyphenyl)thiazole-2-carbothioamide**
NMR	^{1}H	(DMSO-d_6) δ 3.89 (s, 3H), 7.21 – 7.29 (m, 1H), 7.85 (d, J = 8.8 Hz, 1H), 7.98 (d, J = 13.0 Hz, 1H), 8.34 (s, 1H), 9.98 (s, 1H), 10.21 (s, 1H)
	^{13}C	(DMSO-d_6) δ 39.02, 39.19, 39.35, 39.52, 39.69, 39.85, 40.02, 101.30, 106.77, 108.55, 120.25, 121.60, 127.98, 147.54, 147.86, 155.27, 167.64, 186.46.
ESI-MS	[M+1]	269.1
b_7		**4-(6-bromopyridin-3-yl)thiazole-2-carbothioamide**
NMR	^{1}H	(DMSO-d_6) δ 7.80 (d, J=7.98 Hz, 1 H,) 8.39 (d, J=8.25 Hz, 1 H) 8.62 (br. s., 1 H) 9.11 (br. s., 1 H) 10.05 (br. s., 1 H) 10.29 (br. s., 1 H)
	^{13}C	(DMSO-d_6) δ 125.65, 128.67, 129.62, 137.14, 141.41, 148.63, 151.76, 169.20, 186.61
ESI-MS	[M+1] [M+1]	299.9 301.9
b_8		**4-(6-fluoropyridin-3-yl)thiazole-2-carbothioamide**
NMR	^{1}H	(DMSO-d_6) δ 7.33 (d, J = 8.5 Hz, 1H), 8.54 (d, J = 3.1 Hz, 1H), 8.61 (d, J = 8.7 Hz, 1H), 8.97 (s, 1H), 10.03 (s, 1H), 10.27 (s, 1H)
	^{13}C	(DMSO-d_6) δ 109.69, 124.24, 128.13, 128.16, 139.67, 139.74, 145.50, 145.63, 151.45, 161.86, 163.75, 168.62, 186.24.
ESI-MS	[M+1]	240.0

b_9		**4-(2-chloropyrimidin-4-yl)thiazole-2-carbothioamide**
NMR	^{1}H	(DMSO-d_6) δ 8.70 (s, 1H), 9.42 (s, 2H), 10.08 (s, 1H), 10.32
	^{13}C	(DMSO-d_6) δ 126.43, 126.74, 148.29, 157.64, 159.18, 160.95, 169.13, 185.99
ESI-MS	[M+1]	257.2
b_{10}		**4-(2-fluoropyrimidin-4-yl)thiazole-2-carbothioamide**
NMR	^{1}H	(DMSO-d_6) δ 8.65 (q, J = 2.4 Hz, 1H), 9.44 (s, 1H), 10.07 (s, 1H), 10.31 (s, 1H)
	^{13}C	(DMSO-d_6) δ 125.99, 127.09, 127.13, 148.82, 159.47, 159.57, 161.37, 163.08, 169.47, 186.50
ESI-MS	[M+1]	241.2
b_{11}		**4-(5-hydroxypyrimidin-2-yl)thiazole-2-carbothioamide**
NMR	^{1}H	(DMSO-d_6) δ 8.43 (d, J = 2.5 Hz, 2H), 8.50 (d, J = 2.5 Hz, 1H), 9.81 (s, 1H), 10.23 (s, 1H), 10.72 (s, 1H).
	^{13}C	(DMSO-d_6) δ 128.73, 144.52, 150.99, 151.66, 155.06, 168.74, 186.67.
ESI-MS	[M+1]	239.2
b_{12}		**4-(3-fluoro-4-hydroxyphenyl)thiazole-2-carbothioamide**
NMR	^{1}H	(DMSO-d_6) δ 7.01 (t, J = 8.7 Hz, 1H), 7.69 (dd, J = 2.1, 8.4 Hz, 1H), 7.91 (dd, J = 2.1, 12.7 Hz, 1H), 8.25 (s, 1H), 9.94 (s, 1H), 10.15 (s, 1H), 10.19 (s, 1H).
	^{13}C	(DMSO-d_6) δ 114.23, 114.38, 117.92, 117.95, 121.50, 122.62, 122.64, 125.59, 125.64, 145.30, 145.40, 150.25, 152.16, 154.69, 154.71, 167.77, 186.46.
ESI-MS	[M+1]	255.2
b_{13}		**4-(4-hydroxyphenyl)thiazole-2-carbothioamide**
NMR	^{1}H	(DMSO-d_6) δ 6.79 – 6.87 (m, 2H), 7.88 (dd, *J* = 2.2, 8.7 Hz, 2H), 8.14 (d, *J* = 2.1 Hz, 1H), 9.70 (s, 1H), 9.86 (s, 1H), 10.16 (s, 1H).
	^{13}C	(DMSO-d_6) δ 115.51, 120.45, 124.91, 127.80, 156.03, 157.94, 167.67, 186.61.
ESI-MS	[M+1]	237.1
b_{14}		**4-(4-chloro-3-nitrophenyl)thiazole-2-carbothioamide**
NMR	^{1}H	(DMSO-d_6) δ 7.90 (dd, *J* = 2.3, 8.4 Hz, 1H), 8.38 (dd, *J* = 2.3, 8.4 Hz, 1H), 8.67 (d, *J* = 2.3 Hz, 1H), 8.78 (d, *J* = 2.3 Hz, 1H), 10.11 (s, 1H), 10.29 (s, 1H).
	^{13}C	(DMSO-d6) δ 122.75, 124.25, 125.72, 130.83, 132.13, 134.04, 148.31, 151.90, 168.58, 186.12.
ESI-MS	[M+1]	299.9
	[M-1]	297.9
b_{15}		**4-(2-chloropyridin-4-yl)thiazole-2-carbothioamide**
NMR	^{1}H	(DMSO-d_6) δ 8.02 – 8.08 (m, 1H), 8.24 (d, *J* = 2.7 Hz, 1H), 8.47 – 8.54 (m, 1H), 8.83 (d, *J* = 2.1 Hz, 1H), 10.12 (s, 1H), 10.31 (s, 1H).
	^{13}C	(DMSO-d_6) δ 39.78, 120.20, 121.17, 128.56, 144.40, 151.04, 151.80, 151.90, 169.30, 186.56.
ESI-MS	[M+1]	256.1
b_{16}		**4-(2,4-dihydroxyphenyl)thiazole-2-carbothioamide**
NMR	^{1}H	(DMSO-d_6) δ 6.32 (dd, *J* = 2.3, 8.6 Hz, 1H), 6.41 (d, *J* = 2.2 Hz, 1H), 8.00 (d, *J* = 8.6 Hz, 1H), 8.14 (s, 1H), 9.56 (d, *J* = 1.4 Hz, 1H), 9.91 (s, 1H), 10.13 (s, 1H), 10.14 (s, 1H).
	^{13}C	(DMSO-d_6) δ 102.84, 107.08, 111.69, 122.59, 130.19, 153.42, 156.33, 158.64, 166.17, 186.60.
ESI-MS	[M+1]	253.1
d_1		**5-(4'-(benzo[d][1,3]dioxol-5-yl)-[2,2'-bithiazol]-4-yl)-2-methoxyphenol**

NMR	^{1}H	(DMSO-d_6) δ 3.82 (s, 3H), 6.09 (s, 2H), 7.03 (dd, J = 8.3, 10.5 Hz, 2H), 7.43 (dd, J = 22, 8.4 Hz, 1H), 7.48 (d, J = 2.2 Hz, 1H), 7.59 (d, J = 8.0 Hz, 2H), 8.11 (s, 1H), 8.21 (s, 1H), 9.21 (s, 1H)
	^{13}C	(DMSO-d_6) δ 55.65, 101.37, 106.40, 108.69, 112.35, 113.48, 114.94, 115.36, 117.40, 120.30, 126.42, 127.69, 146.71, 147.58, 147.91, 148.20, 155.15, 155.64, 160.03, 160.31.
ESI-MS	[M+1]	411.1
d_2		**4-(benzo[d][1,3]dioxol-5-yl)-4'-(3-fluoro-4-methoxyphenyl)-2,2'-bithiazole**
NMR	^{1}H	(DMSO-d_6) δ 3.90 (s, 3H), 6.09 (s, 2H), 7.04 (d, J = 8.0 Hz, 1H), 7.29 (t, J = 8.7 Hz, 1H), 7.56 – 7.61 (m, 2H), 7.80 – 7.89 (m, 2H), 8.23 (s, 1H), 8.30 (s, 1H).
	^{13}C	(DMSO-d_6) 2-δ 56.11, 101.37, 106.39, 108.68, 113.67, 114.13, 115.57, 116.14, 120.29, 122.65, 126.57, 127.64, 147.43, 147.91, 150.65, 152.58, 154.17, 155.20, 160.05, 160.43.
ESI-MS	[M+1]	413.1.
d_3		**5-(4'-([1,3]dioxolo[4,5-b]pyridin-6-yl)-[2,2'-bithiazol]-4-yl)-2-methoxyphenol**
NMR	^{1}H	(DMSO-d_6) δ 9.26 (s, 1H), 8.29 (d, J = 10.6 Hz, 2H), 8.10 (s, 1H), 7.80 (s, 1H), 7.46 (s, 1H), 7.42 (d, J = 7.4 Hz, 1H), 7.01 (d, J = 8.4 Hz, 1H), 6.21 (s, 2H), 3.81 (s, 3H).
	^{13}C	(DMSO-d_6)1-δ 55.72, 100.88, 112.30, 112.40, 113.52, 115.23, 116.65, 117.52, 124.52, 126.45, 136.85, 140.54, 146.77, 148.30, 152.64, 155.75, 158.23, 159.79, 160.95.
ESI-MS	[M+1]	412.1.
d_4		**6-(4'-(3-fluoro-4-methoxyphenyl)-[2,2'-bithiazol]-4-yl)-[1,3]dioxolo[4,5-b]pyridine**
NMR	^{1}H	(DMSO-d_6/THF-d_8 4:3 vol.) δ 3.92 (s, 3H), 6.22 (s, 2H), 7.25 – 7.33 (m, 1H), 7.82 – 7.89 (m, 3H), 8.29 – 8.38 (m, 3H).
	^{13}C	(DMSO-d_6/THF-d_8 4:3 vol.) δ 55.90, 100.84, 112.00, 113.45, 113.61, 113.89, 115.99, 116.43, 122.47, 122.50, 124.52, 126.69, 126.74, 136.96, 140.48, 147.57, 147.65, 150.87, 152.80, 152.85, 154.48, 158.26, 160.27, 160.71.
ESI-MS	[M+1]	414.1.
d_5		**4-(benzo[d][1,3]dioxol-5-yl)-4'-(6-bromopyridin-3-yl)-2,2'-bithiazole**
NMR	^{1}H	(DMSO-d_6) δ 6.10 (s, 2H), 7.05 (dd, J = 0.8, 7.7 Hz, 1H), 7.59 (d, J = 7.8 Hz, 2H), 7.80 (dd, J = 0.7, 8.3 Hz, 1H), 8.27 (s, 1H), 8.34 (dd, J = 2.6, 8.3 Hz, 1H), 8.59 (s, 1H), 9.04 (dd, J = 0.7, 2.5 Hz, 1H).
	^{13}C	(DMSO-d_6) 1- δ 101.42, 106.42, 108.74, 115.96, 119.33, 120.35, 127.58, 128.43, 128.93, 136.78, 140.96, 147.67, 147.95, 151.30, 155.31, 159.74, 161.36.
ESI-MS	[M+1] [M+1]	444.2 446.2
d_6		**4-(benzo[d][1,3]dioxol-5-yl)-4'-(6-fluoropyridin-3-yl)-2,2'-bithiazole**
NMR	^{1}H	(DMSO-d_6) δ 6.07 – 6.12 (m, 2H), 7.04 (dd, J = 2.8, 7.9 Hz, 1H), 7.34 (d, J = 8.5 Hz, 1H), 7.59 (dd, J = 2.8, 10.5 Hz, 2H), 8.23 – 8.27 (m, 1H), 8.48 – 8.52 (m, 1H), 8.54 – 8.61 (m, 1H), 8.89 (s, 1H)
	^{13}C	(DMSO-d_6) δ 101.40, 106.40, 108.71, 109.85, 110.15, 115.85, 118.31, 120.32, 127.59, 127.90, 127.94, 139.75, 139.81, 145.23, 145.35, 147.64, 147.93, 151.42, 155.28, 159.80, 161.20, 161.84, 163.73.
ESI-MS	[M+1]	384.0
d_7		**6-(4'-(6-bromopyridin-3-yl)-[2,2'-bithiazol]-4-yl)-[1,3]dioxolo[4,5-b]pyridine**
NMR	^{1}H	(DMSO-d_6/THF-d_8 4:3 vol.) δ 6.22 (s, 2H), 7.78 (d, J = 8.8 Hz, 1H), 7.82 – 7.87 (m, 1H), 8.35 – 8.41 (m, 3H), 8.62 (s, 1H), 9.08 (s, 1H).
	^{13}C	(DMSO-d_6/THF-d_8 4:3 vol.) 1-δ 100.85, 111.99, 116.75, 119.17, 124.46, 128.22, 129.00, 136.51, 137.02, 140.50, 141.02, 147.88, 151.56, 153.00, 158.31, 160.34, 161.24.
ESI-MS	[M+1] [M+1]	445.3 447.2.

d_8		**6-(4'-(6-fluoropyridin-3-yl)-[2,2'-bithiazol]-4-yl)-[1,3]dioxolo[4,5-b]pyridine**
NMR	^1H	(DMSO-d_6/THF-d_8 4:3 vol.) δ 6.23 (s, 2H), 7.29 – 7.35 (m, 1H), 7.85 (d, J = 5.9 Hz, 1H), 8.34 – 8.40 (m, 2H), 8.54 (s, 1H), 8.61 (s, 1H), 8.93 (d, J = 3.9 Hz, 1H).
	^{13}C	(DMSO-d_6/THF-d_8 4:3 vol.) 1-δ 100.85, 109.59, 109.89, 112.02, 116.75, 118.24, 124.46, 127.97, 136.97, 139.55, 139.62, 140.49, 145.27, 145.40, 151.66, 152.93, 158.29, 160.42, 161.07, 162.03, 163.92.
ESI-MS	[M+1]	385.3
d_9		**4-(4'-(2-chloropyrimidin-5-yl)-[2,2'-bithiazol]-4-yl)-[1,3]dioxolo[4,5-b]pyridine**
NMR	^1H	(DMSO-d_6) δ 6.23 (s, 2H), 7.85 (d, J = 1.9 Hz, 1H), 8.34 (d, J = 1.9 Hz, 1H), 8.39 (s, 1H), 8.70 (s, 1H), 9.37 (s, 2H).
ESI-MS	[M+1]	402.3.
d_{10}		**4-(4'-(2-fluoropyrimidin-5-yl)-[2,2'-bithiazol]-4-yl)-[1,3]dioxolo[4,5-b]pyridine**
NMR	^1H	(DMSO-d_6/THF-d_8 4:3 vol.) δ 6.22 (s, 2H), 7.85 (d, J = 6.3 Hz, 1H), 8.38 (d, J = 11.8 Hz, 2H), 8.68 (s, 1H), 9.41 (s, 2H)
	^{13}C	(DMSO-d_6/THF-d_8 4:3 vol.) δ 100.87, 112.00, 116.97, 119.75, 124.42, 126.46, 137.01, 140.50, 148.63, 153.03, 158.32, 158.82, 158.91, 160.16, 161.18, 161.68, 162.90.
ESI-MS	[M+1]	386.3
d_{11}		**2-(4'-([1,3]dioxolo[4,5-b]pyridin-6-yl)-[2,2'-bithiazol]-4-yl)pyrimidin-5-ol**
NMR	^1H	(DMSO-d_6) δ 6.23 (s, 2H), 7.84 (s, 1H), 8.33 (s, 2H), 8.47 (s, 3H), 10.74 (s, 1H).
	^{13}C	(DMSO-d_6) δ 100.81, 112.27, 116.90, 122.87, 124.42, 136.83, 140.49, 144.61, 150.96, 151.51, 152.62, 154.94, 158.20, 160.41, 160.84.
ESI-MS	[M+1]	384.2.
d_{12}		**(4'-(benzo[d][1,3]dioxol-5-yl)-[2,2'-bithiazol]-4-yl)pyrimidin-5-ol**
NMR	^1H	(DMSO-d_6) δ 6.09 (s, 2H), 7.04 (d, J = 11.4 Hz, 1H), 7.56 – 7.62 (m, 2H), 8.23 (s, 1H), 8.43 – 8.49 (m, 3H), 10.74 (s, 1H)
	^{13}C	(DMSO-d_6) 2- δ 101.39, 106.43, 108.71, 115.67, 120.32, 122.65, 127.66, 144.60, 147.61, 147.93, 150.94, 151.54, 154.90, 155.18, 160.27, 160.63.
ESI-MS	[M+1]	383.2.
d_{13}		**(4'-([1,3]dioxolo[4,5-b]pyridin-6-yl)-[2,2'-bithiazol]-4-yl)-2-fluorophenol**
NMR	^1H	(DMSO-d_6) δ 6.22 (s, 2H), 7.05 (t, J = 8.8 Hz, 1H), 7.68 (dd, J = 2.0, 8.4 Hz, 1H), 7.75 – 7.84 (m, 2H), 8.22 (s, 1H), 8.31 (d, J = 1.9 Hz, 2H), 10.20 (s, 1H).
	^{13}C	(DMSO-d_6) δ 100.81, 112.22, 113.86, 114.01, 115.59, 116.74, 118.10, 118.13, 122.68, 122.71, 124.42, 125.21, 125.26, 136.80, 140.47, 145.37, 145.47, 150.21, 152.12, 152.61, 154.63, 154.65, 158.17, 160.04, 160.71.
ESI-MS	[M+1]	400.3
d_{14}		**4-(4'-(benzo[d][1,3]dioxol-5-yl)-[2,2'-bithiazol]-4-yl)phenol**
NMR	^1H	(DMSO-d_6) δ 6.09 (s, 2H), 6.87 (d, J = 8.7 Hz, 2H), 7.01 – 7.07 (m, 1H), 7.59 (d, J = 7.8 Hz, 2H), 7.85 (d, J = 8.7 Hz, 2H), 8.10 (s, 1H), 8.22 (s, 1H), 9.74 (s, 1H).
	^{13}C	(DMSO-d_6) δ 101.39, 106.41, 108.71, 114.17, 115.37, 115.66, 120.30, 124.64, 127.67, 127.71, 147.60, 147.93, 155.15, 155.87, 157.94, 160.06, 160.36, 162.35.
ESI-MS	[M+1]	381.2.
d_{15}		**4-(4'-([1,3]dioxolo[4,5-b]pyridin-6-yl)-[2,2'-bithiazol]-4-yl)phenol**

NMR	^{1}H	(DMSO-d_6) δ 6.22 (s, 2H), 6.87 (dd, *J* = 2.8, 8.6 Hz, 2H), 7.80 – 7.87 (m, 3H), 8.11 (d, *J* = 2.7 Hz, 1H), 8.31 (t, *J* = 3.5 Hz, 2H), 9.76 (s, 1H).
	^{13}C	(DMSO-d_6) δ 100.84, 112.26, 114.42, 115.70, 116.63, 124.49, 124.62, 127.70, 136.82, 140.51, 152.60, 155.93, 157.98, 158.20, 159.85, 160.95.
ESI-MS	[M+1]	382.1
d_{16}		**6-(4'-(4-chloro-3-nitrophenyl)-[2,2'-bithiazol]-4-yl)-[1,3]dioxolo[4,5-b]pyridine**
NMR	^{1}H	(DMSO-d_6) δ 6.23 (s, 2H), 7.85 (d, J = 1.8 Hz, 1H), 7.93 (d, J = 8.5 Hz, 1H), 8.33 – 8.41 (m, 3H), 8.67 – 8.72 (m, 2H).
	^{13}C	(DMSO-d_6) δ 100.87, 112.10, 117.08, 120.10, 122.66, 124.38, 124.52, 130.90, 132.34, 133.67, 136.92, 140.51, 148.29, 152.11, 152.89, 158.28, 160.23, 161.11.
ESI-MS	[M+1]	Not found
d_{18}		**4-(benzo[d][1,3]dioxol-5-yl)-4'-(2-chloropyridin-4-yl)-2,2'-bithiazole**
NMR	^{1}H	(DMSO-d_6/THF-d_8 4:1 vol.) δ 6.08 (s, 2H), 6.98 (d, *J* = 7.5 Hz, 1H), 7.46 (dd, *J* = 1.6, 7.5 Hz, 1H), 7.54 (d, *J* = 1.4 Hz, 1H), 7.61 (d, *J* = 1.5 Hz, 1H), 8.00 (dd, *J* = 1.5, 7.5 Hz, 1H), 8.21 (s, 1H), 8.29 (s, 1H), 8.50 (d, *J* = 7.5 Hz, 1H).
	^{13}C	(DMSO-d_6/THF-d_8 4:1 vol.) δ 101.47, 106.39, 108.59, 115.99, 119.76, 120.30, 120.38, 122.39, 127.64, 143.56, 147.74, 148.00, 150.83, 151.49, 151.50, 155.49, 159.55, 161.53.
ESI-MS	[M+1]	401.2
d_{20}		**6-(4'-(2-chloropyridin-4-yl)-[2,2'-bithiazol]-4-yl)-[1,3]dioxolo[4,5-b]pyridine**
NMR	^{1}H	(DMSO-d_6/THF-d_8 3:2 vol.) δ 6.23 (s, 2H), 7.85 (d, *J* = 1.9 Hz, 1H), 8.05 (dd, *J* = 1.5, 5.1 Hz, 1H), 8.12 (dd, *J* = 0.7, 1.5 Hz, 1H), 8.35 – 8.42 (m, 2H), 8.53 (dd, *J* = 0.7, 5.2 Hz, 1H), 8.86 (s, 1H).
	^{13}C	(DMSO-d_6/THF-d_8 3:2 vol.) δ 100.90, 112.03, 117.06, 119.70, 120.38, 122.46, 124.42, 137.02, 140.54, 143.57, 150.75, 151.62, 151.65, 153.04, 158.35, 160.16, 161.37.
ESI-MS	[M+1]	402.4
d_{22}		**4-(4'-([1,3]dioxolo[4,5-b]pyridin-6-yl)-[2,2'-bithiazol]-4-yl)benzene-1,3-diol**
NMR	^{1}H	(DMSO-d_6) δ 6.22 (s, 2H), 6.38 (dd, *J* = 2.3, 8.5 Hz, 1H), 6.45 (d, *J* = 2.3 Hz, 1H), 7.82 (d, *J* = 1.9 Hz, 1H), 7.91 (d, *J* = 8.5 Hz, 1H), 8.12 (s, 1H), 8.27 – 8.35 (m, 2H), 9.59 (s, 1H), 10.31 (s, 1H).
	^{13}C	(DMSO-d_6) δ 100.77, 102.91, 107.20, 111.52, 112.21, 116.41, 124.48, 129.77, 136.77, 140.44, 152.56, 152.91, 156.31, 158.13, 158.18, 158.63, 161.00.
ESI-MS	[M+1]	398.2
f_4		**6-(4'-(5-(2-fluoroethoxy)pyrimidin-2-yl)-[2,2'-bithiazol]-4-yl)-[1,3]dioxolo[4,5-b]pyridine**
NMR	^{1}H	(DMSO-d_6) δ 4.52 (d, J = 29.9 Hz, 2H), 4.82 (d, J = 48.5 Hz, 2H), 6.23 (s, 2H), 7.81 – 7.90 (m, 1H), 8.31 – 8.37 (m, 2H), 8.48 – 8.59 (m, 1H), 8.67 – 8.78 (m, 2H).
	^{13}C	(DMSO-d_6) δ 68.05, 68.20, 81.34, 82.67, 100.81, 112.26, 116.97, 123.84, 124.40, 136.83, 140.48, 144.37, 151.44, 152.65, 152.86, 154.53, 158.20, 160.60, 160.75.
ESI-MS	[M+1]	430.3.
f_5		**4-(benzo[d][1,3]dioxol-5-yl)-4'-(5-(2-fluoroethoxy)pyrimidin-2-yl)-2,2'-bithiazole**
NMR	^{1}H	(DMSO-d_6) δ 4.48 (t, J = 3.6 Hz, 1H), 4.54 (t, J = 3.5 Hz, 1H), 4.77 (t, J = 5.0 Hz, 1H), 4.87 (t, J = 3.3 Hz, 1H), 6.09 (s, 2H), 7.04 (dd, J = 3.2, 8.2 Hz, 1H), 7.59 (dd, J = 3.1, 8.3 Hz, 2H), 8.24 (d, J = 3.3 Hz, 1H), 8.54 (s, 1H), 8.71 (s, 2H).
	^{13}C	(DMSO-d_6) δ 68.05, 68.20, 81.35, 82.67, 101.39, 106.43, 108.70, 115.73, 120.33, 123.61, 127.64, 144.35, 147.62, 147.92, 151.43, 152.89, 154.50, 155.21, 160.18, 160.82.
ESI-MS	[M+1]	429.3.
f_6		**4-(benzo[d][1,3]dioxol-5-yl)-4'-(5-(2-(2-fluoroethoxy)ethoxy)pyrimidin-2-yl)-2,2'-bithiazole**

NMR	^{1}H	(DMSO-d_6) δ 3.71 (t, J = 3.7 Hz, 1H), 3.75 – 3.80 (m, 1H), 3.82 – 3.87 (m, 2H), 4.34 – 4.40 (m, 2H), 4.49 – 4.54 (m, 1H), 4.61 (t, J = 3.6 Hz, 1H), 6.10 (s, 2H), 7.04 (d, J = 15.6 Hz, 1H), 7.56 – 7.61 (m, 2H), 8.24 (s, 1H), 8.53 (s, 1H), 8.70 (s, 2H).
	^{13}C	(DMSO-d_6) δ 68.23, 68.81, 69.76, 69.91, 82.41, 83.72, 101.40, 106.43, 108.72, 115.74, 120.34, 123.48, 127.65, 144.30, 147.63, 147.93, 151.71, 152.68, 154.57, 155.22, 160.20, 160.80.
ESI-MS	[M+1]	473.3

f_7	**4-(benzo[d][1,3]dioxol-5-yl)-4'-(5-(2-(2-(2-fluoroethoxy)ethoxy)ethoxy)pyrimidin-2-yl)-2,2'-bithiazole**

NMR	^{1}H	(DMSO-d_6) δ 3.56 – 3.67 (m, 5H), 3.67 – 3.71 (m, 1H), 3.79 – 3.84 (m, 2H), 4.33 – 4.38 (m, 2H), 4.44 – 4.50 (m, 1H), 4.54 – 4.59 (m, 1H), 6.10 (s, 2H), 7.01 – 7.07 (m, 1H), 7.59 (d, J = 7.7 Hz, 2H), 8.24 (s, 1H), 8.53 (s, 1H), 8.69 (s, 2H)
	^{13}C	(DMSO-d_6) δ 30.75, 68.25, 68.82, 69.66, 69.81, 69.85, 69.95, 82.43, 83.75, 101.41, 106.44, 108.72, 115.74, 120.33, 123.46, 127.65, 144.28, 147.63, 147.94, 151.73, 152.65, 154.58, 155.21, 160.21, 160.79.
ESI-MS	[M+1]	517.3.

f_8	**6-(4'-(5-(2-(2-fluoroethoxy)ethoxy)pyrimidin-2-yl)-[2,2'-bithiazol]-4-yl)-[1,3]dioxolo[4,5-b]pyridine**

NMR	^{1}H	(DMSO-d_6) δ 3.69 – 3.74 (m, 1H), 3.75 – 3.80 (m, 1H), 3.82 – 3.88 (m, 2H), 4.35 – 4.41 (m, 2H), 4.49 – 4.54 (m, 1H), 4.58 – 4.64 (m, 1H), 6.23 (s, 2H), 7.85 (d, J = 1.9 Hz, 1H), 8.31 – 8.37 (m, 2H), 8.56 (s, 1H), 8.70 (s, 2H).
	^{13}C	(DMSO-d_6) δ 68.24, 68.82, 69.76, 69.91, 82.42, 83.74, 100.84, 112.29, 116.99, 123.73, 124.43, 136.85, 140.51, 144.32, 151.74, 152.66, 154.61, 158.22, 160.59, 160.79.
ESI-MS	[M+1]	474.3

f_9	**6-(4'-(3-(2-(2-fluoroethoxy)ethoxy)-4-methoxyphenyl)-[2,2'-bithiazol]-4-yl)-[1,3]dioxolo[4,5-b]pyridine**

NMR	^{1}H	(DMSO-d_6) δ 3.70 – 3.76 (m, 1H), 3.76 – 3.86 (m, 6H), 4.18 – 4.24 (m, 2H), 4.50 – 4.55 (m, 1H), 4.59 – 4.65 (m, 1H), 6.22 (s, 2H), 7.08 (d, J = 8.4 Hz, 1H), 7.57 – 7.64 (m, 2H), 7.82 (d, J = 1.9 Hz, 1H), 8.27 (s, 1H), 8.32 (d, J = 1.5 Hz, 2H).
	^{13}C	(DMSO-d_6) δ 55.60, 68.04, 69.05, 69.78, 69.93, 82.49, 83.80, 100.81, 111.19, 112.18, 112.22, 115.51, 116.66, 119.32, 124.44, 126.24, 136.80, 140.48, 148.10, 149.52, 152.59, 155.60, 158.17, 159.90, 160.80.
ESI-MS	[M+1]	502.2

f_{10}	**6-(4'-(3-fluoro-4-(2-(2-(2-fluoroethoxy)ethoxy)ethoxy)phenyl)-[2,2'-bithiazol]-4-yl)-[1,3]dioxolo[4,5-b]pyridine**

NMR	^{1}H	(DMSO-d_6) δ 3.71 (t, J = 3.7 Hz, 1H), 3.75 – 3.80 (m, 1H), 3.82 – 3.87 (m, 2H), 4.34 – 4.40 (m, 2H), 4.49 – 4.54 (m, 1H), 4.61 (t, J = 3.6 Hz, 1H), 6.10 (s, 2H), 7.04 (d, J = 15.6 Hz, 1H), 7.56 – 7.61 (m, 2H), 8.24 (s, 1H), 8.53 (s, 1H), 8.70 (s, 2H).
	^{13}C	(DMSO-d_6) δ 68.23, 68.81, 69.76, 69.91, 82.41, 83.72, 101.40, 106.43, 108.72, 115.74, 120.34, 123.48, 127.65, 144.30, 147.63, 147.93, 151.71, 152.68, 154.57, 155.22, 160.20, 160.80.
ESI-MS	[M+1]	473.3.

f_{11}	**4-(benzo[d][1,3]dioxol-5-yl)-4'-(4-(2-fluoroethoxy)phenyl)-2,2'-bithiazole**

NMR	^{1}H	(DMSO-d_6) δ 4.24 – 4.29 (m, 1H), 4.30 – 4.35 (m, 1H), 4.70 – 4.75 (m, 1H), 4.80 – 4.85 (m, 1H), 6.09 (s, 2H), 7.04 (d, J = 7.9 Hz, 1H), 7.09 (d, J = 8.9 Hz, 2H), 7.59 (d, J = 8.2 Hz, 2H), 7.97 (d, J = 8.8 Hz, 2H), 8.22 (d, J = 4.5 Hz, 2H).
	^{13}C	(DMSO-d_6) δ 67.09, 67.24, 81.53, 82.86, 101.40, 106.41, 108.71, 114.87, 115.17, 115.46, 120.31, 126.48, 127.65, 127.70, 147.60, 147.93, 155.18, 155.30, 158.46, 160.27.

ESI-MS	[M+1]	427.2.
f_{12}		**6-(4'-(4-(2-(2-(2-fluoroethoxy)ethoxy)ethoxy)phenyl)-[2,2'-bithiazol]-4-yl)-[1,3]dioxolo[4,5-b]pyridine**
NMR	^{1}H	(DMSO-d_6) δ 3.56 – 3.61 (m, 2H), 3.61 – 3.66 (m, 3H), 3.66 – 3.72 (m, 1H), 3.75 – 3.81 (m, 2H), 4.13 – 4.18 (m, 2H), 4.45 – 4.50 (m, 1H), 4.54 – 4.60 (m, 1H), 6.23 (s, 2H), 7.03 – 7.10 (m, 2H), 7.83 (d, *J* = 1.8 Hz, 1H), 7.92 – 7.99 (m, 2H), 8.22 (s, 1H), 8.32 (d, *J* = 2.4 Hz, 2H).
	^{13}C	(DMSO-d_6) δ 67.24, 68.97, 69.67, 69.82, 69.87, 69.97, 82.43, 83.75, 100.82, 112.24, 114.83, 115.25, 116.69, 124.45, 126.13, 127.61, 136.81, 140.49, 152.62, 155.43, 158.18, 158.82, 160.00, 160.85.
ESI-MS	[M+1]	515.2
f_{13}		**6-(4'-(5-(2-(2-(2-fluoroethoxy)ethoxy)ethoxy)pyrimidin-2-yl)-[2,2'-bithiazol]-4-yl)-[1,3]dioxolo[4,5-b]pyridine**
NMR	^{1}H	(DMSO-d_6) δ 3.58 – 3.64 (m, 5H), 3.66 – 3.71 (m, 1H), 3.79 – 3.84 (m, 2H), 4.33 – 4.39 (m, 2H), 4.44 – 4.50 (m, 1H), 4.54 – 4.59 (m, 1H), 6.23 (s, 2H), 7.84 (d, *J* = 1.8 Hz, 1H), 8.33 (d, *J* = 1.9 Hz, 1H), 8.34 (s, 1H), 8.55 (s, 1H), 8.69 (s, 2H).
	^{13}C	(DMSO-d_6) δ 68.27, 68.83, 69.67, 69.82, 69.87, 69.96, 82.44, 83.76, 100.84, 112.29, 116.99, 123.71, 124.43, 136.85, 140.51, 144.31, 151.76, 152.63, 152.66, 154.62, 158.22, 160.59, 160.79.
ESI-MS	[M+1]	518.2
f_{14}		**4-(benzo[d][1,3]dioxol-5-yl)-4'-(3-(2-(2-(2-fluoroethoxy)ethoxy)ethoxy)-4-methoxyphenyl)-2,2'-bithiazole**
NMR	^{1}H	(DMSO-d_6) δ 3.60 (dt, *J* = 2.0, 6.0 Hz, 2H), 3.61 – 3.67 (m, 3H), 3.67 – 3.72 (m, 1H), 3.77 – 3.84 (m, 5H), 4.17 – 4.23 (m, 2H), 4.43 – 4.49 (m, 1H), 4.52 – 4.59 (m, 1H), 6.10 (s, 2H), 7.01 – 7.06 (m, 1H), 7.08 (d, *J* = 8.4 Hz, 1H), 7.56 – 7.65 (m, 4H), 8.24 (d, *J* = 11.8 Hz, 2H).
	^{13}C	(DMSO-d_6) δ 55.59, 68.01, 69.05, 69.68, 69.83, 69.90, 69.98, 82.44, 83.76, 101.41, 106.41, 108.73, 111.13, 112.16, 115.30, 115.45, 119.27, 120.30, 126.28, 127.70, 147.61, 147.94, 148.14, 149.48, 155.17, 155.58, 160.15, 160.25.
ESI-MS	[M+1]	545.2
f_{15}		**4-(benzo[d][1,3]dioxol-5-yl)-4'-(5-methoxypyrimidin-2-yl)-2,2'-bithiazole**
NMR	^{1}H	(DMSO-d_6) δ 3.99 (s, 3H), 6.10 (s, 2H), 7.02 – 7.08 (m, 1H), 7.57 – 7.63 (m, 2H), 8.25 (s, 1H), 8.54 (s, 1H), 8.68 (s, 2H).
	^{13}C	(DMSO-d_6) δ 56.29, 101.39, 106.42, 108.71, 115.72, 120.32, 123.44, 127.64, 143.85, 147.62, 147.93, 152.30, 152.65, 154.58, 155.20, 160.19, 160.79.
ESI-MS	[M+1]	397.2
f_{16}	**NMR**	**6-(4'-(5-methoxypyrimidin-2-yl)-[2,2'-bithiazol]-4-yl)-[1,3]dioxolo[4,5-b]pyridine**
NMR	^{1}H	(DMSO-d_6) δ 4.01 (s, 3H), 6.22 (s, 2H), 7.85 (d, *J* = 3.8 Hz, 1H), 8.33 – 8.43 (m, 2H), 8.53 (t, *J* = 2.9 Hz, 1H), 8.68 (t, *J* = 3.0 Hz, 2H).
	ESI-MS	(DMSO-d_6) δ 56.44, 100.03, 111.31, 117.52, 120.71, 123.64, 140.92, 142.11, 142.22, 148.29, 150.03, 151.62, 153.87, 153.89, 160.40, 161.89.
ESI-MS	[M+1]	398.3
f_{17}		**6-(4'-(4-methoxyphenyl)-[2,2'-bithiazol]-4-yl)-[1,3]dioxolo[4,5-b]pyridine**
NMR	^{1}H	(DMSO-d_6) δ 3.82 (s, 3H), 6.23 (s, 2H), 7.03 – 7.09 (m, 2H), 7.84 (d, *J* = 1.9 Hz, 1H), 7.94 – 7.99 (m, 2H), 8.22 (s, 1H), 8.33 (d, *J* = 2.6 Hz, 2H).
	^{13}C	(DMSO-d_6) δ 55.28, 100.83, 112.25, 114.34, 115.26, 116.70, 118.19, 124.46, 126.09, 127.61, 136.81, 140.50, 152.62, 155.47, 158.20, 159.60, 160.01, 160.86.
ESI-MS	[M+1]	396.3
f_{18}		**6-(4'-(3,4-dimethoxyphenyl)-[2,2'-bithiazol]-4-yl)-[1,3]dioxolo[4,5-b]pyridine**

NMR	^{1}H	(DMSO-d_6) δ 3.71 (s, 1H), 3.83 (s, 4H), 6.23 (s, 3H), 7.07 (d, *J* = 8.3 Hz, 1H), 7.60 (d, *J* = 2.0 Hz, 1H), 7.84 (d, *J* = 1.9 Hz, 1H), 8.28 (s, 1H), 8.32 – 8.37 (m, 3H).
ESI-MS	[M+1]	426.2
f_{19}		**6-(4'-(2,4-dimethoxyphenyl)-[2,2'-bithiazol]-4-yl)-[1,3]dioxolo[4,5-b]pyridine**
NMR	^{1}H	(DMSO-d_6) δ 3.84 (s, 3H), 3.95 (s, 3H), 6.23 (s, 2H), 6.67 – 6.74 (m, 2H), 7.83 (d, *J* = 2.0 Hz, 1H), 8.09 – 8.17 (m, 2H), 8.29 – 8.34 (m, 2H).
	^{13}C	(DMSO-d_6) δ 55.41, 55.73, 98.66, 100.82, 105.61, 112.24, 114.79, 116.54, 118.28, 124.49, 130.21, 136.79, 140.49, 151.52, 152.58, 157.88, 158.17, 158.32, 160.68, 161.06.
ESI-MS	[M+1]	426.2
f_{20}		**6-(4'-(3,4-bis(2-(2-fluoroethoxy)ethoxy)phenyl)-[2,2'-bithiazol]-4-yl)-[1,3]dioxolo[4,5-b]pyridine**
NMR	^{1}H	(DMSO-d_6) δ 3.68 – 3.86 (m, 6H), 3.89 – 3.97 (m, 2H), 4.17 – 4.23 (m, 2H), 4.25 – 4.35 (m, 2H), 4.47 – 4.59 (m, 2H), 4.59 – 4.68 (m, 2H), 6.23 (s, 2H), 6.68 – 6.81 (m, 2H), 7.83 (d, *J* = 1.9 Hz, 1H), 8.14 (d, *J* = 8.7 Hz, 1H), 8.26 – 8.34 (m, 3H).
	^{13}C	(DMSO-d_6) δ 67.33, 67.51, 68.77, 68.98, 69.63, 69.77, 69.92, 82.47, 83.79, 100.01, 100.81, 106.49, 112.24, 115.08, 116.53, 118.19, 124.49, 130.15, 136.79, 140.49, 151.55, 152.58, 157.00, 158.17, 158.22, 159.73, 161.07.
ESI-MS	[M+1]	578.1
h_4		**6-(4'-(5-(2-bromoethoxy)pyrimidin-2-yl)-[2,2'-bithiazol]-4-yl)-[1,3]dioxolo[4,5-b]pyridine,**
NMR	^{1}H	(DMSO-d_6) δ 3.75 – 4.00 (m, 2H), 4.50 – 4.66 (m, 2H), 6.23 (s, 2H), 7.84 (d, J = 1.9 Hz, 1H), 8.23 – 8.44 (m, 2H), 8.56 (s, 1H), 8.71 (s, 2H).
ESI-MS	[M+1] [M+1]	490.2 491.2.
h_5		**4-(benzo[d][1,3]dioxol-5-yl)-4'-(5-(2-bromoethoxy)pyrimidin-2-yl)-2,2'-bithiazole**
NMR	^{1}H	(DMSO-d_6) δ 3.72 (t, J = 7.1 Hz, 2H), 4.38 (t, J = 7.1 Hz, 2H), 6.07 (s, 2H), 6.97 (d, J = 7.5 Hz, 1H), 7.47 (dd, J = 1.5, 7.4 Hz, 1H), 7.53 (d, J = 1.5 Hz, 1H), 7.69 (s, 1H), 8.23 (s, 1H), 8.27 (s, 2H).
	^{13}C	(DMSO-d_6) δ 31.02, 68.73, 101.40, 106.43, 108.71, 115.75, 120.33, 123.68, 127.64, 144.46, 147.63, 147.93, 151.24, 152.99, 154.48, 155.22, 160.18, 160.83.
ESI-MS	[M+1] [M+2]	489.2 490.3.
h_{5*}		**2-((2-(4'-(benzo[d][1,3]dioxol-5-yl)-[2,2'-bithiazol]-4-yl)pyrimidin-5-yl)oxy)ethyl 4-methylbenzenesulfonate**
ESI-MS	[M+1]	581.2
h_6		**2-(2-((2-(4'-(benzo[d][1,3]dioxol-5-yl)-[2,2'-bithiazol]-4-yl)pyrimidin-5-yl)oxy)ethoxy)ethyl 4-methylbenzenesulfonate**
NMR	^{1}H	(DMSO-d_6) δ 2.38 (s, 3H), 3.65 – 3.70 (m, 2H), 3.72 – 3.78 (m, 2H), 4.13 – 4.18 (m, 2H), 4.26 – 4.32 (m, 2H), 6.10 (s, 2H), 7.02 – 7.07 (m, 1H), 7.46 (s, 1H), 7.59 (s, 2H), 7.76 – 7.80 (m, 2H), 8.25 (s, 1H), 8.54 (s, 1H), 8.65 (d, J = 13.3 Hz, 3H).
	^{13}C	(DMSO-d_6) δ 21.11, 68.06, 68.13, 68.69, 69.97, 101.41, 106.44, 108.73, 115.75, 120.34, 123.51, 127.69, 130.17, 132.35, 144.27, 144.96, 147.64, 147.94, 151.67, 152.69, 154.58, 155.22, 160.21, 160.82.
ESI-MS	[M+1]	625.3.
h_{6*}		**4-(benzo[d][1,3]dioxol-5-yl)-4'-(5-(2-(2-iodoethoxy)ethoxy)pyrimidin-2-yl)-2,2'-bithiazole**
NMR	^{1}H	(DMSO-d_6) δ 3.37 (d, *J* = 6.4 Hz, 2H), 3.75 (t, *J* = 6.4 Hz, 2H), 3.84 – 3.91 (m, 2H), 4.33 – 4.40 (m, 2H), 6.10 (s, 2H), 7.02 – 7.10 (m, 1H), 7.59 (d, *J* = 1.2 Hz, 2H), 8.25 (s, 1H), 8.54 (s, 1H), 8.69 (s, 2H).

	^{13}C	(DMSO-d_6) δ 5.32, 68.24, 71.02, 101.42, 106.44, 108.74, 115.76, 120.35, 123.51, 127.66, 144.35, 147.64, 147.95, 151.72, 152.68, 154.58, 155.23, 160.22, 160.81.
ESI-MS	[M+1]	581.3
h_7		**2-(2-(2-((2-(4'-(benzo[d][1,3]dioxol-5-yl)-[2,2'-bithiazol]-4-yl)pyrimidin-5-yl)oxy)ethoxy)ethoxy)ethyl 4-methylbenzenesulfonate**
NMR	^{1}H	(DMSO-d_6) δ 2.40 (s, 3H), 3.46 – 3.51 (m, 2H), 3.51 – 3.61 (m, 4H), 3.63 – 3.70 (m, 1H), 3.75 – 3.85 (m, 2H), 4.06 – 4.14 (m, 2H), 4.30 – 4.39 (m, 2H), 6.05 – 6.12 (m, 2H), 7.04 (dt, J = 1.1, 7.5 Hz, 1H), 7.44 – 7.49 (m, 2H), 7.60 (dd, J = 1.3, 7.6 Hz, 2H), 7.74 – 7.81 (m, 2H), 8.25 (d, J = 1.2 Hz, 1H), 8.53 (d, J = 1.2 Hz, 1H), 8.65 – 8.71 (m, 2H).
	^{13}C	(DMSO-d_6) δ 21.13, 67.95, 68.24, 68.80, 69.73, 69.83, 70.04, 101.41, 106.44, 108.73, 115.75, 120.34, 123.47, 125.53, 127.68, 128.08, 130.18, 132.38, 144.28, 144.96, 147.63, 147.94, 151.72, 152.65, 154.58, 155.22, 160.21, 160.80.
ESI-MS	[M+1]	669.3.
h_{7°		**4-(benzo[d][1,3]dioxol-5-yl)-4'-(5-(2-(2-(2-chloroethoxy)ethoxy)ethoxy)pyrimidin-2-yl)-2,2'-bithiazole**
NMR	^{1}H	(DMSO-d_6) δ 3.59 – 3.64 (m, 4H), 3.66 – 3.74 (m, 4H), 3.79 – 3.85 (m, 2H), 4.33 – 4.39 (m, 2H), 6.10 (s, 2H), 7.02 – 7.08 (m, 1H), 7.59 (d, *J* = 1.1 Hz, 2H), 8.25 (s, 1H), 8.53 (s, 1H), 8.69 (s, 2H).
	^{13}C	(DMSO-d_6) δ 43.63, 68.26, 68.82, 69.69, 69.93, 70.58, 101.41, 106.44, 108.72, 115.74, 120.34, 123.47, 127.65, 144.30, 147.63, 147.94, 151.73, 152.65, 154.58, 155.22, 160.21, 160.79.
ESI-MS	[M+1]	533.2
h_{7^*}		**4-(benzo[d][1,3]dioxol-5-yl)-4'-(5-(2-(2-(2-iodoethoxy)ethoxy)ethoxy)pyrimidin-2-yl)-2,2'-bithiazole**
NMR	^{1}H	(DMSO-d_6) δ 3.32 (d, *J* = 6.5 Hz, 2H), 3.58 – 3.64 (m, 4H), 3.67 (t, *J* = 6.5 Hz, 2H), 3.81 – 3.84 (m, 2H), 4.34 – 4.39 (m, 2H), 6.10 (s, 2H), 7.02 – 7.08 (m, 1H), 7.57 – 7.63 (m, 2H), 8.25 (s, 1H), 8.53 (s, 1H), 8.69 (s, 2H).
	^{13}C	(DMSO-d_6) δ 5.49, 68.27, 68.85, 69.34, 69.96, 71.01, 101.40, 106.44, 108.72, 115.74, 120.34, 123.47, 127.65, 144.31, 147.63, 147.94, 151.74, 152.65, 154.59, 155.22, 160.21, 160.80.
ESI-MS	[M+1]	625.2
h_8		**2-(2-((2-(4'-([1,3]dioxolo[4,5-b]pyridin-6-yl)-[2,2'-bithiazol]-4-yl)pyrimidin-5-yl)oxy)ethoxy)ethyl 4-methylbenzenesulfonate**
NMR	^{1}H	(DMSO-d_6) δ 2.28 (s, 3H), 3.63 – 3.70 (m, 4H), 4.13 – 4.18 (m, 4H), 6.19 (s, 2H), 7.08 – 7.13 (m, 2H), 7.71 (d, *J* = 1.8 Hz, 1H), 8.20 – 8.26 (m, 2H), 8.52 – 8.60 (m, 5H).
ESI-MS	[M+1]	626.3
h_9		**2-(2-(5-(4'-([1,3]dioxolo[4,5-b]pyridin-6-yl)-[2,2'-bithiazol]-4-yl)-2-methoxyphenoxy)ethoxy)ethyl 4-methylbenzenesulfonate**
NMR	^{1}H	(DMSO-d_6)δ 2.35 (s, 3H), 3.71 – 3.74 (m, 4H), 3.81 (s, 5H), 4.08 – 4.14 (m, 2H), 4.14 – 4.20 (m, 2H), 6.23 (s, 2H), 7.08 (d, J = 8.5 Hz, 1H), 7.40 – 7.45 (m, 2H), 7.56 (d, J = 2.0 Hz, 1H), 7.61 (dd, J = 2.0, 8.3 Hz, 1H), 7.76 – 7.81 (m, 2H), 7.83 (d, J = 1.9 Hz, 1H), 8.27 (s, 1H), 8.33 (t, J = 1.0 Hz, 2H).
	^{13}C	(DMSO-d_6) δ 21.10, 55.61, 67.91, 68.06, 68.94, 70.08, 100.82, 111.13, 112.20, 112.23, 115.53, 116.67, 119.32, 124.45, 125.53, 126.24, 127.69, 128.09, 130.14, 132.39, 136.80, 140.49, 144.91, 148.08, 149.49, 152.60, 155.60, 158.18, 159.92, 160.80.
ESI-MS	[M+1]	654.3.
h_{10}		**2-(2-(2-(4-(4'-([1,3]dioxolo[4,5-b]pyridin-6-yl)-[2,2'-bithiazol]-4-yl)-2-fluorophenoxy)ethoxy)ethoxy)ethyl 4-methylbenzenesulfonate**
NMR	^{1}H	(DMSO-d_6) δ 2.40 (s, 3H), 3.46 – 3.51 (m, 2H), 3.52 – 3.61 (m, 3H), 3.73 – 3.79 (m, 2H), 4.08 – 4.14 (m, 2H), 4.19 – 4.24 (m, 2H), 6.23 (s, 2H), 7.29 (t, J = 8.8 Hz, 1H), 7.44 – 7.50 (m, 2H), 7.76 – 7.89 (m, 5H), 8.32 (m, J = 1.2 Hz, 2H), 8.34 (s, 1H).

	^{13}C	(DMSO-d_6) δ 21.12, 67.93, 68.37, 68.81, 69.72, 69.90, 70.03, 100.82, 112.23, 113.66, 113.81, 115.18, 116.44, 116.84, 122.60, 122.63, 124.41, 125.53, 126.64, 126.70, 127.68, 128.08, 130.17, 132.38, 136.81, 140.49, 144.94, 146.60, 146.68, 150.76, 152.65, 152.70, 154.20, 154.22, 158.19, 160.22, 160.65.
ESI-MS	[M+1]	686.3
h_{10*}		**6-(4'-(3-fluoro-4-(2-(2-(2-iodoethoxy)ethoxy)ethoxy)phenyl)-[2,2'-bithiazol]-4-yl)-[1,3]dioxolo[4,5-b]pyridine**
NMR	^{1}H	(DMSO-d_6) δ 3.32 (d, *J* = 6.5 Hz, 2H), 3.59 – 3.66 (m, 4H), 3.68 (d, *J* = 6.5 Hz, 2H), 3.80 – 3.83 (m, 2H), 4.22 – 4.28 (m, 2H), 6.24 (s, 2H), 7.31 (t, *J* = 8.8 Hz, 1H), 7.79 – 7.85 (m, 2H), 7.85 – 7.91 (m, 1H), 8.31 – 8.37 (m, 3H).
	^{13}C	(DMSO-d_6) δ 5.47, 68.42, 68.86, 69.35, 70.00, 71.01, 100.82, 112.23, 113.66, 113.81, 115.22, 116.43, 116.83, 122.60, 122.63, 124.41, 126.69, 136.81, 140.48, 146.61, 146.70, 150.77, 152.64, 152.71, 154.20, 154.22, 158.19, 160.21, 160.64.
ESI-MS	[M+1]	642.2
h_{11}		**2-(4-(4'-(benzo[d][1,3]dioxol-5-yl)-[2,2'-bithiazol]-4-yl)phenoxy)ethyl 4-methylbenzenesulfonate**
NMR	^{1}H	(DMSO-d_6) δ 2.42 (s, 3H), 4.20 – 4.27 (m, 2H), 4.33 – 4.40 (m, 2H), 6.10 (s, 2H), 6.95 (s, 1H), 7.05 (s, 1H), 7.46 (s, 2H), 7.58 (s, 2H), 7.73 (s, 2H), 7.81 (s, 1H), 7.93 (s, 1H), 8.22 (d, *J* = 7.0 Hz, 2H).
	^{13}C	(DMSO-d_6) δ 21.17, 65.42, 67.91, 69.15, 101.40, 106.41, 108.72, 114.86, 115.24, 115.48, 120.31, 127.58, 127.67, 127.77, 130.24, 130.27, 131.84, 132.20, 145.12, 145.29, 147.61, 147.94, 155.19, 155.26, 158.02, 160.26, 160.28.
ESI-MS	[M+1]	427.2
h_{12}		**6-(4'-(4-(2-(2-(2-iodoethoxy)ethoxy)ethoxy)phenyl)-[2,2'-bithiazol]-4-yl)-[1,3]dioxolo[4,5-b]pyridine**
NMR	^{1}H	(DMSO-d_6) δ 3.32 (d, *J* = 6.5 Hz, 2H), 3.61 (ttt, *J* = 1.5, 3.1, 6.4 Hz, 3H), 3.68 (t, *J* = 6.5 Hz, 2H), 3.74 – 3.81 (m, 2H), 4.13 – 4.19 (m, 2H), 6.23 (s, 2H), 7.04 – 7.10 (m, 2H), 7.84 (d, *J* = 1.8 Hz, 1H), 7.93 – 7.99 (m, 2H), 8.22 (s, 1H), 8.30 – 8.34 (m, 2H).
	^{13}C	(DMSO-d_6) δ 5.52, 67.26, 68.99, 69.36, 69.98, 71.03, 100.82, 112.24, 114.85, 115.26, 116.69, 124.45, 126.13, 127.61, 136.81, 140.49, 152.62, 155.43, 158.19, 158.82, 160.00, 160.86.
ESI-MS	[M+1]	624.1
h_{13}		**6-(4'-(5-(2-(2-(2-iodoethoxy)ethoxy)ethoxy)pyrimidin-2-yl)-[2,2'-bithiazol]-4-yl)-[1,3]dioxolo[4,5-b]pyridine**
NMR	^{1}H	(DMSO-d_6) δ 3.33 (d, *J* = 6.4 Hz, 2H), 3.58 – 3.70 (m, 6H), 3.78 – 3.86 (m, 2H), 4.33 – 4.40 (m, 2H), 6.23 (s, 2H), 7.85 (d, *J* = 1.8 Hz, 1H), 8.31 – 8.37 (m, 2H), 8.55 (s, 1H), 8.70 (d, *J* = 2.6 Hz, 2H).
	^{13}C	(DMSO-d_6) δ 5.51, 68.28, 68.85, 69.34, 69.96, 71.02, 100.83, 112.28, 116.98, 123.70, 124.42, 136.84, 140.50, 144.32, 151.76, 152.61, 152.65, 154.62, 158.21, 160.57, 160.78.
ESI-MS	[M+1]	626.2
h_{14}		**4-(benzo[d][1,3]dioxol-5-yl)-4'-(3-(2-(2-(2-iodoethoxy)ethoxy)ethoxy)-4-methoxyphenyl)-2,2'-bithiazole**
NMR	^{1}H	(DMSO-d_6) δ 3.32 (t, *J* = 6.4 Hz, 2H), 3.55 – 3.73 (m, 5H), 3.81 (d, *J* = 10.5 Hz, 5H), 4.20 (dt, *J* = 3.9, 7.0 Hz, 2H), 6.10 (s, 2H), 6.98 – 7.13 (m, 2H), 7.50 – 7.69 (m, 4H), 8.12 – 8.34 (m, 2H).
	^{13}C	(DMSO-d_6) δ 5.51, 55.56, 55.62, 68.04, 69.07, 69.40, 69.96, 71.02, 101.38, 101.40, 106.38, 106.40, 108.72, 111.20, 112.16, 115.31, 115.45, 119.27, 120.27, 120.30, 126.27, 127.70, 147.61, 147.90, 147.94, 148.11, 148.13, 149.47, 149.50, 155.16, 155.54, 155.57, 160.14, 160.24.
ESI-MS	[M+1]	653.1